Investigation of the laser-based Target Normal Sheath Acceleration (TNSA) process for high-energy ions — an analytical and numerical study

Dissertation
zur Erlangung des akademischen Grades
doctor rerum naturalium (Dr. rer. nat.)

vorgelegt dem Rat der
Physikalisch-Astronomischen Fakultät
der Friedrich-Schiller-Universität Jena

von Dipl.-Phys. Thomas Kiefer
geboren am 23.05.1982 in Saalfeld/Saale

Gutachter

1. Prof. Dr. Malte C. Kaluza
   Institut für Optik und Quantenelektronik
   Friedrich-Schiller-Universität Jena
   Jena, Deutschland
2. Jun.-Prof. Dr. Stefan Skupin
   Institut für Festkörpertheorie und -optik
   Friedrich-Schiller-Universität Jena
   Jena, Deutschland
3. Prof. Dr. Patrick Mora
   Centre de Physique Théorique
   École Polytechnique
   Palaiseau, Frankreich
4. Prof. Dr. Vladimir T. Tikhonchuk
   Centre Lasers Intenses et Applications
   Université Bordeaux 1
   Talence, Frankreich

Tag der Disputation: 9. Januar 2014

Zusammenfassung

Die vorliegende Arbeit beschäftigt sich mit der laserbasierten Ionenbeschleunigung im Target Normal Sheath Acceleration (TNSA) Prozess. Verschiedene, eindimensionale Modelle für die Plasmaexpansion in ein Vakuum, die auf die Pionierarbeit von Gurevich[1] zurückgehen, werden untersucht, um grundlegende Zusammenhänge zwischen den verschiedenen Anfangsgrößen — wie etwa Elektronenparameter, Laser- und Targeteigenschaften —- und den experimentell beobachteten Ionenspektren und den maximalen Ionenenergien abzuleiten.

Die Lösung der Problemstellungen dieser Arbeit erfolgt sowohl analytisch als auch numerisch. Der entwickelte Hybridcomputercode behandelt die Ionen entsprechend einem Particle-In-Cell (PIC) Code kinetisch, die Elektronen hingegen werden in einem Gleichgewichtszustand mit dem elektrischen Potential des Ladungstrennungsfeldes auf der Targetrückseite angenommen.

Im ersten Teil der Arbeit wird der Zusammenhang zweier verschiedener Ansätze zur Beschreibung der heißen Elektronenpopulation innerhalb dieser Modelle untersucht. Hierbei zeigt sich, dass ein in der Literatur häufig benutzter hydrodynamischer Zugang in der allgemeinen kinetischen Beschreibung der Elektronen enthalten ist, unter der Annahme einer bestimmten Klasse von Phasenraumdichten. Diese Klasse enthält eine stufenförmige Energieverteilung, welche die Energieerhaltung während der Expansion selbstkonsistent sicherstellt, d.h. die Expansion verläuft adiabatisch.

Der Einfluss einer stufenförmigen Energieverteilung der heißen Elektronen auf den Ionenbeschleunigungsprozess wird im zweiten Teil dieser Arbeit untersucht, insbesondere im Vergleich zu weitverbreiteten adiabatischen Modellen, welche eine anfängliche Maxwellverteilung der heißen Elektronen annehmen. Die Annahme einer stufenförmigen Energieverteilung, welche deutlich von einer Maxwellverteilung abweicht, führt auf eine Skalierung der maximalen Ionenenergie als Funktion der Laserintensität, welche um fast eine Größenordnung von dem Skalierungsgesetz abweicht, das man unter der Annahme einer anfänglichen Maxwellverteilung erhält. Die Anwendung der verschiedenen adiabatischen Expansionsmodelle auf Daten von Experimenten mit ultrakurzen Pulsen (d.h. mit Pulsdauern kürzer als 80 fs) zeigt klar, dass sich die Vorhersagen des Expansionsmodelles unter Annahme einer stufenförmigen Energieverteilung gut mit den experimentellen Resultaten für die maximale Ionenenergien und die Ionenspektren decken, während dies für die Modelle, welche eine anfängliche Maxwellverteilung annehmen, nicht der Fall ist. Dieses essenzielle Resultat sollte bei der Interpretation von Experimenten in Zukunft berücksichtigt werden.

Nach der Betrachtung des Einflusses der speziellen Form der Energieverteilung der heißen Elektronen auf den Prozess der Plasmaexpansion, wird im dritten Teil der Arbeit die Auswirkung eines anfänglichen Ionendichtegradienten auf der Targetrückseite untersucht. Hierbei behandeln wir ein Expansionsmodell für ein Target welches einen linearen Dichteabfall auf der Targetrückseite besitzt. Das entwickelte analytische Modell ist — unter der Annahme eines empirischen Zusammenhanges zwischen der Skalenlänge des initialen Dichtegradientens und der initialen Targetdicke — in der Lage den experimentell beobachteten Zusammenhang zwischen der maximalen Ionenenergie und der initialen Targetdicke zu reproduzieren. Mittels unseres Modells können die Auswirkungen eines Laservorpulses auf den Plasmaexpansionsprozess betrachtet werden, einschließlich der experimentell beobachteten optimalen Targetdicke.

Zusammenfassend haben wir gezeigt, dass nicht nur die qualitativen Eigenschaften des Lasers, des Targets und der heißen Elektronen — wie etwa die Laserintensität, die Targetdicke, die Temperatur und Dichte der heißen Elektronen — das Ionenspektrum und die maximale Ionenenergie bestimmen, sondern auch die spezielleren Eigenschaften des Lasers und der heißen Elektronenpopulation — wie etwa der Laservorpuls und die Form der heißen Elektronenverteilung. Mit diesen Erkenntnissen sind neue Einsichten in die laserbasierte Ionenbeschleunigung möglich, welche in Zukunft helfen könnten den Beschleunigungsprozess zu optimieren.

Abstract

The present work is dealing with the theoretical description of laser-driven ion acceleration in the Target Normal Sheath Acceleration (TNSA) process. Various, one-dimensional models describing the laser-heated plasma expansion into vacuum, which were inspired by the pioneering work of Gurevich,[1] are studied to derive principal relations between the initial conditions of the laser-target interaction — such as electron parameters, laser and target properties — and the ion spectra and maximum ion energies which can be observed in experiments.

The solutions of the physical problems considered in this thesis are derived analytically as well as numerically. The developed hybrid computer code treats the ions kinetically similar to a Particle-in-Cell (PIC) code, whereas the electrons are assumed to be in equilibrium with the electric potential of the charge-separation field on the rear surface of the target.

In the first part of this work, two different approaches for the description of the hot electron population are compared when applied to these models. It turns out that a hydrodynamic ansatz for the electron density, which has widely been used in the literature, is contained in the general kinetic treatment of the electrons under the assumption of a particular class of electron energy distributions. This class contains a step-like electron energy distribution which self-consistently ensures energy conservation during the plasma expansion, i.e. the expansion is adiabatic.

The impact of a step-like hot electron energy distribution on the ion acceleration process is described in the second part of this thesis, with the focus on the comparison to adiabatic plasma expansion models assuming an initially Maxwellian hot electron distribution. The assumption of a step-like distribution, which remarkably deviates from a Maxwellian phase space density, leads to a scaling of the maximum ion energy with the laser intensity which differs by almost one order of magnitude from the scaling law found for the case of an initially Maxwellian distribution. The application of the various adiabatic plasma expansion models to the data from ultrashort-pulse experiments (i.e. with laser pulse durations shorter than 80 fs) convincingly shows that the analytic results of the expansion model assuming a step-like electron energy distribution reproduce the observed maximum ion energies and the corresponding ion spectra quite well, while this is not the case for the models assuming Maxwellian electron distributions. This is an essential fact which has to be considered in the interpretation of future experiments.

After the consideration of the influence of the particular shape of the hot electron energy distribution on the plasma expansion process, the third part of this work covers the impact of an initial density gradient at the rear surface of the target. Here, we discuss an expansion model for a target with an initially linear density ramp at the target rear surface. The developed analytical model is able — under the assumption of an empirical relation between the scale length of the initial density gradient and the initial target thickness —- to closely reproduce the experimentally observed relation between the maximum ion energy and the initial target thickness. By using our model prepulse effects in the plasma expansion process can be considered, explaining the experimental observation of an optimal target thickness.

In summary, we show that not only the qualitative parameters of the laser, the target and the hot electrons — such as the laser intensity, the target thickness, the hot electron temperature and density — determine the ion spectrum and the maximum ion energy but also the more specific details of the laser and the hot electron population — such as the laser prepulse and the shape of the hot electron distribution. With these findings, new insights into the laser-driven ion acceleration process are possible which might help to optimize the ion acceleration in the future.

Contents

I. Introduction and thesis outline 1

II. Basics 6

1 Laser plasma ion acceleration — the TNSA process 6

2 Basic concepts of plasma theory 10
- 2.1 Kinetic description 13
- 2.2 Hydrodynamic approach 15
- 2.3 Stationary electron model 17

3 The central model of high-intensity laser-driven plasma expansion 19

III. Plasma models assuming Maxwellian hot electrons 22

4 The free expansion of a plasma slab into vacuum 22
- 4.1 The self-similar solution 23
- 4.2 Mora's model 24

5 Extensions of the Mora model 27
- 5.1 Advanced description of the electrons 27
  - 5.1.1 The adiabatic Maxwellian model 28
  - 5.1.2 The kinetic Maxwellian model 30
- 5.2 Inclusion of cold electrons 35
- 5.3 Extensions regarding the ion distribution 39

IV. Expansion caused by a step-like electron energy distribution 44

6 The stationary hydrodynamic approach 44
- 6.1 Relation to the stationary kinetic description of the electrons 46
- 6.2 Equivalence and deviations of the different approaches 47
- 6.3 Generalization to relativistic energies 49

7 Plasma expansion properties 54
- 7.1 Analytics for step-like distributed electrons 54
- 7.2 Comparison to adiabatic models assuming Maxwellian electrons 61

7.3 Application of the different adiabatic models to experimental results 66

V. Expansion of a target with a linear density gradient **75**

8 Connection of the Mora model to experiments and the prepulse influence **75**

9 Extension of the Mora model assuming an initial density gradient **79**
9.1 Influence of an initial density gradient on the ion acceleration process 80
9.2 Expansion model assuming an initially linear density gradient 85
9.3 Application of the developed expansion model to experimental results 87

VI. Conclusion and outlook **94**

Bibliography **101**

List of Figures **117**

List of Symbols **119**

Appendix **125**

A The simulation code **125**
A.1 The Particle-in-Cell (PIC) approach 127
A.1.1 The concept 127
A.1.2 Weighting of particle and grid quantities 130
A.2 The Störmer Verlet algorithm 132
A.3 A relativistic particle-stepper 133
A.4 Solution of the nonlinear Poisson equation 135

B Maths **140**
B.1 Inversion of the integral equation (6.13) 140
B.2 Evaluation of the limit in Eq. (B.15) 142
B.3 Proof of Eq. (7.18) 146

Lebenslauf **151**

Ehrenwörtliche Erklärung **153**

I. Introduction and thesis outline

In physics and applied science, there is a broad interest in the production of highly energetic ion beams. Beside the use of conventional accelerators, the possibility of laser-plasma-based ion accelerators has been discussed since the 1970's.[2–5] In the beginning of the 21st century, the focus on laser-driven acceleration has been renewed by the first experiments using short-pulse high-power lasers[6–9] which became widely available at that time. The large interest is mainly motivated by the remarkable properties of the produced ion beams, which are characterized by (i) a short duration, which is initially of the order of the laser pulse length,[6,8,10] (ii) a small divergence angle,[11] (iii) a highly laminar flux[12,13] and (iv) a large number of ions (e.g., up to 10^{13} protons[14]). That makes laser-based ion accelerators a potential and promising source for various applications in medical physics,[15–21] for new diagnostics techniques,[22–27] for astrophysical investigations concerning high-energy matter interactions,[28–33] for isotope production,[17,34] as pre-accelerators for conventional accelerators[12,35] and for fast ignition.[36–43]

The primary ion acceleration mechanism in most of the experiments performed so far is the so-called *Target Normal Sheath Acceleration* (TNSA), see chapter 1. This process was realized with short-pulse lasers in the femto- and picosecond range with intensities above $10^{18}\,\mathrm{W/cm^2}$ for the first time in the beginning of the 21st century by Snavely, Hatchett, Clark, Wilks and others.[6–9] Here, a laser pulse ionizes atoms at the front side of the target, forming a plasma. Due to the interaction of the laser pulse with that plasma, electrons are accelerated up to relativistic energies.[44,45] These energetic electrons penetrate through the target,[46–49] creating a hot electron cloud at the rear side of target.[50] The induced charge separation is the source for a strong, longitudinal electric field in the $\mathrm{TV\,m^{-1}}$ range. It immediately ionizes atoms at the target back side. Driven by the strong electrostatic field, the ions overcome the bonding force and start to expand into the adjacent vacuum, finally reaching energies up to several tens of MeV per nucleon.[6]

Beside the experimental progress achieved in the recent past, the expansion of a plasma into vacuum has already been investigated theoretically over several decades. On account of the complex physics and the limited computer power during the early stages, the first theoretical approaches are based on a one-dimensional and purely electrostatic description.[1,2,51] Here, one starts with a plasma, which is composed of a single species of ions and a single population of electrons. Initially, the spatial ion density n_i is modeled by a semi-infinite slab,

$$n_\mathrm{i}(t=0) = \begin{cases} n_{\mathrm{i},0} & : x \leq 0 \\ 0 & : x > 0\,, \end{cases} \tag{0.1}$$

where x and t refer to the spatial coordinate and the time, respectively, while $n_{\mathrm{i},0}$ denotes the initial value of the ion number density in the plasma slab(1). In contrast to the ions, which are initially at rest, the energy distribution of the laser-heated, hot electrons is assumed to be Maxwellian with a temperature $T_{\mathrm{e},0} > 0$. A central aspect of the pioneering studies[1,2,51] is the assumption that the electrons arrange themselves in a stationary configuration with the electric potential ϕ on a time scale which is small compared to the characteristic time of changes in the ion distribution. Under this assumption, the relation(2)

---

(1) Usually, $Z_\mathrm{i}\, n_{\mathrm{i},0}$ is set equal to the initial number density $n_{\mathrm{e},0}$ of the hot electrons, which has been estimated before (see chapter 8, especially Eq. (8.3)).

$$n_\mathrm{e} = n_{\mathrm{e},0} \exp\left(\frac{e\,\phi}{T_{\mathrm{e},0}}\right) \tag{0.2}$$

for the spatial electron density n_e can be derived (see Sec. 2.3). Here, $n_{\mathrm{e},0}$ denotes the hot electron density in absence of a potential, $\phi \equiv 0$, and e is the elementary charge. In the electrostatic description, the electric potential is specified by the Poisson equation. However, due to the coupling of the electron density to the potential via Eq. (0.2), the Poisson equation becomes nonlinear,

$$\varepsilon_0 \frac{\partial^2 \phi}{\partial x^2} = e \cdot (n_\mathrm{e}(\phi) - Z_\mathrm{i}\, n_\mathrm{i}) = e \cdot \left(n_{\mathrm{e},0} \exp\left(\frac{e\,\phi}{T_{\mathrm{e},0}}\right) - Z_\mathrm{i}\, n_\mathrm{i}\right) . \tag{0.3a}$$

Finally, the model is completed by the equations of motion for the ions. Commonly, the ideal fluid approach

$$\frac{\partial n_\mathrm{i}}{\partial t} + \frac{\partial}{\partial x}(n_\mathrm{i}\, v_\mathrm{i}) = 0 \tag{0.3b}$$

$$\frac{\partial v_\mathrm{i}}{\partial t} + v_\mathrm{i} \frac{\partial v_\mathrm{i}}{\partial x} = -\frac{Z_\mathrm{i}\, e}{m_\mathrm{i}} \frac{\partial \phi}{\partial x} \tag{0.3c}$$

is used, with v_i, Z_i and m_i denoting the ion fluid velocity, the ion charge state and the ion mass, respectively. Due to the nonlinear character of the system it is impossible to give an exact analytic solution without any further constraints. However, one can formulate a result[1,2,51] for $t \to \infty$. This solution is based on the assumption of quasi-neutrality $Z_\mathrm{i}\, n_\mathrm{i}(x) = n_\mathrm{e}(\phi(x))$. This ansatz is motivated by the fact that the initially step-like ion density distribution gets smoother with increasing time. As a consequence, the electron distribution, which cannot follow strong local changes in the ion density due to the thermal motion of the electrons, gets closer to that of the ions.

In the following years, different aspects of the obtained self-similar solution were extensively studied.[2–5,52–56] For example, Mora and Pellat generalized the pioneering work of Gurevich[1] for the case of an arbitrary, non-Maxwellian electron energy distribution.[56] Although, the quasi-neutral self-similar solution is useful for the principal understanding of different physical observations in the TNSA process, e.g., the broad ion energy spectrum,[6,8,57,58] it is not suitable to describe the whole plasma expansion process, since it is only valid for large times but diverges for $t \to 0$.

In order to overcome this limitation, Mora considered the full system (0.3) and gave an empiric expression for the electric field strength at the ion front which is valid for all times.[59] Based on it, relations for different physical quantities are found, as for example for the maximum kinetic energy as a function of time. Those results were used in many further studies of the TNSA process, especially in the interpretation of experiments,[10,60] see chapter 8. The popularity of the Mora model is based on its simplicity and the fact that advanced models often give not manageable explicit results. However, from the theoretical point of view there is a weak point. Due to the isothermal behavior of the electrons, the kinetic energy of the ions increases towards infinity for $t \to \infty$. Therefore, the acceleration of the ions has to be terminated at some empirical instant of time, see Ref. 10 for example. In order to resolve that problem, the expansion of finite size targets was investigated.[61,62] In these studies, the total energy of the system is conserved and the hot electron temperature decreases with time because of the energy transfer from the thermal energy of the electrons into the kinetic energy of the ions. As a consequence, the maximum ion energy is limited.

---

(2) Note from Eq. (0.2), that the "temperature", $T_{\mathrm{e},0}$, is strictly speaking a thermal energy. However throughout the hole thesis, the notation "temperature" is used and the Boltzmann constant k is suppressed.

So far, all approaches assumed a Maxwellian electron energy distribution at all instants of time. However, in general from the physics point of view, there is no a priori reason for the electrons to preserve an initially Maxwellian distribution since the laser heating of electrons is almost collisionless in most TNSA experiments.[63] To abolish this limitation, Grismayer and Mora used the concept of the adiabatic invariant to model the temporal evolution of the electron phase space density in more detail.[64,65] Here, the electron distribution is not restricted to a special class of functions. Instead, the algorithm of Ref. 64 describes the correct temporal evolution of an arbitrary electron energy distribution. Moreover, it preserves automatically the total energy of the system. Thus it is an alternative approach for the adiabatic plasma expansion, extending the mentioned studies.[61,62] The work of Grismayer and Mora could profit from earlier studies on the temporal evolution of the electron distribution under the assumption of quasi-neutrality[66–68] as well as from the discussion of the concept of the adiabatic invariants.[66] However, they showed first that the ansatz is almost equivalent to a fully dynamic treatment of the electrons by means of simulations. Consequently, one can model the electron dynamics on the time scale of the ions, which is an enormous computational advantage.

In parallel, also the influence of the cold background electrons has been studied. Since the beginnings,[4,53–55] the knowledge has been enlarged in the last decade by works of Kovalev, Passoni, Tikhonchuk and others.[14,68–70] Here, it was shown that the cold electrons can not only increase the initial field strength at the plasma boundary, but they especially dominate the skin depth of the electric field[14,71] inside the plasma. The last fact becomes important in the case of ”thin” targets, which play a central role in the production of quasi-mono-energetic ion beams,[72–76] since the skin depth specifies the value of the target thickness up to which a target may be considered as ”thin”. However, a detailed analysis[77,78] of the expansion process also shows that the properties of the ion front, which is formed by the most energetic ions, is mainly dominated by the hot electron population (see Sec. 5.2). For that reason, we will only account for a single hot electron distribution in this thesis.

Beside the kinetic approach discussed so far, other analytic models were developed. For example, Andreev et al. considered a hydrodynamic plasma description.[79,80] Starting from the Euler equation for a perfect fluid, the adiabatic relation for an ideal gas with the adiabatic index κ and the assumption of massless electrons, one obtains the electron density relation

$$n_\mathrm{e} = n_{\mathrm{e},0} \cdot \left(1 + \frac{\kappa - 1}{\kappa}\frac{e\phi}{T_{\mathrm{e},0}}\right)^{1/(\kappa-1)} , \tag{0.4}$$

in contrast to the Maxwellian expression (0.2). By relating the electron density (0.4) to the general kinetic description of the hot electrons, it turns out that the electron density of the hydrodynamic approach implies a particular class of phase space densities for the hot electrons[81] (see Sec. 6.1). This class contains a step-like electron energy distribution which self-consistently ensures energy conservation during the plasma expansion. Therefore, it may serve as another, alternative model for the adiabatic expansion of a plasma, complementing the studies[61,62,64,65] mentioned above. Due to the remarkably different hot electron energy distribution, the acceleration process also shows qualitative differences in comparison to the common case assuming a Maxwellian hot energy distribution,[61,62,64,65] as shown in Ref. 82, respectively in Sec. 7.2. Concerning the initial electron distribution, there are also studies assuming other forms, e.g., a truncated Maxwellian distribution,[83–87] a super-Gaussian distribution[68,69] or a Crain distribution,[88] and there are still ongoing debates which form should be used.[88,89]

Note further, that also alternative analytic models exist. For example, Schreiber et al. evaluated the electrostatic potential induced by a spot of hot electrons, which are assumed to be situated at the back side of the target.[90] To describe the characteristic properties of the accelerated protons, they are treated as test-particles in that potential. The model, which has been used in different studies, e.g. Ref. 91, can been seen as a complementary model to that of Gurevich and followers, where the protons dominate the electrostatic potential. A short comparison of the test-particle approach and the plasma slab expansion model is given in Sec. 5.3

In the last decade, considerable progress was made towards the understanding of the TNSA process, and the related experiments have demonstrated the remarkable properties of the generated proton/ion beams. However, there are still unresolved challenges. For example, in contrast to the broad energy spectrum reported by the first TNSA experiments[6,8] and verified theoretically,[1,59] most of the applications require an ion beam with defined energy and narrow spectrum. In order to realize a peak-like spectrum different ideas were suggested. Probably, the most popular one is based on targets consisting of multiple ion species (see Sec. 5.3). Here, one can distinguish between two versions. (i) The first one is based on heterogeneous targets, where a thin layer of light ions (protons) is attached to a layer of heavy ions. These so-called double-layer targets were originally proposed by Bulanov[92] and were experimentally realized for the first time by Hegelich and Schwoerer.[93,94] Thereby, the plasma expansion leads to a peak in the proton spectrum, which is caused by the so-called Coulomb-Piston effect. Although the principal mechanism is well understood, analytic calculations[69,70,95,96] are challenging and often limited in its validity. Therefore, most of the investigations on double-layer targets are based on numerics.[15,71,97–100] (ii) The other multi-ion species approach is based on homogeneous targets which consist of several ion species. Experimentally, the idea can be realized using droplets of heavy water,[101] for example. Again, from the theoretical point of view most of the investigations were done numerically.[71,98,99,102]

In general, a central condition for the production of quasi-monoenergetic peaks is a small proton density within the initial target.[71,99] Because this is technically hard to realize in case of double-layer targets, the use of homogeneous foils seems to be the better choice.[100,102,103] Another important aspect which influences the resulting proton spectrum is the transverse dimension of the proton source compared to the dimension of the hot electron spot. In order to get a homogeneous energy spectrum the proton source should be small. Experimentally this can be realized by microstructured targets.[94,104] Numerically, this was studied by Robinson et al.[73,105] Another possibility to limit the size of the proton source is given by the use of so-called mass-limited targets.[100,103,106–110] Beside the multi-ion strategy discussed so far, also the use of multiple laser pulses was studied.[111,112] In addition, numerical investigations[79,80,103,113–116] and experiments[74–76,117,118] augur that ultra-thin targets are promising objects for the production of narrow, high-energy peaks in the ion spectra.

Most of the approaches have in common, that the appearance of narrow ion-energy peaks is enhanced by laser pulses with a high contrast, i.e., a small prepulse intensity, since an intense laser prepulse can already initiate an expansion of the rear side of the target before the main pulse drives the ion acceleration process in the proper sense. In other words, the prepulse leads to an increase of the ion density scale length at the target rear side present at the beginning of the TNSA process. According to theoretical studies,[119,120] a finite initial ion density gradient at the target rear side decreases the maximum electric field strength, which in turn leads to lower ion energies. Also, a large laser prepulse could completely disintegrate a small-scale target. Therefore, a high laser contrast is essential for experiments with mass-limited targets. The principal influence of a laser prepulse as well as of a finite initial plasma scale length on the maximum ion energy were widely studied,[60,91,120–123] both experimentally and theoretically.

It can be reasoned that the laser prepulse has an essential impact on the experimentally observed data[60,79,80,124,125] and there is an optimum target thickness for each set of experimental conditions, which provides the highest maximum ion energy. It shows that Mora's model,[59] utilizing some empirical estimates[10,60,126] which connect the electron parameters $n_{\mathrm{e},0}$ and $T_{\mathrm{e},0}$ as well as the effective ion acceleration time to the experimentally known quantities, is able to explain the influence of the target thickness on the maximum ion energies for targets thicker than the optimal thickness.[10,60] However, this is not the case for targets thinner than this value. To close this gap, we extended the model of Mora to the case of targets with an initial density gradient (see part V).

The thesis is structured as follows. In part II, selected terms and definitions from plasma physics and laser plasma interactions are recalled. This includes an overview on the TNSA process (chapter 1) as well as an introduction to some theoretical concepts (chapter 2) which are essential for the further studies in this thesis. Afterwards, in chapter 3 we discuss the central model of this thesis. In part III, we begin our investigations with the discussion of the well-known Mora model (chapter 4) as well as some extensions of it (chapter 5). It shows that there are primarily two degrees of freedom in the model, (i) the initial electron energy distribution and (ii) the initial spatial ion distribution. The models which are discussed in part III assume an initially Maxwellian electron distribution as well as an initially step-like ion distribution. Later on, we explore the impact of these assumptions on the ion acceleration process.

In part IV, the role of a step-like hot electron energy distribution in the TNSA process is examined. We start by analyzing the stationary hydrodynamic description of the hot electron gas with the stationary kinetic ansatz — two models for the description of the electrons — as a preliminary consideration (chapter 6). It turns out that the stationary hydrodynamic approach implies a particular class of non-Maxwellian electron energy distributions, among which the step-like electron energy distribution plays a special role and may ensure physical self-consistency. Assuming such a step-like energy distribution, the ion acceleration process is remarkable modified and the results might be suitable to explain observed data from ultra-short pulse experiments (chapter 7).

Then, in part V we deal with the initial spatial ion distribution. At first, we briefly recall the application of the existing theoretical models to experimental findings (chapter 8). In this context, it shows that the Mora model cannot fully explain the experimentally observed relation between the maximum proton energy and the initial target thickness. By replacing the initially step-like ion distribution used in this model by an ion distribution with an initial density gradient one might be able to reproduce the experimental data. In chapter 9, we discuss the principal effect of such a density gradient, present a theoretical model which describes the corresponding ion characteristics, and finally apply it to published experimental data.

II. Basics

1. Laser plasma ion acceleration — the TNSA process

Schematically, the TNSA process can be divided into three parts[127] (see Fig. 1.1).

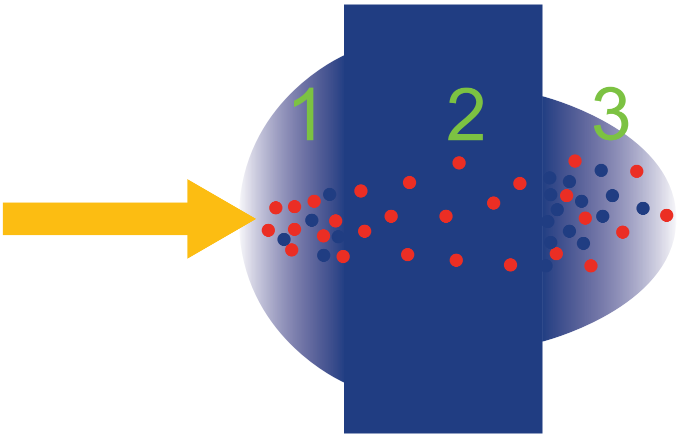

Figure 1.1.: Sketch illustration of the TNSA process. 1: A high-intensity laser (yellow arrow) irradiates a solid target (blue) from the left, ionizing the front surface. The plasma starts to expand towards the laser. A distribution of hot electrons (red dots) is generated in the laser plasma interaction. 2: The hot electrons penetrate through the target getting inhibited by an internal electric field. 3: A part of the hot electrons escapes at the rear side of the target inducing a strong longitudinal electric field which ionizes atoms in the surface layer and accelerates them in the target normal direction.

(i) Plasma formation and fast electron generation at the target front surface. As soon as the laser hits the front side of the target, the intense radiation starts to ionize the irradiated surface. Since the energy of a single photon for a laser with a wavelength in the red or infrared spectral range is usually smaller than the work function(1) of the target material, the classical photoelectric effect plays a negligible role. Hence, a bound electron may be excited by the absorption of a photon but it cannot overcome the potential barrier. However, for intensities I_L above $10^{10}\,\mathrm{W/cm^2}$ multi-photon processes become important.[128] In this case, the photon density is that large that the probability for an exited but still bound electron to absorb another photon (or even multiple photons sequentially) in a timespan which is smaller or equal to the characteristic lifetime of its excitation state is increased essentially. If an electron gets unbound in this stepwise manner, the process is called *multi-photon ionization*.[129–131] For increasing laser intensities,[128] $I_\mathrm{L} \gtrsim 10^{13}\,\mathrm{W/cm^2}$, a noticeable fraction of electrons might even absorb more photons than strictly necessary to become unbound. This particular case of multi-photon ionization is called *above-threshold ionization*.[132–135] For still higher intensities, $I_\mathrm{L} \gtrsim 10^{14}\,\mathrm{W/cm^2}$, the electric field strength of the laser light becomes comparable to the inner-atomic field strength(2) and modifies the effective electric potential of the bound electrons. As a consequence, the effective binding energy is lowered and the probability for an electron to tunnel through the potential barrier is increased. This process is called *tunneling ionization*.[136–140] If the laser light is that intense that the effective binding energy is lowered to zero, the electron is freed immediately, which is called *barrier suppression ionization* or alternatively *over-the-barrier ionization*.[141–143]

---

(1) The energy which is needed to free a bound electron from a solid target.

Due to the rapid ionization of the target surface material in the laser focus, a plasma is formed which starts to expand into the vacuum, i.e. in the opposite direction of laser propagation.[9] During the interaction of the laser with the plasma electrons, they may be accelerated up to relativistic energies.[44,45] Here, numerous mechanism for the generation of these hot electrons were proposed. An overview is given in Refs. 128, 144, 145, for example. While at modest laser intensities between $10^{12}\,\mathrm{W/cm^2}$ and $10^{14}\,\mathrm{W/cm^2}$ electron heating through collisional effects such as *inverse bremsstrahlung heating*[145–147] plays a major role, collisionless absorption of laser energy by the electrons dominates for higher laser intensities.[128] In the collisionless regime, several heating processes were specified. For short-pulse lasers with intensities above $10^{15}\,\mathrm{W/cm^2}$ and an electric field component directed normally to the target surface, one considers *resonance absorption*[145,148–150] and *vacuum heating* (also called *Brunel heating*)[151–156] as the predominant absorption mechanisms. In case of intensities above $10^{18}\,\mathrm{W/cm^2}$, where the electrons oscillate in the electric field of the laser light with relativistic velocities, the $\mathbf{j} \times \mathbf{B}$ *heating*[157–159] is another important absorption mechanisms.[127] Another essential heating process at such high laser intensities is the so-called ponderomotive electron acceleration in a spatially dependent laser field.[128,145,159] Here, the corresponding force is proportional to the spatial gradient of the laser field pressure[145] which may be very large in the region of the evanescent field at the critical density.

In the resonance absorption regime, the electric vector of the incident laser field lies in the plane of incidence (P-polarization). The component directed along the density gradient of the expanding plasma excites an electron plasma wave, which accelerates the electrons towards the laser source. At sufficiently high wave amplitudes, strong particle trapping may occur and the plasma wave breaks(3) efficiently transferring the field energy to the particles.[128] The accelerated electrons will be returned then into the dense target by the evolving space charge field. If the scale length of the undercritical plasma is rather short, electron oscillations are directly driven by the normal laser field component. Due to the space charge, this motion becomes anharmonic, and the electrons may gain energy. That mechanism is known as vacuum heating.

In contrast, relativistic electron oscillations in the transverse electromagnetic field of the laser may also lead to electron acceleration normally to the target surface due to the $\mathbf{j} \times \mathbf{B}$ term in the Lorentz force. While the influence of the magnetic field is small compared to that of the electric field for modest laser intensities, $I_\mathrm{L} < 10^{18}\,\mathrm{W/cm^2}$, the $\mathbf{j} \times \mathbf{B}$ force becomes relevant in laser pulses with relativistic intensities, $I_\mathrm{L} \gtrsim 10^{18}\,\mathrm{W/cm^2}$. Therefore, the $\mathbf{j} \times \mathbf{B}$ heating mechanism is also called *relativistic* $\mathbf{j} \times \mathbf{B}$ *heating*. Since the longitudinal excursion of the electrons in this process may exceed the skin depth of the laser field, there is no restoring force at higher densities, and the electrons will proceed to move into the overcritical part of the target after crossing the critical density region(4) .

---

(2) About $5 \cdot 10^{9}\,\mathrm{V\,m^{-1}}$ in case of hydrogen.[128]

(3) Note that this process is similar to the wakefield acceleration[128] of electrons in an underdense plasma.

Beside the heating mechanisms mentioned above, there is a hole range of other processes and models which are discussed in the literature, such as the *anomalous skin effect*,[160–162] *sheath inverse bremsstrahlungs heating*,[162–164] *diffusive heating*[165] as well as heating through *stochastic electron acceleration in fluctuating fields*,[166] *Landau damping*,[167] *surface plasmon excitation*,[168–170] *wave breaking*,[171] *laser dephasing*[172] and parametric processes like *oscillating-two-stream* or *ion acoustic decay instabilities*.[145]

(ii) Electron transport and field generation at target rear side. As discussed above, the heating process generates high-energetic electrons which are pushed into the target. However, as shown by Bell,[46] the flux of electrons cannot stream freely through the target. Since the energy density of the magnetic field associated with the hot electron current would violate the energy conservation in a typical short-pulse laser experiment by several orders of magnitude.[46, 128] Instead, the hot electron flux induces a return current of background electrons which leads to a close-to-zero net current density.[46, 127, 128] While a warm dense plasma could easily provide the amount of free electrons which is necessary to form the return current, the reduced conductivity in a cold solid target leads to a considerable limitation of the return current density. Hence, there is initially an imbalance between the hot and the return current density. As a consequence, an electric field is induced which inhibits the flux of hot electrons, ensuring eventually that the local net current density is zero again.[46] Due to this inhibition of the hot electron flux, the energetic electrons are stopped over a distance which is small in comparison to the mean free path corresponding to their initial kinetic energy.[46] By considering the electron transport in more detail, especially by taking multi-dimensional effects into account, the analysis becomes much more complicated. Here, various processes are observed, for example, filamentation,[47] instabilities[48] and collimation[49] effects.

In a TNSA experiment, the target thickness is chosen to be smaller than the stopping distance of the fast electrons. As a consequence, a fraction of the generated hot electrons penetrates through the whole target leaving it at its rear side. The cloud of hot electrons propagating away from the target induces a charge separation which creates a strong, longitudinal electrostatic field since in vacuum no return current can be formed. While the most energetic electrons may escape from the target towards infinity,[85, 86, 173–175] the majority is stopped by this electric field after some distance beyond the target and returns back into the target. As long as the laser generates new hot electrons, the processes of electron escaping and electron returning happen simultaneously. Since the hot electrons are almost collisionless,[63] both processes do not influence each other and a quasi-stationary(5) sheath of hot electrons is formed at the rear side of target[50] which is the source of a quasi-stationary, longitudinal electrostatic field in $\mathrm{TV\,m^{-1}}$ range.

(iii) Ion acceleration. This strong field immediately ionizes atoms at the target rear surface.[176] In the strong electric field the ions overcome the bounding forces and escape into the adjacent vacuum. As a consequence, a configuration of unbound electrons and ions is formed which may be described as a plasma. Driven by the strong electrostatic field, the plasma starts to expand parallel to the target normal direction, finally reaching ion energies up to several tens of MeV per nucleon.[6] This last part of the laser-ion acceleration process is called *Target Normal Sheath Acceleration* (TNSA)(6). Since the electric field is damped on a nanometer scale length inside a solid target (see Sec. 5.2), only a few layers of atoms adjacent to the surface get initially ionized. These parts form the ion front which contains the most energetic particles. As the expansion continues, a rarefaction wave propagates into the target creating a local charge separation at its front and, hence, inducing an electric field which is co-propagating with the rarefaction wave.[59] Although this electric field is decreasing with time, it is strong enough for a while to ionize further layers of atoms and accelerate the generated ions. Those ions build the low-energy parts of the broad ion spectrum usually observed in TNSA experiments.[6,8,57,58] Beside the heavy ions of the actual target material, the plasma normally contains high-energetic protons too which originate from the target contaminations. Since the thickness of the contamination layer is approximately equal to the skin depth of the electric field, usually of the order of a few nanometers,[9,177] it screens initially the heavier target atoms and leads to lower maximum energies of the heavy target ions(7).

---

(4) Note the similarity to the vacuum heating process

(5) Here, the notation ”quasi-stationary” refers to the time scale of the electrons. As soon as the plasma starts to expand the electron configuration as well as the induced electric field evolves, of course.

This discussion indicates the dependence of the resulting ion spectra on all aspects of the laser-ion acceleration process. This is evident from the fact that the resulting ion energies depend on the accelerating field which is determined by the electron distribution at the target rear side. The corresponding hot electron characteristics are affected by the electron distribution at the target front side and the issues of the electron transport. The electron distribution at the target front side in turn results from the specific laser-matter interaction. Hence, in order to describe the TNSA mechanism precisely, one has to account for all aspects of the laser-driven ion acceleration process including the influence of the numerous parameters which describe the laser as well as the target. However, this seems to be a hopeless task. For example in case of short-pulse lasers, the plasma density and temperature can vary over many orders of magnitude and the description of the ionization process asks for non-equilibrium calculations.[128] Also, the primary heating process depends on numerous experimental conditions, such as the laser pulse duration, the laser intensity, the temporal profile of the laser (including laser prepulse effects), its polarization and angle of incidence, the target material, etc. Furthermore, several mechanisms are not totally distinguishable and overlap in different aspects. In addition, they may be present simultaneously during the laser-matter interaction and the dominant heating mechanism may change over time as well, since the laser intensity and the properties of the front-side plasma are functions of time. This statement is underlined by experimental findings where two different populations of hot electrons have been observed,[178–180] a population moving in the normal direction of the target front and another population propagating in the laser forward direction. While the first population is generated by the low-intensity part of the laser pulse (i.e. the laser prepulse) through resonance absorption, the second population — containing the most energetic electrons — is generated by the high-intensity part of the laser pulse through the $\mathbf{j} \times \mathbf{B}$ mechanism.[179–182] To make things worse, the modeling of the electron transport is a challenge on its own, see Refs. 127, 128. This is due to the fact that most of the electron transport effects discussed above ask for a multi-dimensional treatment, which is demanding in case of solid targets, since the physical quantities span many orders of magnitude. From a more sophisticated point of view, also the formation of the hot electron sheath at the target rear side contains effects which need a multi-dimensional description, such as electron recirculation,[183] the electron fountain effect[184–187] and the loss of the most energetic electrons which escape from the target.[85,86,173–175]

---

(6) However, note that since the ion acceleration, part (iii), is not independent of the processes described in parts (i) and (ii) — see discussion at the end of this chapter — we will sometimes denote the hole laser-ion acceleration process, parts (i)–(iii), as TNSA.

(7) Thus, to gain higher energies for the heavy ions, the target contaminations have to be removed before the TNSA experiment starts.[176]

Due to these difficulties, there is no model so far which is able to describe all processes contributing to the laser-driven acceleration of ions comprehensively. Instead, all existing models make assumptions and simplifications. In this thesis, we consider theoretical models and simulations for the last part of the laser-ion acceleration process — the ion acceleration from the rear surface of a solid target via TNSA. Here, one usual makes assumptions for the initial electron energy distribution as well as for the initial spatial ion distribution (at the rear side). In most plasma expansion models, beginning with the pioneering work of Gurevich,[1] one starts with a Maxwellian hot electron energy distribution and a step-like ion density profile. In the parts III–V, we deal with the impact of these assumptions on the properties of the ion acceleration process. Before regarding these aspects, we want to give a brief overview on some theoretical concepts for the description of a plasma in chapter 2. Afterwards, in chapter 3, the central model will be introduced which serves as the starting point for the further investigations in the parts III–V.

2. Basic concepts of plasma theory

Laser-plasma experiments up to an intensity of about $10^{24}\,\mathrm{W/cm^2}$ may be well described by the classical field theory of electrodynamics(1). Here, the electromagnetic fields(2) $\mathbf{E}$ and $\mathbf{B}$ are specified by the Maxwell equations

$$\mathrm{rot}\,\mathbf{B} = \mu_0\,\mathbf{J} + \frac{1}{c^2}\frac{\partial \mathbf{E}}{\partial t} \tag{2.1a}$$

$$\mathrm{rot}\,\mathbf{E} = -\frac{\partial \mathbf{B}}{\partial t} \tag{2.1b}$$

$$\mathrm{div}\,\mathbf{E} = \frac{1}{\varepsilon_0}\,\rho \tag{2.1c}$$

$$\mathrm{div}\,\mathbf{B} = 0\,. \tag{2.1d}$$

The charge density ρ and the current density $\mathbf{J}$, which are associated with the charged particles (ions, electrons), are the source for the electromagnetic fields(3). Assuming a plasma with N point-like particles – hence, reducing the information of a single particle α to its position $(\mathbf{r}_\alpha, \mathbf{p}_\alpha)$

---

(1) At intensities above $\approx 10^{24}\,\mathrm{W/cm^2}$ quantum electrodynamical effects may become important. Such as photon-photon interaction.

(2) Notation: bold printed symbols refer to three-dimensional vector quantities.

(3) External fields, such as a laser pulse, are included in the relations (2.1) via the boundary conditions.

in the phase space, its mass m_α and its charge number Z_α – these densities are given by

$$\rho(\mathbf{r}) = e \sum_{\alpha=1}^{N} Z_\alpha \, \delta(\mathbf{r} - \mathbf{r}_\alpha) \tag{2.2a}$$

$$\mathbf{J}(\mathbf{r}) = e \sum_{\alpha=1}^{N} Z_\alpha \, \mathbf{v}_\alpha \, \delta(\mathbf{r} - \mathbf{r}_\alpha) \, , \tag{2.2b}$$

with δ denoting the *Dirac Delta distribution*. In the electromagnetic fields, each charged particle α is affected by the *Lorentz force*

$$\mathbf{F}_{\mathrm{L},\alpha}(\mathbf{r}_\alpha, \mathbf{v}_\alpha) = e \cdot Z_\alpha \cdot (\mathbf{E}(\mathbf{r}_\alpha) + \mathbf{v}_\alpha \times \mathbf{B}(\mathbf{r}_\alpha)) \ . \tag{2.3}$$

In the classical approach, the motion of the point like particles is described by the special relativity equations of motion

$$\frac{\partial \mathbf{r}_\alpha}{\partial t} = \mathbf{v}_\alpha \tag{2.4a}$$

$$\frac{\partial \mathbf{p}_\alpha}{\partial t} = \mathbf{F}_{\mathrm{L},\alpha} \ . \tag{2.4b}$$

Here, $\mathbf{p}_\alpha$ denotes the momentum of the particle α, which is connected to its velocity $\mathbf{v}_\alpha$ by

$$\mathbf{p}_\alpha = m_\alpha \, \gamma(\mathbf{v}_\alpha) \, \mathbf{v}_\alpha \ , \tag{2.5}$$

with the gamma factor

$$\gamma(\mathbf{v}_\alpha) = \frac{1}{\sqrt{1 + \frac{\mathbf{v}_\alpha \cdot \mathbf{v}_\alpha}{c^2}}} \ , \tag{2.6a}$$

respectively

$$\gamma(\mathbf{p}_\alpha) = \sqrt{1 + \frac{\mathbf{p}_\alpha \cdot \mathbf{p}_\alpha}{m_\alpha^2 \, c^2}} \ . \tag{2.6b}$$

From the dynamical point of view, the relations (2.1)–(2.4) form a closed set of equations for the evolution of the electromagnetic fields and the motion of the particles. However, in order to describe laser-plasma experiments with sufficient precision, in general, additional assumptions and relations have to be applied. For example, collision effects(4) may have to be taken into account. Also, ionization and recombination processes may have to be considered in the model. Then the charge numbers become functions of time, $Z_\alpha = Z_\alpha(t)$.

A simple estimate shows that the modeling of a TNSA experiment by directly applying the above framework is almost hopeless, since the laser-plasma interaction involves a huge number of particles. Currently, the fastest supercomputer in the world, the *Titan-Cray XK7* at the Oak Ridge National Laboratory, United States, can perform up to 17590 TeraFLOPS.[188] The unit *FLOPS* is the short form for *Floating Point Operations Per Second* and simply measures the number of basic arithmetic operations on real numbers — such as addition and multiplication — per second. Roughly spoken, the Titan supercomputer is able to proceed about $1.8 \cdot 10^{16}$ basic operations per second. In comparison, in Ref. 50, which represents a typical experiment involving a laser-foil interaction, there are about $1.3 \cdot 10^{17}$ particles (ions and electrons) involved(5). To calculate the motion of these particles in a given electromagnetic field for one time step, one would need about $4.7 \cdot 10^{18}$ floating point operations(6). The standard approach to solve the Maxwell equations is based on a finite difference scheme, where the electromagnetic fields are evaluated on a uniform grid. The minimum efforts for the determination of the electromagnetic field strengths at the particle positions can be estimated as $5.9 \cdot 10^{18}$ per time step(7). Hence, there are about 10^{19} floating operations necessary for a single time step, which would take the Titan supercomputer about $56\,\mathrm{s} \approx 1\,\mathrm{min}$ to carry out these operations. The size of the time step should be chosen in such a way that it resolves the fastest electron oscillations. Here, these oscillations have a period(8) of about $1.2 \cdot 10^{-17}$ s. According to the Nyquist–Shannon sampling theorem the time step must have a minimum size of $0.5 \cdot 10^{-17}$ s, hence, is of the order of 10^{-18} s. Normally, the ion acceleration takes place on a time scale which is comparable to the laser pulse duration. Assuming a simulation time of about 280 fs(9) there would be about $2.8 \cdot 10^{5}$ time steps to perform, which would take the fastest supercomputer at least 1800 days$\approx$ 5 years. Apart from the enormous calculation efforts, there are other disadvantages which would arise from a straightforward use of the system (2.1)–(2.4). For example, it is almost impossible to derive analytic results within that framework. Another drawback is the enormous amount of data which would be produced by the straightforward implementation of this approach from which one could only hardly gain the relevant physical insights.

---

(4) Note: Here, ”collisions” are corrections to the system (2.1)–(2.4) which pay attention to the fact that a point-like treatment of the particles gets inaccurate when the distance between the particles gets too small, i.e. when the distance becomes comparable to the actual, physical size of the particles.

In order to simplify the situation, different approaches are used. In the context of this thesis, firstly, in Sec. 2.1 we will discuss a kinetic description of the plasma particles. In this approach one reduces the information of the individual particles to a distribution function which only provides information on averaged quantities of the particles. Then, in Sec. 2.2, the situation will be simplified again by the introduction of the hydrodynamic approach. In this ansatz, one tries to calculate macroscopic quantities characterizing the particle distribution functions instead of trying to evaluate the distribution functions itself. Finally, in Sec. 2.3, we will discuss a simplification of the kinetic approach of Sec. 2.1 for the description of the plasma electrons. The obtained results are essential for the central model (see chapter 3) of this thesis.

---

(5) In Ref. 50, titanium foils of a thickness of 6 µm are irradiated. The diameter of the electron spot on the target rear side is about 42 µm. Based on that, the simulation area should have a minimum size of $6\,\mu\mathrm{m} \times 42\,\mu\mathrm{m} 42\,\mu\mathrm{m} \approx 10^{4}\,\mu\mathrm{m}^{3}$, containing about $1.3 \cdot 10^{17}$ particles (titanium ions and electrons).

(6) Using the Störmer-Verlet algorithm (see Sec. A.2), the calculation of the Lorentz force needs about 15 steps and the evaluation of the position and velocity vector needs another 21 operations.

(7) It takes 45 operations to evaluate the electromagnetic fields at each particle position. However, in the standard approach one solves the Maxwell equations on a uniform spatial grid. Then the fields at the particle positions are obtained by interpolation. The numerical efforts of this procedure are even higher.

(8) According to an electron density of about $1.25 \cdot 10^{24}\,\mathrm{cm}^{-3}$ of fully ionized titanium the electron plasma frequency is about $6.3 \cdot 10^{16}$ Hz, resulting in the given period.

(9) In Ref. 50 the laser pulse duration is about 80 fs and the minimum acceleration time of the ions has been found to be 280 fs.

2.1. Kinetic description

With respect to the problems discussed in chapter 2, one has to simplify the situation. In general, one therefore chooses a statistical approach. Hence, instead of trying to calculate the information for each single particle involved in the physical process, one evaluates averaged/ensemble quantities. A common example for such a statistical quantity is the one-particle distribution function $f_\alpha(\mathbf{r},\mathbf{p})$. It determines the probability density for an arbitrary particle of the species(10) α to be found at the phase space position $(\mathbf{r},\mathbf{p})$. In other words, for a given (small) volume $\Delta\mathbf{r}\,\Delta\mathbf{p}$ around the point $(\mathbf{r},\mathbf{p})$ in the phase space, the probability of finding an arbitrary particle of the species α within that volume is given by $f_\alpha(\mathbf{r},\mathbf{p})\,\Delta\mathbf{r}\,\Delta\mathbf{p}$. Mathematically, the accurate derivation of relations which specify the evolution of the ensemble quantities starting form basic physical models, such as the system (2.1)–(2.4), is a complex task and the details of that process are beyond the scope of this thesis. In case of the one-particle distribution function f_α a standard result is the relativistic *Vlasov* equation[189, 190]

$$\frac{\partial f_\alpha}{\partial t} + \frac{\mathbf{p}}{m_\alpha\gamma}\,\frac{\partial f_\alpha}{\partial \mathbf{x}} + Z_\alpha\, e\cdot\left(\mathbf{E} + \frac{\mathbf{p}}{m_\alpha\gamma}\times\mathbf{B}\right)\cdot\frac{\partial f_\alpha}{\partial \mathbf{p}} = 0\,. \tag{2.7}$$

Concerning Eq. (2.7) different points have to be noted. (i) The electromagnetic fields, $\mathbf{E}$ and $\mathbf{B}$, are smoothed quantities. Again, they are determined by the Maxwell equations (2.1). However, the total charge density ρ and the total current density $\mathbf{J}$ contained in Eqs. (2.1) are now smoothed distributions, too. They are given by

$$\rho(\mathbf{r}) = \sum_{\alpha=1}^{N}\rho_\alpha \tag{2.8a}$$

$$\mathbf{J}(\mathbf{r}) = \sum_{\alpha=1}^{N}\mathbf{J}_\alpha\,, \tag{2.8b}$$

with ρ_α and $\mathbf{J}_\alpha$ being the charge and current density of each single particle species α. Note that N refers to the number of particle species (in contrast to its meaning in chapter 2). The quantities ρ_α and $\mathbf{J}_\alpha$ are associated with the distribution function f_α via

$$\rho_\alpha(\mathbf{r}) = Z_\alpha\, e\int\limits_{\mathbb{R}^3} f_\alpha(\mathbf{r},\mathbf{p})\;\mathrm{d}\mathbf{p} \tag{2.8c}$$

$$\mathbf{J}_\alpha(\mathbf{r}) = Z_\alpha\, e\int\limits_{\mathbb{R}^3} \frac{\mathbf{p}}{m_\alpha\gamma} f_\alpha(\mathbf{r},\mathbf{p})\;\mathrm{d}\mathbf{p}\,. \tag{2.8d}$$

In the context of this discussion, "smoothed" means that the densities ρ, $\mathbf{J}$ and, as a consequence, the fields $\mathbf{E}$, $\mathbf{B}$ do not contain the micro-scale fluctuations which are caused by the individual particles. Hence, the electromagnetic fields and densities occurring in the Eqs. (2.7)–(2.8) are different from the original fields and densities specified via the Eqs. (2.1)–(2.2) and one might better describe them using extra symbols, such as $\langle\mathbf{E}\rangle$, $\langle\mathbf{B}\rangle$, $\langle\rho\rangle$ and $\langle\mathbf{J}\rangle$. However, we will use the same symbols since it is common practice.

---

(10) Note the different meaning of the index α in this context in comparison to the previous discussion, chapter 2. While in the relations (2.1)–(2.6) the index labels each single particle (independent of its species), here, the index distinguishes the different particles species.

(ii) The Vlasov equation (2.7) is collisionless, i.e. the right-hand side of Eq. (2.7) is identical to zero. In a more advanced model one might consider the corrections in the particle distributions f_α which arise from the micro-scale interaction of the particles. In this case a collision term would be added to the right-hand side of Eq. (2.7) (e.g., see Ref. 145). However, for most of the laser-plasma interactions in the TNSA regime, collisions can be neglected.[63]

Note that (iii) the fundamental N-particle description (see chapter 2) is formally contained in the Vlasov model. By setting the initial phase space density $f_\alpha(t=0)$ equal to a sum of N_α point-like particles

$$f_\alpha(t=0)(x,p) = \sum_{k=1}^{N_\alpha} q_\alpha\, \delta(x_k - x_{k,0})\, \delta(p_k - p_{k,0}) \tag{2.9}$$

one gets back to the fundamental system of equations (2.1)–(2.4). Here, N_α corresponds to the number of particles of the species α and $(x_{k,0}, p_{k,0})$ denotes the initial phase space points of the particles. The phase space density (2.9) is known as the *Klimontovich* distribution function. However, the distribution (2.9) is only of theoretical interest. In order to profit from the kinetic approach, in praxis, one has to approximate the initial particle distribution (2.9) by a phase space density with fewer degrees of freedom. For example, this can be achieved by replacing the distribution (2.9) by a smoother function(11). Another possibility is realized in the PIC approach (see Sec. A.1). Here, the number of degrees of freedom is "simply" reduced by summarizing n_α real, physical particles by a single, virtual particle. Thus, the number of virtual particles in the species α to be modeled is given by $N_\alpha/n_\alpha < N_\alpha$.

Although the degree of complexity is already reduced considerably in the Vlasov approach, the solution of the system (2.1), (2.7)–(2.8) is still challenging. Mainly due to the Vlasov equation (2.7), which is a non-linear partial differential equation in the 6-dimensional space $\mathbf{r} \times \mathbf{p}$. Hence, in order to evaluate analytical estimates, one has to reduce the complexity of the problem further. A noticeable simplification is achieved by limiting the problem to a one-dimensional geometry. Thus, all physical quantities may only depend on one spatial coordinate. In this thesis we will refer to this coordinate as x and the corresponding momentum in this direction is denoted by p. Moreover, one assumes that there are initially (i) no particles with momenta transverse to the x-direction, (ii) no transverse electrical fields and (iii) no magnetic fields at all. As a consequence of these assumptions, the problem stays one-dimensional and purely electrostatic, with the electric field vector pointing in the x-direction, at all instants of time(12). In this situation, the Maxwell equations (2.1) are reduced to the Poisson equation

$$\varepsilon_0 \frac{\partial^2 \phi}{\partial x^2} = -\rho \tag{2.10}$$

for the electrostatic potential ϕ, which is related to the electric field E in the x direction by $E = -\partial\phi/\partial x$. In addition, the Vlasov equation (2.7) is reduced to its one-dimensional electrostatic version,

$$\frac{\partial f_\alpha}{\partial t} + \frac{p}{m_\alpha \gamma} \frac{\partial f_\alpha}{\partial x} - Z_\alpha e \frac{\partial \phi}{\partial x} \frac{\partial f_\alpha}{\partial p} = 0\,, \tag{2.11a}$$

---

(11) Since a smoother function is well described by a smaller number of sampling points, one can reduce the numerical efforts by evaluating the change in the distribution function at these sampling points.

(12) This follows directly from the equation system (2.1)–(2.4).

and the distributions f_α are now functions in the two-dimensional phase space $x \times p$. In the nonrelativistic case, $\gamma \to 1$, Eq. (2.11) simply becomes

$$\frac{\partial f_\alpha}{\partial t} + \frac{p}{m_\alpha}\frac{\partial f_\alpha}{\partial x} - Z_\alpha e \frac{\partial \phi}{\partial x}\frac{\partial f_\alpha}{\partial p} = 0\,. \tag{2.11b}$$

The charge density ρ is evaluated by the one-dimensional version of Eq. (2.8),

$$\rho(x) = \sum_{\alpha=1}^{N} \rho_\alpha \tag{2.12a}$$

with ρ_α being the charge density of the particle species α, which is connected to the distribution function f_α by

$$\rho_\alpha(x) = Z_\alpha e \int_{\mathbb{R}} f_\alpha(x,p)\ \mathrm{d}p\,. \tag{2.12b}$$

The set of equations (2.10)–(2.12) forms a closed system for the electrostatic potential ϕ and the distribution functions f_α. They constitute a one-dimensional *kinetic approach* for plasma phenomena, which will serve as the starting point for the further discussions in this thesis, such as the hydrodynamical approach introduced below (Sec. 2.2) or the Mora model (see Sec. 4.2).

Although the complexity of the system (2.10)–(2.12) is remarkably reduced in comparison to the starting point, Eqs. (2.1)–(2.4), and is often implemented in simple computer codes (e.g., in PIC codes, see chapter A), it is in general still a hard task to find analytic results — mainly due to the nonlinear character of the system. To obtain analytic estimates, one has to simplify the approach further. Here, the necessary and useful simplifications depend on the particular physical phenomena to be described. For example, in Sec. 2.3 we will discuss a special assumption for the electrons. Based on that, one is able to derive analytical estimates for the maximum ion energy in an expanding plasma slab (see chapter 4).

2.2. Hydrodynamic approach

A more general simplification for the plasma model can be achieved by the introduction of a hydrodynamical approach$^{(13)}$. Here, one is no longer interested in the details of the particle distributions f_α. Instead one tries to evaluate the spatial and temporal evolution of several macroscopic quantities, such as the particle density n_α, the mean particle velocity (resp. fluid velocity) v_α and the partial pressure P_α, directly. The corresponding hydrodynamical relation which determines the evolution of the quantities can be derived from the Vlasov equation (2.11b). To proceed, one first introduces$^{(14)}$ the *moments of the distributions functions* f_α,

$$M_\alpha^k = \int_{\mathbb{R}} v^k(p)\, f_\alpha(x,p)\ \mathrm{d}p\,, \tag{2.13}$$

---

(13) Note that, since the hydrodynamical description is most often used in terms of the ions, which in the present experiments do not gain relativistic energies, we will concentrate on the nonrelativistic situation.

(14) More generally, one would start from the Vlasov equation (2.7). In this case one would replace the v^k term in the integral on the right-hand side by the product $v_x^k v_y^n v_z^m$, with the velocity components $\mathbf{v} = (v_x, v_y, v_z)$. Hence, the moments of the distribution functions than become tensor-like quantities.

which are related to the macroscopic variables through

$$n_\alpha = M_\alpha^0 \tag{2.14a}$$

$$v_\alpha = \frac{1}{n_\alpha} M_\alpha^1 \tag{2.14b}$$

$$P_\alpha = M_\alpha^2 - m_\alpha v_\alpha^2 \,. \tag{2.14c}$$

Then, by multiplying the Vlasov equation (2.11b) with v^k, for $k = 0, 1, \ldots$, and integrating over R one can derive transport equations which determine the temporal evolution of the moments M_α^k and, hence, of the associated hydrodynamical variables (2.14). The first two hydrodynamical equations, related to $k = 0$ and $k = 1$, can be written as

$$\frac{\partial n_\alpha}{\partial t} + \frac{\partial}{\partial x}(n_\alpha v_\alpha) = 0 \tag{2.15a}$$

$$m_\alpha n_\alpha \cdot \left(\frac{\partial v_\alpha}{\partial t} + v_\alpha \frac{\partial v_\alpha}{\partial x}\right) = -Z_\alpha e n_\alpha \frac{\partial \phi}{\partial x} - \frac{\partial P_\alpha}{\partial x} \tag{2.15b}$$

Form these expressions one can recognize that the continuity equation (2.15a) specifying the spatial particle density n_α, which is associated with M_α^0, contains the fluid velocity v_α, which is linked to M_α^1, as another unknown quantity. In turn, the equation of motion (2.15b) determining v_α contains the yet unknown partial pressure P_α, linked to the moment M_α^2. That illustrates a general problem. Each relation determining a specific macroscopic quantity which is linked to a moment M_α^k always contains at least one quantity associated with the next higher moment M_α^{k+1} of the distribution function f_α. Thus, in this approach one ends by a hierarchal, infinitely large set of equations. In order to gain profit form the hydrodynamical approach one has to cut-off the hierarchy at some point. In context of plasma phenomena this is often done utilizing the equation of state for an ideal gas

$$P_\alpha = n_\alpha T_\alpha \tag{2.16}$$

and by making assumptions concerning the heat flow within the plasma.[145] In other words, by connecting P_α and n_α via an equation of state, one introduces another unknown quantity, namely the temperature(15) T_α, which has to be determined by another relation. Mostly this is done by using either the isothermal approach,

$$T_\alpha = \text{constant} = T_{\alpha,0} \,, \tag{2.17a}$$

with $T_{\alpha,0}$ being the initial (and constant) temperature of species α, or by assuming an adiabatic process, which leads to

$$T_\alpha = T_{\alpha,0} \cdot \left(\frac{n_\alpha}{n_{\alpha,0}}\right)^{\kappa-1} \tag{2.17b}$$

---

(15) As mentioned above, in this thesis we denote the mean thermal energy of the particles by the term ”temperature”. Although this is strictly spoken not accurate. Hence, T_α is the short form for $k\Theta_\alpha$, with k being the Boltzmann constant and Θ_α denoting the temperature in the classical sense (measured in Kelvin).

with the initial particle density $n_{\alpha,0}$ of the species α and κ referring to the adiabatic index(16).

To summarize, the equations (2.15)–(2.16) together with one of the relations (2.17) form another ansatz for the modeling of plasma phenomena — the *hydrodynamical approach*. Using this way to address the physical problems has the advantage of being relatively simple in comparison to the kinetic model (2.10)–(2.12). However, in some cases the hydrodynamical description is not suitable, e.g. then wave-breaking effects come into play.[119] In this case the particle distribution cannot longer be characterized by single-valued functions (see discussion in Sec. 9.1). Therefore the actual description of the plasma particles has to be well adapted to the actual problem.

2.3. Stationary electron model

So far, in the theoretical descriptions we have not distinguished between different kinds of particle species. Instead, we have treated all particle populations α in exactly the same way. This approach has the advantage that it is as general as possible. However, it ignores the very different mass of ions and electrons. This difference in the mass gives rise to a much higher mobility of the electrons in comparison to the ions. In this section we want to include this aspect into the theoretical description by introducing a special treatment for the electrons, which will simplify the approach.

To proceed, we begin with a kinetic description of the electrons, following Sec. 2.1. Here, the evolution of the electron distribution f_e is evaluated by the one-dimensional Vlasov equation (2.11a),

$$\frac{\partial f_\mathrm{e}}{\partial t} + \frac{p}{m_\mathrm{e}\gamma}\frac{\partial f_\mathrm{e}}{\partial x} + e\frac{\partial \phi}{\partial x}\frac{\partial f_\mathrm{e}}{\partial p} = 0\,. \tag{2.18}$$

Now, due to much higher mobility of the electrons in comparison to the ions, one may reason that the electron distribution f_e quickly evolves into a stationary configuration in a time scale which is small in comparison to the time scale in which the ion configuration changes remarkably. Mathematically this implies that one is only interested in the stationary solutions $\partial f_\mathrm{e}/\partial t = 0$ of Eq. (2.18),

$$\frac{p}{m_\mathrm{e}\gamma}\frac{\partial f_\mathrm{e}}{\partial x} + e\frac{\partial \phi}{\partial x}\frac{\partial f_\mathrm{e}}{\partial p} = 0\,. \tag{2.19}$$

Now, the crux of the matter is that Eq. (2.19) can be solved analytically in terms of the electric potential. In the general this solution reads as follows

$$f_\mathrm{e}(x,p) = f_{\mathrm{e},0}\left(c^{-1}\sqrt{(m_\mathrm{e}\gamma c^2 - e\,\phi(x))^2 - {m_\mathrm{e}}^2 c^4}\right)\,. \tag{2.20a}$$

In the particular situation where the electrons can be treated by the nonrelativistic version of the Vlasov equation its solution becomes

$$f_\mathrm{e} = f_{\mathrm{e},0}\left(\sqrt{p^2 - 2m_\mathrm{e}\,e\,\phi(x)}\right)\,. \tag{2.20b}$$

---

(16) The adiabatic ansatz (2.17b) contains the isothermal approach (2.17a) in the limit $\kappa \to 1$.

In Eq. (2.20), $f_{\mathrm{e},0}$ is an arbitrary function which fulfills the symmetry condition $f_{\mathrm{e},0}(-p) = f_{\mathrm{e},0}(p)$. It is the boundary condition to the stationary Vlasov equation (2.19) and it simply determines the phase space density at zero potential. Thus one has

$$f_{\mathrm{e}}(x,p)|_{\phi(x)=0} = f_{\mathrm{e}}\ . \tag{2.21}$$

Corresponding to the result (2.20a), in general, the electron density

$$n_{\mathrm{e}}(x) = \int\limits_{\mathbb{R}} f_{\mathrm{e}}(x,p)\ \mathrm{d}p = \int\limits_{\mathbb{R}} f_{\mathrm{e},0}\left(c^{-1}\sqrt{(m_{\mathrm{e}}\,\gamma c^2 - e\,\phi(x))^2 - m_{\mathrm{e}}{}^2 c^4}\right)\mathrm{d}p \tag{2.22a}$$

is coupled to the electric potential ϕ in a nonlinear way. In the nonrelativistic limit (2.20b), one finds the similar result

$$n_{\mathrm{e}}(x) = \int\limits_{\mathbb{R}} f_{\mathrm{e},0}\left(\sqrt{p^2 - 2\,m_{\mathrm{e}}\,e\,\phi(x)}\right)\mathrm{d}p\ . \tag{2.22b}$$

As a consequence, the Poisson equation (2.10) becomes nonlinear, too. Beside that, the stationary modeling of the electrons leads to another drawback: The temporal evolution of the electron distribution function is no longer given intrinsically. Instead one has to specify it applying additional assumptions (see Sec. 5.1).

Since the first publications,[1,2,51] the electron distribution $f_{\mathrm{e},0}$ is in almost all cases modeled by a Maxwellian distribution. Here, $f_{\mathrm{e},0}$ is given by the classical Maxwell distribution[191]

$$f^{\mathrm{M}}_{\mathrm{e},0}(p) = \frac{n_{\mathrm{e},0}}{\sqrt{2\pi\,m_{\mathrm{e}}\,T_{\mathrm{e},0}}}\exp\left(-\frac{p^2}{2\,m_{\mathrm{e}}\,T_{\mathrm{e},0}}\right)\ , \tag{2.23a}$$

in the nonrelativistic case, whereas in the relativistic case one has to use the Maxwell-Jüttner function,[192]

$$f^{\mathrm{MJ}}_{\mathrm{e},0}(p) = \frac{n_{\mathrm{e},0}}{2\,m_{\mathrm{e}}\,c}\,\frac{1}{\mathrm{K}_1(\beta)}\exp\left(-\beta\,\gamma(p)\right)\ . \tag{2.23b}$$

Here, $n_{\mathrm{e},0}$ denotes the electron density in absence of a potential ($\phi \equiv 0$) and $T_{\mathrm{e},0}$ is the electron temperature. Moreover, K_1 is the *modified Bessel function* of the second kind and first order, γ denotes the gamma factor and $\beta = m_{\mathrm{e}}\,c^2/T_{\mathrm{e},0}$ refers to the inverse normalized electron temperature. By substituting the Maxwell-Jüttner distribution (2.23b) into the solution (2.20a) of the stationary Vlasov equation and then evaluating Eq. (2.22), one obtains the relation (0.2),

$$n_{\mathrm{e}} = n_{\mathrm{e},0}\exp\left(\frac{e\,\phi}{T_{\mathrm{e},0}}\right)\ , \tag{2.24}$$

for the electron density as a function of the potential. This result also holds true in the nonrelativistic version, as one can immediately check by evaluating the corresponding nonrelativistic terms(17). Consequently, the Poisson equation (2.10) becomes(18)

$$\varepsilon_0\,\frac{\partial^2\phi}{\partial x^2} = e\,n_{\mathrm{e},0}\exp\left(\frac{e\,\phi}{T_{\mathrm{e},0}}\right) - \rho_i\ , \tag{2.25}$$

---

(17) That the result (2.24) also holds true in the nonrelativistic case is also obvious from the fact, that the expression is no function of β at all. Hence, Eq. (2.24) is already the result one gains in the limit $\beta \to 0$.

(18) Note that, Eq. (2.25) equals Eq. (0.3a) for the case of a single ion species.

with ρ_i being the total ion charge density. Relation (2.25) is a particular case of the general form of the *Poisson-Boltzmann equation*. To summarize, through the assumption of a stationary electron configuration on can directly solve the Vlasov equation (2.11) in terms of ϕ. From that the number of unknown quantities in the model is reduced and one can focus on the ion dynamics. In the next sections we will see how some analytic results for the ion acceleration process can be derived based on these expressions.

3. The central model of high-intensity laser-driven plasma expansion

Here, we want to outline the central framework of this thesis. It is based on the theoretical concepts described in chapter. 2 and it is the starting point for the further studies in this thesis.

We start with a plasma consisting of N particle species α. In more detail, one has N_i species of ions and $N_\mathrm{e} = N - N_\mathrm{i}$ species of electrons. As a consequences, the ions correspond to the values $\alpha = 1, \ldots, N_\mathrm{i}$ while the electrons are labeled by $\alpha = N_\mathrm{i} + 1, \ldots, N$. Here, the number of electrons and ions of the several species are assumed to be constant. Hence, ionization and recombination effects are ignored in this model. Furthermore, the model is one-dimensional. Following Sec. 2.1, the electromagnetic fields are reduced to the electrostatic potential ϕ which is specified by the Poisson equation (2.10),

$$\varepsilon_0 \frac{\partial^2 \phi}{\partial x^2} = -\rho \; . \tag{3.1}$$

The temporal evolution of the different ion species are given either by a hydrodynamic ansatz (see Sec. 2.2),

$$\frac{\partial n_\alpha}{\partial t} + \frac{\partial}{\partial x}\left(n_\alpha v_\alpha\right) = 0 \tag{3.2a}$$

$$m_\alpha n_\alpha \cdot \left(\frac{\partial v_\alpha}{\partial t} + v_\alpha \frac{\partial v_\alpha}{\partial x} \right) = -Z_\alpha e n_\alpha \frac{\partial \phi}{\partial x} - \frac{\partial P_\alpha}{\partial x} \; , \tag{3.2b}$$

or they are modeled via a kinetic ansatz (see Sec. 2.1),

$$\frac{\partial f_\alpha}{\partial t} + \frac{p}{m_\alpha} \frac{\partial f_\alpha}{\partial x} - Z_\alpha e \frac{\partial \phi}{\partial x} \frac{\partial f_\alpha}{\partial p} = 0 \; . \tag{3.3}$$

Note that while the spatial ion density n_α is evaluated directly in the hydrodynamic ansatz (3.2), it has to be evaluated via

$$n_\alpha(x) = \int_{\mathbb{R}} f_\alpha(x,p) \; \mathrm{d}p \tag{3.4}$$

in the kinetic approach (3.3). In case of the electrons we use the stationary approach described in Sec. 2.3. Here, the phase-space densities f_α of the different electron species α at an instant of time are coupled to the electric potential at the same instant of time(1). In this ansatz, the electron phase space densities are given by Eq. (2.20),

$$f_\alpha = \begin{cases} f_{\alpha,0}\left(c^{-1}\sqrt{(m_\mathrm{e}\,\gamma c^2 - e\,\phi(x))^2 - {m_\mathrm{e}}^2\,c^4}\right) & \text{: general case} \\ f_{\alpha,0}\left(\sqrt{p^2 - 2\,m_\mathrm{e}\,e\,\phi(x)}\right) & \text{: nonrelativistic limit .} \end{cases} \tag{3.5}$$

As a consequence, the expression for the spatial electron density, Eq. (3.4), becomes a nonlinear relation of the electrostatic potential, $n_\alpha = n_\alpha(\phi)$. Hence, the total charge density ρ in Eq. (3.1) is given by

$$\rho(x) = e\sum_{\alpha=1}^{N} Z_\alpha\, n_\alpha = e\cdot\left[\sum_{\alpha=1}^{N_\mathrm{i}} Z_\alpha\, n_\alpha - \sum_{\alpha=N_\mathrm{i}+1}^{N} n_\alpha(\phi)\right] \tag{3.6}$$

and the nonlinear Poisson equation (3.1) becomes

$$\varepsilon_0\,\frac{\partial^2\phi}{\partial x^2} = -e\cdot\left[\sum_{\alpha=1}^{N_\mathrm{i}} Z_\alpha\, n_\alpha - \sum_{\alpha=N_\mathrm{i}+1}^{N} n_\alpha(\phi)\right]\ . \tag{3.7}$$

To summarize, the model consists of: (i) the nonlinear Poisson equation (3.7). It determines the electrostatic potential at an instant of time t once the total charge density at time t is known. The relation is nonlinear due to the coupling of the electron distributions to the potential via Eq. (3.5). (ii) The relations (3.2), respectively, Eq. (3.3) which describe the evolution of the ion distributions. To complete the model one further has to specify: (iii) the initial ion distributions and (iv) the electron phase space densities at zero potential, $f_{\alpha,0}$, at each instant of time. Note that from a purely mathematical point of view the functions $f_{\alpha,0}$ at a specific instant of time can be chosen arbitrarily from the phase space densities at an previous point of time. However, from the physics point of view this is not correct and one has to make further assumptions which (v) specify the evolution of the functions $f_{\alpha,0}$. This aspect will be part of Sec. 5.1. A sketch illustration of the central model is given in Fig. 3.1.

---

(1) This is contrary to the kinetic approach of the ions, Eq. (3.3), where the electric potential only determines the rate of change of the phase space density.

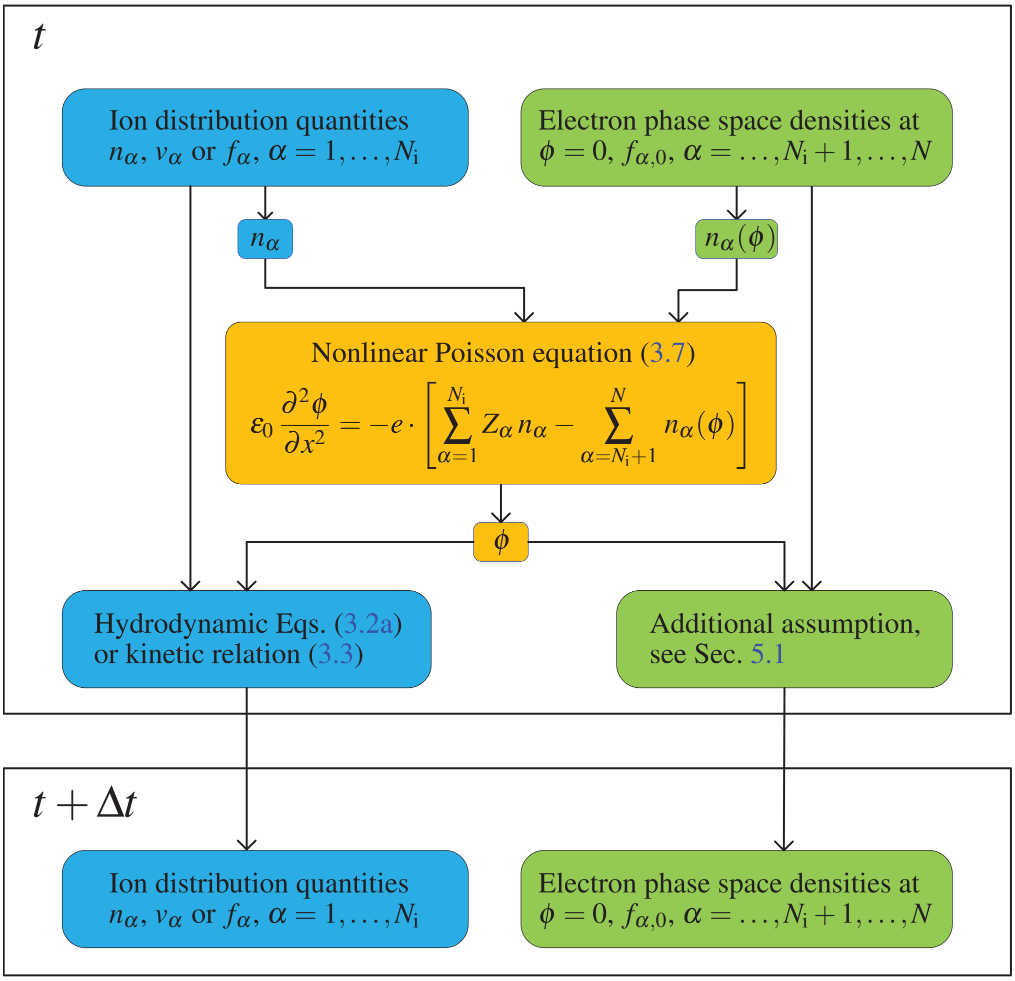
t
Ion distribution quantities n_α, v_α or f_α, $\alpha = 1, \dots, N_\mathrm{i}$
Electron phase space densities at $\phi = 0$, $f_{\alpha,0}$, $\alpha = \dots, N_\mathrm{i}+1, \dots, N$
n_α
$n_\alpha(\phi)$
Nonlinear Poisson equation (3.7)
$\varepsilon_0 \frac{\partial^2 \phi}{\partial x^2} = -e \cdot \left[\sum_{\alpha=1}^{N_\mathrm{i}} Z_\alpha n_\alpha - \sum_{\alpha=N_\mathrm{i}+1}^{N} n_\alpha(\phi) \right]$
ϕ
Hydrodynamic Eqs. (3.2a) or kinetic relation (3.3)
Additional assumption, see Sec. 5.1
$t + \Delta t$
Ion distribution quantities n_α, v_α or f_α, $\alpha = 1, \dots, N_\mathrm{i}$
Electron phase space densities at $\phi = 0$, $f_{\alpha,0}$, $\alpha = \dots, N_\mathrm{i}+1, \dots, N$

Figure 3.1.: Flowchart of the central model of this thesis. Starting from the ion distributions and the electron phase space densities at $\phi = 0$, the electric potential at the current instant of time is calculated. Then, by using the hydrodynamic equations of motion (3.2) or the Vlasov equation (3.3), respectively, the ion distributions at the next instant of time can be evaluated. Also, by applying additional assumptions (see Sec. 5.1), the variation of the electron distributions at $\phi = 0$ can be determined.

III. Plasma models assuming Maxwellian hot electrons

4. The free expansion of a plasma slab into vacuum

In this chapter, we will describe the free expansion of a plasma-slab driven by laser-generated hot electrons. The model we are going to discuss here is a particular case of the general framework presented in chapter 3. It it used in the theoretical description of numerous experimental studies (see, e.g., Ref. 10). Following the discussion of chapters 2 and 3, we will ignore the details of the laser-plasma interaction and the electron transport. Instead we start with a plasma consisting of a single species of ions and a single population of hot electrons(1). Here, the ions are assumed initially to be at rest and their spatial distribution is given by a semi-infinite slab

$$n_\mathrm{i}(x) = \begin{cases} n_\mathrm{i,0} & : x \leq 0 \\ 0 & : \text{otherwise} \; . \end{cases} \tag{4.1}$$

The temporal evolution of the ions will be modeled by the hydrodynamic approach, Eq. (3.2), assuming $P_\mathrm{i} = 0$ (caused by $T_\mathrm{i} = 0$),

$$\frac{\partial n_\mathrm{i}}{\partial t} + \frac{\partial}{\partial x}(n_\mathrm{i}\, v_\mathrm{i}) = 0 \tag{4.2a}$$

$$\frac{\partial v_\mathrm{i}}{\partial t} + v_\mathrm{i}\,\frac{\partial v_\mathrm{i}}{\partial x} = -\frac{Z_\mathrm{i}\, e}{m_\mathrm{i}}\,\frac{\partial \phi}{\partial x} \; . \tag{4.2b}$$

This approach is only suitable as long as the motion is fluid-like. In other words it holds true, as long as there is no overtaking by particles (no wave-breaking)(2) — or as long as one can at least neglect these effects. In the physical problem to be discussed here, that is the case.

Following the general model, chapter 3, the hot electrons will be assumed in a stationary configuration with the potential ϕ. Moreover, their energy distribution is set to be Maxwellian. Thus the spatial electron density is given by Eq. (2.24) and the Poisson equation becomes the nonlinear expression (2.25). For a single ion species it reads

$$\varepsilon_0\,\frac{\partial^2 \phi}{\partial x^2} = e \cdot \left(n_\mathrm{e,0} \exp\left(\frac{e\,\phi}{T_\mathrm{e,0}}\right) - Z_\mathrm{i}\, n_\mathrm{i} \right) \; . \tag{4.3}$$

The equations (4.2)–(4.3) form a closed system for the unknown quantities n_i, v_i and ϕ. Based on it, the free expansion of a plasma configuration, such as the semi-infinite plasma-slab (4.1), can be modeled and different issues of the ion acceleration process can be investigated. This will be the topic of this chapter. Firstly, in Sec. 4.1 we will outline a solution of the Eqs. (4.2)–(4.3) which is valid for large times. Then, in Sec. 4.2 we will give a short summary of Mora's results, who derived analytic estimates for the expansion of a plasma slab into vacuum, specified by the Eqs. (4.1)–(4.3), by utilizing simulation results.

---

(1) In consequence, we will ignore the cold background electrons. Sec. 5.2 will deal with the question in which way the presence of the cold electrons modifies the expansion process.

(2) See Sec. 9.1 for a discussion of wave-breaking and the associated problems.

4.1. The self-similar solution

Although the description of the plasma based on the Eqs. (4.2)–(4.3) is already remarkable simplified in comparison to our starting point – the three-dimensional N-particle model (2.1)–(2.4) – it is still impossible to solve the system (4.2)–(4.3) analytically without any further assumptions. To further simplify the problem, one makes the assumption of *quasi-neutrality*. In this ansatz, one assumes that the electron charge density almost neutralizes the ion charge density, hence $n_\mathrm{e}(x) = Z_\mathrm{i}\, n_\mathrm{i}(x)$. Due to this relation the equation system (4.2)–(4.3) becomes over-determined(3) . Therefore, one has to drop one expression. For the reason that the Poisson equation provides no information under the quasi-neutral condition – except the fact that the electric field is constant – it will be dropped. Instead, ϕ is determined by the particle densities, n_e, resp. n_i. Consequently, one studies the approximative system

$$\frac{\partial n_\mathrm{i}}{\partial t} + \frac{\partial}{\partial x}\left(n_\mathrm{i}\, v_\mathrm{i}\right) = 0 \tag{4.4a}$$

$$\frac{\partial v_\mathrm{i}}{\partial t} + v_\mathrm{i}\,\frac{\partial v_\mathrm{i}}{\partial x} = -\frac{Z_\mathrm{i}\, e}{m_\mathrm{i}}\,\frac{\partial \phi}{\partial x} \tag{4.4b}$$

$$n_\mathrm{e}(\phi) = n_{\mathrm{e},0}\, \exp\left(\frac{e\,\phi}{T_{\mathrm{e},0}}\right) = Z_\mathrm{i}\, n_\mathrm{i}\ , \tag{4.4c}$$

instead of trying to solve the original system (4.2)–(4.3) in terms of ϕ, n_i and v_i. According to Refs. 1, 51 the solution of the system (4.4) is given by

$$n_{\mathrm{i,ss}} = n_{\mathrm{i},0}\, \exp\left(-\frac{x}{c_\mathrm{s}\, t} - 1\right) \tag{4.5a}$$

$$v_{\mathrm{i,ss}} = c_\mathrm{s} + \frac{x}{t} \tag{4.5b}$$

$$\phi_\mathrm{ss} = -\frac{T_{\mathrm{e},0}}{e}\left(\frac{x}{c_\mathrm{s}\, t} + 1\right)\ . \tag{4.5c}$$

Here, $n_{\mathrm{i},0} = n_{\mathrm{e},0}/Z_\mathrm{i}$ is the initial ion density and c_s denotes the ion-acoustic velocity, given by $c_\mathrm{s} = \sqrt{Z_\mathrm{i}, T_{\mathrm{e},0}/m_\mathrm{i}}$. From the *self-similar solution* (4.5) different physical aspects can be reasoned. (i) According to Eq. (4.5c) the electric field strength $E = -\partial\phi/\partial x$ is given by

$$E_\mathrm{ss} = \frac{E_0}{\omega_\mathrm{pi}\, t}\ , \tag{4.6}$$

with $\omega_\mathrm{pi} = \sqrt{Z_\mathrm{i}\, n_{\mathrm{e},0}\, e^2/\varepsilon_0\, m_\mathrm{i}}$ being the ion plasma frequency and $E_0 = \sqrt{n_{\mathrm{e},0}\, T_{\mathrm{e},0}/\varepsilon_0}$ denoting the characteristic electric field strength of the self-similar solution. Obviously, Eq. (4.6) decreases with $\mathscr{O}\left(t^{-1}\right)$. Due to this scaling an particle which is effected by the self-similar field will be gain an infinitely high energy as time goes towards infinity. As we will see in Sec. 4.2, that issue is still contained in the solution of the exact system (4.2)–(4.3). As a consequence, when using the model in the interpretation of experiments one has to make empirical assumptions about a finite acceleration time (see chapter 8).

---

(3) The Eqs. (4.2)–(4.3) together with the quasi-neutral condition form a system of four relations for the three unknown quantities ϕ, n_i and v_i.

(ii) Starting from Eqs. (4.5) one can calculate the ion spectrum[59] to

$$\frac{\partial^2 N_\mathrm{i}}{\partial \varepsilon \partial A} = \frac{\partial^2 N_\mathrm{i}}{\partial x \partial A}\,\frac{\partial x}{\partial v}\,\frac{\partial v}{\partial \varepsilon} = n_\mathrm{i}(x)\,t\,\frac{1}{\sqrt{2m_\mathrm{i}\,\varepsilon}} = \frac{n_{\mathrm{i},0}\,t}{\sqrt{2m_\mathrm{i}\,\varepsilon}}\exp\left(-\sqrt{\frac{2\,\varepsilon}{Z_\mathrm{i}\,T_{\mathrm{e},0}}}\right)\,, \tag{4.7}$$

with N_i being the total number of ions. The expression (4.7) describes an exponentially decreasing spectrum of the kinetic energy ε. Note that for any instant $t > 0$ there is no maximum ion energy. (iii) Moreover, one can follow from Eq. (4.5a), that for each instant $t > 0$ the particles cover the complete right domain $x > 0$.

(iv) The population of the ions is a single-valued function $v_\mathrm{i}(x)$. Hence, at an arbitrary instant t, there is a unique value v_i for each spatial position x. Moreover, the function $v_\mathrm{i}(x)$ is monotonously increasing in v_i with increasing value of x. Due to this aspect the ions do not overtake each other. In other words, there are no wave-breaking effects and from that the hydrodynamical description of the ions is justified in retrospective. (v) The self-similar solution (4.5) diverges for $t \to 0$. Hence, the system (4.5) cannot be used as an estimate for the original system (4.2)–(4.3) at this instant. Moreover, the self-similar solution (4.5) is only valid⁽⁴⁾ for $x \geq -c_\mathrm{s}t$, since one has negative values of v_i for positions $x < -c_\mathrm{s}t$.

According to the properties (i), (iii) and (v) of the self-similar solution (4.5), it is evident that it cannot describe the ion acceleration process in all aspects. Therefore, one has to study the original system (4.2)–(4.3) in more detail. Since the system (4.2)–(4.3) cannot be solved in an exact analytical way, one relies on numerical solutions and empirical results gained from it. This will be part of the next section, Sec. 4.2.

4.2. Mora's model

In this section, we are going to discuss some important aspects of the solution of the system (4.2)–(4.3), which serves as a model for the ion acceleration process driven by a stationary cloud of hot Maxwellian electrons (see again, Sec. 2.3). As discussed in the last section, Sec. 4.1, it is not possible to solve the Eqs. (4.2)–(4.3) analytically. Therefore, Mora studied it numerically.[59] Here, we want to shortly summarize some aspects of this study because it serves as the starting point for further discussions in this thesis.

We begin the discussion by considering the simulation results⁽⁵⁾ for the spatial distributions of the ions and electrons at the two instants $t = 0$ and $\omega_\mathrm{pi}t = 10$, see Fig. 4.1a and Fig. 4.1b, respectively. It is obvious, that at the beginning of the expansion process ($t = 0$), the quasi-neutral condition is not fulfilled at the ion front ($x = 0$). From the physics point of view, this gets plausible by the fact, that the ion density has a jump discontinuity at $x = 0$. In contrast, the electron

---

(4) According to numerical solutions of the system (4.2)–(4.3), for an initially step-like ion distribution, Eq. (4.1), there are no ions with $v_\mathrm{i} < 0$ at all.

(5) The simulations were performed with the hybrid code described in Appendix A.

distribution cannot follow this discontinuity due to the thermal motion of the electrons, which leads to a smoothing of the spatial electron density(6). Due to the absence of quasi-neutrality, the self-similar solution (4.5) cannot describe the expansion at the ion front initially. However, with increasing time the expansion process smooths the ion distribution and the jump at the ion front decreases. As a consequence the electron density neutralizes the local changes of the ion charge density more rapidly. Therefore, the quasi-neutrality is realized with increasing accuracy for increasing time (see Fig. 4.1b) and, although the quasi-neutral condition is a necessary but not a sufficient condition for the validity of the self-similar solution (4.5), the simulations show that the self-similar solution describes the expansion of the plasma-slab quite well over a large spatial domain for times $\omega_{\text{pi}} t \gg 1$. This is illustrated in Fig. 4.1c where the self-similar expression for the ion velocity as a function of x, Eq. (4.5b), is shown against the simulation result.

However, even for large times $\omega_{\text{pi}} t \gg 1$ the quasi-neutrality condition fails close to the ion front and the value of the electric field is larger than the value (4.6) predicted by the self-similar solution (see Fig. 4.1d). However, from the simulation one finds empirically(7) that the ratio of the electric field to the self-similar value is approximately 2 (see Ref. 59). According to that result, the electric field at the ion front E_{f} is given by

$$E_{\text{f}}(t) \simeq \frac{2E_0}{\omega_{\text{pi}} t} \tag{4.8}$$

in the asymptotic limit $\omega_{\text{pi}} t \gg 1$. Beside the asymptotic behavior one is able to calculate the exact value of the electric field at the ion front at $t = 0$, $E_{\text{f}}(0$. By integration of the Poisson equation (2.25) one obtains[3]

$$E_{\text{f}}(0) = \sqrt{\frac{2}{\exp(1)}} E_0 \,. \tag{4.9}$$

Now, Mora introduced the expression

$$E_{\text{f}}(t) = \frac{E_{\text{f}}(0)}{\sqrt{1+\tau^2}} \tag{4.10}$$

which describes empirically the electric field strength at the ion front for each instant of time[59] and which, in addition, reproduces the relations (4.8) and (4.9). Here, $\tau = \omega_{\text{pi}} t / \sqrt{2\exp(1)}$ is a normalized time. From that the velocity of the ion front

$$v_{\text{f}} = 2c_{\text{s}} \operatorname{arcsinh}(\tau) \tag{4.11}$$

as well as its position

$$x_{\text{f}} = 2\sqrt{2\exp(1)}\,\lambda_{\text{D}} \cdot \left(\tau \operatorname{arcsinh}(\tau) - \sqrt{1+\tau^2} + 1\right) \tag{4.12}$$

---

(6) Mathematically this gets plausible from the fact that the electron density n_{e} is a smooth function of the electric potential ϕ. The electric potential in turn is defined by the Poisson equation (2.10), which is a second order equation for ϕ. Thus, ϕ is obtained through a repeated integration. Hence, even in the case that the right hand side of the Poisson equation (2.10) (containing the ion charge density) has a jump, the electric potential ϕ is a differentiable (especially continuous) function, and from that n_{e} is continuous as well.

(7) Beside the pure numerical observation, the ratio can be physically motivated by some arguments.[59] However, there is no exact derivation.

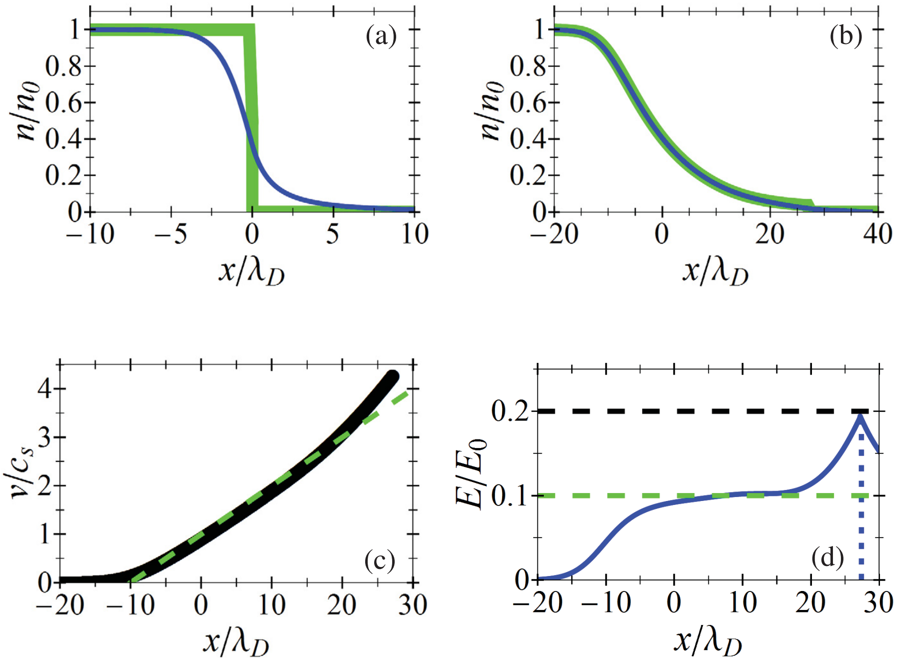

Figure 4.1.: Comparison of the self-similar solution for the expansion of a plasma-slab driven by hot Maxwellian electrons, Eq. (4.5), against simulation results. As depicted in (a), the quasi-neutrality condition is not fulfilled at the ion front at $t = 0$. Here, the bold green curve corresponds to the ion density whereas the electron density is depicted by the blue curve. However, as shown in (b), for $\omega_{\mathrm{pi}}\, t = 10$ quasi-neutrality is already achieved in a large domain. In (c), the ion distribution in the phase space is plotted for $\omega_{\mathrm{pi}}\, t = 10$. Here, the black curve corresponds to the simulation result, whereas the dashed green curve depicts the self-similar relation (4.5b). Furthermore, in (d) the simulation result (blue curve) for the electric field at $\omega_{\mathrm{pi}}\, t = 10$ is compared with the self-similar result (4.6) (dashed green curve) and its doubled value (dashed black curve). Obviously, the value of the electric field at the ion front (dotted vertical line) is approximately twice the value of the self-similar solution (4.6).

follow directly by integration. Here, $\lambda_{\mathrm{D}} = \sqrt{\varepsilon_0\, T_{\mathrm{e},0}/e^2\, n_{\mathrm{e},0}}$ denotes the Debye length of the electrons — the length scale at which an electric field is approximately damped to $1/\exp(1)$ of its initial value through the Debye shielding of the electrons.[193] The value of the kinetic energy of the ions at the ion front ε_{f} — which is identical with the maximum ion energy — follows directly from Eq. (4.11),

$$\varepsilon_{\mathrm{f}} = 2 Z_{\mathrm{i}}\, T_{\mathrm{e},0} \operatorname{arcsinh}(\tau)^2 \ . \tag{4.13}$$

As shown in Fig. 4.2, the analytic estimates (4.10) and (4.11) fit the numerical findings quite well — actually the deviation is of the oder of one percent for all instants of time. From the result (4.11) it gets obvious that the maximum ion velocity increases unlimited as the time goes towards infinity. Hence, there is no final maximum ion energy for the expansion of a semi-infinite plasma slab assuming Maxwellian electrons. Concerning the application of this model for the theoretical description of experiments this is problematic, since in reality the final maximum ion

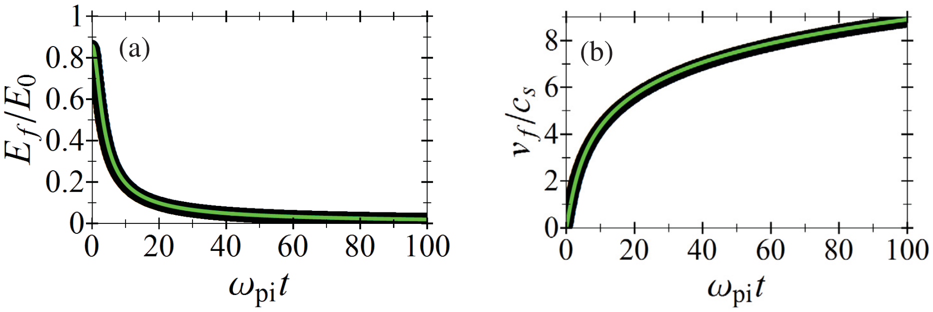

Figure 4.2.: (a) and (b) show Mora's results[59] for the electric field strength at the ion front and the ion front velocity of an expanding semi-infinite plasma slab, respectively. Here, black curves correspond to simulation results will green curves depict the analytic findings Eq. (4.10) and Eq. (4.11), respectively.

energy is always finite, of course. In the Sec. 5.1 we will discuss two approaches to circumvent this problem by a modification of the model presented here.

5. Extensions of the Mora model

In this chapter, we will discuss different extensions and variations of the plasma expansion model of chapter 4. In Sec. 5.1 two possible variations of the temporal evolution of the hot electron distribution will be studied. In Sec. 5.2 we will account for the cold electrons and we will shortly discuss in which way the results are modified through their presence. Finally, in Sec. 5.3 some extensions of the model with respect to the ion distribution are discussed.

5.1. Advanced description of the electrons

In chapter 4, the free expansion of a plasma slab under the action of laser-heated electrons has been studied. For these considerations, the electrons were assumed to have a Maxwellian energy distribution. Hence, at each instant of time, they were described by the density relation (2.24),

$$n_{\text{e}} = n_{\text{e},0} \exp\left(\frac{e\phi}{T_{\text{e},0}}\right) , \tag{5.1}$$

according to Sec. 2.3. In this approach, the temperature of the electrons was constant in time, $T_{\text{e}} \equiv T_{\text{e},0}$. Therefore we refer to it as the *isothermal Maxwellian approach*. In this framework the final maximum ion velocity is a divergent function with increasing time. In addition, the total energy of the system is not conserved. To solve this problem, in a first approach, Mora considered the electron temperature to be a function of time.[62] This possible variation of the original model will be the content of Sec. 5.1.1. However, there is no a priori reason for the electron energy distribution to preserve its initial Maxwellian shape during the expansion process. To remove this weak point, in a second approach, the evolution of an initially Maxwellian energy distribution into an well defined, but arbitrary energy distribution was investigated.[64,65] This ansatz will be briefly discussed in Sec. 5.1.2.

5.1.1. The adiabatic Maxwellian model

In this subsection, we consider the plasma expansion driven by Maxwellian hot electrons under the condition of energy conservation. In context of this model, the total energy of the system is given through the sum of the energy of the electric field, the thermal energy of the hot electrons and the kinetic energy of the ions,[62] whereas the kinetic energy of the electrons as well as the thermal energy of the ions is negligible(1) . As a consequence, the energy gain of the ions has to be compensated by the energy loss of the electric field and the thermal energy of the electrons. Since a reduction of the thermal energy of the electrons is related to a decreasing electron temperature (see Eq. (B.43)), the electron temperature is now assumed to be time-dependent,[62] $T_\mathrm{e} = T_\mathrm{e}(t)$, and the density relation (5.1) is replaced by the expression

$$n_\mathrm{e} = n_{\mathrm{e},0} \exp\left(\frac{e\phi}{T_\mathrm{e}(t)}\right) . \tag{5.2}$$

Here, the variation of the temperature is determined in such a way that the total energy of the system is conserved. To realize the adiabatic Maxwellian model, one furthermore has to change the initial ion distribution from a semi-infinitely extended plasma slab into a target having a finite thickness. Since a semi-infinitely large plasma slab contains an infinitely large number of electrons, the resulting initial thermal energy of the hot electrons is also infinite. As a consequence, the energy transfer into the ions would not change the temperature of the electrons. Thus, by starting with a semi-infinite plasma slab, one would end up by the isothermal Maxwellian model again.

Following Ref. 62, the rate of change in the thermal electron energy ε_e is given by the work of the electric field done on the electron population

$$\frac{\partial \varepsilon_\mathrm{e}}{\partial t} = e \int\limits_{\mathbb{R}} \phi \, \frac{\partial n_\mathrm{e}}{\partial t} \, \mathrm{d}x . \tag{5.3}$$

Then, the rate of change in the electron temperature is given by the relation

$$\frac{\partial T_\mathrm{e}}{\partial t} = \frac{\frac{\partial \varepsilon_\mathrm{e}}{\partial t}}{\frac{\partial \varepsilon_\mathrm{e}(T_\mathrm{e})}{\partial T_\mathrm{e}}} , \tag{5.4}$$

with $\varepsilon_\mathrm{e}(T_\mathrm{e})$ denoting the thermal energy of the electrons as a function of their temperature. In general, $\varepsilon_\mathrm{e}(T_\mathrm{e})$ is evaluated by the expression

$$\varepsilon_\mathrm{e} = \int_{\mathbb{R}} m_\mathrm{e} c^2 \, (\gamma(p) - 1) \, f_\mathrm{e}(x,p) \, \mathrm{d}p . \tag{5.5}$$

---

(1) The first statement follows from the fact that the mean electron velocity, i.e the electron fluid velocity, is zero in the stationary approach, Sec. 2.3, since the electron distribution function f_e is symmetric with respect to the momentum, see Eq. (2.20). Initially, the ion temperature T_i is much smaller than the hot electron temperature T_e — as a consequence of the negligibly direct impact of the laser on the ions. Moreover, the relation $T_\mathrm{i} \ll T_\mathrm{e}$ also holds true during the plasma expansion, since one can ignore collisions between the ions as well as between the ions and the electrons. Thus, one has $T_\mathrm{i} \ll T_\mathrm{e}$ for all instants, which confirms the second statement.

By setting f_e equal to the Maxwell-Jüttner distribution (2.23b), one finds the relation

$$\varepsilon_\mathrm{e} = \frac{\mathbb{Z}(T_\mathrm{e})}{2}\, n_\mathrm{e}(\phi)\, T_\mathrm{e}\,. \tag{5.6}$$

Here, $n_\mathrm{e}(\phi)$ is the electron density (5.2) and $\mathbb{Z}(T_\mathrm{e})$ refers to the internal degrees of freedom of the electron gas

$$\mathbb{Z}(T_\mathrm{e}) = 2 \cdot \left[1 + \beta \cdot \left(\frac{\mathrm{K}_0(\beta)}{\mathrm{K}_1(\beta)} - 1\right)\right]\,, \tag{5.7}$$

with $\beta = m_\mathrm{e} c^2 / T_{\mathrm{e},0}$ denoting the inverse normalized electron temperature and K_n being the *modified Bessel functions* of second kind and n-th order. Expectedly, $\mathbb{Z}(T_\mathrm{e})$ fulfills the relation $\lim_{T_\mathrm{e}\to 0} \mathbb{Z}(T_\mathrm{e}) = 1$ (nonrelativistic case). In contrast, in the ultrarelativistic limit, one finds $\lim_{T_\mathrm{e}\to\infty} \mathbb{Z}(T_\mathrm{e}) = 2$. Note that a change in the electron temperature leads to a modification in $n_\mathrm{e}(x)$, too. As a consequence, the value of Eq. (5.3) — which is the precondition for Eq. (5.4) — is varied, too. Therefore, the implementation of the above procedure has to be done either iteratively or implicitly.

Following Ref. 62, the adiabatic approach leads to a temperature scaling of $T_\mathrm{e} \propto t^{-2}$ when starting from nonrelativistic electron temperatures, i.e. $T_{\mathrm{e},0} \ll m_\mathrm{e} c^2$ (see Fig. 5.1a). In contrast, one has $T_\mathrm{e} \propto t^{-1}$ in the ultrarelativistic case, i.e. $T_{\mathrm{e},0} \gg m_\mathrm{e} c^2$ (see Fig. 5.1a). Thus, an increasing $T_{\mathrm{e},0}$ leads to a slower decrease of T_e. This results from an increase in the internal degrees of freedom Z of the electron gas with increasing $T_{\mathrm{e},0}$ (see Eq. (5.7)). The time-dependent electron temperature leads to a different scaling of the electric field strength at the ion front E_f in comparison to the isothermal situation. While in the isothermal Maxwellian model the asymptotic behavior is given by $E_\mathrm{f} \propto t^{-1}$ (see Eq. (4.8)), in the adiabatic Maxwellian approach one finds the relations[62] $E_\mathrm{f} \propto t^{-2}$ and $E_\mathrm{f} \propto t^{-3/2}$ for nonrelativistic and ultrarelativistic electrons, respectively. Thus, for an arbitrary value of the electron temperature the electric field at the ion front drops with t^n, with $n > 3/2$. This leads to an asymptotic behavior of the ion front velocity of the form $v_\mathrm{final} - 1/t^m$, with $m > 1/2$. In other words, in contrast to the isothermal case, the maximum ion velocity has a finite limiting value v_final for $t \to \infty$. The behavior of the ion front velocity in the different approaches is shown in Fig. 5.1b.

To describe the motion of ion front in the adiabatic Maxwellian case, we have proposed a generalization[82] of Mora's ansatz (4.10) for the electric field strength at the ion front in the isothermal expansion. For nonrelativistic temperatures it takes the form

$$E_\mathrm{f} = \frac{E_\mathrm{f}(0)}{\sqrt{1 + \alpha\,\tau^2 + \beta\,\tau^4}}\,, \tag{5.8}$$

with α, β being functions of the normalized target thickness $l = L/\lambda_\mathrm{D}$, only. Here, L denotes the initial target thickness (in physical units) and $\tau = \omega_\mathrm{pi}\, t / \sqrt{2\exp(1)}$ is the normalized time. Starting from simulation results, we found empirically the following fits,

$$\begin{aligned} \alpha &= \frac{\chi_1\, l^{3/2} + \chi_2\, l^2 + \chi_3\, l^{5/2} + \chi_4\, l^3}{1 + \chi_5\, l^{3/2} + \chi_6\, l^2 + \chi_7\, l^{5/2} + \chi_4\, l^3} \\ \beta &= \left(\frac{\eta_1\, l + \eta_2\, l^{3/2} + \eta_3\, l^2}{1 + \eta_4\, l^{1/2} + \eta_5\, l^2 + \eta_6\, l^{7/3}}\right)^4\,, \end{aligned} \tag{5.9a}$$

with the coefficients

$$\begin{aligned}(\chi_j) &= (-0.0129981, 0.525472, -0.144767, 0.0325432,\\ &\quad -0.70989, 0.860559, -0.199045)\\ (\eta_j) &= (0.0926025, 5.65707, 0.2323, 12.9501,\\ &\quad 2.09728, 0.0701358)\,.\end{aligned} \tag{5.9b}$$

By integration of the Poisson equation (4.3), the initial electric field strength at the ion front can be estimated as

$$E_\mathrm{f}(0) = \sqrt{\frac{2}{\exp(1)}}\sqrt{\frac{l^2}{8+l^2}\cdot\exp\left(\frac{8}{8+l^2}\right)}\,E_0\,. \tag{5.10}$$

By using the relations (5.9) and (5.10) in Eq. (5.8), the deviation $|E(t) - E_\mathrm{num}(t)|/E_0$ of the ansatz (5.8) compared to the simulation values $E_\mathrm{num}(t)$ is less than 1% for $0.5\,\lambda_\mathrm{D} \leq L \leq 500\,\lambda_\mathrm{D}$. The integration of Eq. (5.8) yields expressions for the ion front velocity

$$\frac{v_\mathrm{f}(t)}{c_\mathrm{s}} = \sqrt{2\exp(1)}\,\frac{\sigma}{\sqrt{-a}}\,\mathrm{F}\left[\arcsin\left(\sqrt{-a}\,\tau\right)\,|\,\frac{b}{a}\right]\,, \tag{5.11}$$

and for the displacement of the ion front

$$\frac{\Delta x_\mathrm{f}(t)}{\lambda_\mathrm{D}} = 2\exp(1)\,\sigma\cdot\left(\frac{\tau}{\sqrt{-a}}\,\mathrm{F}\left[\arcsin\left(\sqrt{-a}\,\tau\right)\,|\,\frac{b}{a}\right] - \frac{1}{\sqrt{ab}}\ln\left[\frac{\sqrt{b}\sqrt{1+a\tau^2}+\sqrt{a}\sqrt{1+b\tau^2}}{\sqrt{a}+\sqrt{b}}\right]\right) \tag{5.12}$$

as functions of time. Here, F is the *incomplete elliptic integral* of the first kind and the coefficients a and b are given by $(\alpha \mp \sqrt{\alpha^2 - 4\beta})/2$. By evaluating the limit $t \to \infty$ in Eq. (5.11), one obtains the final maximum ion energy,

$$\varepsilon_\mathrm{max}/Z_\mathrm{i} = T_\mathrm{e,0}\exp(1)\,\frac{\sigma^2}{a}\,\mathrm{K}\left[1-\frac{b}{a}\right]^2\,, \tag{5.13}$$

where K denotes the *complete elliptic integral* of the first kind. Relation (5.13) is in good agreement with Ref. 62, where some alternative, heuristic formulas for v_final for large values of L/λ_D are given. In the ultrarelativistic regime an ansatz equivalent to Eq.(5.8) could be made, however, this was not part of our studies in Ref. 82.

5.1.2. The kinetic Maxwellian model

The adiabatic Maxwellian model[62] introduced in Sec. 5.1.1 describes a simple, possible variation of the original isothermal expansion model[1–3] (see Sec. 5.1.1) which ensures the conservation of the total energy of an expanding plasma-slab with an initially finite thickness. Especially, the approach leads to a finite final maximum ion energy. In this approach, the electron distribution

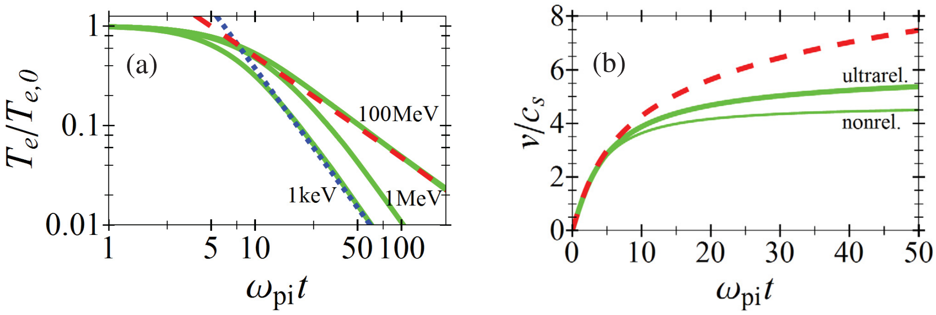

Figure 5.1.: Simulation results for the adiabatic expansion of a foil with an initial thickness of $20\lambda_{\mathrm{D}}$ assuming different initial electron temperatures. The plot corresponds to an example given by Mora.[62] In (a), the temporal evolution of the electron temperature for three different initial values of $T_{\mathrm{e},0}$ is depicted (green curves). In addition, the asymptotic scaling laws $T_{\mathrm{e}} \propto t^{-2}$ (dotted blue line) and $T_{\mathrm{e}} \propto t^{-1}$ (dashed red line) are shown, corresponding to the non- and the ultrarelativistic situation, respectively. In (b), the ion front velocity is shown for the adiabatic Maxwellian approach (green curves) for the non- and the ultrarelativistic case, respectively, in comparison to the isothermal result (red dashed curve). Generally, the velocity saturates more quickly in the nonrelativistic than in the ultrarelativistic case. Here, the asymptotic values are $4.7\,c_{\mathrm{s}}$ and $6.5\,c_{\mathrm{s}}$ for the nonrelativistic and the ultrarelativistic case, respectively.

is assumed to be Maxwellian with a time-dependent temperature. However, from the physics point of view, there is no a priori reason for the electron distribution to preserve its Maxwellian structure since the hot electrons are almost collisionless.[63] An approach — in the following we refer to it as the *kinetic appproach* — which remedies that weak point was studied in Ref. 64 by Grismayer et al. It is based on the concept of the adiabatic invariants[194] and allows the initial electron phase space density to evolve arbitrarily. Following Ref. 81, we will give a short summary of this concept here.

In the kinetic approach, one starts with an arbitrary one-particle phase space density $f(p) = f_{\mathrm{e},0}(p,t)$ at an arbitrary instant of time t. Next, one considers the points $(p_j, f_j = f(p_j))$ corresponding to particles with the momentum p_j in absence of a potential, i.e. $\phi \equiv 0$. The different values p_j of the momentum are related to different values ε_j of the total energy. Now, one regards the motion of a particle with the total energy ε_j in the electrostatic potential ϕ over a full period $\mathscr{T}_j$ of its motion(2). If the potential ϕ is time-independent, hence conservative, then the total energy will be conserved. However, in general, the potential will vary during the time $\mathscr{T}_j$ and therefore the total energy of the particle will be changed, $\varepsilon_j \to \varepsilon_j + \Delta\varepsilon_j = \varepsilon_j'$. Following Ref. 64, the change $\Delta\varepsilon_j$ of the total energy during a small amount of time Δt is evaluated via $\Delta\varepsilon_j = \left\langle \frac{\partial \varepsilon_j}{\partial t} \right\rangle \Delta t$, with $\left\langle \frac{\partial \varepsilon_j}{\partial t} \right\rangle$ being the mean variation rate of the total energy over a full period of motion of the particle,

---

(2) The finite extent of the ion distribution implies the boundary conditions $\phi(\pm\infty) = -\infty$. As a consequence, the trajectory of an electron j is restricted to the finitely sized region $[x_1, x_2]$, with $-\phi(x_{1,2}) = \varepsilon_j$. Hence, its motion is periodic as long as the total energy ε_j does not decrease too rapidly — in this case the oscillations would become critically damped or even overdamped.

$$\left\langle \frac{\partial \varepsilon_j}{\partial t} \right\rangle = -e \left\langle \frac{\partial \phi}{\partial t} \right\rangle_j = -\frac{e}{\mathscr{T}_j} \int\limits_{\mathscr{T}_j} \frac{\partial \phi(x(t),t)}{\partial t} \, \mathrm{d}t \, . \tag{5.14}$$

Here, $x(t)$ denotes the particle position as a function of time. The variation of the energy values, $e_j \to e'_j$, is equivalent to a change in the momenta at $\phi = 0$, $p_j \to p_j + \Delta p_j = p'_j$. In contrast, the values f_j are preserved.[64] Therefore, the electron distribution at the instant $t' = t + \Delta t$ is given by the function f' which fulfills the relation $f'(p'(p)) = f(p)$ for all values of p. The described procedure is illustrated in Fig. 5.2. As already mentioned, the kinetic approach works for an arbitrary initial phase space density. For example, in part IV we will use the ansatz for a step-like electron distribution. However, most commonly $f_{\mathrm{e},0}$ is initially set to a Maxwell distribution. In this case we refer to the kinetic model as the *kinetic Maxwellian approach*.

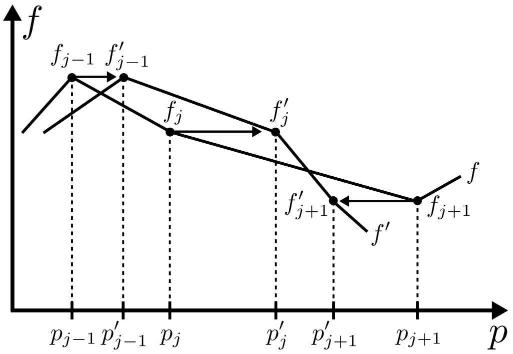

Figure 5.2.: Illustration of the approach[64] which describes the modification of an electron phase space density f to the function f' during a time step Δt. Here, the function values $f_j = f(p_j)$ of the electron distribution are kept constant for arbitrary values p_j. In contrast, the values p_j are varied by the algorithm, $p_j \to p'_j$. The figure is taken from Ref. 81.

In the following, we want to point out some aspects of the kinetic algorithm. (i) Since the variation Δp of the momentum p is a function of the value p itself, the procedure leads to complex electron distributions. Note especially that in general, an initially Maxwellian electron energy distribution is not preserved.[64,65] For example, during the expansion of an initially step-like target with a finite thickness, an initially Maxwellian electron energy distribution evolves into a distribution with a pronounced high-energy tail,[64,65] which is plotted in Fig. 5.3. The phase space density is formed by the following process.

According to Eq. (5.14), the energy variation rate of an electron with an energy ε_j has to be evaluated over a full period of its motion. For a low-energy electron — i.e., $\varepsilon_j \leq -e \cdot (\phi(x_\mathrm{f}) - \phi(0))$, with x_f denoting the position of the ion front and $x = 0$ being the center of the foil — the turning point(3) x_turn of the electron's period lays close to the ion front or even inside the expanding ion distribution, $x_\mathrm{turn} \lesssim x_\mathrm{f}$. Since for $x \lesssim x_\mathrm{f}$ the temporal variation rate of the ion density, $\partial n_\mathrm{i}/\partial t$, is comparatively large due to the plasma expansion process, in this domain the electric potential evolves quickly, too. For that reason, Eq. (5.14) predicts a relatively large absolute

---

(3) Since the situation is symmetric with respect to $x = 0$, i.e. $n_\mathrm{i}(x) = n_\mathrm{i}(-x)$, etc., we only consider the part of the motion in the right half space $x \geq 0$.

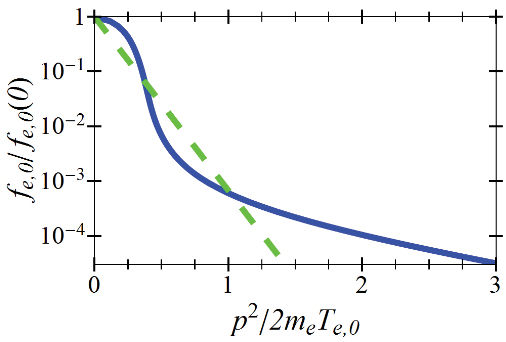

Figure 5.3.: Electron phase space density at $\phi = 0$, $f_{\mathrm{e},0}(p)$, for the expansion of an foil with an initial thickness of $L/\lambda_\mathrm{D} = 40$ at the instant $\omega_\mathrm{pi}t = 30$. Here, the results of the kinetic Maxwellian model and the adiabatic Maxwellian model are depicted by the solid blue and the dashed green curve, respectively. While the latter corresponds to a Maxwellian distribution, on obtains a non-Maxwellian phase space density in the kinetic approach.

value. In contrast, in case of a high-energy electron, $\varepsilon_j \gg -e\cdot(\phi(x_\mathrm{f})-\phi(0))$, the turning point of the period is situated far beyond the ion-front, $x_\mathrm{turn} \gg x_\mathrm{f}$. Thus, large parts of the electron's motion take place in the domain $x > x_\mathrm{f}$. Here, one has $\partial n_\mathrm{i}/\partial t = 0$, and, as a consequence, in this domain the potential is evolving comparatively slowly. With increasing electron energy, this part of the motion outweighs the inner part of the motion in Eq. (5.14) more and more, since x_turn tends towards infinity in the limit $\varepsilon_j \to \infty$. Summarizing, high-energy electrons are barely influenced by the plasma expansion process in comparison to low-energy electrons, which results eventually in a pronounced high-energy tail.

(ii) The kinetic approach is equivalent to a fully time-dependent solution of the Vlasov equation (2.11) for the electrons as long as the changes in the electrostatic potential are not to rapid. More precisely, the necessary condition[64] can be written as $\mathscr{T}_j/t_\phi \ll 1$ for all electrons j, with $t_\phi = |1/\phi\cdot\partial\phi/\partial t|^{-1}$ being the characteristic time of change in the electrostatic potential.

(iii) In the kinetic model the total energy of the expanding system is conserved. Thus, the ansatz serves as a model for an adiabatic plasma expansion, too. Therefore, here, we want to briefly compare the kinetic Maxwellian approach to the adiabatic Maxwellian model for the non-relativistic case. A more comprehensive discussion is given in Sec. 7.2 and Ref. 82.

In contrast to the adiabatic Maxwellian approach, which predicts a scaling of t^{-2} for the electric field at the ion front, one observes the scaling law t^{-n}, with $1 < n < 2$, in the kinetic version.[64] As a consequence, the final maximum ion velocity is finite in both approaches but it saturates more slowly in the kinetic model (see Fig. 5.4a). The different scaling of the electric field at the ion front in both approaches is caused by a different evolution of the electron temperature at the ion front.[64,82] Naturally, at $t = 0$ the situation is identical in both models since the initial electron distributions are identical, too. However for $\omega_\mathrm{pi}t > 0$, the situation is different in both models. Firstly, in the adiabatic Maxwellian model one has a uniform spatial electron temperature distribution⁽⁴⁾. In contrast, in the kinetic ansatz the local electron temperature is a function of x for $\omega_{\mathrm{pi}} t > 0$ (see Fig. 5.4b and Refs. 64, 65). Here, it shows that the electron temperature in the inner plasma region $x \lesssim x_{\mathrm{f}}$, with x_{f} denoting the position of the ion front, is decreasing quickly, due to the energy transfer into the kinetic energy of the ions. In contrast, the local temperature for $x \gtrsim x_{\mathrm{f}}$ decreases more slowly and is significantly higher than in the inner regions. Moreover, for $x \to \infty$ the local electron temperature tends towards its initial value. Note that the local electron temperature distribution, which has a structure similar to that in the solar corona although the physical origin is different,[65] is caused by the high-energy tail of the electron distribution[65] shown in Fig. 5.3.

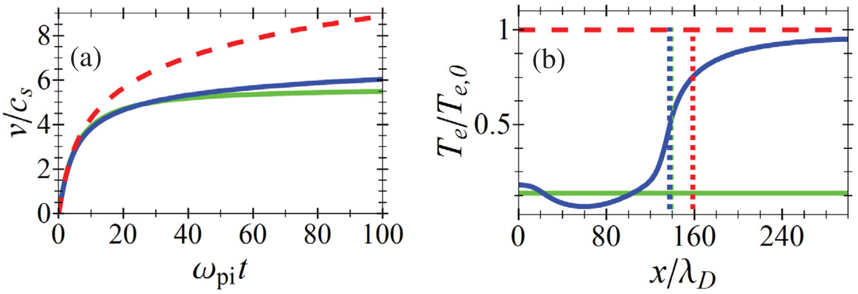

Figure 5.4.: Expansion of a foil with an initial thickness of $L/\lambda_{\mathrm{D}} = 40$ in the kinetic Maxwellian model (solid blue curves) in comparison to the adiabatic Maxwellian model (solid green curve) and the isothermal Maxwellian model (dashed red curve). (a) shows the maximum ion velocity. Here, the velocities in the limit $t \to \infty$ are $v_{\max} = 8.6\,c_{\mathrm{s}}$ and $v_{\max} = 5.7\,c_{\mathrm{s}}$ for the kinetic and the adiabatic Maxwellian model, respectively, while there is no finite final velocity in the isothermal approach (see Sec. 4.2). In (b), the spatial distribution of the electron temperature is shown for $\omega_{\mathrm{pi}} t = 30$. The positions of the ion front are depicted by dashed vertical lines in the corresponding colors of the respective models.

The different spatial electron temperature distributions lead to a higher electron temperature at the ion front in the kinetic approach in comparison to the adiabatic Maxwellian model. Since, assuming nonrelativistic electrons, the electric field strength is generally given by $E(t) = \sqrt{2/\varepsilon_0}\,\sqrt{n_{\mathrm{e}}(t)\,T_{\mathrm{e}}(t)}$ (see Sec. B.3) and the electron density at the ion front, $n_{\mathrm{e}}(t)$, evolves similar in both approaches (see Sec. 7.2), the slower decrease of the electron temperature induces a slower decrease of the electric field at the ion front in the kinetic approach.

Although the maximum ion velocity evolves different in both approaches, the simulations also show that its value in the limit $t \to \infty$ is of the same order of magnitude in both models. Moreover, from Fig. 5.4a it is obvious, that the curves go apart at late times only. This is especially important for the application on experiments. Here, the effective acceleration time of the ions, t_{acc}, can be approximated by the time which it takes for the plasma expansion to become multidimensional (see Sec. 7.3 and Ref. 82). Starting from the isothermal Mora model,[59] this time can be estimated by $\omega_{\mathrm{pi}}\, t_{\mathrm{acc}} = (2\exp(1))^{1/4}\sqrt{D_{\mathrm{e}}/\lambda_{\mathrm{D}}}$, with D_{e} being the transverse size of the electron spot on the target rear side and $\lambda_{\mathrm{D}} = \sqrt{\varepsilon_0\, T_{\mathrm{e},0}/e^2\, n_{\mathrm{e},0}}$ denot-

---

(4) This can be verified by evaluating the local thermal energy of the electrons via Eq. (B.45) for a Maxwellian phase space density, Eq. (2.23), and finally applying the relation (B.43) between the local temperature and the local thermal energy of the electrons.

ing the hot electron Debye length. Assuming parameters for the hot electrons in the range of $T_{\mathrm{e},0} \approx 0.1\mathrm{MeV} \ldots 10\mathrm{MeV}$ and $n_{\mathrm{e},0} \approx 10^{20}\mathrm{cm}^{-3} \ldots 10^{21}\mathrm{cm}^{-3}$, one finds $\lambda_{\mathrm{D}} \approx 0.1\mathrm{\mu m} \ldots 2.5\mathrm{\mu m}$. Moreover, one has $D_{\mathrm{e}} \approx 5\mathrm{\mu m} \ldots 100\mathrm{\mu m}$ (see Ref. 82). From these values one obtains effective acceleration times of $2 \leq \omega_{\mathrm{pi}} t_{\mathrm{acc}} \geq 50$. As shown in Fig. 5.4a, for $\omega_{\mathrm{pi}} t \leq 50$ the maximum ion velocity is quite similar in both models.

5.2. Inclusion of cold electrons

So far, in all expansion models we have exclusively focused on the hot electrons (5) with some density $n_{\mathrm{e,h}}$ and some mean thermal energy $T_{\mathrm{e,h}}$. However, in reality there is also a cold electron background density $n_{\mathrm{e,c}}$. Normally, one assumes these electrons to have a Maxwellian energy distribution with a certain temperature $T_{\mathrm{e,c},0}$.

Thus, in analogy with the expression (5.1) for the hot electrons, in the stationary model discussed in Sec. 2.3 the cold electron species is described by the density relation

$$n_{\mathrm{e,c}} = n_{\mathrm{e,c},0} \exp\left(\frac{e\phi}{T_{\mathrm{e,c},0}}\right) . \tag{5.15}$$

Here, $n_{\mathrm{e,c},0}$ is the cold electron density in absence of a potential ($\phi \equiv 0$) and $T_{\mathrm{e,c},0}$ denotes the (initial) cold electron temperature. Furthermore, we restrict the cold electron parameters to the case of(6)

$$\begin{aligned} &T_{\mathrm{e,c},0} \ll T_{\mathrm{e,h},0} \\ &n_{\mathrm{e,c},0} \gg n_{\mathrm{e,h},0} \\ &n_{\mathrm{e,c},0}\, T_{\mathrm{e,c},0} \lesssim n_{\mathrm{e,h},0}\, T_{\mathrm{e,h},0} . \end{aligned} \tag{5.16}$$

In addition, in order to realize charge neutrality at $\phi = 0$, one sets $n_{\mathrm{e,c},0} + n_{\mathrm{e,h},0} = Z_{\mathrm{i}} n_{\mathrm{i},0}$. By taking the cold electrons into account, the Poisson equation (4.3) is modified to

$$\varepsilon_0 \frac{\partial^2 \phi}{\partial x^2} = e \cdot \left(n_{\mathrm{e,h},0} \exp\left(\frac{e\phi}{T_{\mathrm{e,h},0}}\right) + n_{\mathrm{e,c},0} \exp\left(\frac{e\phi}{T_{\mathrm{e,c},0}}\right) - Z_{\mathrm{i}}\, n_{\mathrm{i}} \right) . \tag{5.17}$$

Thus, the expansion of a plasma slab is now modeled by the equations (4.1), (4.2) and (5.17). As in the case of a single electron species, the coupled system is not analytically solvable. Moreover, for $T_{\mathrm{e,h},0}/T_{\mathrm{e,c},0} \geq 5 + \sqrt{24} \approx 10$ collisionless shocks appear in the expanding plasma.[54,70] As a consequence, the fluid description for the ions, Eqs. (4.2), is no longer valid and a self-similar solution does not exist even under the assumption of quasi-neutrality $Z_{\mathrm{i}}\, n_{\mathrm{i}} \approx n_{\mathrm{e,h}} + n_{\mathrm{e,c}}$. Since in a typical laser-plasma foil experiment one has $T_{\mathrm{e,h},0}/T_{\mathrm{e,c},0} > 10$, most of the investigations have to be carried out numerically.

---

(5) Apart from this section, we only have to deal with one electron population, namely the hot one. Thus an extra index at the hot electron quantities would be redundant. However, here, in order to distinguish clearly between the two electron populations, we label the quantities referring to the hot electrons with an additional index "h", while quantities corresponding to the cold electrons are labeled with an extra index "c".

(6) Following Ref. 14, one can assume the upper limit for the cold electron temperature to be approximately in the range of $0.1\,\mathrm{keV} \ldots 1\,\mathrm{keV}$. Furthermore, one can assume $n_{\mathrm{e,c},0} \approx 10^{23}\,\mathrm{cm}^{-3}$ according to a typical solid density. By assuming the hot electron parameters to be in the range of $T_{\mathrm{e,h},0} \approx 1\,\mathrm{MeV} \ldots 10\,\mathrm{MeV}$ and $n_{\mathrm{e,h},0} \approx 10^{20}\,\mathrm{cm}^{-3} \ldots 10^{21}\,\mathrm{cm}^{-3}$, this motivates the relations (5.16).

In the two-temperature case, the initial field strength at the target boundary is given by

$$E_\mathrm{f}(0)/E_0 = \sqrt{2}\sqrt{\exp\left(\frac{e\,\phi_\mathrm{f}(0)}{T_{\mathrm{e,h},0}}\right) + \frac{n_{\mathrm{e,c},0}\,T_{\mathrm{e,c},0}}{n_{\mathrm{e,h},0}\,T_{\mathrm{e,h},0}}\exp\left(\frac{e\,\phi_\mathrm{f}(0)}{T_{\mathrm{e,c},0}}\right)}\,, \tag{5.18}$$

with the characteristic field strength $E_0 = \sqrt{n_{\mathrm{e,h},0}\,T_{\mathrm{e,h},0}/\varepsilon_0}$ and $\phi_\mathrm{f}(0)$ denoting the initial electric potential at the ion front, $x = 0$, for which we find

$$e\,\phi_\mathrm{f}(0) = -\frac{n_{\mathrm{e,h},0}\,T_{\mathrm{e,h},0} + n_{\mathrm{e,c},0}\,T_{\mathrm{e,c},0}}{n_{\mathrm{e,h},0} + n_{\mathrm{e,c},0}}\,. \tag{5.19}$$

In a situation where the cold electron pressure is comparable to that of the hot electrons, $n_{\mathrm{e,c},0}\,T_{\mathrm{e,c},0} \approx n_{\mathrm{e,h},0}\,T_{\mathrm{e,h},0}$, Eq. (5.19) reads

$$e\,\phi_\mathrm{f}(0) \approx -2\,T_{\mathrm{e,c},0}\,, \tag{5.20}$$

and the electric field strength (5.18) is given by

$$E_\mathrm{f}(0)/E_0 \approx \sqrt{2}\,\sqrt{1+\exp(-2)}\,. \tag{5.21}$$

Otherwise, when the cold electron pressure is negligible, i.e. $n_{\mathrm{e,c},0}\,T_{\mathrm{e,c},0} \ll n_{\mathrm{e,h},0}\,T_{\mathrm{e,h},0}$, one finds

$$e\,\phi_\mathrm{f}(0) \approx -\frac{n_{\mathrm{e,h},0}}{n_{\mathrm{e,c},0}}\,T_{\mathrm{e,h},0}\,, \tag{5.22}$$

and, as a consequence,

$$E_\mathrm{f}(0)/E_0 \approx \sqrt{2}\,. \tag{5.23}$$

Since $\sqrt{1+\exp(-2)} \approx 1$, one may conclude that Eq. (5.23) serves as a general expression for the electric field strength in the two-temperature case under the conditions (5.16). By comparing Eq. (5.23) with the one-temperature situation, Eq. (4.9), one can see that the presence of the cold electrons enlarges the initial electric field strength at the ion front by a factor of $\sqrt{\exp(1)} \approx 1.65$. This is also illustrated in Figs. 5.5a and 5.5b.

Apart from that, the cold electrons also have a remarkable influence on the skin depth λ_skin inside the plasma. Commonly, the skin depth is equated with the length scale on which the absolute value of the electric field drops to $1/\exp(1)$ of its value at the target boundary ($x = 0$). Since inside the plasma slab ($x < 0$) the Poisson equation (5.17) cannot be solved analytically, we make the empirical ansatz

$$\phi_\mathrm{ansatz} = \phi_\mathrm{f}(0)\,\exp\left(\frac{x}{\lambda_\mathrm{skin}}\right)\,, \tag{5.24}$$

for $x < 0$. This ansatz is motivated by numerical studies and it implies immediately the expression

$$E_\mathrm{ansatz} = E_\mathrm{f}(0)\,\exp\left(\frac{x}{\lambda_\mathrm{skin}}\right) \tag{5.25}$$

for the electric field inside the target, with

$$\lambda_{\mathrm{skin}} = -\frac{\phi_{\mathrm{f}}(0)}{E_{\mathrm{f}}(0)} \,. \tag{5.26}$$

By substituting the relations (5.20) and (5.23) for ϕ_{f} and E_{f} into Eq. (5.26) we obtain the expression

$$\lambda_{\mathrm{skin}} = \sqrt{2}\,\frac{T_{\mathrm{e,c},0}}{T_{\mathrm{e,h},0}}\,\lambda_{\mathrm{D,h}} \tag{5.27}$$

for the skin depth in the case $n_{\mathrm{e,c},0}\,T_{\mathrm{e,c},0} \approx n_{\mathrm{e,h},0}\,T_{\mathrm{e,h},0}$. Here, $\lambda_{\mathrm{D,h}} = \sqrt{\varepsilon_0\,T_{\mathrm{e,h},0}/e^2\,n_{\mathrm{e,h},0}}$ refers to the hot electron Debye length. Since $T_{\mathrm{e,c},0}/T_{\mathrm{e,h},0} \approx n_{\mathrm{e,h}}/n_{\mathrm{e,h},0}$, the last relation can be rewritten as

$$\lambda_{\mathrm{skin}} = \sqrt{2}\,\frac{n_{\mathrm{e,h},0}}{n_{\mathrm{e,c},0}}\,\lambda_{\mathrm{D,h}}. \tag{5.28}$$

Equivalently, in the case $n_{\mathrm{e,c},0}\,T_{\mathrm{e,c},0} \ll n_{\mathrm{e,h},0}\,T_{\mathrm{e,h},0}$ one obtains the result

$$\lambda_{\mathrm{skin}} = \frac{1}{\sqrt{2}}\,\frac{n_{\mathrm{e,h},0}}{n_{\mathrm{e,c},0}}\,\lambda_{\mathrm{D,h}} \,. \tag{5.29}$$

By summarizing (5.28) and (5.29) we obtain a skin depth of the order

$$\lambda_{\mathrm{skin}} \approx \frac{n_{\mathrm{e,h},0}}{n_{\mathrm{e,c},0}}\,\lambda_{\mathrm{D,h}} \tag{5.30}$$

for the parameter region (5.16). The last result can also be rewritten in terms of the cold electron Debye length $\lambda_{\mathrm{D,c}} = \sqrt{\varepsilon_0\,T_{\mathrm{e,c},0}/e^2\,n_{\mathrm{e,c},0}}$ as

$$\lambda_{\mathrm{skin}} \approx \sqrt{\frac{n_{\mathrm{e,h},0}\,T_{\mathrm{e,h},0}}{n_{\mathrm{e,c},0}\,T_{\mathrm{e,c},0}}}\,\lambda_{\mathrm{D,c}} \,. \tag{5.31}$$

According to Eqs. (5.30)–(5.31), we can conclude the relations

$$\lambda_{\mathrm{D,c}} \leq \lambda_{\mathrm{skin}} < \lambda_{\mathrm{D,h}} \tag{5.32}$$

for the parameter region of our interest, Eq. (5.16). From Eq. (5.30) it is obvious that the skin depth is normally smaller than the hot electron Debye length by several orders of magnitude. The very different skin depth in the one- and the two-temperature model is illustrated in Figs. 5.5a and 5.5b. Of course, the difference in the electric field is also related to a difference in the electric potential (see Figs. 5.5c and 5.5d). In addition, since the electric potential and the electron densities are coupled via Eqs. (5.1) and (5.15), the electron densities are also remarkable different (see Figs. 5.5e and 5.5f). Especially note that the electric field in the two-temperature case leads to a total displacement of the cold electrons in the region of the skin depth into the target (see Fig. 5.5f).

This result is especially important for *ultra-thin* targets. Commonly, a target is denoted as ultra-thin when its thickness is of the order of the skin depth or even less. By only taking the hot electrons into account and assuming typical values $T_{\mathrm{e,h},0} \approx 1\,\mathrm{MeV}$, $n_{\mathrm{e,h},0} \approx 10^{20}\,\mathrm{cm}^{-3}$, one would

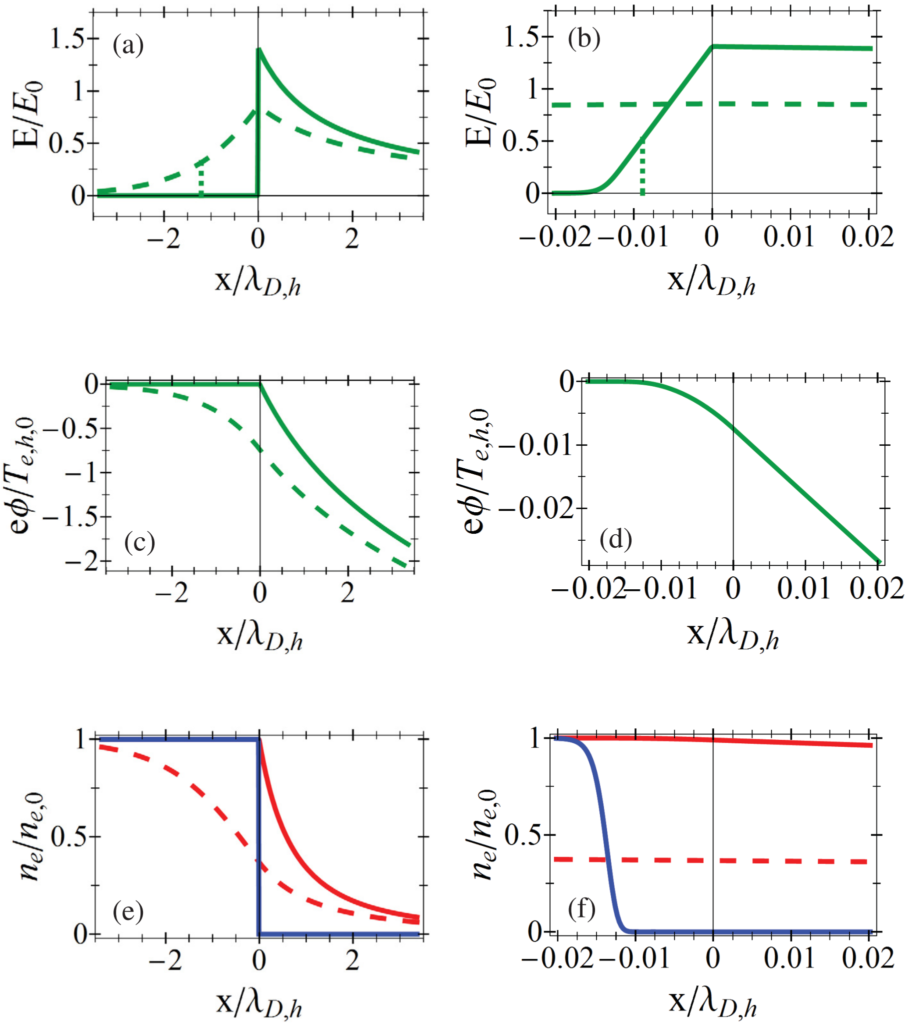

Figure 5.5.: The two-temperature case in comparison to the one-temperature case at $t = 0$. The hot electron parameters $n_{\mathrm{e,h,0}}$ and $T_{\mathrm{e,h,0}}$ are the same in both cases. In the two-temperature case the cold electron parameters are $n_{\mathrm{e,c,0}} = 100 n_{\mathrm{e,h,0}}$ and $T_{\mathrm{e,c,0}} = 10^{-4} T_{\mathrm{e,h,0}}$. (a) and (b) show the electric field for different intercepts of the x-axis, (c) and (d) display the corresponding electric potential. Here, the dashed curves correspond to the one-temperature case while the solid ones depict the case of two electron populations. In addition, in (a) and (b), the skin depth (measured from $x = 0$) is marked by the dashed vertical line for the one-temperature and the two-temperature case, respectively. (e) and (f) depict the spatial electron densities. Here, the hot electron density of the one-temperature case is depicted by the dashed red curves. In addition, the solid red and the solid blue curves correspond to the hot and the cold electron density for the two-temperature case, respectively. The hot and the cold electron density are normalized to $n_{\mathrm{e,h,0}}$ and $n_{\mathrm{e,c,0}}$, respectively.

expect a skin depth λ_{skin} which is of the order of the hot electron Debye length $\lambda_{\mathrm{D,h}} \approx 1\,\mu\mathrm{m}$. However, by considering cold electrons with a density of the order of $10^{23}\,\mathrm{cm}^{-3}$ the actual skin depth (5.30) is three orders below the hot electron Debye length. Hence, here, an ultra-thin target has to have a thickness of the order of nanometers or less. The skin depth is also important for computer simulations. Commonly, the electric field is calculated numerically at the discrete points of a uniform spatial grid (see Sec. A.4). Assuming a resolution of 10 grid points per skin depth — in order to resolve the decay of the electric field sufficiently well — the grid has to have 10 nodes per micrometer in the one-temperature case. In contrast, one needs about 10^4 grid points per micrometer when considering the cold electrons, too. Thus a large simulation area of the order of $\mathscr{O}(100\,\mu\mathrm{m})$ implies about 10^6 nodes for an uniform grid — a large computational effort.

So far, we have focused on the initial situation assuming a step-like target. Here, we saw that the initial electric field strength at the ion front is enlarged by a factor of ≈ 1.65. Based on that one might expect that the ion acceleration process is also noticeably different for $t > 0$. Of course, the cold electrons also influence the physical results(7) for times $t > 0$. However utilizing simulation results, one can see that in the parameter region (5.16) the impact of the cold electrons on the ion front characteristics is not that large. As shown in Fig. 5.6a the electric field at the ion front in the two-temperature case asymptotically approaches that of the one-temperature case. Hence, despite the presence of the cold electrons, for $\omega_{\mathrm{pi,h}}\, t \gg 1$ the electric field strength is approximately given by twice the self-similar expression (4.6) — equivalently to the one-temperature case (see Sec. 4.2). According to the evolution of the electric fields, the difference in the ion front velocities is decreasing, too. Especially, the velocity in the two-temperature case is significantly lower than the 1.65-fold value of the one-temperature result, for $\omega_{\mathrm{pi,h}}\, t \gg 1$ (see Fig. 5.6b). More precisely, the ratio of the ion front velocities is decreasing from 1.65 to 1, i.e. the relative deviation in the results tends towards zero. For the example plotted in Fig. 5.6, it is found to be less than 20% for $\omega_{\mathrm{pi,h}}\, t \gg 1$.

The asymptotic equivalence of the one- and the two-temperature case is caused by the behavior of the hot and cold electron densities. As depicted in Figs. 5.6c and 5.6d, as the ion front expands into the vacuum, the cold electrons are left behind. In contrast, a fraction of the hot electrons is co-propagating which almost neutralizes the ion charge. Hence, close to the ion front the hot electrons dominate the expansion process and the quasi-neutral condition $n_{\mathrm{e,h}} \approx Z_{\mathrm{i}}\, n_{\mathrm{i}}$ is fulfilled. As a consequence, at later times, the one-temperature self-similar result (4.5) describes the plasma expansion quite well.

5.3. Extensions regarding the ion distribution

In the previous sections 5.1–5.2, the original model for the expansion of a plasma slab, introduced in chapter 4, has been extended with respect to the electrons. First, the description of the temporal evolution of the hot electron distribution was improved in Sec. 5.1. Then, in Sec. 5.2, the cold electrons were taken into account. All theses models have in common that they assume a single ion distribution with an initial step-like density profile. Either in form of a semi-infinite plasma slab (chapter 4 and Sec. 5.2) or in form of a step-like target with a finite thickness (Sec. 5.1).

However, there are also studies which deal with an altered initial ion distribution. For example, in Ref. 195 the expansion of a Gaussian ion density profile is investigated. Another example is given in Ref. 119, where the influence of a finite initial density gradient at the target rear side on

---

(7) A more detailed analysis of the impact of the cold electrons on the expansion process, especially in terms of the rarefaction wave and shock waves is given in Refs. 77, 78.

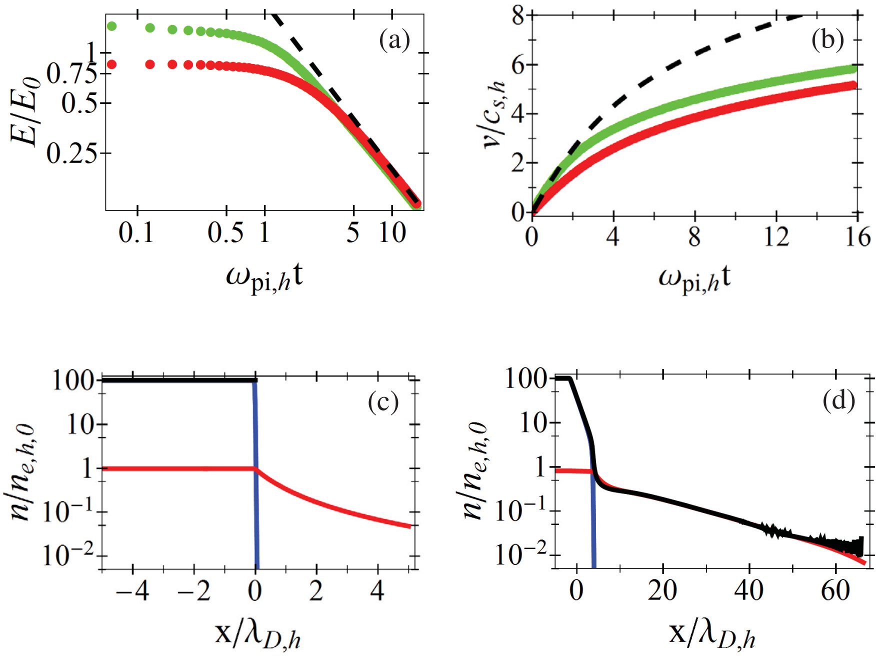

Figure 5.6.: Plasma expansion process assuming two electron populations. In (a) and (b) the evolution of the electric field strength at the ion front and the ion front velocity is shown, respectively, for the two-temperature case (green curves) in comparison to the one-temperature case (red curves). In addition, in (a) the electric field strength of the one-temperature self-similar solution, $2E_0/(\omega_{\mathrm{p,i,h}t})$, is depicted (dashed black curve). In (b), the dashed black curve corresponds to the 1.65-fold of the one-temperature velocity. In (c) and (d), the spatial densities of the cold electrons (blue), the hot electrons (red) and the protons (black) are plotted for the instants $\omega_{\mathrm{pi,h}}t = 0$ and $\omega_{\mathrm{pi,h}}t \approx 15.8$.

the plasma expansion is studied. Here, the initial ion distribution is given by a plasma slab with an exponential gradient at the target boundary. In both studies, the target rear is no longer steep but has a density gradient $l_{\mathrm{ss}} = |n_{\mathrm{i}}/(\partial n_{\mathrm{i}}/\partial x)| > 0$. It shows that, in general, this influences the plasma expansion process remarkably, including effects as wave breaking and a reduction of the maximum ion velocity(8).

In numerous studies — analytical and numerical — another possible extension of the original expansion model with respect to the ions is investigated: the case of multiple ion species. Here, the target(9) consists either of a homogeneous mixture of more than one ion species — so called *homogeneous multi-ion species targets*[71,98,99,102] — or the target is composed of several layers each containing a single ion species — so called *multi-layer targets*.[95–99] In the multi-layer approach, one operates commonly with two layers — mostly denoted as *double-layer targets*. Here, a layer which contains light ions is attached in front of a layer which consists of heavy ions. A sketch illustration of the two kinds of multi-ion species targets is given in Fig. 5.7. In general,

---

(8) See Sec. 9.1 for further explanations.

(9) Of course, in principal also a combination of both kinds of multi-ion species targets is possible, i.e., a target composed of several layers where at least one layer consists of multiple ion species.

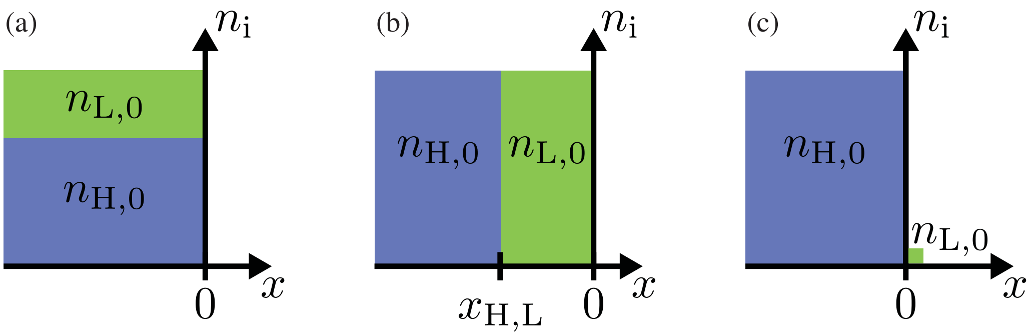

Figure 5.7.: In (a) a homogeneous target is shown. The light and the heavy ion species are uniformly distributed in the target with initial densities $n_{\mathrm{L},0}$ and $n_{\mathrm{H},0}$, respectively. (b) shows a double-layer target. Here, both ion species are separated in different layers. In (c), the test-particle model is shown, which is a particular case of (b) assuming $n_{\mathrm{L},0} \ll n_{\mathrm{H},0}$ and $|x_{\mathrm{H,L}}| \ll \lambda_\mathrm{D}$. Note that: (i) Normally, one sets $Z_\mathrm{H} n_{\mathrm{H},0} + Z_\mathrm{L} n_{\mathrm{L},0} = n_{\mathrm{e},0}$ and $Z_\mathrm{H} n_{\mathrm{H},0} = Z_\mathrm{L} n_{\mathrm{L},0} = n_{\mathrm{e},0}$ for (a) and (b), respectively. (ii) In (b), we have set $Z_\mathrm{H} = Z_\mathrm{L}$.

the plasma expansion of multi-ion targets show interesting properties. Especially in the context of the ion-energy spectra. While in the case of an expanding plasma slab consisting of a single ion species one obtains an exponentially decaying ion energy spectrum,[59] the expansion of a multi-ion species target can lead, under certain conditions, to the formation of monoenergetic peaks in the spectra.[71,98,99] Since the most applications rely on the availability of quasi-monoenergetic ion beams, these models are of great interest. However, in the present work, we will not discuss the details of multi-ion-species targets. Instead, we will only briefly consider the test-particle model, which can be seen as a special case of a double-layer target. The test-particle ansatz may serve as another simple plasma model, which in some sense is complementary to the basic plasma slab model of chapter 4. In the following, it will be briefly introduced(10).

In the multi-ion-species approach, the plasma slab (see chapter 4) can be seen as a limiting case: Starting from a double-layer target, as depicted in Fig. 5.7b), the expansion process will be equivalent to that of a plasma slab (consisting of light ions only) as long as the rarefaction wave has not reached the boundary of the two layers at $x_{\mathrm{H,L}}$. Since the rarefaction wave propagates with a velocity of c_s, see Ref. 70, the expansion of both targets will be equivalent for $t \lesssim -x_{\mathrm{H,L}}/c_\mathrm{s}$. Thus, the plasma slab is obtained from the double-layer target assuming an infinitely thick layer of light ions, hence, for $|x_{\mathrm{H,L}}| \to \infty$. In this limit, the light ions dominate the expansion — since they determine exclusively the electric field. Now, the test-particle model is obtained in the opposite limit, assuming(11) $n_{\mathrm{L},0} \to 0$ and $|x_{\mathrm{H,L}}| \ll \lambda_\mathrm{D}$, see Fig. 5.7c. Here, the heavy ions dominated the electric field and the light ions behave as test-particles. The corresponding fields are obtained by the integration of the nonlinear Poisson equation (4.3) in the region $x > x_\mathrm{f}$, with x_f denoting the heavy ion front. One finds

---

(10) Here, we only discuss the one-dimensional test-particle model. However, there are multi-dimensional versions as well, see Refs.[90,91,120] e.g.

(11) Often one also assumes a thin layer of light ions, $|x_{\mathrm{H,L}}| \ll \lambda_\mathrm{D}$. However, this condition is not necessary as long as the ion density $n_{\mathrm{L},0}$ is low against the local density of the hot electrons $n_\mathrm{e}(x)$, for all positions x in the layer of the light ions. In this case, the light ions will behave as test-particles.

$$\phi(x) = -\frac{2T_{\mathrm{e},0}}{e} \ln\left[\frac{1}{\sqrt{2}}\frac{x-x_{\mathrm{f}}}{\lambda_{\mathrm{D}}} + \exp\left(-\frac{e\phi_{\mathrm{f}}}{2T_{\mathrm{e},0}}\right)\right] \tag{5.33a}$$

$$E(x) = \frac{\sqrt{2}E_0}{\frac{1}{\sqrt{2}}\frac{x-x_{\mathrm{f}}}{\lambda_{\mathrm{D}}} + \exp\left(-\frac{e\phi_{\mathrm{f}}}{2T_{\mathrm{e},0}}\right)} \, . \tag{5.33b}$$

Here, ϕ_{f} refers to the value of the electric potential at the heavy ion front. Commonly, one considers the heavy ions as immobile, $m_{\mathrm{H}} \gg m_{\mathrm{L}}$. Then, the heavy ion layer stays step-like on the time-scale of the light ions, and, as a result, one has $x_{\mathrm{f}} = 0$ and $\phi_{\mathrm{f}} = -T_{\mathrm{e},0}/e$. Next, the motion of the light ions is given via the equation of motion for a test-particle in the electric field (5.33),

$$m_{\mathrm{L}}\ddot{x} = Z_{\mathrm{L}}\, e\, E(x) \, . \tag{5.34}$$

By solving the above relation, one obtains the position x and the velocity v of the test-particle as well as the electric field E which acts on it,

$$x(t) = x_{\mathrm{f}} + \sqrt{2}\lambda_{\mathrm{D}} \cdot \left\{\alpha \exp\left[\operatorname{erfi}^{-1}\left(\sqrt{\frac{2}{\pi}}\frac{\omega_{\mathrm{pi}}t}{\alpha}\right)^2\right] - b\right\} \tag{5.35a}$$

$$v(t) = 2c_{\mathrm{s}} \operatorname{erfi}^{-1}\left(\sqrt{\frac{2}{\pi}}\frac{\omega_{\mathrm{pi}}t}{\alpha}\right) \tag{5.35b}$$

$$E(t) = \frac{\sqrt{2}E_0}{\alpha} \exp\left[-\operatorname{erfi}^{-1}\left(\sqrt{\frac{2}{\pi}}\frac{\omega_{\mathrm{pi}}t}{\alpha}\right)^2\right] , \tag{5.35c}$$

with

$$\alpha = \frac{1}{\sqrt{2}}\frac{x(0)-x_{\mathrm{f}}}{\lambda_{\mathrm{D}}} + b \tag{5.36a}$$

$$b = \exp\left(-\frac{e\phi_{\mathrm{f}}}{2T_{\mathrm{e},0}}\right) \, . \tag{5.36b}$$

Here, $x(0)$ refers to the initial position of the test-particle, $\lambda_{\mathrm{D}} = \sqrt{\varepsilon_0 T_{\mathrm{e},0}/e^2 n_{\mathrm{e},0}}$ and $E_0 = \sqrt{n_{\mathrm{e},0} T_{\mathrm{e},0}/\varepsilon_0}$ are the Debye length and the characteristic field strength associated with the hot electrons, respectively, and $\omega_{\mathrm{pi}} = \sqrt{Z_{\mathrm{L}} n_{\mathrm{e},0} e^2/\varepsilon_0 m_{\mathrm{L}}}$ and $c_{\mathrm{s}} = \sqrt{Z_{\mathrm{L}} T_{\mathrm{e},0}/m_{\mathrm{L}}}$ denote the ion plasma frequency and the ion acoustic velocity for the light ions, respectively. Moreover, erfi^{-1} is the inverse of the complex error function erfi, which is defined as $\operatorname{erfi}(x) = \operatorname{erf}(ix)/i$, with erf denoting the error function and i being the imaginary unit. As shown in Fig. 5.8a, the maximum ion velocity is lower than that of the Mora model. This is caused by a faster decay of the electric field at the ion front. However, for a time domain of $\omega_{\mathrm{pi}}t \lesssim 25$, which is typical for many TNSA experiments,[82] both models lead to a result which is of the same order of magnitude.

Starting from the result (5.35) also the energy spectrum for a layer of test-particles can be evaluated. Initially, a small interval $[x(0), x(0)+\Delta x(0)]$ in the light ions layer contains $n_{\mathrm{L},0}\Delta x(0)$ particles per area, with $n_{\mathrm{L},0}$ being the initial light ion density. At time t the velocities of these

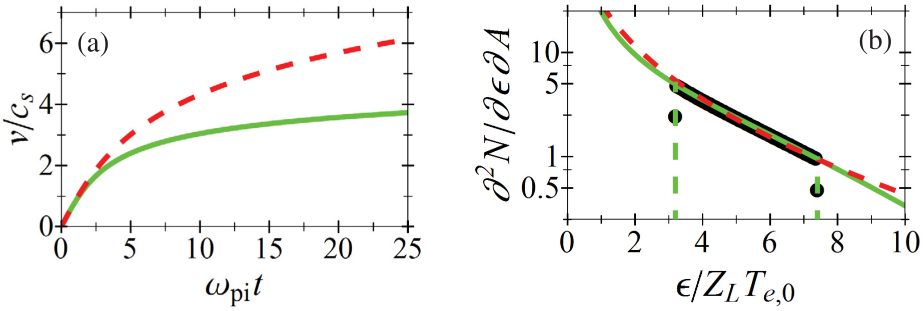

Figure 5.8.: In (a) and (b) the maximum ion velocity (5.35b) and the ion spectrum (5.38) of the test-particle model (green curves) are shown in comparison to the results (4.11) and (4.7) of the Mora model (dashed red curves), respectively. In addition, in (b) black dots correspond to simulation results and the vertical dashed lines mark the minimum and the maximum energy in the test-particle model, obtained from Eq. (5.35b). Note that: (i) The spectrum of the Mora model is normalized in such a way that the number of particles per area in between the minimum and maximum energy is equal to that of the test-particle model. (ii) In (b), the number of ions per unit surface and unit energy is normalized to $n_{\mathrm{L},0}\,\lambda_{\mathrm{D}}/Z_{\mathrm{L}}\,T_{\mathrm{e},0}$ and the plot corresponds to the time $\omega_{\mathrm{pi}}\,t = 30$, with ω_{pi} being the plasma frequency of the light ions.

particles will lie in the interval $[v-\Delta v, v]$, with v and $v-\Delta v$ being the velocities (5.35b) of the particles which were initially located at $x = x(0)$ and $x(0)+\Delta x(0)$, respectively[(12)]. Moreover, the interval Δv is given by $\partial \Delta v/\partial x(0)\,\Delta x(0)$ and by using the result (5.35) one finds

$$\frac{\partial v}{\partial x(0)} = -\frac{\pi}{2t}\,\mathrm{erfi}\left(\frac{v}{2c_{\mathrm{s}}}\right)^2 \cdot \exp\left(-\left(\frac{v}{2c_{\mathrm{s}}}\right)^2\right) . \tag{5.37}$$

Therewith, one can finally evaluate the energy spectrum as

$$\frac{\partial^2 N_{\mathrm{i}}}{\partial A \partial \varepsilon} = \frac{\partial v}{\partial \varepsilon}\frac{\partial^2 N_{\mathrm{i}}}{\partial A \partial v} = \frac{\partial v}{\partial \varepsilon}\frac{\Delta \frac{\partial N}{\partial A}}{\Delta v} = \frac{\partial v}{\partial \varepsilon}\frac{n_{\mathrm{i},0}\,\Delta x(0)}{\frac{\partial v}{\partial x(0)}\Delta x(0)} = \frac{\sqrt{2}}{\pi}\frac{n_{\mathrm{L},0}\,t}{\sqrt{m_{\mathrm{L}}\,\varepsilon}}\frac{\exp\left(\frac{\varepsilon}{2Z_{\mathrm{L}}\,T_{\mathrm{e},0}}\right)}{\mathrm{erfi}\left(\sqrt{\frac{\varepsilon}{2Z_{\mathrm{L}}\,T_{\mathrm{e},0}}}\right)^2} . \tag{5.38}$$

Since $\exp(x^2)/\,\mathrm{erfi}(x)^2 \approx \pi x^2 \exp(-x^2)$, for $x \gg 1$, one gets the asymptotic expression

$$\frac{\partial^2 N_{\mathrm{i}}}{\partial A \partial \varepsilon} \approx \frac{n_{\mathrm{L},0}\,t}{Z_{\mathrm{L}}\,T_{\mathrm{e},0}}\sqrt{\frac{\varepsilon}{2m_{\mathrm{L}}}}\exp\left(-\frac{\varepsilon}{2Z_{\mathrm{L}}\,T_{\mathrm{e},0}}\right) \tag{5.39}$$

for values of $\varepsilon \gg Z_{\mathrm{L}}\,T_{\mathrm{e},0}$. The spectrum (5.38) is illustrated in Fig. 5.8b.

[(12)] Note that the velocity v is strictly monotonically decreasing with increasing $x(0)$. Hence, it comes to overtaking in the ions. However, if the initial interval $\Delta x(0)$ is very small than the overtaking happens almost instantaneously at $t = 0$.

IV. Expansion caused by a step-like electron energy distribution

6. The stationary hydrodynamic approach

A key aspect of the central model (see chapter 3) is the assumption that each electron distribution $f_{\alpha,0}$ is in a stationary configuration with the electric potential ϕ. By solving the stationary Vlasov equation (2.19),

$$\frac{p}{m_{\mathrm{e}}\gamma}\,\frac{\partial f_\alpha}{\partial x} + e\,\frac{\partial \phi}{\partial x}\,\frac{\partial f_\alpha}{\partial p} = 0\,, \tag{6.1}$$

we found the result (3.5),

$$f_\alpha = \begin{cases} f_{\alpha,0}\left(c^{-1}\sqrt{(m_{\mathrm{e}}\gamma c^2 - e\,\phi(x))^2 - {m_{\mathrm{e}}}^2 c^4}\right) & : \text{general case} \\ f_{\alpha,0}\left(\sqrt{p^2 - 2\,m_{\mathrm{e}}\,e\,\phi(x)}\right) & : \text{nonrelativistic limit}\,, \end{cases} \tag{6.2}$$

for the electron phase space densities under this assumption. As a consequence, the spatial electron densities n_α,

$$n_\alpha = \int\limits_{\mathbb{R}} f_\alpha(x,p)\;\mathrm{d}p\,, \tag{6.3}$$

are coupled to the electric potential ϕ by relations of the form $n_\alpha(\phi)$ and the Poisson equation becomes the nonlinear expression (3.7),

$$\varepsilon_0\,\frac{\partial^2\phi}{\partial x^2} = -e\cdot\left[\sum_{\alpha=1}^{N_{\mathrm{i}}} Z_\alpha\,n_\alpha - \sum_{\alpha=N_{\mathrm{i}}+1}^{N} n_\alpha(\phi)\right]\,. \tag{6.4}$$

The stationary approach offers the possibility to treat the plasma expansion on the time-scale of the ions by ignoring the details of the electron dynamics. From a mathematical point of view, it is the relation $n_\alpha(\phi)$ which constitutes the advantage of this model.

In the literature,[79,80,196,197] another ansatz has been used which also leads to a relation of the form $n_\alpha(\phi)$ for the electrons. In contrast to the discussion above, it is based on a hydrodynamic description (see Sec. 2.2). Here, we only consider hot electrons. The corresponding hydrodynamic relations (2.15) are given by

$$\frac{\partial n_{\mathrm{e}}}{\partial t} + \frac{\partial}{\partial x}\,(n_{\mathrm{e}}\,v_{\mathrm{e}}) = 0 \tag{6.5a}$$

$$m_{\mathrm{e}}\,n_{\mathrm{e}}\cdot\left(\frac{\partial v_{\mathrm{e}}}{\partial t} + v_{\mathrm{e}}\,\frac{\partial v_{\mathrm{e}}}{\partial x}\right) = e\,n_{\mathrm{e}}\,\frac{\partial \phi}{\partial x} - \frac{\partial P_{\mathrm{e}}}{\partial x}\,, \tag{6.5b}$$

with m_e denoting the electron mass and P_e and v_e referring to the pressure and the fluid velocity of the electron gas, respectively. As in the kinetic approach one makes the assumption of stationarity for the electrons, hence, one assumes that the electrons equilibrate instantaneously with the electric potential. Therefore, we refer to this ansatz as the *stationary hydrodynamic approach*. In the context of the hydrodynamic relations (6.5), the instantaneous equilibration of the electrons is realized by letting m_e tend to zero. In this limiting case, from Eq. (6.5b) one gets

$$e\,n_\mathrm{e}\,\frac{\partial\phi}{\partial x} = \frac{\partial P_\mathrm{e}}{\partial x}\ . \tag{6.6}$$

As explained in Sec. 2.2, the hydrodynamic description has to be complemented by an equation of state and a relation which specifies the temperature in terms of the electron density. Here, we use the equation of state of an ideal gas (2.16),

$$P_\mathrm{e} = n_\mathrm{e}\,T_\mathrm{e}\ , \tag{6.7}$$

and the relation (2.17b),

$$T_\mathrm{e} = T_{\mathrm{e},0}\cdot\left(\frac{n_\mathrm{e}}{n_{\mathrm{e},0}}\right)^{\kappa-1}\ , \tag{6.8}$$

describing an adiabatic process with the adiabatic index κ. By combining Eqs. (6.7) and (6.8) one obtains the expression

$$P_\mathrm{e} = P_{\mathrm{e},0}\cdot\left(\frac{n_\mathrm{e}}{n_{\mathrm{e},0}}\right)^{\kappa} = T_{\mathrm{e},0}\,\frac{n_\mathrm{e}^{\kappa}}{n_{\mathrm{e},0}^{\kappa-1}}\ . \tag{6.9}$$

In the last step we used the equation of state (6.7), $P_{\mathrm{e},0} = n_{\mathrm{e},0}\,T_{\mathrm{e},0}$, with $P_{\mathrm{e},0}$ referring to the pressure of the electron fluid at the density $n_{\mathrm{e},0}$ and the temperature $T_{\mathrm{e},0}$. According to Eq. (6.9), P_e is a function of n_e. Moreover, in context of the model, n_e is a function of the potential ϕ which in turn is a function of x. This leads to

$$\frac{\partial P_\mathrm{e}}{\partial x} = \frac{\partial P_\mathrm{e}}{\partial n_\mathrm{e}}\frac{\partial n_\mathrm{e}}{\partial\phi}\frac{\partial\phi}{\partial x} \tag{6.10}$$

and Eq. (6.6) becomes

$$e\,n_\mathrm{e} = \frac{\partial P_\mathrm{e}}{\partial n_\mathrm{e}}\frac{\partial n_\mathrm{e}}{\partial\phi}\ . \tag{6.11}$$

By using Eq. (6.9), the last expression can be integrated analytically. The final result reads(1)

$$n_\mathrm{e}(\phi) = n_{\mathrm{e},0}\cdot\left(1+\frac{\kappa-1}{\kappa}\,\frac{e\,\phi}{T_{\mathrm{e},0}}\right)^{1/(\kappa-1)}\ . \tag{6.12}$$

In summary, starting form the hydrodynamic equation (6.5b) for the hot electrons, the adiabatic relation for an ideal gas with adiabatic index κ, Eq. (6.9), and assuming massless electrons one obtains the expression (6.12). Like the result of the kinetic approach, Eqs. (6.2)–(6.3), the hydrodynamic relation Eq. (6.12) relates the electron density to the electric potential by a function of the form $n_\mathrm{e} = n_\mathrm{e}(\phi)$.

---

(1) As usual, we have set the reference value for the potential ϕ equal to zero. Hence, $n_{\mathrm{e},0}$ still denotes the value of the electron density in absence of a potential ($\phi = 0$).

In a first study,[81] we investigated (i) the question whether the hydrodynamic result (6.12) is included in the general kinetic approach (6.2)–(6.3) and (ii) which physical consequences for the TNSA process will arise from the usage of the relation (6.12). In the context of this thesis, the first aspect will be discussed in Sec. 6.1, while we deal with the second point in Sec. 6.2. First we discuss the case with nonrelativistic electrons, afterwards this study will be generalized for relativistic temperatures in Sec. 6.3.

6.1. Relation to the stationary kinetic description of the electrons

In this section, we relate the stationary hydrodynamic approach to the stationary kinetic approach. While the hydrodynamic approach is characterized by the density relation (6.12), the corresponding expression in the kinetic approach is given via Eqs. (6.2) and (6.3), which in the nonrelativistic case(2) reads as(3)

$$n_\mathrm{e}(\phi) = \int_{\mathbb{R}} f_{\mathrm{e},0}\left(\sqrt{p^2 - 2m_\mathrm{e}\,e\,\phi(x)}\right)\mathrm{d}p\,. \tag{6.13}$$

In the kinetic approach, the hot electron energy distribution at $\phi = 0$, $f_{\mathrm{e},0}$, plays a central role. In contrast, in the hydrodynamic description nothing has been assumed about the phase space density of the hot electrons so far. This information is suppressed in the hydrodynamic approach since the relations (2.15) constitute expressions for averaged quantities, which are derived by integration over the particle distribution function (see Eqs. (2.13) and (2.14)). Commonly, one thinks of a Maxwellian particle distribution when dealing with fluids. This is due to the fact that a Maxwellian distribution is present in a situation where collisions between the particles dominate the physical processes. This is normally assumed when "fluids" are considered. However, as already mentioned, in context of the TNSA mechanism the hot electrons are almost collisionless.[63] Hence, a hydrodynamic description of the hot electrons may become invalid and as demonstrated below, in this case, the stationary hydrodynamic approach implies a non-Maxwellian energy distribution.

To prove the formal correspondence of the both approaches and to demonstrate the non-Maxwellian character of the electron energy distribution which is implied by the stationary hydrodynamic approach, one has to find a specific electron distribution $f_{\mathrm{e},0}$ which — when applied in the kinetic density expression (6.13) — leads to the hydrodynamic electron density relation (6.12). In other words, one has to invert Eq. (6.13) in terms of $f_{\mathrm{e},0}$. The inversion of this integral equation has been studied in Ref. 81 and is outlined in Sec. B.1. Here, we only give the final result

$$f_{\mathrm{e},0}(p) = \frac{m_\mathrm{e}}{\pi}\int\limits_{-\infty}^{-\frac{p^2}{2m_\mathrm{e}}} \frac{n_\mathrm{e}\left(-\frac{p^2}{2m_\mathrm{e}}\right) - n_\mathrm{e}(\zeta)}{|p^2 + 2m_\mathrm{e}\,\zeta|^{3/2}}\,\mathrm{d}\zeta\,. \tag{6.14}$$

---

(2) Here, we first concentrate on the nonrelativistic case. In Sec. 6.3 we will generalize the result to the relativistic case.

(3) See also Eq. (2.22b).

Note that Eq. (6.14) is valid for an arbitrary electron density $n_{\mathrm{e},0}(\phi)$.

By applying the inversion formula (6.14) to the hydrodynamic result for the electron density, Eq. (6.12), we obtain the electron phase space density $f_{\mathrm{e},0}$ as

$$f_{\mathrm{e},0}(p) = \frac{\alpha\, n_{\mathrm{e},0}}{\sqrt{m_{\mathrm{e}} T_{\mathrm{e},0}}} \cdot \Theta\left[1 - \frac{\kappa-1}{\kappa} \frac{p^2}{2 m_{\mathrm{e}} T_{\mathrm{e},0}}\right] \cdot \left(1 - \frac{\kappa-1}{\kappa} \frac{p^2}{2 m_{\mathrm{e}} T_{\mathrm{e},0}}\right)^{(3-\kappa)/(2\kappa-2)} . \tag{6.15}$$

The function Θ denotes the *Heaviside Theta function* and the constant α is given by

$$\alpha = \frac{1}{\sqrt{2\pi}} \sqrt{\frac{\kappa-1}{\kappa}}\, \frac{\Gamma\left[\frac{\kappa}{\kappa-1}\right]}{\Gamma\left[\frac{1}{2} + \frac{1}{\kappa-1}\right]} , \tag{6.16}$$

where Γ is the common *gamma function*. It is obvious that the phase space density (6.15) is not Maxwellian. This is also illustrated in Fig. 6.1. Moreover, the electron distribution $f_{\mathrm{e},0}$ has a cutoff at

$$\frac{p_{\max}^2}{2 m_{\mathrm{e}} T_{\mathrm{e},0}} = \frac{\kappa}{\kappa-1} . \tag{6.17}$$

In addition, for $\kappa > 3$ one finds a pole at this maximum. In the isothermal limit $\kappa \to 1$, however, the expression (6.15) tends towards the common (non-relativistic) Maxwellian distribution. To summarize, if one applies the phase space density (6.15) in Eq. (6.13), one ends up with the hydrodynamic density relation (6.12).

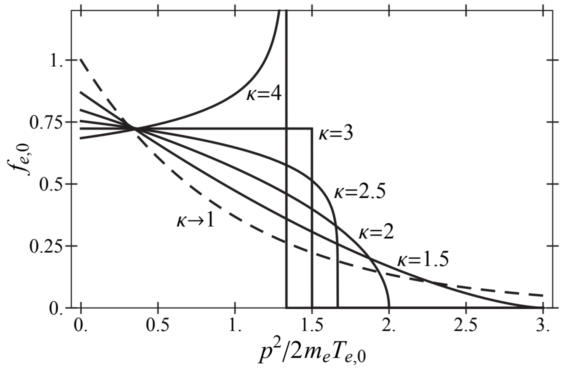

Figure 6.1.: Illustration of the electron phase space density (6.15) which is implied by the hydrodynamic ansatz (6.12) for different values of κ. Obviously, Eq. (6.15) does not describe Maxwellian distributions. However, it tends towards a Maxwellian distribution in the limit $\kappa \to 1$ (dashed line). The figure is taken from Ref. 81.

6.2. Equivalence and deviations of the different approaches

Before we are going to discuss further consequences of the hydrodynamic approach, we want to briefly discuss it in the context of the central model, chapter 3. In Sec. 6.1 we have shown that the particular electron energy distribution (6.15) leads to the spatial density relation (6.12) of the hydrodynamic approach. Now, in the stationary model this density relation is used for each instant of time. As a consequence, the stationary hydrodynamic model corresponds to the kinetic model with an electron phase space density which is time-independently given by the distribution (6.15). In other words, in the stationary hydrodynamic model the electron distribution is (implicitly) assumed to be constant in time. This is equivalent to the isothermal model discussed in chapter 4 where a Maxwellian electron energy distribution, Eq. (2.23), is assumed at each moment in time. Thus, in the context of the central model (see chapter 3), the stationary hydrodynamic model corresponds to the isothermal model with the electron density relation (2.24) replaced by the expression (6.12).

Generally, the assumption of a time-independent electron distribution is not realistic and can cause problems. For example, as discussed in Sec. 5.1, if $f_{\mathrm{e},0}$ is chosen as a Maxwellian distribution, the total energy of the system diverges as time goes on.[59] Due to the fact that the hydrodynamic approach uses a time-independent electron distribution, one therefore might ask about the accuracy of this assumption. In order to address this problem, one has to apply the extended electron model of Grismayer and Mora.[64] As discussed earlier in Sec. 5.1.2, applying this kinetic approach one is able to describe the temporal evolution of an arbitrary electron distribution $f_{\mathrm{e},0}$.

Here, it is useful to recall the essential property of this model: An electron phase density $f_{\mathrm{e},0}(p)$ at time t evolves into the distribution $f'_{\mathrm{e},0}(p)$ at time $t+\Delta t$ which is given by $f'_{\mathrm{e},0}(p'(p)) = f_{\mathrm{e},0}(p)$. Here, p' has the following meaning: We consider an (arbitrary) electron at time t which has an momentum p in a region with $\phi = 0$. Now, due to the slowly temporally varying electric potential ϕ the total energy of the electron may change in the time step Δt. As a consequence, at time $t+\Delta t$ the electron will have a different momentum $p' = p + \Delta p$ in the regions of $\phi = 0$. Because the electron was chosen arbitrarily and the potential is assumed to vary slowly, the change $p \to p'$ in the momentum effects all electrons having initially the momentum p. Since $f_{\mathrm{e},0}(p)$ is connected to the total number of electrons with momentum p, one has $f'_{\mathrm{e},0}(p') = f_{\mathrm{e},0}(p)$. It is plausible that the change Δp in the momentum p is a function of the momentum p itself. Otherwise the phase space density would experience a global shift and the conservation of the total energy would be violated. Hence, we have $p' = p'(p) = p + \Delta p(p)$. Altogether this leads to the evolution formula $f'_{\mathrm{e},0}(p'(p)) = f_{\mathrm{e},0}(p)$. Mathematically, it corresponds to a dilation of parts of the p-axis while other parts are contracted. At the same time the f-axis is conserved. As a result, a given function $f_{\mathrm{e},0}(p)$ will be blurred (see Fig. 5.2).

In other words, generally the kinetic approach does not conserve the initial choice $f_{\mathrm{e},0}$. Consequently, it also does not conserve the electron distribution (6.15), which leads to the hydrodynamic spatial density distribution $n_{\mathrm{e}}(\phi)$, Eq. (6.12). Thus, strictly speaking, the hydrodynamic ansatz, which is using the relation (6.12) at each instant in time, implies incorrect results for $t > 0$. Moreover, the inaccuracy is getting worse with increasing time.

However, there is an exceptional case. For the adiabatic constant $\kappa = 3$ the corresponding function $f_{\mathrm{e},0}$ is given as

$$f_{\mathrm{e},0}^{(\kappa=3)}(p) = \frac{n_{\mathrm{e},0}}{2\sqrt{3 m_{\mathrm{e}} T_{\mathrm{e},0}}} \cdot \Theta\left(1 - \frac{2}{3}\frac{p^2}{2 m_{\mathrm{e}} T_{\mathrm{e},0}}\right). \tag{6.18}$$

This distribution is a step-like function, also called a waterbag distribution. As one can easily understand, the variation of such a function according to the concept described above preserves the step-like structure. Contrary to that, the energy conservation supposed by the hydrodynamic approach is violated for $\kappa \neq 3$. This seems plausible due to the fact that the concept[64] is energy conservative and predicts a temporal evolution, which is different from that predicted by the pure hydrodynamic modeling.

In order to illustrate the incorrect temporal behavior predicted by the hydrodynamic approach at arbitrary values κ, we have performed two series of simulations with our code (see chapter A). The first set (I) uses $\kappa = 2$, while in the second one (II) the coefficient κ equals 3. Each set of simulations contains a hydrodynamic simulation using the spatial electron density given by Eq. (6.12) and a kinetic simulation following Ref. 64. Here, the initial electron density $f_{\mathrm{e},0}$ for the kinetic simulations was given by Eq. (6.15), with $\kappa = 2$ and $\kappa = 3$ for the sets (I) and (II), respectively. The parameters of the simulation were taken from an example in Ref. 64. The target is located symmetrically relative to the x-axis and has initially a half-width of $20\,\lambda_{\mathrm{D}}$, with $\lambda_{\mathrm{D}} = \sqrt{\varepsilon_0\, T_{\mathrm{e},0}/n_{\mathrm{e},0}\, e^2}$ being the electron Debye length. The initial ion density is $n_{\mathrm{i},0} = 10^{20}/\mathrm{cm}^3$. The hot electrons are characterized by the parameters $n_{\mathrm{e},0} = Z_{\mathrm{i}}\, n_{\mathrm{i},0}$ and $T_{\mathrm{e},0} = 1\,\mathrm{MeV}$. Moreover, no cold background electrons were taken into account as mentioned above. The simulation time T was always chosen $\omega_{\mathrm{pi}}\, T = 100$, where $\omega_{\mathrm{pi}} = \sqrt{Z_{\mathrm{i}}\, n_{\mathrm{e},0}\, e^2/\varepsilon_0\, m_{\mathrm{i}}}$ is the ion plasma frequency.

As depicted in Figs. 6.2 and 6.3, the initial electric field which is obtained from the hydrodynamic simulations is equal to the corresponding result of the kinetic simulations within both sets. This is what we expect according to the equivalence of both approaches as discussed in Sec. 6.1. But with increasing time, the results become more and more different for $\kappa = 2$ (see Fig. 6.2). In contrast, they stay identical (with a small error caused by numerical effects) for $\kappa = 3$, which is evident from Fig. 6.3. Altogether, this comparison illustrates the faultiness of the hydrodynamic ansatz in the case $\kappa \neq 3$.

6.3. Generalization to relativistic energies

In Sec. 6.2, we pointed out that the hydrodynamic approach with $\kappa \neq 3$ leads to a wrong description of the electron dynamics. In contrast, the step-like electron distribution ($\kappa = 3$), corresponding to $n_{\mathrm{e}}(\phi, t) \equiv n_{\mathrm{e}}(\phi) = n_{\mathrm{e},0}\sqrt{1 + 2\,e\,\phi/3\,T_{\mathrm{e},0}}$, automatically guarantees the correct evolution. This is an interesting property because of the fact that it is in general nearly impossible to give exact analytic expressions for the electron density at $t > 0$. However, so far the discussion was completely based on nonrelativistic relations.

For high-energy electrons with mean energies $T_{\mathrm{e},0} \gtrsim m_{\mathrm{e}}c^2$ the results need to be revisited. To remind, the derivation of Eq. (6.12) involves the Euler equation (6.5b) together with the assumption $m_{\mathrm{e}} \to 0$ as well as the adiabatic relation $P \cdot n_{\mathrm{e}}^{-\kappa} = \mathrm{const}$ for an ideal gas. For relativistic temperatures of the electron gas the derivation has to be modified. While the right-hand side of Eq. (6.5b) still holds, the relation $P \cdot n_{\mathrm{e}}^{-\kappa} = \mathrm{const}$ does not. That is because the derivation of $P \cdot n_{\mathrm{e}}^{-\kappa} = \mathrm{const}$ needs the assumption that the parameter κ does not depend on temperature. Indeed, in the nonrelativistic case κ is only a function of the dimension of the electron plasma. However in the relativistic theory of an ideal gas, the degrees of freedom $\mathbb{Z}$ depend on the temperature as well. Concerning a one-dimensional ideal gas, they are determined by Eq. (5.7),

$$\mathbb{Z}(\beta) = 2 \cdot \left(1 + \beta \cdot \left[\frac{\mathrm{K}_0(\beta)}{\mathrm{K}_1(\beta)} - 1\right]\right) . \tag{6.19}$$

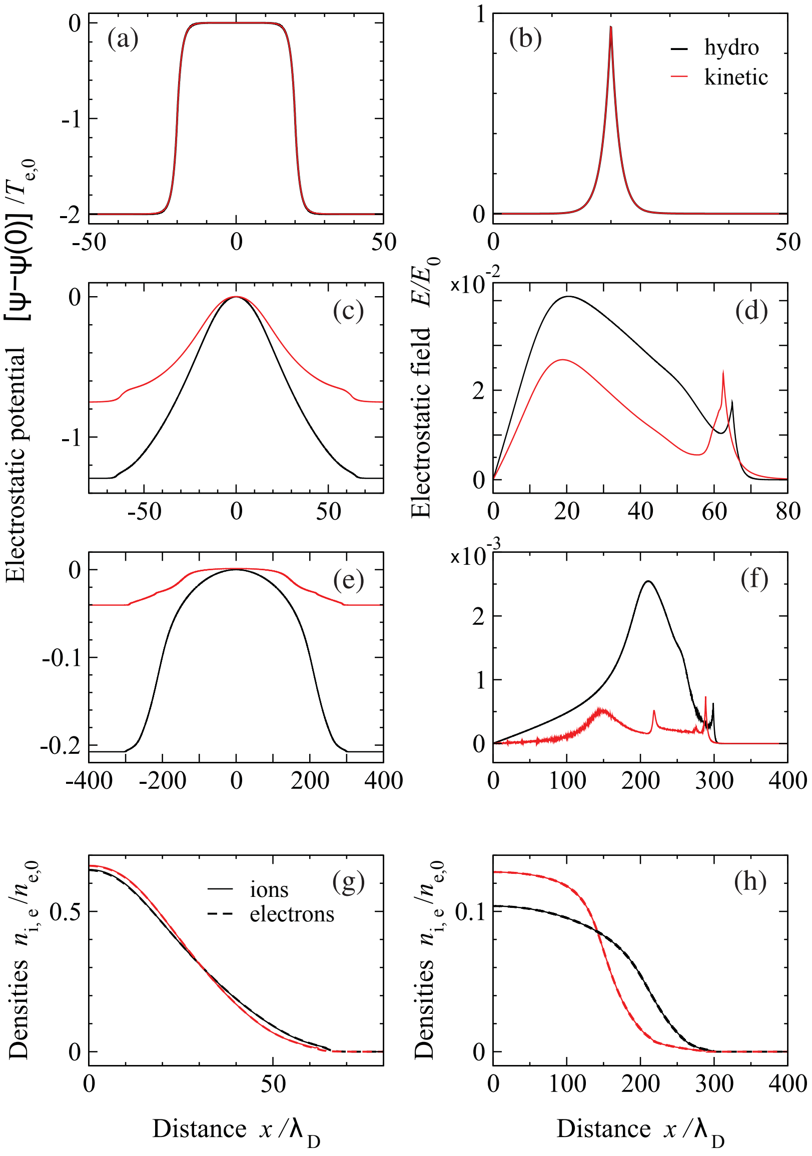

Figure 6.2.: Comparison of the stationary kinetic and the stationary hydrodynamic approach for $\kappa = 2$. In (a), (c) and (e) the electrostatic potential is plotted for the instants $\omega_{\mathrm{pi}} t = 0$, $\omega_{\mathrm{pi}} t = 20$ and $\omega_{\mathrm{pi}} t = 100$. The corresponding electric field is plotted in (b), (d) and (f) for the same instants of time. Here, the results of the kinetic simulations are displayed by red curves, for hydrodynamical modeling in black. The corresponding spatial ion (solid lines) and spatial electron densities (dashed curves) are shown in (g) and (h) for $\omega_{\mathrm{pi}} t = 20$ and $\omega_{\mathrm{pi}} t = 100$, respectively. The figure is taken from Ref. 81.

According to Eq. (6.19), $\mathbb{Z}$ varies from 1 in the low-temperature limit to 2 in the case of ultra-high temperatures. Therefore $\kappa = 1 + 2/\mathbb{Z}$ does depend on the electron temperature as well.

To avoid the associated difficulties, we address the problem from the kinetic point of view starting from the stationary relativistic Vlasov equation (6.1). Its solutions are given by Eq. (6.2),

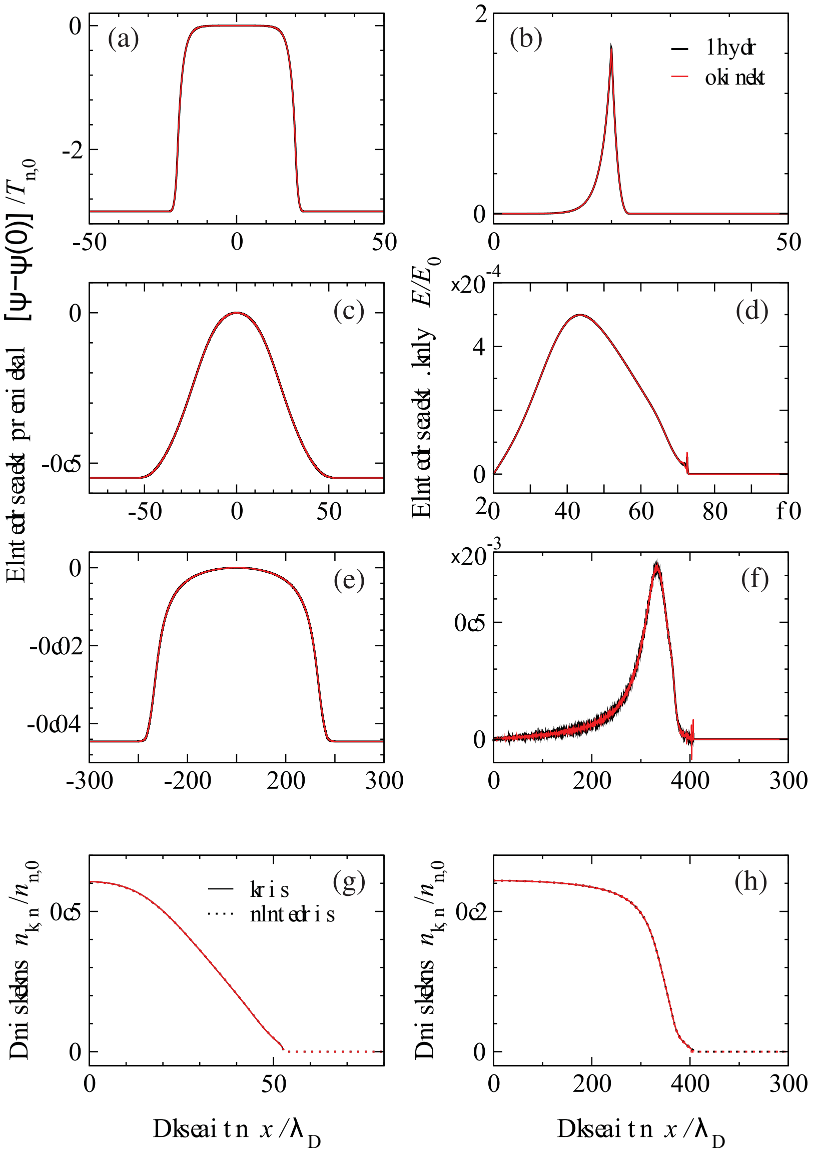

Figure 6.3.: Comparison of the stationary kinetic and the stationary hydrodynamic approach for $\kappa = 3$. The plot legend is identical to Fig. 6.2. The figure is taken from Ref. 81.

and, as a consequence, in the relativistic case the electron density (6.3) becomes [4],

$$n_e(\phi) = \int_{\mathbb{R}} f_{e,0}\left(c^{-1}\sqrt{(m_e\,\gamma c^2 - e\,\phi(x))^2 - {m_e}^2 c^4}\right) \mathrm{d}p\,. \tag{6.20}$$

unlike the nonrelativistic expression (6.13). Next we are going to rewrite the phase space density as a function of x and the kinetic energy $\varepsilon_{\mathrm{kin}}$. This can be done without loss of generality[5] due to the fact that $f_{\mathrm{e},0}$ is assumed to be symmetric in p (see Sec. 2.3). By introducing the definition

---

[4] See also Eq. (2.22a).

[5] Of course, this is also true in the nonrelativistic limit.

$$g_{\mathrm{e},0}(\varepsilon_{\mathrm{kin}}) = \sqrt{2m_{\mathrm{e}}}\, f_{\mathrm{e},0}\left(p(\varepsilon_{\mathrm{kin}})\right) \,, \tag{6.21}$$

with $p(\varepsilon_{\mathrm{kin}}) = \sqrt{2m_{\mathrm{e}}\,\varepsilon_{\mathrm{kin}}}\,\sqrt{1+\varepsilon_{\mathrm{kin}}/(2m_{\mathrm{e}}\,c^2)}$ being the relativistic relation between the momentum and the kinetic energy, the electron density in the relativistic kinetic approach is expressed by

$$n_{\mathrm{e}}^{\mathrm{rel}}(\psi) = \int_0^\infty g_{\mathrm{e},0}\left(\varepsilon_{\mathrm{kin}} - \psi\right) \cdot \frac{1+\frac{\varepsilon_{\mathrm{kin}}}{m_{\mathrm{e}}\,c^2}}{\sqrt{1+\frac{\varepsilon_{\mathrm{kin}}}{2m_{\mathrm{e}}\,c^2}}}\,\frac{d\varepsilon_{\mathrm{kin}}}{\sqrt{\varepsilon_{\mathrm{kin}}}} \,. \tag{6.22}$$

Here, we denote the relativistic expression for the electron density by $n_{\mathrm{e}}^{\mathrm{rel}}$ in order to distinguish it clearly from the nonrelativistic expression. The adequate nonrelativistic distribution

$$g_{\mathrm{e},0}(\varepsilon_{\mathrm{kin}}) = \frac{n_{\mathrm{e},0}}{\sqrt{6T_{\mathrm{e},0}}} \cdot \Theta\left(\frac{3}{2}T_{\mathrm{e},0} - \varepsilon_{\mathrm{kin}}\right) \tag{6.23}$$

for $\kappa = 3$ follows from Eq. (6.15).

To get the relativistic equivalent, we make the more general ansatz

$$g_{\mathrm{e},0}(\varepsilon_{\mathrm{kin}}) = C\,n_{\mathrm{e},0} \cdot \Theta\left(w\,T_{\mathrm{e},0} - \varepsilon_{\mathrm{kin}}\right) \,, \tag{6.24}$$

with w being a positive function of $T_{\mathrm{e},0}$, and C some normalization constant. First one identifies C with help of the initial condition $n_{\mathrm{e}}^{\mathrm{rel}}(\psi = 0) \overset{!}{=} n_{\mathrm{e},0}$. Then Eq. (6.24) reads

$$g_{\mathrm{e},0}(\varepsilon_{\mathrm{kin}}) = \frac{n_{\mathrm{e},0}}{\sqrt{2w\,T_{\mathrm{e},0}}}\,\frac{\sqrt{\beta}}{\sqrt{w+2\beta}} \cdot \Theta\left(w\,T_{\mathrm{e},0} - \varepsilon_{\mathrm{kin}}\right) \,. \tag{6.25}$$

By inserting Eq. (6.25) into Eq. (6.22) we obtain the relation

$$n_{\mathrm{e}}^{\mathrm{rel}}(\psi) = \frac{n_{\mathrm{e},0}}{\sqrt{1+\frac{2\beta}{w}}}\sqrt{1+\frac{\psi}{w\,T_{\mathrm{e},0}}} \cdot \sqrt{1+\frac{2\beta}{w}+\frac{\psi}{w\,T_{\mathrm{e},0}}} \,. \tag{6.26}$$

The phase space density (6.25) is preserved during the plasma expansion according to the kinetic algorithm discussed above, respectively, in Sec. 5.1.2, independently on the choice of w. Therefore Eq. (6.26) automatically ensures the correct temporal behavior. From the kinetic point of view one could choose w arbitrarily. However, in order to connect Eq. (6.26) to the hydrodynamic approach one has to specify w. To do so, we examine the low- and high-temperature limits of Eq. (6.26).

For the nonrelativistic approximation, $T_{\mathrm{e},0}/m_{\mathrm{e}}\,c^2 \ll 1$, the expression (6.26) takes the shortened form

$$n_{\mathrm{e}}^{\mathrm{rel}}(\psi) = n_{\mathrm{e},0}\sqrt{1+\frac{\psi}{w\,T_{\mathrm{e},0}}} \,. \tag{6.27}$$

In the nonrelativistic case one has $\kappa = 3$ for a one-dimensional ideal gas and one observes a correspondence of Eq. (6.27) with Eq. (6.12) for $w = 3/2$. For an ultrarelativistic one-dimensional gas one has $\mathbb{Z}=2$ and $\kappa=2$. As mentioned above, Eq. (6.12) has to be modified for temperatures $T_{\mathrm{e},0}\approx m_\mathrm{e}\,c^2$ because it was initially derived under the assumption that κ is independent on the electron temperature. However, for $T_{\mathrm{e},0}\gg m_\mathrm{e}\,c^2$ the variation of κ in $T_{\mathrm{e},0}$ goes to zero. This can be seen by calculating the first derivative of Eq. (6.19) with respect to $T_{\mathrm{e},0}$. For that reason Eq. (6.12) becomes suitable also for $T_{\mathrm{e},0}\gg m_\mathrm{e}\,c^2$ and one obtains

$$n_\mathrm{e}(\psi)=n_{\mathrm{e},0}\cdot\left(1+\frac{1}{2}\frac{\psi}{T_{\mathrm{e},0}}\right). \tag{6.28}$$

By comparing the last expression with the asymptotic expansion of Eq. (6.26) for $T_{\mathrm{e},0}/m_\mathrm{e}\,c^2\gg 1$, which is given by

$$n_\mathrm{e}^{\mathrm{rel}}(\psi)=n_{\mathrm{e},0}\cdot\left(1+\frac{\psi}{w\,T_{\mathrm{e},0}}\right), \tag{6.29}$$

we find $w=2$. To summarize, we obtain $w=3/2$ for $\kappa=3$ and $w=2$ for $\kappa=2$. Although it is mathematically not a unique choice, both limiting cases together motivate the selection $w=\kappa(\beta)/(\kappa(\beta)-1)=(2+\mathbb{Z}(\beta))/2$, with $\mathbb{Z}(\beta)$ given by Eq. (6.19).

In summary, we find the following energy phase space density for the general case

$$g_{\mathrm{e},0}(\varepsilon_\mathrm{kin})=\frac{\sqrt{2}}{2+\mathbb{Z}(\beta)}\,\frac{n_{\mathrm{e},0}}{\sqrt{T_{\mathrm{e},0}}}\sqrt{\frac{\beta}{1+\frac{4\beta}{2+\mathbb{Z}(\beta)}}}\cdot\Theta\left(\frac{2+\mathbb{Z}(\beta)}{2}\,T_{\mathrm{e},0}-\varepsilon_\mathrm{kin}\right), \tag{6.30}$$

which implies the spatial density

$$n_\mathrm{e}^{\mathrm{rel}}(\psi)=\frac{n_{\mathrm{e},0}}{\sqrt{1+\frac{4\beta}{\mathbb{Z}(\beta)+2}}}\sqrt{1+\frac{2}{\mathbb{Z}(\beta)+2}\frac{\psi}{T_{\mathrm{e},0}}}\cdot\sqrt{1+\frac{4\beta}{\mathbb{Z}(\beta)+2}+\frac{2}{\mathbb{Z}(\beta)+2}\frac{\psi}{T_{\mathrm{e},0}}}\,. \tag{6.31}$$

It is interesting to note that the nonrelativistic result (6.12) is a good approximation for Eq. (6.31)

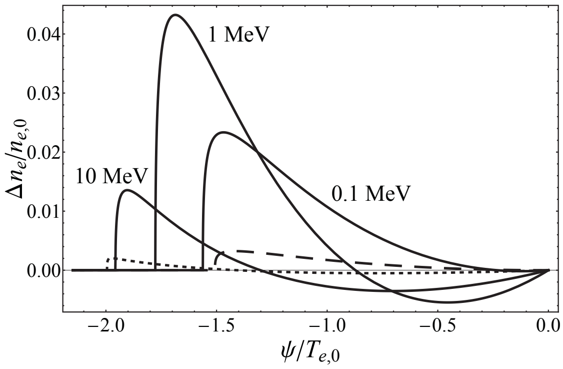

Figure 6.4.: Plot of the discrepancy $\Delta n_\mathrm{e}(\psi)=n_\mathrm{e}^{\mathrm{rel}}-n_\mathrm{e}^{\mathrm{approx}}$ between the relativistic result for the electron density, Eq. (6.31), and the quasi-nonrelativistic approximation (6.32). The dotted curve corresponds to the ultrarelativistic case $T_{\mathrm{e},0}=100\,\mathrm{MeV}$, whereas the dashed curve was calculated for the nonrelativistic energy $T_{\mathrm{e},0}=0.01\,\mathrm{MeV}$. The figure is taken from Ref. 81.

by setting $\kappa = \kappa(\beta) = 1 + 2/\mathbb{Z}(\beta)$ in Eq. (6.12). Thus one has

$$n_{\mathrm{e}}^{\mathrm{rel}}(\psi) \approx n_{\mathrm{e}}^{\mathrm{approx}}(\psi) = n_{\mathrm{e},0} \cdot \left(1 + \frac{2}{\mathbb{Z}(\beta) + 2} \frac{\psi}{T_{\mathrm{e},0}}\right)^{\frac{\mathbb{Z}(\beta)}{2}} . \tag{6.32}$$

Here, we want to emphasize the difference between the two expressions (6.12) and (6.32) which have formally the same structure. Eq. (6.12) is an expression derived by nonrelativistic relations and it contains the adiabatic constant κ which is determined by the dimension of the electron gas only. In contrast, Eq. (6.32) is just an empiric fit to Eq. (6.31) which contains the degrees of freedom of a one-dimensional ideal gas with temperature $T_{\mathrm{e},0}$, determined by Eq. (6.19). Figure 6.4 demonstrates the proper approximation of the relativistic expression (6.31) by the relation (6.32) for arbitrary values $\beta = m_{\mathrm{e}} c^2 / T_{\mathrm{e},0}$ in between the limiting nonrelativistic (6.27) and ultrarelativistic (6.29) cases.

7. Plasma expansion properties

In chapter 6, we have shown that the electron density relation of the stationary hydrodynamic approach (6.12) corresponds to the particular electron energy distribution (6.15). Moreover, we pointed out that the case of a step-like electron phase space density plays a special role, since it implies automatically the correct evolution of the electron distribution⁽¹⁾. For that reason the plasma expansion driven by this special electron energy distribution is energy-conserving. Hence, it may serve as an alternative to the adiabatic expansion models assuming an initially Maxwellian energy distribution,[62,64,65] which were studied in Sec. 5.1. Following our second study,[82] in this chapter we want to investigate the impact of a step-like electron energy distribution on the ion acceleration process. Firstly, in Sec. 7.1, we are going to derive analytic results for the expansion process assuming a step-like electron energy distribution. In Sec. 7.2 we will compare the obtained results with the case assuming an initial Maxwell distribution. Finally, in Sec. 7.3, we will apply the different adiabatic models to experimental data.

7.1. Analytics for step-like distributed electrons

As usual we start the investigations from the central model, chapter 3. According to the discussion of Sec. 5.2 we will ignore the presence of cold electrons since they do not have a noticeable influence on the high-energy part of the ion spectrum. Hence, we consider only the hot electron population which is assumed to have a step-like energy distribution. In order to keep the discussion as general as possible the hot electrons are treated using the relativistic Vlasov ansatz. Following Sec. 6.3, the electron density relation is given by Eq. (6.31). However, since the result is complex — causing difficulties in the following analytic calculations — we will use the

---

(1) In the sense of the kinetic modeling of Ref. 64.

approximative result (6.32) instead. Thus, the electron density relation is given by

$$n_\mathrm{e}(\phi) = n_{\mathrm{e},0} \cdot \left(1 + \frac{\kappa - 1}{\kappa} \frac{e\,\phi}{T_{\mathrm{e},0}}\right)^{1/(\kappa-1)} , \tag{7.1a}$$

with κ denoting the adiabatic index given via

$$\kappa = 1 + 2/\mathbb{Z} \tag{7.1b}$$

and $\mathbb{Z}$ being the degrees of freedom specified by expression (6.19),

$$\mathbb{Z}(\beta) = 2 \cdot \left(1 + \beta \cdot \left[\frac{\mathrm{K}_0(\beta)}{\mathrm{K}_1(\beta)} - 1\right]\right) . \tag{7.1c}$$

The degrees of freedom increase from $\mathbb{Z} = 1$ to $\mathbb{Z} = 2$ when the electron temperature rises from $T_{\mathrm{e},0} \ll m_\mathrm{e}\,c^2$ (nonrelativistic case) to $T_{\mathrm{e},0} \to \infty$ (ultrarelativistic case). At the same time, the adiabatic index is decreasing from $\kappa = 3$ to $\kappa = 2$. Thus from a practical point of view, only the domain $2 \leq \kappa \leq 3$ turns out to be important for our studies, especially in the Secs. 7.2 and 7.3. However, in this section we want to keep the analytic results as general as possible assuming the weaker limitation(2) $\kappa \geq 1$. As in the isothermal model, chapter 4, the ion distribution is assumed to be step-like at $t = 0$, i.e. is given by Eq. (4.1), and its evolution will be described by the hydrodynamic equations (3.2). Hence, we have

$$n_\mathrm{i}(x) = \begin{cases} n_{\mathrm{i},0} & : x \leq 0 \\ 0 & : \text{otherwise} \end{cases} \tag{7.1d}$$

and

$$\frac{\partial n_\mathrm{i}}{\partial t} + \frac{\partial}{\partial x}(n_\mathrm{i}\,v_\mathrm{i}) = 0 \tag{7.1e}$$

$$\frac{\partial v_\mathrm{i}}{\partial t} + v_\mathrm{i}\frac{\partial v_\mathrm{i}}{\partial x} = -\frac{Z_\mathrm{i}\,e}{m_\mathrm{i}}\frac{\partial \phi}{\partial x} . \tag{7.1f}$$

According to the central model, the electrostatic potential is determined by the nonlinear Poisson equation (3.7),

$$\varepsilon_0 \frac{\partial^2 \phi}{\partial x^2} = e \cdot [n_\mathrm{e}(\phi) - Z_\mathrm{i}\,n_\mathrm{i}] . \tag{7.1g}$$

Following Ref. 56 one can derive a self-similar solution for the system (7.1) under the assumption of charge quasi-neutrality, $n_\mathrm{e} = Z_\mathrm{i}\,n_\mathrm{i}$. It takes the form

$$\phi_\mathrm{ss} = \frac{T_{\mathrm{e},0}}{e}\left[\frac{\kappa - 1}{(\kappa+1)^2}\left(\frac{x}{c_\mathrm{s}\,t}\right)^2 - \frac{4\sqrt{\kappa}}{(\kappa+1)^2}\frac{x}{c_\mathrm{s}\,t} - \frac{\kappa\cdot(\kappa+3)}{(\kappa+1)^2}\right] \tag{7.2a}$$

$$v_{\mathrm{i,ss}} = \frac{2\,c_\mathrm{s}}{1+\kappa}\left(\frac{x}{c_\mathrm{s}\,t} + \sqrt{\kappa}\right) \tag{7.2b}$$

$$Z_\mathrm{i}\,n_{\mathrm{i,ss}} = n_{\mathrm{e},0} \cdot \left(\frac{2}{\kappa+1}\left(1 - \frac{\kappa-1}{2\sqrt{\kappa}}\frac{x}{c_\mathrm{s}\,t}\right)\right)^{2/(\kappa-1)} , \tag{7.2c}$$

---

(2) The case $\kappa = 1$, which corresponds to the isothermal situation, has to be understood as a limiting process $\kappa \to 1$.

with the ion-acoustic velocity $c_\mathrm{s} = \sqrt{Z_\mathrm{i} T_{\mathrm{e},0}/m_\mathrm{i}}$. Note that equations (7.2) are identical with the self-similar result of Ref. 196. Considering the self-similar solution (7.2) mathematically, it is valid in the domain⁽³⁾ $-\sqrt{\kappa} < x/c_\mathrm{s} t \leq 2\sqrt{\kappa}/(\kappa - 1)$. Also, we would like to point out that in a general situation the quasi-neutrality condition is a necessary but not a sufficient condition. However, with respect to the problem discussed here, one may regard it as a sufficient condition, too⁽⁴⁾. In case of an ion distribution with strong spatial variations the quasi-neutrality condition is violated, because the electron distribution cannot follow these variations instantaneously due to the thermal smoothing of the electron density. Hence, the self-similar solution is not suitable as a model for the expansion of a target with an initially step-like density profile at the very beginning of the acceleration process. At later times, however, when the ion density profile smoothes out due to the expansion itself, the relations (7.2) provide a good approximation to the exact solution of the system (7.1) within the quasi-neutral region (see Fig. 7.1).

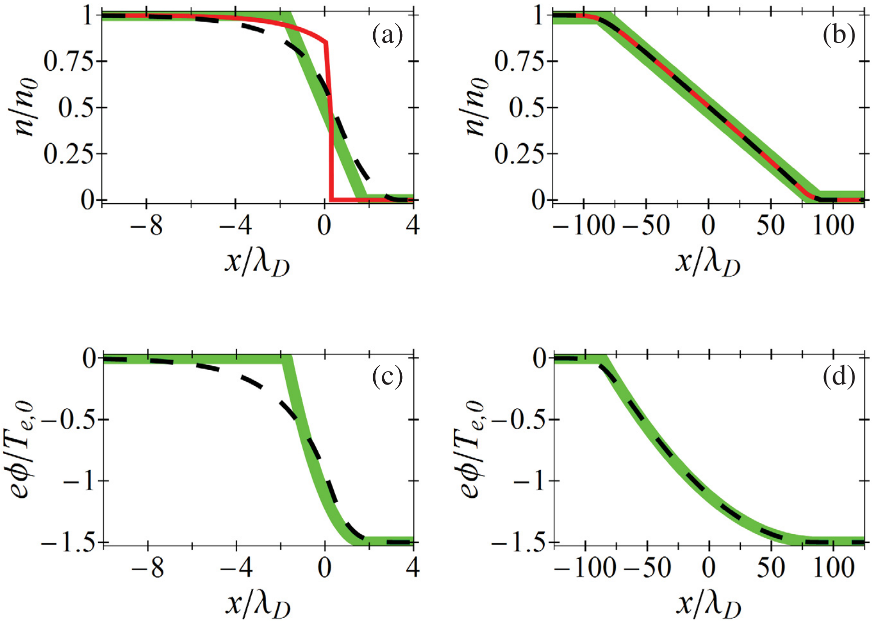

Figure 7.1.: Comparison of the self-similar solution (7.2) for $\kappa = 3$ with the exact solution of the equations (7.1). (a) and (b) show the spatial particle density distributions of the particles at the instants $\omega_\mathrm{pi} \cdot t = 1$ and $\omega_\mathrm{pi} \cdot t = 50$, respectively. Here, the dashed black and the solid red curves correspond to the exact electron and ion densities, respectively, whereas the broad green lines represent the self-similar result (7.2c). In (c) and (d), the exact electric potential (dashed black curve) is compared with the self-similar relation (7.2a) (broad green curve) for $\omega_\mathrm{pi} \cdot t = 1$ and $\omega_\mathrm{pi} \cdot t = 50$, respectively. Note that $Z_\mathrm{i} = 1$ is assumed in the plotted example. The figure is taken from Ref. 82.

⁽³⁾ For $x > 2\sqrt{\kappa} \cdot c_\mathrm{s} t/(\kappa - 1)$ the solution is continued by $\phi_\mathrm{ss} \equiv -\kappa T_{\mathrm{e},0}/(e \cdot (\kappa - 1))$ and $n_\mathrm{i,ss} \equiv 0$. Here, the ion velocity $v_\mathrm{i,ss}$ is not defined due to the absence of ions. Moreover, for $x < -\sqrt{\kappa} c_\mathrm{s} t$, the expressions (7.2) become meaningless. Instead one has $v_\mathrm{i} \equiv 0$, $n_\mathrm{i} \equiv n_{\mathrm{e},0}/Z_\mathrm{i}$ and $\phi_\mathrm{ss} \equiv 0$.

⁽⁴⁾ This is different to the situation of part V. There, the initial target has a linear density ramp and the quasi-neutral condition is initially fulfilled quite well. Nevertheless, the self-similar solution describes the plasma expansion only for large times, $\omega_\mathrm{pi} t \gg 1$.

While the lower boundary of this quasi-neutral region is approximately given by the position of the rarefaction wave $-\sqrt{\kappa}\, c_\mathrm{s}\, t$, which is identical to the lower boundary of the range of validity of Eq. (7.2), the upper boundary of the quasi-neutral region is not identical to the upper boundary $2\, c_\mathrm{s}\, t \sqrt{\kappa}/(\kappa-1)$ of the self-similar solution (7.2). Instead, it is approximately given by the point where the local electron Debye length, $\lambda_\mathrm{D,local} = \sqrt{\varepsilon_0\, T_\mathrm{e,0}/(n_\mathrm{e}(x)\, e^2)}$, exceeds the scale length l_ss of the spatial variation in the ion density (see Refs. 59, 83). By evaluating the local scale length $l_\mathrm{ss} = |n_\mathrm{i}/(\partial n_\mathrm{i}/\partial x)|$ of the self-similar ion density (7.2c) at the initial target boundary ($x = 0$), which we take as a representative position, one finds $l_\mathrm{ss} = \sqrt{\kappa}\, c_\mathrm{s}\, t$. Consequently, $\lambda_\mathrm{D,local}$ exceeds l_ss at the position

$$x_\mathrm{f,ss} = \frac{2\sqrt{\kappa}}{\kappa-1}\, c_\mathrm{s}\, t \cdot \left(1 - \frac{\kappa+1}{2} \left(\sqrt{\kappa}\, \omega_\mathrm{pi}\, t\right)^{1-\kappa}\right) , \tag{7.3}$$

with $\omega_\mathrm{pi} = \sqrt{Z_\mathrm{i}\, n_\mathrm{e,0}\, e^2/(m_\mathrm{i}\, \varepsilon_0)}$ denoting the ion plasma frequency.

From a physics point of view, Eq. (7.3) is an approximative expression for the position of the ion front, because the quasi-neutral condition fails here as a result of the jump discontinuity in the ion density, which the electron density cannot follow directly. According to the self-similar solution, the ion velocity at the position $x_\mathrm{f,ss}$ is given by

$$v_\mathrm{f,ss} = 2\, c_\mathrm{s}\, \frac{\sqrt{\kappa}}{\kappa-1} \left(1 - \left(\sqrt{\kappa}\, \omega_\mathrm{pi}\, t\right)^{1-\kappa}\right) . \tag{7.4}$$

Note, that Eq. (7.4) equals the velocity at which the upper boundary of the range of validity of the self-similar solution is propagating in the limit $t \to \infty$. In addition, Eq. (7.4) is consistent with the expression given by Mora[59] for $\kappa \to 1$. By taking the derivative of Eq. (7.4) we deduce the corresponding scaling of the electric field strength at the ion front as

$$E_\mathrm{f,ss}(t) \propto t^{-\kappa} . \tag{7.5}$$

Although the self-similar solution is useful for the investigation of the general properties of the plasma expansion, it does not allow for a characterization of the complete process. Firstly, it cannot specify the expansion in the early stages due to the non-negligible violation of quasi-neutrality. Moreover, even for later times this condition is violated at the ion front. Consequently, the self-similar solution does not provide a precise deduction of the electric field strength at the ion front. In case of isothermal electrons, $\kappa \to 1$, Mora circumvented the latter difficulty by utilizing numerical results implying that the electric field $E(t)$ at the ion front for $\omega_\mathrm{pi}\, t \gg 1$ is approximately twice the value $E_\mathrm{f,ss}(t)$ given by the self-similar solution.[59] But for parameters $\kappa \neq 1$, simulations show that the ion front surpasses the upper boundary of the self-similar solution, $2\, c_\mathrm{s}\, t\, \sqrt{\kappa}/(\kappa+1)$, at some instant t_sur (see Fig. 7.2). Hence, the self-similar solution (7.2) cannot formally be used to characterize the motion of the ion front also at later times. However, simulations also reveal saturation in the increase of the ion front velocity when approaching this moment of surpassing, as it becomes clear from Fig. 7.2d. Therefore, the description of the electric field strength at the ion front beyond the point of surpassing by the self-similar relation does not introduce an essential error. Summarizing, we may argue that the scaling of the electric field predicted by the self-similar solution (7.5) approximates the evolution of the electric field at the ion front for times $\omega_\mathrm{pi}\, t \gg 1$ sufficiently well, despite the principal restrictions mentioned above.

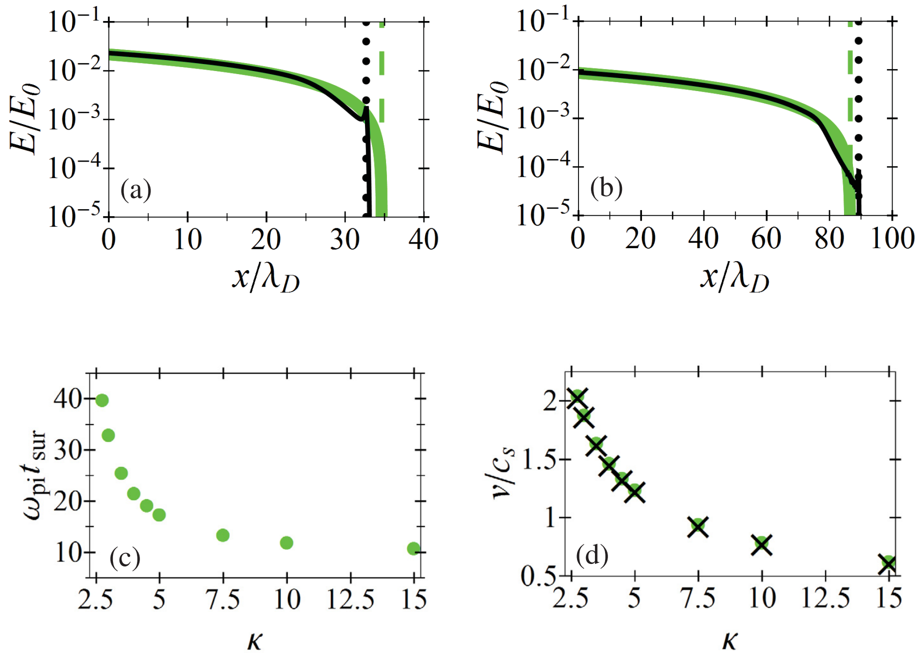

Figure 7.2.: (a) and (b) show the self-similar electric field (bold green) in comparison with simulation results (black) for $\kappa = 3$ at the instants $\omega_{\mathrm{pi}} t = 20$ and $\omega_{\mathrm{pi}} t = 50$, respectively. Clearly, the ion front — marked by the dotted black line — surpasses the upper boundary $2c_s t\sqrt{\kappa}/(\kappa-1)$ of the self-similar solution (dashed green line) at some instant $\omega_{\mathrm{pi}} \cdot t_{\mathrm{sur}}$ in between 20 and 50. As shown in (c), such an instant $\omega_{\mathrm{pi}} \cdot t_{\mathrm{sur}}$ exists for each value of κ. In (d), the velocity of the ion front at the instant of surpassing (green dots) is shown against the final velocity of the ion front (black crosses) for different κ. Both velocities differ by less than 1%. The figure is taken from Ref. 82.

In order to express the electric field at the ion front at all instants of time, we propose — in analogy to the isothermal fit in Ref. 59 — the generalized expression

$$E_{\mathrm{f}}(t) \approx \frac{E_{\mathrm{f}}(t=0)}{\left(1+C(\kappa)\cdot(\omega_{\mathrm{pi}} t)^2\right)^{\kappa/2}}\,, \tag{7.6}$$

which obeys the asymptotic behavior (7.5). Here, $C(\kappa)$ is a function of κ only and $E_{\mathrm{f}}(t=0)$ denotes the initial field strength at the ion front. The latter value can be determined by integration of Eq. (7.1g) with the electron density relation (7.1a). Before proceeding, it is useful to specify the boundary conditions.

First, we set $\phi'(\pm\infty) = 0$, since we assume there is no electric field at infinity. The absence of an electric field at $x = \pm\infty$ implies physically that the net charge density at $x = \pm\infty$ is zero, thus $n_{\mathrm{i}}(\pm\infty) = n_{\mathrm{e}}(\pm\infty)$. With the common choice $n_{\mathrm{i},0} = n_{\mathrm{e},0}$ this leads to the boundary values $\phi(-\infty) = 0$ and $\phi(\infty) = -\kappa/(\kappa-1)$. Now, under consideration of the boundary conditions, the integration from $x = -\infty$ to $x = 0$ yields

$$\frac{\varepsilon_0}{2}\,\phi'(0)^2 = n_{\mathrm{e},0}\,T_{\mathrm{e},0}\cdot\left[\left(1+\frac{\kappa-1}{\kappa}\,\frac{e\,\phi(0)}{T_{\mathrm{e},0}}\right)^{\frac{\kappa}{\kappa-1}}-1\right]-e\,n_{\mathrm{i},0}\,\phi(0)\,. \tag{7.7a}$$

In addition, the integration from $x=\infty$ to $x=0$ results in

$$\frac{\varepsilon_0}{2}\,\phi'(0)^2 = n_{\mathrm{e},0}\,T_{\mathrm{e},0}\cdot\left(1+\frac{\kappa-1}{\kappa}\,\frac{e\,\phi(0)}{T_{\mathrm{e},0}}\right)^{\frac{\kappa}{\kappa-1}}\ . \tag{7.7b}$$

By combining the Eqs. (7.7), one obtains $\phi(0)=-T_{\mathrm{e},0}/e$. Using that result in Eq. (7.7b), we find

$$E_{\mathrm{f}}(t=0)=\sqrt{2}\,\kappa^{-\frac{\kappa}{2\cdot(\kappa-1)}}\,E_0\ , \tag{7.8}$$

where $E_0=\sqrt{n_{\mathrm{e},0}\,T_{\mathrm{e},0}/\varepsilon_0}$.

For values $\kappa\lesssim 10$, the expression (7.6) properly fits the simulation results, as long as $C(\kappa)$ is well chosen. This is demonstrated in Fig. 7.3a for three values of κ. Since relation (7.6) is a heuristic fit, $C(\kappa)$ cannot be determined unambiguously. However, a comparison with the best-fit values $C_n=C(\kappa_n)$ gained from a series of simulations with various values κ_n shows that

$$C(\kappa)=\frac{1}{2}\,\frac{1}{\exp(1)+\kappa-1} \tag{7.9}$$

is a good approximation, as illustrated in Fig. 7.3b. Furthermore, expression (7.6) together with Eq. (7.9) leads to the fit formula found by Mora for the case $\kappa=1$.

Using the empiric fit (7.6), we obtain the velocity,

$$\frac{v_{\mathrm{f}}(t)}{c_{\mathrm{s}}}=\sqrt{2}\,\kappa^{-\frac{\kappa}{2\cdot(\kappa-1)}}\,\omega_{\mathrm{pi}}t\ {}_2\mathrm{F}_1\left[\frac{1}{2},\frac{\kappa}{2};\frac{3}{2};-C(\kappa)\cdot\left(\omega_{\mathrm{pi}}t\right)^2\right]\ , \tag{7.10}$$

as well as the position of the ion front

$$\begin{aligned}\frac{x_{\mathrm{f}}(t)}{\lambda_{\mathrm{D}}}=\sqrt{2}\,\kappa^{-\frac{\kappa}{2\cdot(\kappa-1)}}\Bigg\{&\frac{\left(1+C(\kappa)\cdot\left(\omega_{\mathrm{pi}}t\right)^2\right)^{1-\frac{\kappa}{2}}-1}{C(\kappa)\cdot(\kappa-2)}\\&+\left(\omega_{\mathrm{pi}}t\right)^2\ {}_2\mathrm{F}_1\left[\frac{1}{2},\frac{\kappa}{2};\frac{3}{2};-C(\kappa)\cdot\left(\omega_{\mathrm{pi}}t\right)^2\right]\Bigg\}\ ,\end{aligned} \tag{7.11}$$

as functions of time. Here, ${}_2\mathrm{F}_1$ denotes the Gaussian hypergeometric function and $\lambda_{\mathrm{D}}=\sqrt{\varepsilon_0\,T_{\mathrm{e},0}/(n_{\mathrm{e},0}\,e^2))}$ refers to the electron Debye length. Relations (7.10) and (7.11) are displayed in Figs. 7.3c and 7.3d and reproduce the simulation data well. The fit precision decreases slightly with increasing κ. However, for the relevant values $\kappa\leq 3$ the relative error in $v(t)$ is still less than 1% for all times t.

From relation (7.10), we deduce the maximum ion velocity in the limit $t\to\infty$ as

$$v_{\max}/c_{\mathrm{s}}=\sqrt{2\,\chi(\kappa)}\ . \tag{7.12}$$

The function $\chi(\kappa)$ depends on κ only and is defined as

$$\chi(\kappa)=4\,\pi\,\frac{\Gamma\left[\frac{\kappa+3}{2}\right]^2}{\Gamma\left[\frac{\kappa}{2}\right]^2}\,\frac{\kappa^{-\frac{\kappa}{\kappa-1}}}{C(\kappa)\cdot\left(\kappa^2-1\right)^2}\ . \tag{7.13}$$

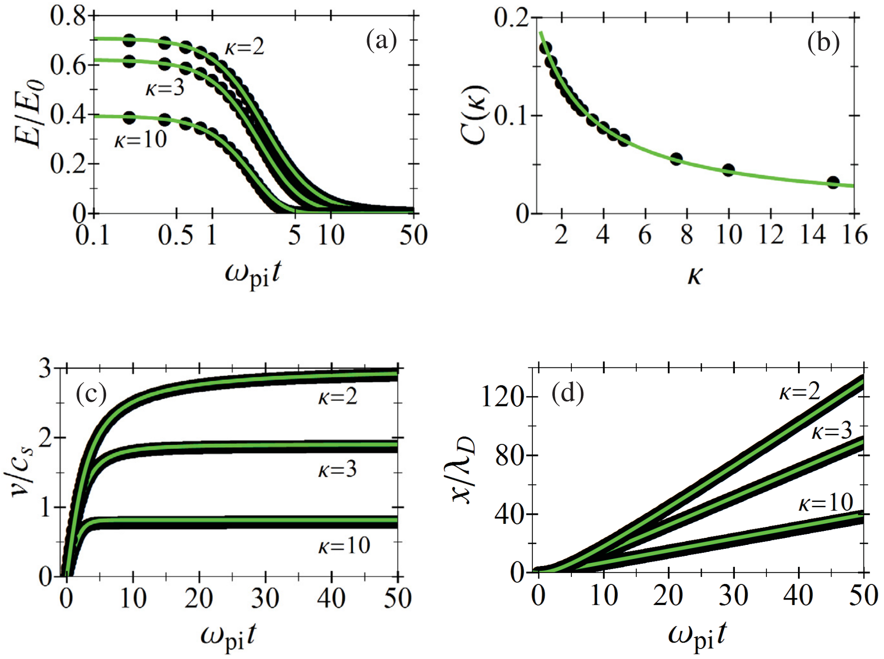

Figure 7.3.: In (a), the electric field strength at the ion front as a function of time is shown for $\kappa = 2$, 3 and 10. Black dots correspond to simulation results, while the green curves represent the analytical estimate (7.6). (b) displays the best-fit values for $C(\kappa)$ (black dots) found by simulations in comparison with Eq. (7.9) (green curve). In (c) and (d), the time dependence of the ion front velocity and its position are plotted, respectively. The corresponding estimates (7.10) and (7.11) are depicted by green lines, black dots show the results of simulations. The figure is taken from Ref. 82.

From Eq. (7.12) it is evident, that the final maximum ion velocity is finite for $\kappa > 1$, in contrast to the isothermal case ($\kappa \to 1$). This is not surprising, since the step-like electron energy distribution does have a finite cut-off energy. As a consequence, the difference of the potential values at $x = -\infty$ (deep inside the target) and $x = \infty$ (in vacuum) is finite and hence the maximum kinetic energy a test particle can gain is limited, too. The correlation between a finite cut-off energy in the electron energy distribution and the limitation of the final maximum ion energy has been studied in the case of a truncated Maxwellian distribution for (i) the free expansion of a plasma consisting of one ion species[83,84] and (ii) the acceleration of light ions, which were assumed as test particles in the field of immobile heavy ions.[85–87]

As mentioned above and illustrated in Fig. 7.2d, the maximum velocity (7.12) is always greater than the velocity $2c_{\mathrm{s}}\sqrt{\kappa}/(\kappa-1)$ of the upper boundary of the self similar solution (7.2). However, it is interesting to note, that the relative difference between both terms is less then 15% for all $\kappa \leq 10$. Furthermore, from Eq. (7.12) we can derive the final maximum ion energy per charge number,

$$\varepsilon_{\mathrm{max}}/Z_{\mathrm{i}} = T_{\mathrm{e},0} \cdot \chi(\kappa)\,. \tag{7.14}$$

Substituting κ by the number of degrees of freedom $\mathbb{Z}$ via Eq. (7.1b) and expressing this parameter in terms of the initial electron temperature $T_{\mathrm{e},0}$ by using Eq. (7.1c), the relation (7.14) will depend on $T_{\mathrm{e},0}$ only. For practical use, we give an approximative expression (see also Fig. 7.4),

$$\varepsilon_{\max}/Z_{\mathrm{i}} \approx T_{\mathrm{e},0}\,\frac{1.36312+4.58725\,T_{\mathrm{e},0}/\mathrm{MeV}}{0.750591+T_{\mathrm{e},0}/\mathrm{MeV}}\ . \tag{7.15}$$

From this relation one can extract the minorant and majorant functions

$$1.82\,T_{\mathrm{e},0} \le \varepsilon_{\max}/Z_{\mathrm{i}} \le 4.59\,T_{\mathrm{e},0}\ . \tag{7.16}$$

Finally, the number of ions per unit energy and unit surface (energy spectrum) can be approximately calculated from the self-similar solution (7.2) as

$$\frac{\partial^2 N}{\partial\varepsilon\partial A} = \frac{\kappa+1}{2^{3/2}}\,\frac{n_{\mathrm{i},0}\,c_{\mathrm{s}}\,t}{\sqrt{Z_{\mathrm{i}}\,T_{\mathrm{e},0}\,\varepsilon}}\left(1-\frac{\kappa-1}{\sqrt{2}\,\kappa}\sqrt{\frac{\varepsilon}{Z_{\mathrm{i}}\,T_{\mathrm{e},0}}}\right)^{\frac{2}{\kappa-1}}\ . \tag{7.17}$$

In the limit $\kappa \to 1$, this relation reproduces the isothermal result[59] (4.7).

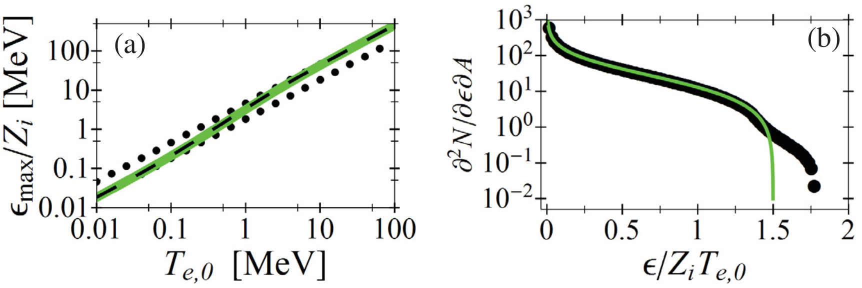

Figure 7.4.: (a) displays the final maximum ion energy as a function of the initial electron energy. The bold green curve corresponds to Eq. (7.14) with κ expressed as a function of the electron temperature $T_{\mathrm{e},0}$ by applying the relation $\kappa = 1+2/\mathbb{Z}$ and Eq. (5.7). That exact curve is almost perfectly covered by the approximation (7.15) (dashed black curve). In addition, the minorant and majorant functions (7.16) are displayed by dotted black lines. (b) shows the energy spectrum for $\kappa = 3$ at $\omega_{\mathrm{pi}} \cdot t = 50$. The black dots correspond to the results of a simulation, while the green curve is determined by Eq. (7.17). Here, the number of ions per unit surface and unit energy is normalized to $n_{\mathrm{i},0}\,\lambda_{\mathrm{D}}/Z_{\mathrm{i}}\,T_{\mathrm{e},0}$. The figure is taken from Ref. 82.

7.2. Comparison to adiabatic models assuming Maxwellian electrons

In the following we want to compare the hydrodynamic approach with the adiabatic Maxwellian model[62] (see Sec. 5.1.1) and the kinetic Maxwellian model[64] (see Sec. 5.1.2). We again point out that the essential difference between the different models is the electron energy distribution. While the hydrodynamic ansatz (7.1a) with κ depending on $T_{\mathrm{e},0}$ via Eqs. (7.1b) and (7.1c) implies a step-like phase space density for all instants $t \ge 0$ (see Sec. 6.3), in the adiabatic Maxwellian model the electron energy distribution is Maxwellian for all times $t \ge 0$ (see Sec. 5.1.1). We recall that the correct temporal evolution of the electron energy distribution in the hydrodynamic approach is automatically fulfilled since the step-like phase space density is conserved (see Sec. 6.2). For the adiabatic Maxwellian ansatz the evolution is modeled by a time-dependent electron temperature. Like in the adiabatic Maxwellian model, in the kinetic Maxwellian approach the electron phase space density is initially given by a Maxwell distribution. However, due to the treatment of the temporal evolution, the Maxwellian shape of the electron distribution is in general not preserved for times $t > 0$ (see Sec. 5.1.2). Despite their different electron distributions, all these approaches conserve the total energy of the system and are therefore in principal suitable for the description of an adiabatic plasma expansion. However, because of the complex interplay between the expansion and the electron cooling this task is complicated within the Maxwellian models.

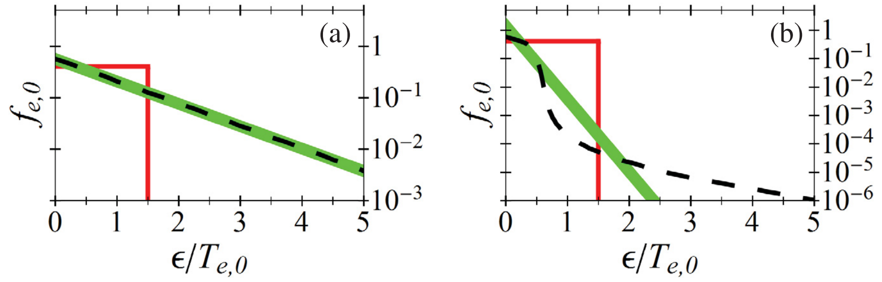

Figure 7.5.: Panels (a) and (b) show the different electron distributions underlying the different models (nonrelativistic case) for a target with an initial thickness $L/\lambda_\mathrm{D} = 80$ at $\omega_\mathrm{pi} t = 0$ and $\omega_\mathrm{pi} t = 50$, respectively. The results of the adiabatic and the kinetic Maxwellian approach are depicted by the bold green and the dashed black curve, respectively, whereas the solid red curve corresponds to the hydrodynamic approach. Here, $f_\mathrm{e,0}$ is normalized to $n_\mathrm{e,0}/\sqrt{2m_\mathrm{e}T_\mathrm{e,0}}$. The figure is taken from Ref. 82.

The various electron distributions, which are illustrated in Fig. 7.5, lead to different behavior during the ion acceleration process. While no finite velocity for the ion front exists in the case of Maxwellian-distributed electrons and half-infinite plasma slabs, we identify the limit (7.12) for a step-like electron energy distribution. In order to get finite ion energies in the case of Maxwellian electrons, one has to operate with foils (i.e. targets of limited thickness). This leads to different final ion energies in dependence on the target thickness, as shown in Fig. 7.6a. In contrast, in the hydrodynamic approach, the final maximum energy of the ions quickly saturates for an increasing thickness of the foil, as also illustrated in Fig. 7.6a. Moreover, these values are lower by almost one order of magnitude for foil thicknesses L in the range of $\lambda_\mathrm{D} \leq L \leq 100\lambda_\mathrm{D}$, as compared with the results assuming Maxwellian hot electrons.

The final energy in the case of nonrelativistic Maxwell-like electrons is given by Eq. (5.13), which is approximately equal to $\varepsilon_\mathrm{max}/Z_\mathrm{i} = 2T_\mathrm{e,0}\ln(0.32L/\lambda_\mathrm{D} + 4.2)^2$ for $L/\lambda_\mathrm{D} \geq 20$, see Ref. 62. This expression depends on $T_\mathrm{e,0}$ as well as on $n_\mathrm{e,0}$ (through λ_D), whereas the relation (7.14) of the hydrodynamic model is only a function of the electron temperature $T_\mathrm{e,0}$.

To give an explanation for the remarkable difference in the final maximum ion energies, predicted by the Maxwellian and the hydrodynamic approaches, we may exclude differences in the initial electric field strength as an essential reason, because for foils thicker than a few De-

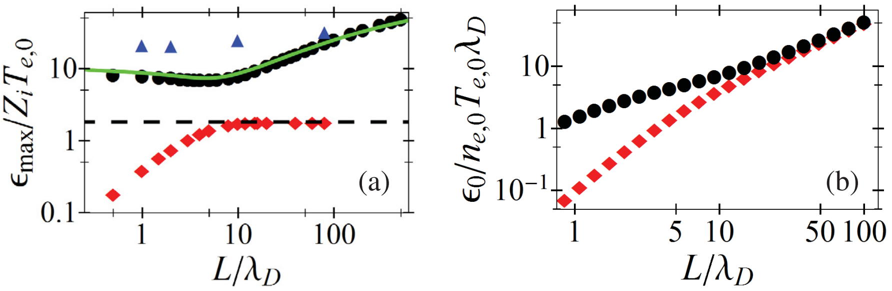

Figure 7.6.: (a) shows the final maximum ion energy as a function of the initial target thickness L/λ_{D}. Here, the black dots and the blue triangles correspond to the nonrelativistic adiabatic and the kinetic Maxwellian approach, respectively, whereas the hydrodynamic approach for the nonrelativistic case ($\kappa = 3$) is depicted by the red diamonds. The broad green curve depicts the analytical result for the maximum ion energy of the nonrelativistic adiabatic Maxwellian approach, Eq. (5.13). The dashed black line displays the maximum ion energy for thick targets and nonrelativistic electrons with a step-like energy distribution ($\kappa = 3$), Eq. (7.14). In (b) simulation results for the total initial energy (per area) of the system as a function of the initial target thickness L/λ_{D} are plotted. Here, the black dots correspond to Maxwell-like distributed electrons, while the red diamonds represent the hydrodynamic approach. The figure is taken from Ref. 82.

bye lengths the ratio $E_{\mathrm{Maxwell}}(t=0)/E_{\mathrm{hydro}}(t=0)$ is given by $\sqrt{\kappa^{\kappa/(\kappa-1)}/\exp(1)}$ (according to Eqs. (4.9) and (7.8)), which is smaller than 1.4 for arbitrary values of $T_{\mathrm{e},0}$. Furthermore, the total energy of the system (initial electric field energy + initial thermal energy of the electrons) does not significantly differ for foils with a thickness greater than or equal $10\,\lambda_{\mathrm{D}}$ (see Fig. 7.6b).

Therefore, the large discrepancy in the ion energies is related to the different temporal behavior of the electric field strength $E(t)$ at the ion front, which is illustrated in Figs. 7.7a and 7.7b. First, we note that the fields in both models using Maxwellian electrons are almost identical over tens of ion plasma periods for thicker foils (see Fig. 7.7a), whereas the adiabatic Maxwellian model predicts a faster decrease of the accelerating field in the case of thinner foils (see Fig. 7.7b). After $\omega_{\mathrm{pi}}\,t = 50$, in the Maxwellian models the field strengths will be reduced by approximately two orders of magnitude. In contrast, the hydrodynamic model predicts a much faster drop of the electric field — approximately four orders of magnitude during the same time interval.

In general, assuming nonrelativistic electrons, the electric field at the ion front is given by(5)

$$E(t) = \sqrt{2/\varepsilon_0}\,\sqrt{n_{\mathrm{e}}(t)\,T_{\mathrm{e}}(t)}\,. \tag{7.18}$$

In general, the above expression fails in the relativistic case(6). However, for Maxwellian electrons, where $f_{\mathrm{e},0}$ is given by the Maxwell-Jüttner distribution (2.23b), the result (7.18) is still true, since the relativistic expression for the electron density and its nonrelativistic limit are identical (see Sec. 2.3). Moreover, since the relativistic result for the density relation assuming a step-like

---

(5) In Sec. B.3 we confirm this statement.

(6) This follows from the consideration of Sec. B.3. In order to prove Eq. (7.18) one needs the assumption that the degrees of freedom $\mathbb{Z}$ are constant. However, in the relativistic case $\mathbb{Z}$ becomes a function of the electron temperature T_{e} and that assumption is violated.

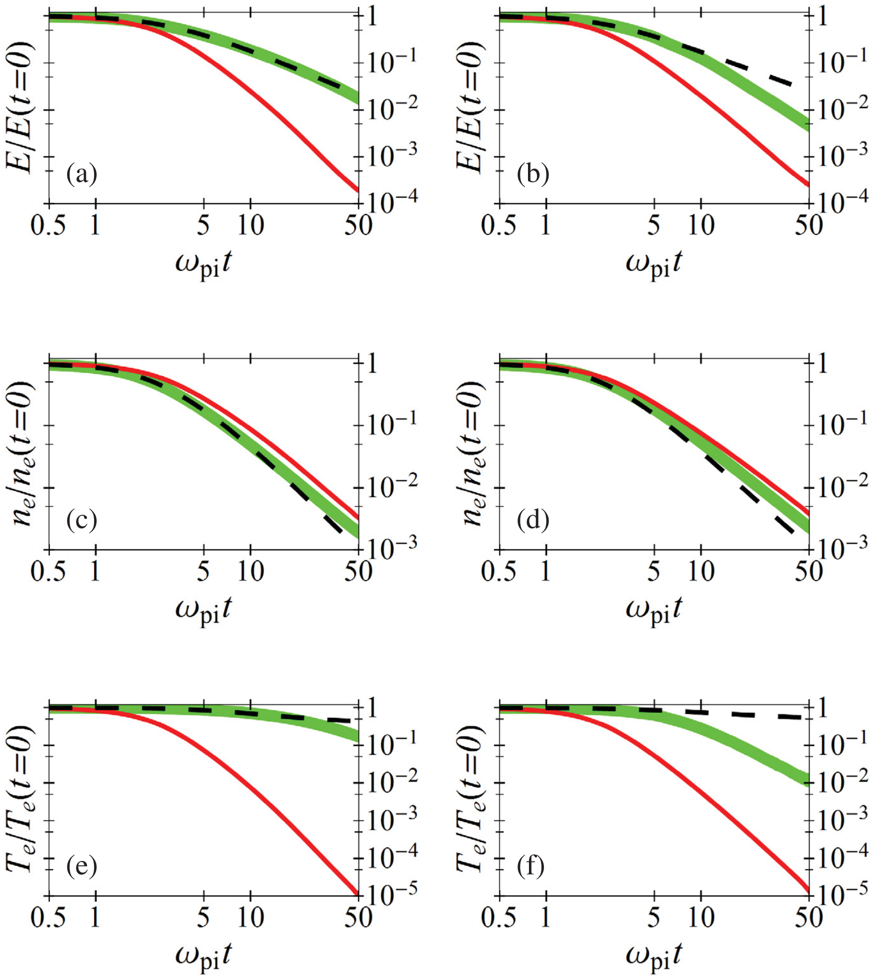

Figure 7.7.: Simulation results for the electric field strength ((a) and (b)), the electron density ((c) and (d)) and the electron temperature ((e) and (f)) at the ion front as functions of time for targets with initial thicknesses $L/\lambda_{\mathrm{D}} = 80$ (left column) and $L/\lambda_{\mathrm{D}} = 2$ (right column), respectively. The curves are normalized to the corresponding initial values. The thick green and dashed black curves follow from the nonrelativistic adiabatic and kinetic Maxwellian models, respectively. The results of the hydrodynamic ansatz are depicted by the solid red curves. The figure is taken from Ref. 82.

electron energy distribution, Eq. (6.31), is quite well approximated by the nonrelativistic expression (6.32), the statement (7.18) is quite well fulfilled in this case, too. To summarize, with respect to the problem to be discussed here, one can apply Eq. (7.18) to express the dependency of the electric field at the ion front on the electron density and temperature at the same point.

Now, as Figs. 7.7c and 7.7d indicate, the temporal behavior of the electron density is similar for both types of model. Thus, according to Eq. (7.18), the difference in the electric field strength at the ion front should be mainly influenced by the behavior of the electron temperature at that position. The graphs in Figs. 7.7e and 7.7f show the evolution of the electron temperature at the ion front. Obviously, the cooling process is much more pronounced in the hydrodynamic model.

To give a qualitative explanation for this behavior, we have to keep in mind that the adiabatic Maxwellian model uses a single, well-defined electron temperature, which is uniform in space, i.e. $T_\mathrm{e}(x,t) = T_\mathrm{e}(t)$. The temporal variation of $T_\mathrm{e}(t)$ is caused by the transfer of thermal energy from electrons to kinetic energy of the ions via the electric field. At the beginning of the expansion, the kinetic energy of the ions gained from the electric field is almost independent on the initial foil thickness, because the electric field at the ion boundary depends only weakly on L for $L > \lambda_\mathrm{D}$, see Eq. (5.10). However, the total initial thermal energy of the electrons strongly depends on L (at constant $n_{\mathrm{e},0}$ and $T_{\mathrm{e},0}$), because the number of hot electrons increases proportionally with increasing target thickness (7). Consequently, the relative energy loss of the hot electrons is smaller for thicker foils. Or, in other words, the temperature $T_\mathrm{e}(t)$ decreases more slowly. This argument also illustrates, why the adiabatic Maxwellian model converges into the isothermal model predicting an infinite maximum ion energy for $L \to \infty$.

In the kinetic Maxwellian model, the temperature is not uniform in space as in the adiabatic Maxwellian approach (see discussion in Sec. 5.1.2 also). However, the deviation of the electron phase space density $f_{\mathrm{e},0}$ from the initial Maxwellian distribution is relatively small in the kinetic model during the essential acceleration time of the ions. Therefore the evolution of the electric field strength as well as of the electron density and the electron temperature at the ion front are very similar to that of the adiabatic case during that period of time, $\omega_\mathrm{pi} t \lesssim 10$, (see Fig. 7.7).

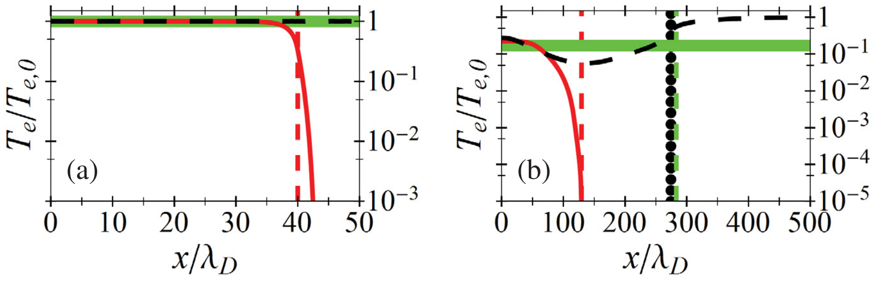

Figure 7.8.: (a) and (b) show the simulation results for the spatial electron temperature distribution at the instants of time $\omega_\mathrm{pi} t = 0$ and $\omega_\mathrm{pi} t = 50$, respectively. The bold green and black dashed curves correspond to Maxwellian electrons (adiabatic and kinetic ansatz, respectively), while the red curves show the results of the hydrodynamic approach ($\kappa = 3$). The dashed red and green vertical lines mark the ion fronts within the hydrodynamic and the adiabatic Maxwellian model, respectively, whereas the dotted black vertical line corresponds to the kinetic Maxwellian approach. Initially, the target thickness was $L/\lambda_\mathrm{D} = 80$ and the ion front was located at $40\,\lambda_\mathrm{D}$. The figure is taken from Ref. 82.

In contrast, the hydrodynamic model gives a local temperature, which is connected to the spatial electron density distribution by the adiabatic relation $T_\mathrm{e}(x) = T_{\mathrm{e},0} \cdot (n_\mathrm{e}(x)/n_{\mathrm{e},0})^{\kappa-1}$ (see Ref. 80). As a consequence, the electron temperature drops rapidly at the ion front while the electron density is decreasing due to the expansion. The obtained effect is much stronger than the reduction of the electron temperature due to the total energy loss of all electrons in the adiabatic Maxwellian model. The differing properties of the spatial temperature profiles of the models are demonstrated in Fig. 7.8.

---

(7) Note that from the experimental point of view, constant values of $n_{\mathrm{e},0}$ and $T_{\mathrm{e},0}$ with an increasing target thickness L imply a constant value of the laser intensity but an increasing focal spot radius and therefore an increasing pulse power. This follows from the discussion in Sec. 7.3 — see especially Eq. (7.32) for $T_{\mathrm{e},0}$ and Eq. (7.30) for the electron plasma frequency (which can be resolved for $n_{\mathrm{e},0}$).

7.3. Application of the different adiabatic models to experimental results

In this section, we will compare the predictions of the plasma expansion models described above with the results of various experiments. Since PIC simulations commonly predict a Maxwellian electron distribution generated during the laser-plasma interaction, the observed ion acceleration is often described by the application of Mora's model[59] with a certain (empirically determined) acceleration time t_{acc} which is proportional to the laser pulse duration[10, 126, 198] τ_{L} (see chapter. 8). This procedure simply assumes that the laser keeps the electrons in a Maxwellian distribution with a temperature approximately given by the ponderomotive potential.[159] Once the laser pulse is over, the hot electrons cool down transferring a fraction of their energy to the ions, and the plasma expansion becomes adiabatic. The maximum ion energy is still increasing in this phase. Its final value will be reached in the limit $t \to \infty$, according to Ref. 62 and Eq. (5.11). However, this is a purely one-dimensional consideration.

In reality, the acceleration efficiency drops as soon as the plasma geometry becomes multi-dimensional. This happens approximately at the time when the displacement of the ion front in forward direction, x_{acc}, exceeds the transverse dimension D_{e} of the electron spot on the rear side of the target.[50, 99, 199] The limitation of the acceleration distance decreases significantly the resulting ion energies[199] in comparison to one-dimensional models used in Refs. 59, 199. Based on the results of Ref. 59, this time $t_{1\text{D}\blacktriangleright 3\text{D}}$ can be estimated for protons as

$$\omega_{\text{pi}}\, t_{1\text{D}\blacktriangleright 3\text{D}} = [2\exp(1)]^{1/4}\sqrt{\frac{D_{\text{e}}}{\lambda_{\text{D}}}}\,, \tag{7.19}$$

which in physical units reads as

$$t_{1\text{D}\blacktriangleright 3\text{D}}\,[\text{fs}] = 134.5\sqrt{\frac{D_{\text{e}}\,[\mu\text{m}]}{\sqrt{n_{\text{e},0}\,[10^{20}\text{cm}^{-3}]\;T_{\text{e},0}\,[\text{MeV}]}}}\,. \tag{7.20}$$

Following Ref. 10, the size of the electron spot on the rear target surface can approximately be evaluated with the help of the relation

$$D_{\text{e}} = D_{\text{L}} + 2\tan(\theta_{\text{e}})\,L\,. \tag{7.21}$$

Here, D_{L} is the laser spot diameter on the target front side, L is the thickness of the target and θ_{e} is the half-opening angle of the electron beam inside the target. According to Ref. 10 one has $\theta_{\text{e}} \approx 25^\circ$. This value will be used throughout this section. Furthermore, $D_{\text{L}} \approx 5\mu\text{m}\ldots 25\mu\text{m}$ (e.g. Ref. 58 and Ref. 6) and normally $L \lesssim 100\mu\text{m}$. For the corresponding quantity D_{e} we obtain values within a range of approximately $5\mu\text{m}\ldots 100\mu\text{m}$. Assuming hot electron temperatures in the range of $T_{\text{e},0} \approx 0.1\text{MeV}\ldots 10\text{MeV}$ and densities $n_{\text{e},0} \approx 10^{20}\text{cm}^{-3}\ldots 10^{21}\text{cm}^{-3}$, we may calculate corresponding times $t_{1\text{D}\blacktriangleright 3\text{D}}$ between 100 fs and 2500 fs.

For relatively long laser pulse durations, $\tau_\mathrm{L} \gtrsim 150\,\mathrm{fs}$, and assuming similar focusing conditions, the ion bunch already reaches a longitudinal extent of the order of the transverse size of the electron spot during the laser pulse duration. Therefore, the acceleration within the subsequent adiabatic regime is almost negligible and the relation $t_\mathrm{acc} \approx t_{1\mathrm{D}\blacktriangleright 3\mathrm{D}} \approx \tau_\mathrm{L}$ holds. As a result, the isothermal theory[10,59] describes the acceleration process sufficiently well.

Although the maximum energy predicted by the isothermal model depends on several experimental quantities, a rough scaling with the laser intensity I_L times the square of the laser wavelength λ_L can be found, $\varepsilon_\mathrm{max\,iso} \propto \sqrt{I_\mathrm{L}\,\lambda_\mathrm{L}^2}$, as it was given by Clark et al.[200] and confirmed in other studies.[174,199] We may derive this characteristic behavior by inserting relation (7.19) for the limited acceleration time into the expression for the maximum proton energy of Ref. 59,

$$\varepsilon_\mathrm{max\,iso} = 2\,T_\mathrm{e,0}\,\mathrm{arcsinh}\left(\frac{\omega_\mathrm{pi}\,t}{\sqrt{2\,\exp(1)}}\right)^2 . \tag{7.22}$$

In the linearized form we have

$$\varepsilon_\mathrm{max\,iso} \approx \sqrt{\frac{2}{\exp(1)}}\,\frac{T_\mathrm{e,0}\,D_\mathrm{e}}{\lambda_\mathrm{D}} . \tag{7.23}$$

Now, applying the estimates of Ref. 10 for the total number of hot electrons generated by the laser pulse, $N_\mathrm{e} = \eta\,\varepsilon_\mathrm{L}/T_\mathrm{e,0}$, and for the hot electron density at the rear side of the target, $n_\mathrm{e} = 4N_\mathrm{e}/(\pi D_\mathrm{e}^2\,\tau_\mathrm{L}\,c)$, as well as the relation $P_\mathrm{L} = \varepsilon_\mathrm{L}/\tau_\mathrm{L}$, with the laser pulse power P_L and the laser pulse energy ε_L in the focal spot, one can express the hot electron density as

$$n_\mathrm{e,0} = \frac{4\,\eta\,P_\mathrm{L}}{\pi\,c\,T_\mathrm{e,0}\,D_\mathrm{e}^2} . \tag{7.24}$$

With help of this relation, we may rewrite the Debye length as

$$\lambda_\mathrm{D} = \frac{D_\mathrm{e}}{2}\sqrt{\frac{1}{\eta}\,\frac{\pi\,\varepsilon_0\,c}{e^2}\,\frac{T_\mathrm{e,0}^2}{P_\mathrm{L}}} . \tag{7.25}$$

Here, η denotes the conversion efficiency of laser energy into hot electron energy within the laser focus. A typical value of the order of 10% (see e.g. Ref. 50) will be used in the estimates below.

From Eq. (7.25) we directly obtain the normalized electron spot size

$$\frac{D_\mathrm{e}}{\lambda_\mathrm{D}} = \sqrt{\eta\,\frac{4\,e^2}{\pi\,c\,\varepsilon_0}\,\frac{P_\mathrm{L}}{T_\mathrm{e,0}^2}} \tag{7.26}$$

and substitute it into Eq. (7.23). We finally get

$$\varepsilon_\mathrm{max\,iso} \approx \sqrt{\eta}\,\sqrt{\frac{8}{\pi\,\exp(1)}\,\frac{e^2}{\varepsilon_0\,c}}\,\sqrt{P_\mathrm{L}} = \frac{r_\mathrm{L}}{\lambda_\mathrm{L}}\,\sqrt{\eta}\,\sqrt{\frac{8}{\exp(1)}\,\frac{e^2}{\varepsilon_0\,c}}\,\sqrt{I_\mathrm{L}\,\lambda_\mathrm{L}^2} \tag{7.27}$$

by relating the pulse power to the laser intensity, $P_\mathrm{L} = \pi\,r_\mathrm{L}^2\,I_\mathrm{L}$. The parameter r_L denotes the laser spot radius at the target front side. In physical units we obtain

$$\varepsilon_\mathrm{max\,iso}\,[\mathrm{MeV}] \approx 3.33\,\frac{r_\mathrm{L}}{\lambda_\mathrm{L}}\,\sqrt{\eta}\,\sqrt{I_\mathrm{L}\,\lambda_\mathrm{L}^2\,[10^{18}\,\mathrm{W/cm^2\,\mu m^2}]} . \tag{7.28}$$

Hence, we find $\varepsilon_{\mathrm{max\,iso}} \propto \sqrt{I_\mathrm{L}\,\lambda_\mathrm{L}^2}$, in agreement with Ref. 200. Note again, that the scaling has been found by setting the acceleration distance x_acc equal to the transverse size of the electron spot on the rear side of the target. Moreover, by changing that acceleration distance to some multiple of the electron spot size, $h D_\mathrm{e}$, the result (7.28) would simply become multiplied by this factor h. The same result would follow from an increase of the normalized focal spot radius by a factor of h, $h r_\mathrm{L}/\lambda_\mathrm{L}$, while assuming the laser intensity I_L to remain constant. Therefore, the particular value of the acceleration distance x_acc does not influence the qualitative scaling law (7.28).

In the ultrashort-pulses regime $\tau_\mathrm{L} \lesssim 100\,\mathrm{fs}$ the situation is different, because the acceleration time exceeds the laser pulse duration, $t_\mathrm{acc} \approx t_{\mathrm{1D}\blacktriangleright\mathrm{3D}} > \tau_\mathrm{L}$. Hence, the adiabatic regime becomes important, and another scaling for the maximum ion energy should be obtained. This is demonstrated in Fig. 7.9, which is based on Fig. 7 of Ref. 201, where the results from a large number of laser-ion acceleration experiments from the last two decades have been collected.

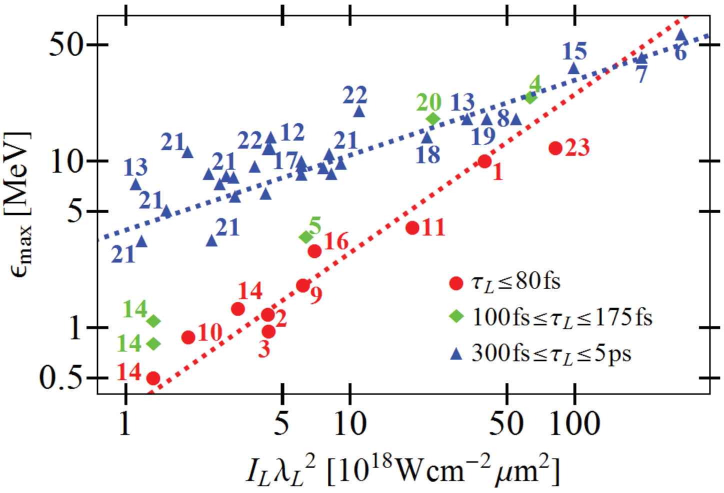

Figure 7.9.: Overview of various experiments performed in the last decades. From the illustration it is obvious that ultrashort pulse experiments (red dots) show a different scaling than experiments with relatively long laser pulses (blue triangles). Dotted lines with the corresponding color are drawn in both regions to guide the eye. Experiments with intermediate pulse durations (green diamonds) fall between both regions. The following experimental data have been used: 1=19, 2=202, 3=124, 4=183, 5=60, 6=6, 7=203, 8=8, 9=121, 10=204, 11=205, 12=206, 13=201, 14=198, 15=207, 16=50, 17=208, 18=209, 19=174, 20=177, 21=210, 22=211, 23=212. The figure is taken from Ref. 82.

The difference between the two regimes, as shown in Fig. 7.9, was previously discussed also by Fuchs et al.[126] Assuming isothermal Maxwellian electrons and laser pulse durations $\tau_\mathrm{L} \gtrsim 150\,\mathrm{fs}$, they found empirically a good agreement between experimental data and Eq. (7.22) by setting the acceleration time proportional to the laser pulse duration τ_L. In contrast, they determined the acceleration time to be almost constant for ultra-short pulse durations, $\tau_\mathrm{L} < 60\,\mathrm{fs}$.

One can immediately show that a fixed acceleration time in Eq. (7.22) will result in a dependency of the maximum ion energy on $T_{\mathrm{e},0}$ only — besides a factor, which contains the laser wavelength, the conversion efficiency and the divergence of the electron beam as well as the ratio of the target thickness and the laser focal spot radius. To prove this statement, we first rewrite the expression for the hot electron density (7.24) in the form

$$n_{\mathrm{e},0} = \frac{\eta \, I_{\mathrm{L}}}{c \, T_{\mathrm{e},0} \cdot \left(1 + \tan(\theta_{\mathrm{e}}) \, \frac{L}{r_{\mathrm{L}}}\right)^2} \tag{7.29}$$

by using the above estimates $P_{\mathrm{L}} = \pi \, r_{\mathrm{L}}^2 \, I_{\mathrm{L}}$ and $D_{\mathrm{e}} = 2 \, r_{\mathrm{L}} + 2 \tan(\theta_{\mathrm{e}}) \, L$. With help of this relation, we can rewrite the ion plasma frequency as

$$\omega_{\mathrm{pi}} = \frac{\sqrt{\eta}}{1 + \tan(\theta_{\mathrm{e}}) \, \frac{L}{r_{\mathrm{L}}}} \sqrt{\frac{Z_{\mathrm{i}} \, e^2}{m_{\mathrm{i}} \, \varepsilon_0 \, c} \, \frac{I_{\mathrm{L}}}{T_{\mathrm{e},0}}} \,, \tag{7.30}$$

which in physical units assuming protons reads

$$\omega_{\mathrm{pi}}[1/fs] = 0.019 \, \frac{\sqrt{\eta}}{1 + \tan(\theta_{\mathrm{e}}) \, \frac{L}{r_{\mathrm{L}}}} \sqrt{\frac{I_{\mathrm{L}} \, [10^{18} \mathrm{W/cm^2}]}{T_{\mathrm{e},0} \, [\mathrm{MeV}]}} \,. \tag{7.31}$$

Next, we express the laser intensity I_{L} in Eq. (7.30) in terms of $T_{\mathrm{e},0}$ by rearranging the relation

$$T_{\mathrm{e},0} = m_{\mathrm{e}} \, c^2 \cdot \left(\sqrt{1 + \frac{I_{\mathrm{L}} \, \lambda_{\mathrm{L}}^2}{1.37 \cdot 10^{18} \mathrm{W/cm^2 \, \mu m^2}}} - 1 \right) \tag{7.32}$$

of Wilks et al.[159] By inserting the resulting expression into Eq. (7.22), we immediately confirm the statement on the pure temperature dependence of the maximum ion energy. It is interesting to note that exactly the same conclusion for the maximum ion energy can be drawn assuming step-like distributed electrons, as shown in Eqs. (7.14) and (7.15), respectively. Moreover, the relation (7.14) fits the experimental results in the ultrashort pulse regime quite well (see Fig. 7.10).

To answer the question whether the illustrated agreement is only a consequence of the intrinsic adiabatic plasma description in the hydrodynamic model or if it is also related to the shape of the initial electron distribution, we also checked the experimental data against the results of the Maxwellian adiabatic modeling (see Sec. 5.1.1). According to the discussion of Sec. 7.2 — see especially Fig. 7.6a — it is evident that the Maxwellian adiabatic expansion gives a different scaling. Fig. 7.11 includes curves, which were calculated with help of relation (5.13) for three different normalized target thicknesses $l = L/\lambda_{\mathrm{D}}$ as well as the result from the hydrodynamic model.

In this context we recall that the applied relations (7.14) and (5.13) express the final energy of the ion front in the limit $t, x_{\mathrm{acc}} \to \infty$. In contrast, as discussed earlier in this section, the one-dimensional expansion — and thus the essential energy gain — occurs over a distance x_{acc} comparable to the transverse size D_{e} of the electron sheath at the rear side of the target. Therefore, we have revisited the above comparison between the two models and the experimental data using a finite acceleration distance x_{acc}. We found that this limitation in the acceleration process does not change the general scaling remarkably. Instead the two models still predict two clearly different scaling laws. In any case the adiabatic Maxwellian model cannot reproduce the scaling implied by the ultrashort pulse experiments over the complete intensity region ($10^{18}\mathrm{W/cm^2}$ – $10^{20}\mathrm{W/cm^2}$). In contrast, the experimental data for the maximum ion energy in the ultrashort pulse regime may

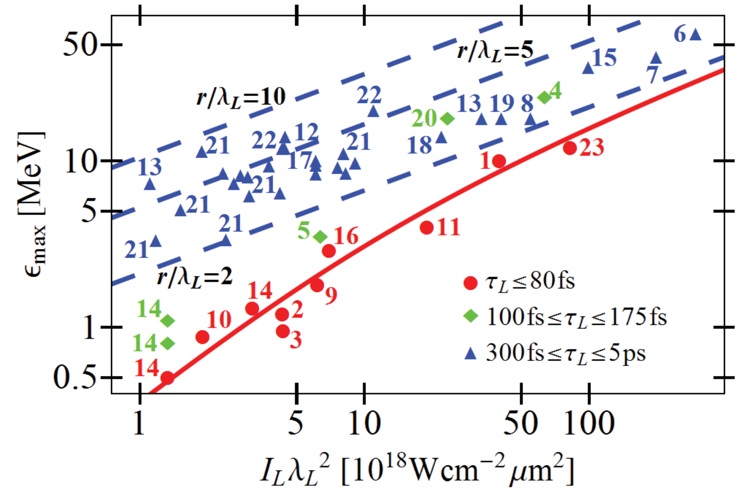

Figure 7.10.: The $\sqrt{I_L\,\lambda^2}$-scaling (dashed blue lines) according to Eq. (7.28) is shown for focal radii $r_L = \{2,\,5,\,10\}\,\lambda_L$. In addition, the red curve represents the maximum energy of the ions in the hydrodynamic ansatz applying Eq. (7.14). The experimental data are identical to those of Fig. 7.9. The figure is taken from Ref. 82.

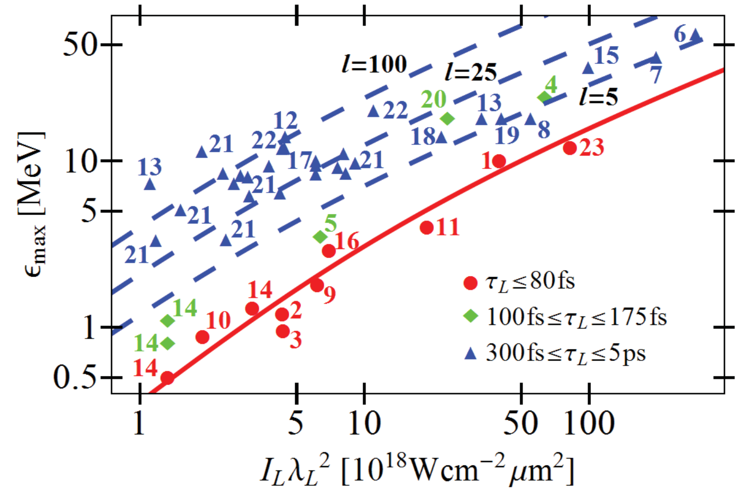

Figure 7.11.: Comparison of the scaling of the maximum ion energy with the laser intensity of the different adiabatic models. The red curve represents the maximum ion energy in the hydrodynamic ansatz, Eq. (7.14). The dashed blue curves show the ion energies for Maxwellian electrons, Eq. (5.13), for three normalized foil thicknesses $l = L/\lambda_D = \{5,\,25,\,100\}$. The experimental data are identical to those of Fig. 7.9. Note that (i) the plotted theoretical curves exhibit the maximum energies in the limit $t \to \infty$. (ii) An increase in the target thickness does not necessarily imply an increase of its normalized value for a given set of laser parameters (I_L, r_L, P_L, ...), since the Debye length (7.25) depends on the size of the electron spot on the rear side of the target, which itself changes with the target thickness. The figure is taken from Ref. 82.

be interpreted well by the hydrodynamic approach.

Since the most important difference between both models is the non-Maxwellian electron distribution in the hydrodynamic approach, this could be an indication for the presence of non-Maxwellian electron spectra generated in ultrashort pulse interactions. This suggestion is supported by the statement in Ref. 99, that approximately 100 fs are needed to evolve the hot electrons into an equilibrium distribution, as well as by simulations in Ref. 213, where a non-Maxwellian distribution has been observed using an ultrashort pulse laser ($\tau_L = 60\,\text{fs}$). Also we recall here about the interaction schemes with truncated Maxwellian distributions.[83–87, 214] This type of energy distribution functions may be induced by the escape of the fastest electrons from the charge separation region. A plausible explanation for this possibility follows from the multi-dimensional nature of the interaction, which does not provide an equilibrium solution for Maxwellian electrons.[110] Because of a finite potential at infinity in this geometry, electrons with kinetic energies exceeding this potential, can escape from the target and a non-Maxwellian distribution will be formed.

As a non-Maxwellian electron distribution should also manifest itself in the shape of the proton spectrum, we checked this aspect using the publications employed in the Figs. 7.9–7.11 and compared it with the theoretical prediction of the hydrodynamic model, Eq. (7.17), as well as with the theoretical spectrum evaluated for Maxwellian electrons, Eq. (4.7). As mentioned above (see, e.g. Secs. 6.1 and 7.1), the hydrodynamic result (7.17) becomes identical with Eq. (4.7) in the limit $\kappa \to 1$, where the electron energy spectrum associated with the hydrodynamic ansatz takes the form of a Maxwellian distribution (see Sec. 6.1). To compare the experimental data with the theoretical models, we have fitted the expressions (7.17) and (4.7) to the measured data. In the case of the hydrodynamic model, the adiabatic index κ was used as a fit parameter. The deviation of its best-fit value κ_{fit} from unity may be considered as a measure for the deviation of the electron energy distribution from a Maxwellian one.

In our analysis we noticed that κ_{fit} is close to 1 for a large number of experiments using relatively long laser pulse durations, $\tau_L \geq 300\,\text{fs}$. Hence, the corresponding proton spectra are quite well described by the theoretical result (4.7) assuming Maxwellian electrons. This is obvious from the right column of panels in Fig. 7.12, where the best-fit results for the hydrodynamic expression (solid green lines) are almost identical with the best-fit results for the Maxwellian case (dashed red curves). In contrast, for numerous ultrashort pulse experiments ($\tau_L \leq 80\,\text{fs}$) the best-fit values for κ are close to numbers(8) 2-3, as illustrated in the left column of Fig. 7.12. Note again, that the values $\kappa = 2$ and $\kappa = 3$ correspond to a step-like electron distribution in the nonrelativistic and ultrarelativistic limit, respectively (see Sec. 6.3).

However, we want to emphasize that this is not necessarily a direct proof for the presence of a step-like electron energy distribution in those ultrashort pulse experiments, since the shape of the proton spectra are in reality influenced by various other aspects, such as the laser prepulse and multi-dimensional as well as multi-ion species effects. But the results reported above support the suggestion about the presence of a non-Maxwellian distribution in those experiments. However, as demonstrated in Fig. 7.13, we found also some exceptional cases in the analysis of the diagnosed proton spectra. Nevertheless, we believe that there is some evidence for a non-Maxwellian distribution in most of the analyzed ultrashort pulse experiments as well as for a Maxwellian

---

(8) Here we want to remind that values of 2 and 3 for κ are associated with a step-like distribution function in the ultrarelativistic and the nonrelativistic limit, respectively (see Sec. 7.1).

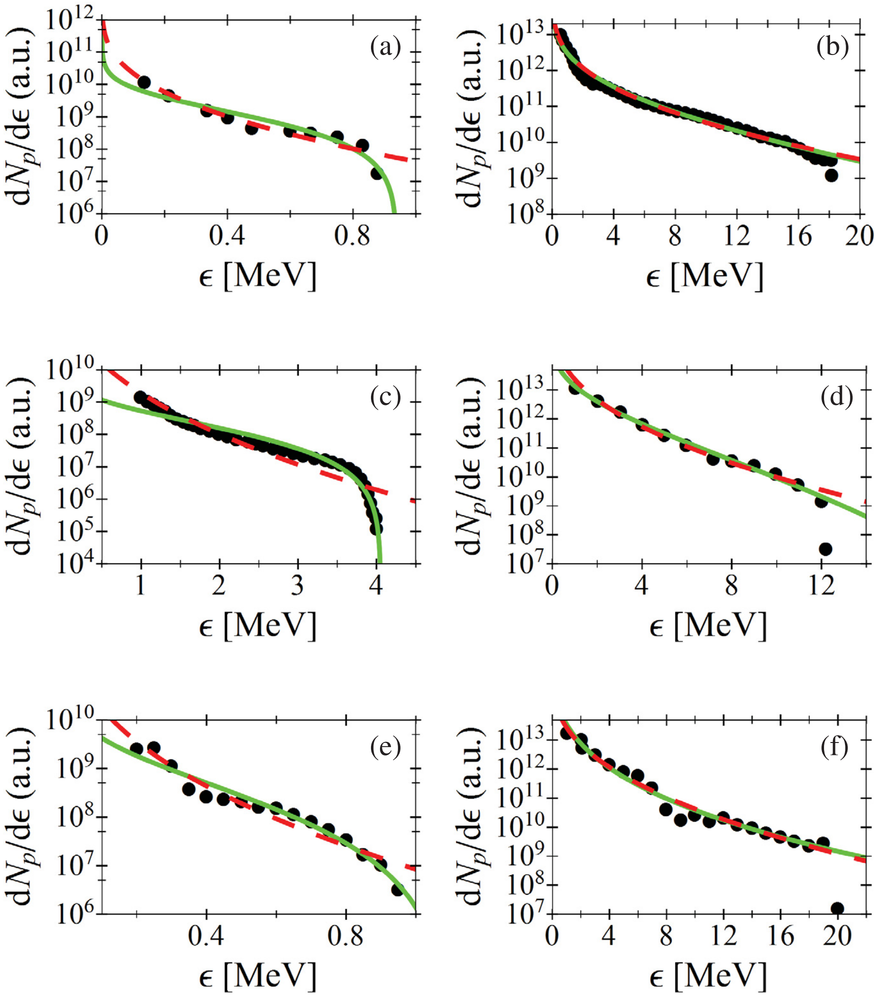

Figure 7.12.: Experimental data (black dots) for the proton spectrum from some of the references used in the Figs. 7.9–7.11. The left column of panels corresponds to ultrashort pulse experiments ($\tau_L \leq 80\,\text{fs}$), the right one concerns experiments with relatively long laser pulse durations ($\tau_L \geq 300\,\text{fs}$). The best fit for the theoretical ion spectrum under the assumption of Maxwellian electrons (4.7) (red dashed curves) is compared against the corresponding fit of the hydrodynamic result (7.17) (green solid curves). The following data and fit parameters correspond to the different panels: (a) data from Ref. 204, $\tau_L = 70\,\text{fs}$, $I_L = 3 \cdot 10^{18}\,\text{W/cm}^2$, $\varepsilon_{\max} = 0.88\,\text{MeV}$, $\kappa_{\text{fit}} = 2.32$, (b) data from Ref. 201, $\tau_L = 350\,\text{fs}$, $I_L = 3 \cdot 10^{19}\,\text{W/cm}^2$, $\varepsilon_{\max} = 18\,\text{MeV}$, $\kappa_{\text{fit}} = 1.08$, (c) data from Ref. 205, $\tau_L = 34\,\text{fs}$, $I_L = 3 \cdot 10^{19}\,\text{W/cm}^2$, $\varepsilon_{\max} = 4\,\text{MeV}$, $\kappa_{\text{fit}} = 2.19$, (d) data from Ref. 211, $\tau_L = 600\,\text{fs}$, $I_L = 4 \cdot 10^{18}\,\text{W/cm}^2$, $\varepsilon_{\max} = 12\,\text{MeV}$, $\kappa_{\text{fit}} = 1.24$, (e) data from Ref. 124, $\tau_L = 60\,\text{fs}$, $I_L = 7 \cdot 10^{18}\,\text{W/cm}^2$, $\varepsilon_{\max} = 0.95\,\text{MeV}$, $\kappa_{\text{fit}} = 1.79$, and (f) data from Ref. 211, $\tau_L = 700\,\text{fs}$, $I_L = 1 \cdot 10^{19}\,\text{W/cm}^2$, $\varepsilon_{\max} = 20\,\text{MeV}$, $\kappa_{\text{fit}} = 0.93$. The figure is taken from Ref. 82.

electron spectrum in the regime with relatively long laser pulse durations. Of course, in reality the details of the laser pulse as well as of the target parameters are likely to have a noticeable influence on the shape of the electron distribution, too. Hence, there is no strictly exclusive dependence of the shape of the electron (and ion) spectra on the pulse duration.

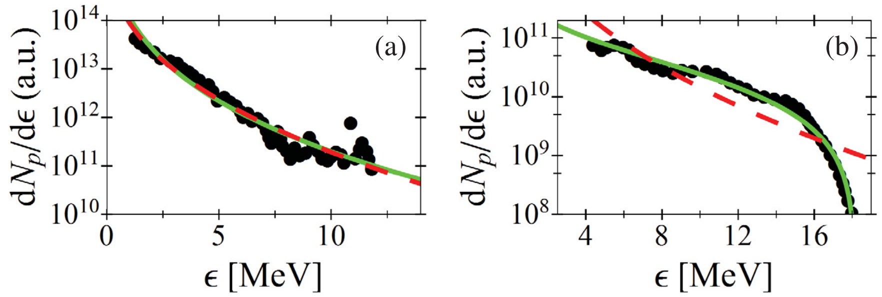

Figure 7.13.: Two exceptional cases for the proton spectrum as compared to the default case, Fig. 7.12. Here, the best-fit for the hydrodynamic expression (7.17) is almost identical to the Maxwellian result (4.7) for the ultrashort pulse experiment (a), while this is not the case for the experiment using a relatively long pulse duration (b). The following data and fit parameters correspond to the different panels: (a) data from Ref. 212: $\tau_{\mathrm{L}} = 50\,\mathrm{fs}$, $I_{\mathrm{L}} = 1.3 \cdot 10^{20}\mathrm{W/cm}^2$, $\varepsilon_{\max} = 12\,\mathrm{MeV}$, $\kappa_{\mathrm{fit}} = 0.88$ and (b) data from Ref. 174: $\tau_{\mathrm{L}} = 300\,\mathrm{fs}$, $I_{\mathrm{L}} = 3.7 \cdot 10^{19}\mathrm{W/cm}^2$, $\varepsilon_{\max} = 18\,\mathrm{MeV}$, $\kappa_{\mathrm{fit}} = 2.46$. The figure is taken from Ref. 82.

We also want to point out that — beside the shape of the electron energy distribution — there could be other explanations for the discrepancy between the results of the plasma expansion model using a Maxwellian hot electron energy distribution and the experimental results at ultrashort laser pulses. A different scaling of the electron temperature as a function of the laser intensity in the ultrashort pulse regime might be a first reason. As shown in Fig. 7.14, the application of a slightly lower temperature scaling $T_{\mathrm{e},0}(I_{\mathrm{L}}\,\lambda_{\mathrm{L}}^2)$ — in comparison to the ponderomotive scaling $T_{\mathrm{e},0,\mathrm{pond}}(I_{\mathrm{L}}\,\lambda_{\mathrm{L}}^2)$, given by Eq. (7.32) — in the result of the adiabatic Maxwellian model, Eq. (5.13), could also explain the energy values observed in the ultrashort pulse regime — which were reproduced quite well by the hydrodynamic result (7.14) where we have used the ponderomotive temperature scaling. Note that a deviation of the electron temperature from the broadly used pondermotive scaling law (7.32) was supposed in Ref. 215 and observed numerically for ultrashort laser pulses in Ref. 125.

However, we also want to emphasize that this simple explanation has a weak point. From Fig. 7.14 it is obvious that the obtained alternative temperature scaling is a function of the normalized target thickness L/λ_{D}. In a more general sense, the assumption of a stationary electron distribution — which is essential for the central model (see chapter 3) and, hence, the analytic results of Sec. 7.1 applied here — may not be fulfilled in the ultrashort pulse regime. To overcome these uncertainties, further investigations of the hot electron spectra — experimentally as well as theoretically — are necessary.

Furthermore, we want to note that the comparison of the results from numerous experiments, which were carried out on different laser systems, with respect to the parameter $I_{\mathrm{L}}\,\lambda_{\mathrm{L}}^2$ (as shown in Fig. 7.9) may be over-simplifying. It is clear that — in addition to the quantity $I_{\mathrm{L}}\,\lambda_{\mathrm{L}}^2$ — numerous other parameters and their complex interplay are likely to influence the interaction and hence the maximum ion energy. It has been shown that parameters such as the laser pulse duration,[90] the focal spot size and the laser power,[216] the temporal shape of the laser beam and its prepulse intensity,[60] the target thickness,[10,60] etc., may have an impact on the ion acceleration process.

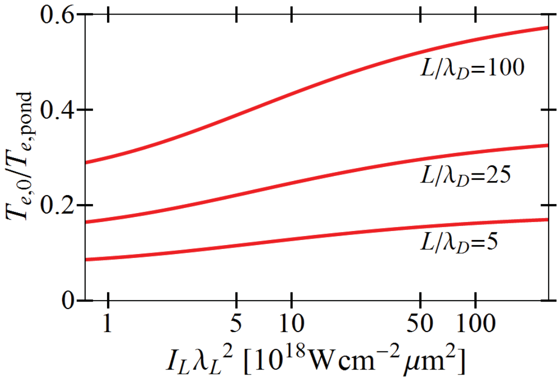

Figure 7.14.: The scaling of the electron temperature with the laser intensity, $T_{e,0}(I_L\,\lambda_L^2)$, in relation to the ponderomotive result $T_{e,0,\mathrm{pond}}(I_L\,\lambda_L^2)$, Eq. (7.32), which would lead to equal maximum ion energies in the adiabatic Maxwellian model as predicted by the hydrodynamic ansatz (7.14) using the common ponderomotive temperature scaling. The result is shown for three values of the normalized target thickness L/λ_D. The figure is taken from Ref. 82.

Also, we remind that our discussion of experimental findings and the related intensity scaling of maximum ion energies refers to laser pulse intensities below 10^{20}W/cm^2. Recently performed experiments at higher laser intensities[91] demonstrate a different intensity scaling, if we compare the observed maximum ion energies with the scaling law for the ultra-short pulse experiments collected in Fig. 7.9 after its extrapolation to higher intensity values. Moreover, the absolute numbers of the maximum ion energy observed in Ref. 91 are lower by almost one order of magnitude in comparison with the numbers predicted by the scaling relation (7.15) applied to intensities above 10^{20}W/cm^2. The established disagreement might be caused by different characteristics of the electron heating process at these high laser intensities, for example. Further efforts are needed to understand this in detail.

V. Expansion of a target with a linear density gradient

8. Connection of the Mora model to experiments and the prepulse influence

From a theoretical point of view, the Mora model, Sec. 4.2, is an approach which describes important characteristics of the plasma expansion quite well, such as the characteristic field strengths, the exponential ion energy spectrum, etc. However, from an experimentalist's point of view, one has to notice two important points: (i) The maximum energy (4.13) diverges towards infinity in the limit $t \to \infty$. Therefore, one has to cut off the acceleration process at an empirical time t_{acc} in order to obtain a finite maximum energy as observed in experiments. (ii) One has to relate the electron parameters, $n_{\mathrm{e},0}$ and $T_{\mathrm{e},0}$, which are usually difficult to measure directly (e.g. Ref. 50, 217, 218), to the parameters of common access in the experiment, such as the laser and target parameters. In Ref. 10, both problems have been addressed using simple estimates. In the following, they will be briefly discussed, since we will use them in our extended model, which is derived in Sec. 9.2. At the end of this chapter we give some examples for the interpretation of experimental findings using the Mora model in combination with those estimates.

Concerning problem (i), Fuchs et al. found empirically the acceleration time t_{acc} to be proportional to the laser pulse duration τ_{L},

$$t_{\mathrm{acc}} \approx 1.3\,\tau_{\mathrm{L}}\ , \tag{8.1a}$$

see Ref. 10. Later, in Ref. 126 they generalized this result to

$$t_{\mathrm{acc}} \approx \alpha \cdot (\tau_{\mathrm{L}} + \beta)\ , \tag{8.1b}$$

with α and β being functions of the laser intensity. However, since we are mainly interested in qualitative results we will use the finding (8.1a) throughout this discussion.

To address problem (ii), different assumptions can be used. At first, for lasers with relativistic intensities, $I_{\mathrm{L}} \geq 10^{18}\,\mathrm{W/cm^2}$, one considers the ponderomotive process as the primary electron heating mechanism. As a consequence, the hot electron temperature $T_{\mathrm{e},0}$ is connected to the laser intensity I_{L} and the laser wave length λ_{L} via the pondermotive potential,[159]

$$T_{\mathrm{e},0} \approx m_{\mathrm{e}}\,c^2 \cdot \left(\sqrt{1 + {a_0}^2} - 1\right)\ , \tag{8.2a}$$

with the *normalized amplitude of the vector potential*(1)

$$a_0 = \sqrt{\frac{I_{\mathrm{L}}\,\lambda_{\mathrm{L}}^2}{1.38 \cdot 10^{18}\,\mathrm{W/cm^2} \times \mu\mathrm{m}^2}}\ . \tag{8.2b}$$

---

(1) Sometimes one refers to a_0 also as the *relativistic amplitude*.

Secondly, the hot electron density $n_{\mathrm{e},0}$ is evaluated in two steps. (1) The total number of hot electrons N_{e} is estimated through an energy balance, $N_{\mathrm{e}} = \eta\, \varepsilon_{\mathrm{L}}/T_{\mathrm{e}}$, with ε_{L} being the energy in the laser spot and η being the conversion efficiency of that amount of energy into the thermal energy of the hot electrons. (2) The hot electron density is calculated through the assumption that the electrons spread uniformly into a volume V_{e} given by the area A_{e} of the electron spot at the rear side of the target times the distance $c\,\tau_{\mathrm{L}}$, which is the distance a highly relativistic electron can propagate as long as new electrons are generated at the front side of the target by the laser pulse. The spot size A_{e} in turn can be estimated from the radius of the laser focus at the front side, r_{L}, the target thickness L and the half-angle divergence of the electron beam, θ_{e}, via $A_{\mathrm{e}} = \pi \cdot (r_{\mathrm{L}} + \tan\theta_{\mathrm{e}} \cdot L)^2$, cf. Eq. (7.21). Finally, one obtains

$$n_{\mathrm{e},0} = \frac{\eta\, \varepsilon_{\mathrm{L}}}{\pi\, c\, \tau_{\mathrm{L}}\, T_{\mathrm{e},0} \cdot (r_{\mathrm{L}} + \tan(\theta_{\mathrm{e}}) \cdot L)^2}\,. \tag{8.3a}$$

Since the laser intensity and the laser pulse energy within the focus are connected through the relation $I_{\mathrm{L}} = \cos(\alpha_{\mathrm{in}})\, \varepsilon_{\mathrm{L}}/(\tau_{\mathrm{L}}\, \pi\, r_{\mathrm{L}}^2)$ the last equation can be rewritten as

$$n_{\mathrm{e},0} = \frac{\eta\, I_{\mathrm{L}}}{\cos(\alpha_{\mathrm{in}})\, c\, T_{\mathrm{e},0} \cdot \left(1 + \frac{L}{r_{\mathrm{L}}} \tan(\theta_{\mathrm{e}})\right)^2}\,. \tag{8.3b}$$

Here, the angle of incidence of the laser on the target is denoted by α_{in}.

Summarizing, according to Ref. 10 the parameters t_{acc}, $n_{\mathrm{e},0}$ and $T_{\mathrm{e},0}$ can be estimated from the quantities r_{L}, λ_{L}, I_{L}, τ_{L}, α_{in}, L, η and θ_{e} by the relations (8.1)–(8.3). The corresponding substitutions in Eq. (4.13) are straightforward and we write the resulting voluminous relation in the formal manner

$$\varepsilon_{\max} = 2 Z_{\mathrm{i}}\, T_{\mathrm{e},0}(\lambda_{\mathrm{L}}, I_{\mathrm{L}}) \cdot \operatorname{arcsinh}\left(\sqrt{\frac{Z_{\mathrm{i}}\, e^2\, n_{\mathrm{e},0}(r_{\mathrm{L}}, L, \lambda_{\mathrm{L}}, I_{\mathrm{L}}, \alpha_{\mathrm{in}}, \theta_{\mathrm{e}}, \eta)}{m_{\mathrm{i}}\, \varepsilon_0}}\, \frac{t_{\mathrm{acc}}(\tau_{\mathrm{L}})}{\sqrt{2\exp(1)}} \right)^2\,. \tag{8.4}$$

While the quantities r_{L}, I_{L}, λ_{L}, τ_{L}, L, α_{in} can be determined experimentally through standard techniques, this is not the case for η and θ_{e}. To address this problem, one can use estimates found by a series of experiments and numerical simulations (e.g., see Refs. 10, 219 for η and Refs. 184,186,220,221 for θ_{e}). However, the results of the different publications vary remarkably, depending on a number of experimental details. For that reason, η and θ_{e} can only be assumed with a large uncertainty, and one often determines them retrospectively by fitting the analytic results depending on these parameters to the experimental data. This approach will also be used below.

The model discussed so far is useful for the interpretation of experiments. Based on it, the scaling of the maximum ion energy with the experimental quantities can be investigated and compared to measured data (e.g. Refs. 10, 60). An example is given in Fig. 8.1, where the measured maximum proton energy for a variation of the thickness of the aluminum foil targets is plotted. In addition, relation (8.4) is shown for the given experimental parameters r_{L}, I_{L}, λ_{L}, τ_{L}, L, α_{in}. Following the discussion above, η and θ_{e} were used to fit Eq. (8.4) to the measured data. The model reproduces the experimental data quite well for relatively thick targets ($L > 5\,\mu\mathrm{m}$ and $L > 10\,\mu\mathrm{m}$ in Figs. 8.1a and 8.1b, respectively). In this region, the experimental data as well as the

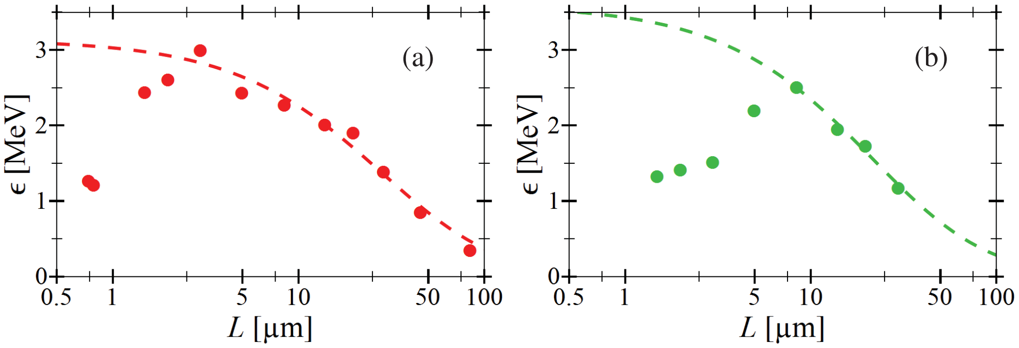

Figure 8.1.: Plot of measured data (color dots) of the maximum ion energy for various foil thicknesses. In addition, the maximum ion energy predicted by the Mora model, Eq. (8.4), is plotted (dashed lines). The quantities η (conversion efficiency) and θ_e (half-opening angle of the electron beam) were used as fit parameters. To realize these fits, only the data of foils with a thickness greater or equal the optimal value for the maximal ion energy were taken into account. The experimental data (dots) are taken from Fig. 1 in Ref. 60 and corresponds to (a) 0.7ns and (b) 2.5ns prepulse duration. The laser parameters are $I_L = 1 \times 10^{19}\mathrm{W/cm^2}$, $r_L = 2.5\mu\mathrm{m}$, $\tau_L = 150\mathrm{fs}$, $\alpha_{in} = 30°$, and $\lambda_L = 800\,\mathrm{nm}$. The ratio between the peak intensity of the laser, I_L, and the intensity of the ASE prepulse, I_{ASE} — often denoted as the LASER CONTRAST — is approximately constant throughout the experiments, $I_L/I_{ASE} = 2 \cdot 10^7$. Hence, here the ASE prepulse intensity is about $5 \cdot 10^{11}\ \mathrm{W/cm^2}$. The targets were aluminum foils. The fit parameters in (a) and (b) are $\eta = 12.4\%$, $\theta_e = 4.5°$ and $\eta = 15.6\%$, $\theta_e = 6.3°$, respectively.

theoretical scaling (8.4) show an increasing maximum ion energy with decreasing foil thickness. This relation follows from the increasing electron density in the electron sheath on the target rear side, $n_{e,0}$, with decreasing L (cf. Eq. (8.3)), which in turn leads to an increasing electric field strength $E \propto \sqrt{n_e}$ (see Eq. (7.18) and the following consideration). Furthermore, Fig. 8.1 shows that in both thickness scans there is an individual optimal thickness L_{opt} at which the maximum proton energy is maximal. On the contrary, the result of the original Mora model, Eq. (8.4), does not lead to a local maximum. Instead it predicts an optimal thickness $L_{opt} \equiv 0$. Therefore, it does not match the experimental data for $L < L_{opt}$. From numerous other publications (e.g. Refs. 10, 60, 79, 80, 124, 125, 222) it follows that experiments always reveal an optimal thickness of the target.

In the literature, there is a broad agreement that the existence of such an optimal thickness $L_{opt} > 0$ is connected to the presence of a laser prepulse and its impact on the ion acceleration process.[60, 121, 123] In order to discuss the effect of the prepulse, we start by taking a closer look at the temporal intensity profile of a laser pulse generated by the POLARIS laser system,[223] which we take as an example for a well-operating high-intensity ultra-short pulse laser. In the ideal case, the intensity of an ultra-short pulse laser as a function of time would be well described by a Gaussian profile,

$$\mathscr{I}_L(t) = I_L \exp\left(-\ln(2) \cdot \left(\frac{t}{\tau_L/2}\right)^2\right) . \tag{8.5}$$

Here, I_L refers to the maximum intensity of the laser pulse and τ_L is the laser pulse duration (FWHM). For POLARIS, one has $I_L \approx 10^{20}\,\mathrm{W/cm^2}$ and $\tau_L \approx 200\,\mathrm{fs}$. According to Eq. (8.5), a picosecond before the pulse reaches its maximum intensity one would expect the intensity to be almost zero, $\mathscr{I}_\mathrm{L}(-1\mathrm{ps}) \approx 10^{-10}\,\mathrm{W/cm^2} \approx 0$. In reality, however, this is not the case, as shown in Fig. 8.2 where a temporal scan of the intensity contrast of POLARIS as measured with a 3rd-order cross correlator is shown. The part of the laser before the main pulse where the laser has an intensity remarkably greater than the intensity in the ideal case, Eq. (8.5), is called prepulse.

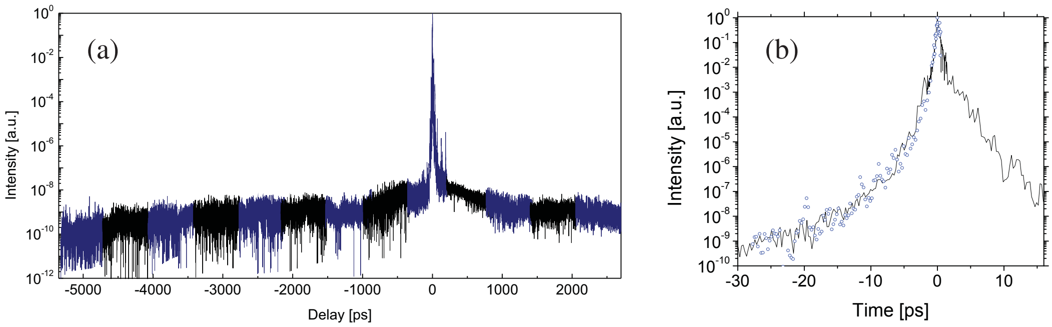

Figure 8.2.: Typical temporal laser profile of the POLARIS system. The laser intensity was measured with a time resolution of about 250 fs and is shown normalized to the laser peak intensity I_L, with $I_\mathrm{L} \approx 2 \cdot 10^{20}\,\mathrm{W/cm^2}$. The zero point on the time axis, i.e. $t = 0$, coincidences with the peak intensity, i.e. the main pulse. As exhibited in (a), in front of the main pulse the averaged intensity is slightly increasing from $\approx 10^{-10} I_\mathrm{L}$ to $\approx 10^{-8} I_\mathrm{L}$ during a time period of several nanoseconds. This broad plateau is connected to the ASE of the laser.[60,223] In addition, the plot shows that the laser intensity is rapidly fluctuating around the mean laser intensity in the ASE region. However, the peaks have typical a width of only a few picoseconds and an intensity which deviates less than 1.5 orders of magnitude in comparison to the averaged local ASE level. As shown in (b), the intensity is increasing from the ASE level up to the peak intensity in a timespan of about 20 ps to 30 ps. This rise time is greater by approximately two orders of magnitude than the duration of the main pulse, $\tau_\mathrm{L} \approx 200\,\mathrm{fs}$ (full width at half maximum). The figures are taken from Ref. 223.

From Fig. 8.2, one can distinguish between two types of prepulses. (i) As exhibited in Fig. 8.2a, there is a broad plateau with a width of several nanoseconds. This part of the laser pulse is connected to the *amplified spontaneous emission (ASE)* of the laser.[60,223] Here, the pulse has an almost constant intensity of 10^{-10}-10^{-8} relative to the peak intensity. Although that may sound small, one should keep in mind that it corresponds to absolute intensities of $10^{10} - 10^{12}\mathrm{W/cm^2}$, which are sufficient for plasma formation on the target front surface.[60,120,122,123,125,180] (ii) Eq. (8.5) predicts that the intensity of POLARIS should increase from the ASE level to the peak intensity over approximately 0.5 ps. As mentioned above, Eq. (8.5) describes an idealized model. In reality, the rise time is about 20 ps to 30 ps, as shown in Fig. 8.2b. This is due to the non-compensated, higher-order spectral phase in the laser pulses.

These contrast issues as discussed for POLARIS are typical for basically all high-intensity laser systems. In the context of laser-driven ion acceleration it was found that primarily the ASE part of the prepulse has an essential effect on the acceleration process.[60,91,120,122,123] Schematically, the underlying physical model, which is based on the studies 91, 181, 182, is the following. For a high-power laser, the ASE prepulse can already induce the formation of a plasma at the target front side. The ablation pressure of the expanding plasma launches a shock wave normally into the target. If the target thickness is small enough, or the prepulse duration is large enough, the shock wave will reach the target rear side before the main pulse starts the TNSA process. In this case the shock wave causes plastic deformations and a material blow off at the target rear side. Thus, the initially sharp-edged target-vacuum transition will be smoothed(2). Hence, the ion acceleration induced by the main pulse does not start from an undistorted step-like plasma slab as assumed in the Mora model, Sec. 4.2. Instead the initial ion distribution at the target rear side has a density gradient with a scale length $l_{\mathrm{ss}} > 0$ and, as a consequence, the final maximum energy of the ions is reduced.[119, 120, 224]

In summary, one has two counteracting processes which influence the variation of the maximum ion energy as a function of the target thickness. On the one hand, a reduction of the initial target thickness L increases the electron density in the rear-surface sheath (see Eq. (8.3)) which leads to an increase in the maximum ion energy $\varepsilon_{\mathrm{max}}$ (see Eq. (8.4)). On the other hand, if the target thickness is further reduced, the influence of the prepulse becomes more and more dominant through the increase of the plasma scale length l_{ss} on the rear side of target, which leads to smaller ion energies (according to Ref. 119). To include such prepulse effects in the analysis of the ion acceleration process, the Mora model[59] needs to be extended. This will be the topic of next chapter 9.

9. Extension of the Mora model assuming an initial density gradient

In chapter 8, we discussed the application of the Mora model[59] for the description of experimental results. In this context, it showed that the Mora model is not able to reproduce the complete experimental data obtained from a series of experiments studying the maximum proton energy as a function the initial target thickness. As stated, this is a result of the prepulse influence, which leads to a density gradient scale length $l_{\mathrm{ss}} > 0$ at the target rear side. Here, we will extend the Mora model to the case of a target with an initially linear density gradient. This chapter is structured as follows. In Sec. 9.1, we will discuss the influence of a finite initial density gradient on the plasma expansion process and we will study mathematical problems associated with that topic, especially in the context of the initial shape of the density gradient. Here, it shows that an initially linear density gradient seems to be a good choice. Afterwards, in Sec. 9.2 we will derive analytic results for the plasma expansion process assuming a target with an initially linear density gradient. Finally, in Sec. 9.3, we will apply our extended model to experimental results in order to show its potential to reproduce the complete experimental data.

---

(2) Here, we want to mention that, in addition to the reduction of the maximum ion energy, there is a second, multi-dimensional influence of the prepulse on the ion acceleration process. Since the shock wave is induced by the ablation pressure of the prepulse in the laser focus, which usually has a transverse extension smaller than that of the target front side, the transverse dimension of the shock wave is limited, too. As a consequence of the finite extension of the shock wave in the transverse target direction, the deformation of the target on its rear side is a function of the transverse position, too. Hence, the surfaces of equal densities are no longer plane and the direction of the density gradient — in other words, the local target normal direction — depends on the transverse position. Moreover, for a laser which is focused obliquely onto the target,[179–182] the most energetic electrons do not propagate through the target parallel to its normal direction. As a result, the local target normal at the point where those electrons cross the target rear side is not parallel to the initial target normal direction. As a consequence, the most energetic ions, which are accelerated parallel to the local target normal by those electrons, are deflected away from the initial target normal direction.[178, 181, 182, 207]

9.1. Influence of an initial density gradient on the ion acceleration process

We start with the specification of the profile of the initial density gradient on the target rear side. Here, numerous shapes for the gradient are conceivable and the actual form may depend on the particular experimental conditions. However, in this section we want to concentrate on two particular shapes, (i) a target with an initial exponential density gradient,

$$n_\mathrm{i}(x,t=0) = \begin{cases} n_{\mathrm{i},0} & : x \leq 0 \\ n_{\mathrm{i},0}\,\exp(-x/l_\mathrm{grad}) & : x > 0\,, \end{cases} \tag{9.1}$$

as studied by Grismayer and Mora in Ref. 119, and (ii) a target with an initial linear density gradient,

$$n_\mathrm{i}(x,t=0) = \begin{cases} n_{\mathrm{i},0} & : x \leq 0 \\ n_{\mathrm{i},0}\cdot\left(1 - x/l_\mathrm{grad}\right) & : 0 < x \leq l_\mathrm{grad} \\ 0 & : l_\mathrm{grad} < x\,. \end{cases} \tag{9.2}$$

In case of Eq. (9.1), the quantity l_grad determines the density decay length of the initial plasma. In contrast, in Eq. (9.2), l_grad refers to the absolute extent of the initial plasma gradient. Following Sec. 7.1, the scale length l_ss of an ion distribution is defined as

$$l_\mathrm{ss} = \left| n_\mathrm{i} \Big/ \frac{\partial n_\mathrm{i}}{\partial x} \right|\,. \tag{9.3}$$

In general, Eq. (9.3) is a function of x. The exponential gradient (9.1) represents a special case, since one has $l_\mathrm{ss}(x) = l_\mathrm{grad}$ for all x as one can immediately check by applying the definition (9.3) to Eq. (9.1). In contrast, for a linear gradient l_ss depends on x. However, by using the approximation $|\partial n_\mathrm{i}/\partial x| \approx \left|(n_\mathrm{i}(l_\mathrm{grad}) - n_\mathrm{i}(0))/l_\mathrm{grad}\right|$, one finds $l_\mathrm{ss}(x) \approx l_\mathrm{grad}$ for the linear gradient as well. Therefore, we rewrite Eqs. (9.1) and (9.2) in the form

$$n_\mathrm{i}(x,t=0) = \begin{cases} n_{\mathrm{i},0} & : x \leq 0 \\ n_{\mathrm{i},0}\,\exp(-x/l_\mathrm{ss}) & : x > 0\,, \end{cases} \tag{9.4}$$

and

$$n_\mathrm{i}(x,t=0) = \begin{cases} n_{\mathrm{i},0} & : x \leq 0 \\ n_{\mathrm{i},0}\cdot(1 - x/l_\mathrm{ss}) & : 0 < x \leq l_\mathrm{ss} \\ 0 & : l_\mathrm{ss} < x\,, \end{cases} \tag{9.5}$$

and we refer to the quantity l_{ss} in Eqs. (9.4) and (9.5) as the plasma scale length — despite the fact that strictly speaking this is only correct for the exponential gradient.

The qualitative impact of a plasma gradient on the plasma expansion process does not depend on its particular form: The presence of a smooth target-vacuum transition reduces the electric field strength(1) which in turn leads to smaller maximum ion energies.[119,120,224] In contrast, the mathematical modeling and the associated difficulties depend crucially on the choice of the initial density gradient. In the following, we want to explain some of these difficulties using the examples of an ion distribution with an exponential and a linear gradient, specified by Eqs. (9.4) and (9.5), respectively.

In general, at the beginning of the expansion process an initial plasma gradient not only reduces the maximum electric field strength on the target rear side but also shifts its position into the target (see Fig. 9.1). As a consequence, the relation $\partial E/\partial x > 0$ is no longer true for all positions inside the ion distribution — as it is the case for a step-like target. As a result, at some instant $t > 0$, ions from inner plasma regions may catch up and surpass ions which were initially situated in front of them. This effect is called *wave breaking*. In this case, the relation between the ion momentum p and the position x is not longer a single-valued function of the form $p(x)$. Instead there are points x where two or more values of p exist (see Fig. 9.2e, e.g.). From this, different mathematical consequences arise: (i) A global hydrodynamical modeling of the ion distribution is no longer possible. For the fact that the corresponding relations, Eqs. (3.2), assume the existence of well-defined single-valued functions for the ion density and the ion momentum. (ii) Moreover, the maximum ion velocity may be reached by different ions at different moments in time (see Fig. 9.3a). Hence, it is in general not possible to deduce the maximum ion velocity at an arbitrary instant of time by calculating the trajectory of a single ion. Instead, one has to calculate the

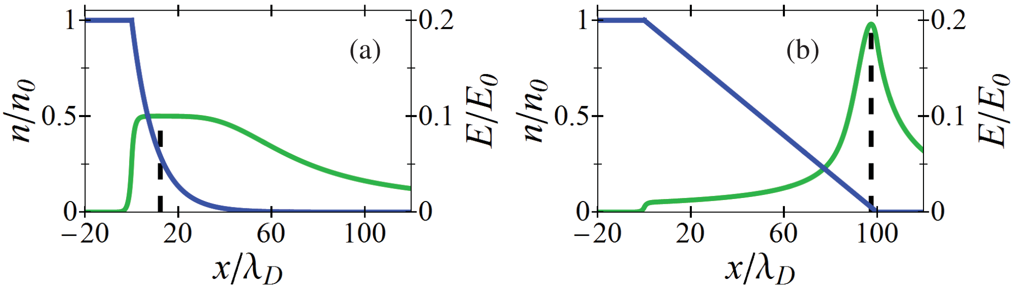

Figure 9.1.: Electric field (green curves) for ion distributions (blue curves) with an initial density gradient. While (a) corresponds to an exponential density gradient (9.4) with a scale length $l_{ss} = 10\,\lambda_D$, (b) shows the case of a linear density gradient (9.5) assuming $l_{ss} = 100\,\lambda_D$. The maxima of the electric field are marked by dashed lines. Obviously, for a linear density gradient the electric field reaches its maximum close to the boundary of the ion distribution and is decaying strictly monotonously inside the target. In contrast, for an exponential density gradient the maximum of the electric field is situated well within the ion distribution and exhibits a broad plateau.

---

(1) In case of an exponential plasma gradient with a scale length l_{ss} which is not too small, $l_{ss} \geq \lambda_D$, the initial maximum field strength is approximately given by $E_{max}(t=0) = T_{e,0}/l_{ss}$, see Ref. 119.

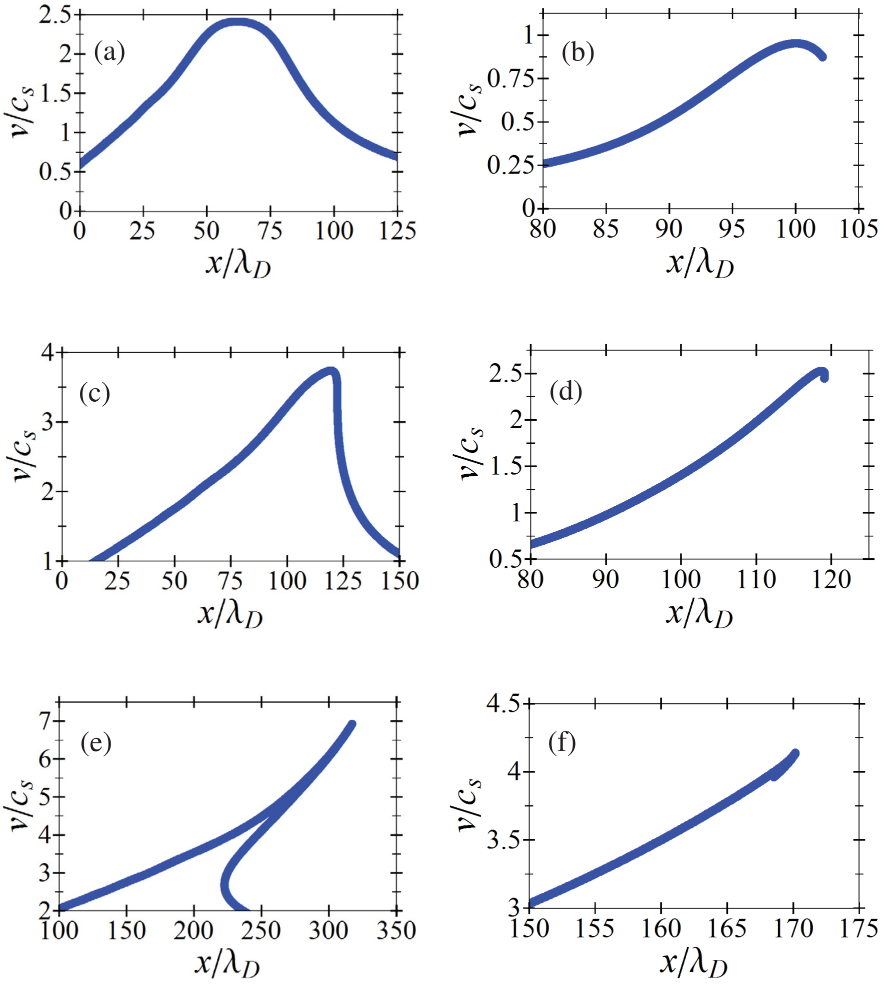

Figure 9.2.: Plot of the ion phase space for different stages of the expansion for targets with different initial density gradients. Left column: exponential density gradient (9.4) with a scale length $l_{\mathrm{ss}} = 10\lambda_{\mathrm{D}}$, right column: linear density gradient (9.5) with $l_{\mathrm{ss}} = 100\lambda_{\mathrm{D}}$. (a) and (b): before wave breaking ($\omega_{\mathrm{pi}} t = 25$ and $\omega_{\mathrm{pi}} t = 5$, resp.), (c) and (d): approximately at the time of wave breaking ($\omega_{\mathrm{pi}} t = 40$ and $\omega_{\mathrm{pi}} t = 15$, resp.) and (e) and (f): after wave breaking has occurred ($\omega_{\mathrm{pi}} t = 75$ and $\omega_{\mathrm{pi}} t = 30$, resp.). Apparently, wave breaking occurs for both gradient shapes. However, the effect is much more pronounced for the exponential gradient.

motion of numerous ions simultaneously. This is in contrast to the situation of a step-like target, where the maximum ion velocity is always determined by the ion initially situated at the target boundary, $x = 0$. (iii) In addition, wave breaking generally leads to an evolution of the electric field which is more complex than the simple, strictly monotonously deceasing field of an initially step-like target (see Fig. 9.4). This is aggravated by the fact that during the expansion of a target with an initial density gradient, one has to distinguish between several fields. The maximum electric field as a function of time, $E_{\max}(t)$, in general does not equal the field strength $E(t)$ which acts on any particular ion. Otherwise this ion would mark the fastest ion for all times,

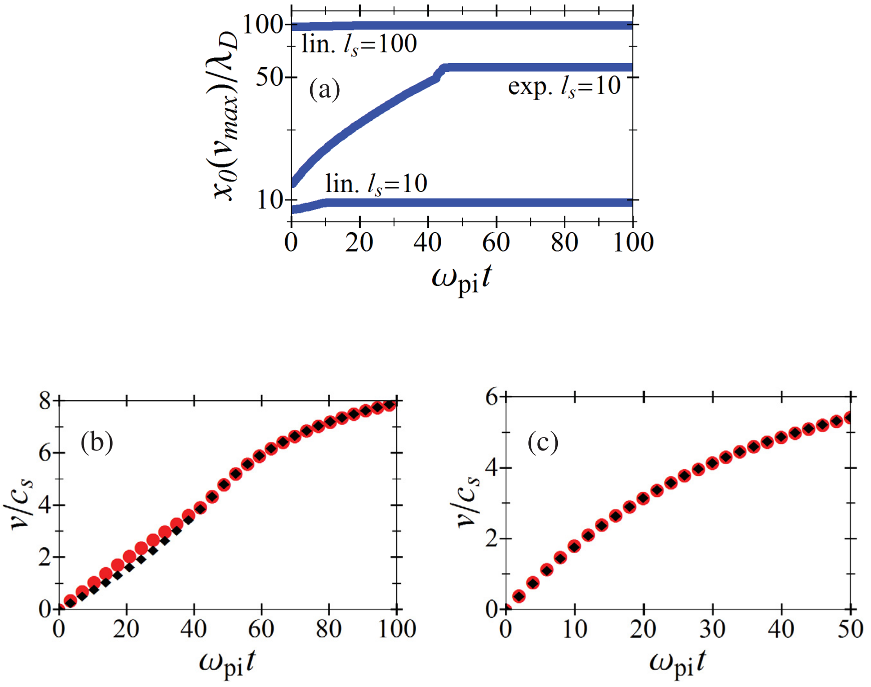

Figure 9.3.: (a): the initial position x_0 of the ions which lead to the maximum ion velocity $v_{\rm max}$ at different times. Here, three examples are shown: a target having an initially exponential gradient (9.4) with $l_{\rm ss} = 10\,\lambda_{\rm D}$, as well as the case of an initially linear gradient (9.5) with $l_{\rm ss} = 10\,\lambda_{\rm D}$ and $l_{\rm ss} = 100\,\lambda_{\rm D}$, respectively. Obviously, in all cases different ions (corresponding to different initial positions x_0) determine the maximum ion velocity at different times. However, the effect of the varying fastest ions is clearly less pronounced for the linear density gradients. This can also be seen from (b) and (c) where the maximum ion velocity (red dots) and the velocity of the asymptotically fastest ion is shown (black diamonds) for an exponential gradient ($l_{\rm ss} = 10\,\lambda_{\rm D}$) and a linear gradient ($l_{\rm ss} = 100\,\lambda_{\rm D}$). Clearly, the velocity of the asymptotically fastest ion is a good approximation for $v_{\rm max}$ at each moment in time for the case of a linear gradient, while this is not the case for the exponential gradient.

contrary to the discussion above. Hence, neither the integration of the maximum field strength $E_{\rm max}(t)$ nor the integration of the electric field $E(t)$ acting on any particular ion results in the maximum ion velocity $v_{\rm max}(t)$. Instead, the electric field strength associated with the maximum ion velocity, $E_{v_{\rm max}} = m_{\rm i}/(Z_{\rm i}\,e)\,\partial v_{\rm max}/\partial t$, is only a theoretical construct.

Despite the mentioned difficulties, it shows that the plasma expansion far beyond the point of wave breaking is well described by the self-similar solution.[1,2,51] Although in these studies one starts form an initially step-like plasma density, this condition is not necessary for the derivation of that solution. Therefore it is not that surprising that the self-similar solution also describes the expansion of a plasma with a finite initial density gradient for late times and it also seems to be natural that the finding of Mora[59] for the asymptotic electric field strength at the ion front, Eq. (4.8), also holds true. For the case of a linear gradient this is illustrated in Fig. 9.5.

To summarize, wave breaking makes it hard to specify the maximum ion velocity as a function of time. However, from the simulation results we may conclude that the shift of the maximum

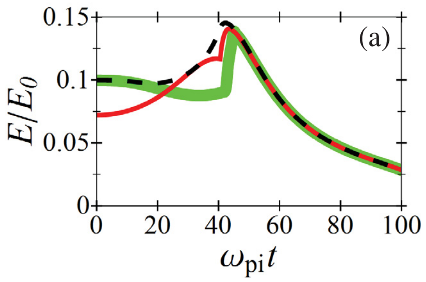

Figure 9.4.: Maximum of the electric field (dashed black curve) as a function of time for a target with an exponential (a) and a target with a linear gradient (b). In both cases $l_{ss} = 10\,\lambda_D$ was assumed. The electric field acting on the asymptotically fastest ion is depicted by solid red curves. In addition, the electric field which would lead to the observed maximum ion velocity as a function of time, $E_{v_{max}}$, is plotted (green curve). Clearly, the evolution of the fields in presence of an initial density gradient is much more complex than for an initially step-like target (cf. Fig. 4.2a). However, for a linear density gradient the shape of the functions is simpler than for those of the exponential gradient. Especially, in the case of a linear gradient the field acting on the asymptotically fastest ion is smooth and decreases monotonously.

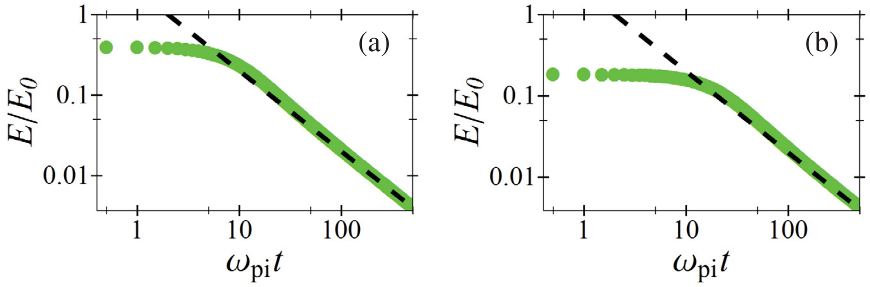

Figure 9.5.: Electric field acting on the asymptotically fastest ion (green dots) in comparison to the relation $2E_0/\omega_{pi}t$ (dashed black lines). (a) and (b) correspond to linear density gradients with $l_{ss} = 10\lambda_D$ and $l_{ss} = 100\lambda_D$, respectively.

of the electric field (see Fig. 9.1), the induced wave breaking effect (see Fig. 9.2) as well as the associated mathematical difficulties (see Figs. 9.3 and 9.4) are much more pronounced in the case of an exponential gradient than for a linear density slope. Indeed, for an initially linear density gradient, the relative difference between the velocity of the asymptotic fastest ion — the ion marking the front for $\omega_{pi}t \gg 1$, after the wave breaking occurred — and the maximum ion velocity is less than 5% for all times and all values of the scale length l_{ss}. In addition, the shape of the electric field acting on that particular ion is smooth and strictly monotonously decreasing for all times. For that reason, we will assume that the initial density gradient, induced by the prepulse, can be well approximated by a linear profile, Eq. (9.5). In addition, we evaluate the actual maximum ion velocity from the motion of the asymptotically fastest ion and we will use the term ”ion front” to refer to the ”fastest ion”, as in the case of the expansion of a step-like target, ignoring the small error one makes by this assumption at the very beginning of the expansion.

9.2. Expansion model assuming an initially linear density gradient

In this section, we consider the expansion of an ion distribution with an initially linear gradient, Eq. (9.5). For the electric field strength at the ion front we make the empirical ansatz

$$E_{\mathrm{f}}(t)=\frac{\sqrt{\frac{2}{\exp(1)}}\,\beta\,E_0}{\frac{\beta}{\alpha}-1+\sqrt{1+\beta^2\,\tau^2}}\,. \tag{9.6}$$

Here, τ is the normalized time $\omega_{\mathrm{pi}}\,t/\sqrt{2\,\exp(1)}$ and α and β are functions of the normalized initial density gradient scale length $l_{\mathrm{ss,n}}=l_{\mathrm{ss}}/\lambda_{\mathrm{D}}$ only. The empirical expression (9.6) is motivated by the following points. (i) It includes the result of Mora,[59] Eq. (4.10), for the expansion of a step-like target — corresponding to the case $l_{\mathrm{ss}}/\lambda_{\mathrm{D}}=0$ — by demanding $\alpha(l_{\mathrm{ss,n}}=0)=1$ and $\beta(l_{\mathrm{ss,n}}=0)=1$. (ii) Eq. (9.6) satisfies the asymptotic behavior $E_{\mathrm{f}}=2\,E_0/\omega_{\mathrm{pi}}\,t$ in agreement with the finding of Mora,[59] see Sec. 4.2. (iii) The expression can be integrated twice, offering analytical expressions for the maximum ion velocity,

$$\begin{aligned}v_{\mathrm{f}}(t)=2\,c_{\mathrm{s}}\cdot\Bigg\{&\operatorname{arcsinh}[\beta\,\tau]+\frac{\alpha-\beta}{\sqrt{\beta\cdot(2\,\alpha-\beta)}}\cdot\Bigg(\\&\arctan\left[\frac{\alpha\,\beta\,\tau}{\sqrt{\beta\cdot(2\,\alpha-\beta)}}\right]+\arctan\left[\frac{\alpha-\beta}{\sqrt{\beta\cdot(2\,\alpha-\beta)}}\,\frac{\beta\,\tau}{\sqrt{1+\beta^2\,\tau^2}}\right]\Bigg)\Bigg\}\,,\end{aligned} \tag{9.7}$$

and the propagation distance of the ion front,

$$\begin{aligned}\Delta x_{\mathrm{f}}(t)=x_{\mathrm{f}}(t)-x_{\mathrm{f}}(t=0)=2\,\sqrt{2\,\exp(1)}\,\lambda_{\mathrm{D}}\cdot\Bigg\{&\tau\,\operatorname{arcsinh}[\beta\,\tau]+\frac{1}{\beta}\cdot\left(1-\sqrt{1+\beta^2\,\tau^2}\right)+\\\frac{\alpha-\beta}{\sqrt{\beta\cdot(2\,\alpha-\beta)}}\,\tau\cdot\Bigg(\arctan\left[\frac{\alpha\,\beta\,\tau}{\sqrt{\beta\cdot(2\,\alpha-\beta)}}\right]&+\arctan\left[\frac{\alpha-\beta}{\sqrt{\beta\cdot(2\,\alpha-\beta)}}\,\frac{\beta\,\tau}{\sqrt{1+\beta^2\,\tau^2}}\right]\Bigg)+\\\frac{\alpha-\beta}{2\,\alpha\,\beta}\Bigg(\ln\left[\frac{\beta}{2\,\alpha-\beta+\beta\,\alpha^2\,\tau^2}\right]&+\ln\left[\frac{\alpha-\beta+\alpha\,\sqrt{1+\beta^2\,\tau^2}}{\beta-\alpha+\alpha\,\sqrt{1+\beta^2\,\tau^2}}\right]\Bigg)\Bigg\}\,.\end{aligned} \tag{9.8}$$

In addition, Eq. (9.7) directly yields the kinetic ion energy at the ion front,

$$\begin{aligned}\varepsilon_{\mathrm{f}}=2\,Z_{\mathrm{i}}\,T_{\mathrm{e,0}}\cdot\Bigg\{&\operatorname{arcsinh}[\beta\,\tau]+\frac{\alpha-\beta}{\sqrt{\beta\cdot(2\,\alpha-\beta)}}\cdot\Bigg(\\&\arctan\left[\frac{\alpha\,\beta\,\tau}{\sqrt{\beta\cdot(2\,\alpha-\beta)}}\right]+\arctan\left[\frac{\alpha-\beta}{\sqrt{\beta\cdot(2\,\alpha-\beta)}}\,\frac{\beta\,\tau}{\sqrt{1+\beta^2\,\tau^2}}\right]\Bigg)\Bigg\}^2\,.\end{aligned} \tag{9.9}$$

To determine the unknown functions α and β a series of simulations with varying value of $l_{\mathrm{ss,n}}$

have been performed. From these results, the following empirical fit functions have been found (see Fig. 9.6)

$$\alpha = \frac{1+0.122814\,l_{\mathrm{ss,n}}^{2}}{1+0.199239\,l_{\mathrm{ss,n}}-0.0113812\,l_{\mathrm{ss,n}}^{2}+0.122814\,l_{\mathrm{ss,n}}^{7/3}}$$
$$\beta = \frac{1+0.435533\,l_{\mathrm{ss,n}}}{1+1.23329\,l_{\mathrm{ss,n}}^{4/3}}\ . \tag{9.10}$$

Note that the relations have been chosen to fulfill $\alpha(l_{\mathrm{ss,n}}=0)=1$ and $\beta(l_{\mathrm{ss,n}}=0)=1$. Hence, the result of Mora[59] is included as the limit $l_{\mathrm{ss}}/\lambda_{\mathrm{D}} \to 0$. Furthermore, we want to point out that α scales with $l_{\mathrm{ss,n}}^{-1/3}$ for large values of $l_{\mathrm{ss,n}}$. Since the initial electric field strength is related to α via $E(t=0)/E_0 = \sqrt{2/\exp(1)}\,\alpha$ (see Eq. (9.6)), Eq. (9.10) implies that the electric field scales with $l_{\mathrm{ss,n}}^{-1/3}$, too.

This asymptotic behavior is also plausible due to the following considerations. The electron density almost neutralizes the ion density up to the point x_* close to the ion boundary where the local Debye length, $\lambda_{\mathrm{D,local}}(x) = \lambda_{\mathrm{D}}\sqrt{n_{\mathrm{e},0}/n_{\mathrm{e}}(x)}$, exceeds the plasma scale length, $n_{\mathrm{i}}/(\partial n_{\mathrm{i}}/\partial x)$. By comparing both expressions for the linear density gradient (9.5), one finds $x_* = l_{\mathrm{ss}} - \lambda_{\mathrm{D}} \cdot (l_{\mathrm{ss}}/\lambda_{\mathrm{D}})^{1/3}$. Form that, the local Debye length at x_* can be written as

$$\lambda_{\mathrm{D,local}}(x_*) = \lambda_{\mathrm{D}} \cdot \left(\frac{l_{\mathrm{ss}}}{\lambda_{\mathrm{D}}}\right)^{1/3}\ . \tag{9.11}$$

Moreover, for a Maxwellian electron distribution the relation leads to

$$E(x) = -\frac{T_{\mathrm{e},0}}{e}\frac{1}{n_{\mathrm{e}}}\frac{\partial n_{\mathrm{e}}}{\partial x} \tag{9.12}$$

as one can immediately prove by inserting the density relation (2.24) into Eq. (9.12). Roughly speaking, the electron density drops from $n_{\mathrm{e}}(x_*)$ to 0 with x increasing from x_* to l_{ss}, which implies $\Delta n_{\mathrm{e}} = -n_{\mathrm{e}}(x_*)$ and $\Delta x = \lambda_{\mathrm{D,local}}$. Hence, the electric field strength at $x = x_*$ scales as

$$E_{\mathrm{asym}} \approx \frac{T_{\mathrm{e},0}}{e}\frac{1}{\lambda_{\mathrm{D,local}}} = E_0 \cdot \left(\frac{l_{\mathrm{ss}}}{\lambda_{\mathrm{D}}}\right)^{-1/3}\ . \tag{9.13}$$

Since Eq. (9.13) is based on estimates, it is a qualitative result. However, comparing it with simulation data one finds that the expression

$$E_{\mathrm{asym}} = \sqrt{\frac{2}{\exp(1)}}\,E_0 \cdot \left(\frac{l_{\mathrm{ss}}}{\lambda_{\mathrm{D}}}\right)^{-1/3}\ , \tag{9.14}$$

is rather accurate (see the dashed curve in Fig. 9.6a).

Generally, the expressions (9.6)–(9.8) for the electric field strength, the velocity and the propagation distance of the ion front together with the found functions α and β, Eq. (9.10), fit the simulation findings quite well, as shown in the Figs. 9.7–9.9.

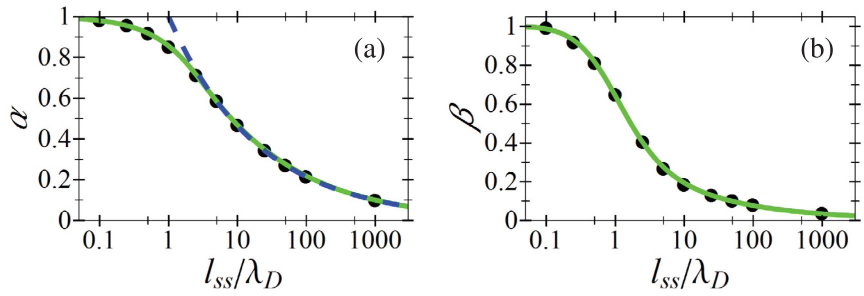

Figure 9.6.: Plot of the best-fit values for α and β (dots) gained from a series of simulations with varying density gradient scale lengths l_{ss} in comparison to the empiric fit functions (9.10) (green curves). In addition, in (a) the scaling $(l_{\mathrm{ss}}/\lambda_{\mathrm{D}})^{-1/3}$ is shown by the dashed blue curve.

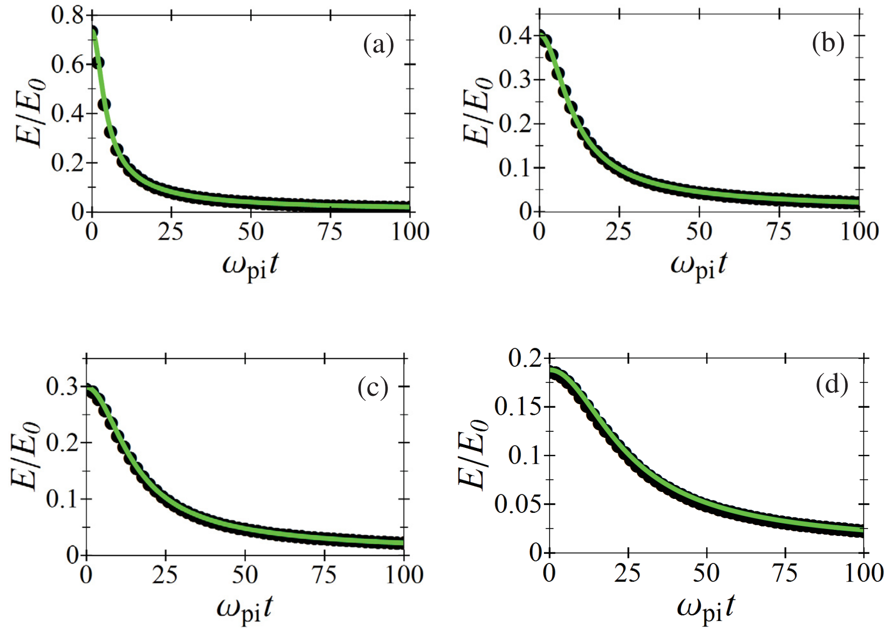

Figure 9.7.: The ansatz for the electric field, Eq. (9.6), with α and β specified by Eqs. (9.10), is shown for different values of the plasma scale length l_{ss} (green curves) in comparison to simulation results (black dots). (a)–(d) correspond to $l_{\mathrm{ss}}/\lambda_{\mathrm{D}} = \{1, 10, 25, 100\}$, respectively.

9.3. Application of the developed expansion model to experimental results

In chapter 8, we have discussed how the analytic result for the maximum ion energy derived for the case of an initially step-like ion distribution, Eq. (4.13), can be used for the description of experiments. This was achieved by connecting the theoretical quantities $n_{\mathrm{e},0}$, $T_{\mathrm{e},0}$, t_{acc} to the experimental parameters r_{L}, λ_{L}, I_{L}, τ_{L}, α_{in}, L, η and θ_{e}. To utilize the analytic result for the

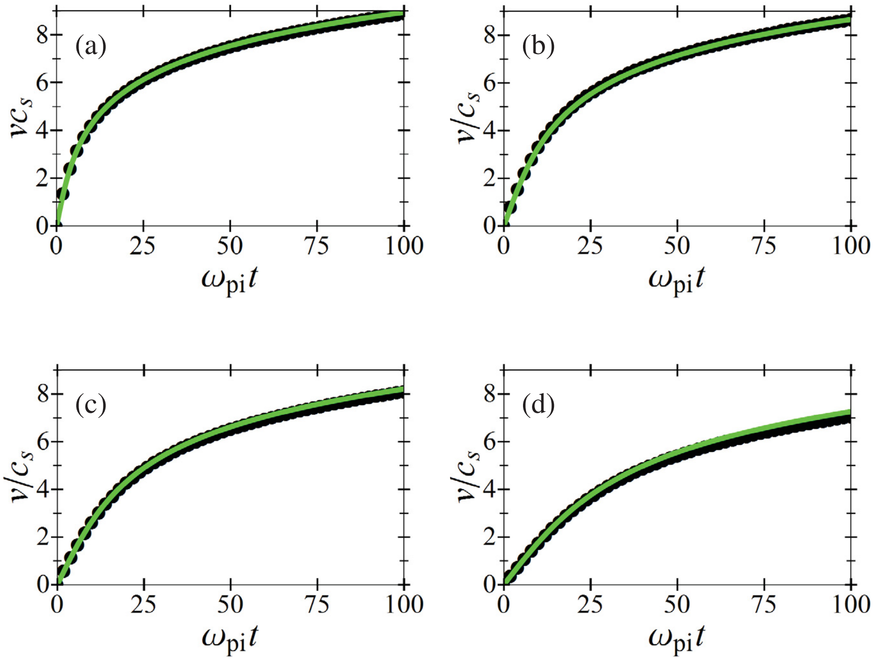

Figure 9.8.: The analytic relation (9.7) for the maximum ion velocity (green curves), with α and β specified by Eqs. (9.10), in comparison to simulation results (black dots). (a)–(d) correspond to $l_{\mathrm{ss}}/\lambda_{\mathrm{D}} = \{1, 10, 25, 100\}$, respectively.

maximum ion energy in the case of a target with an initial density gradient, Eq. (9.9), in the interpretation of experiments, one has to extend this discussion due to the presence of the additional degree of freedom l_{ss}. In the following we consider two aspects: (i) The target thickness L is replaced by the effective target thickness $L + l_{\mathrm{ss}}$. According to Eq. (8.3) this has an impact on the electron density which is now specified by

$$n_{\mathrm{e},0} = \frac{\eta \, I_{\mathrm{L}}}{\cos(\alpha_{\mathrm{in}})\, c\, T_{\mathrm{e},0} \cdot \left(1 + \frac{L + l_{\mathrm{ss}}}{r_{\mathrm{L}}} \tan(\theta_{\mathrm{e}})\right)^2} \, . \tag{9.15}$$

As a consequence, the final maximum ion energy as a function of the experimental parameters is given by

$$\begin{aligned} \varepsilon_{\max} = 2 Z_{\mathrm{i}}\, T_{\mathrm{e},0}(\lambda_{\mathrm{L}}, I_{\mathrm{L}}) \cdot \Bigg\{ & \operatorname{arcsinh}\left[\beta(l_{\mathrm{ss,n}})\, \tau_{\mathrm{acc}}\right] + \\ & \frac{\alpha(l_{\mathrm{ss,n}}) - \beta(l_{\mathrm{ss,n}})}{\sqrt{\beta(l_{\mathrm{ss,n}}) \cdot (2\,\alpha(l_{\mathrm{ss,n}}) - \beta(l_{\mathrm{ss,n}}))}} \cdot \left(\arctan\left[\frac{\alpha(l_{\mathrm{ss,n}})\, \beta(l_{\mathrm{ss,n}})\, \tau_{\mathrm{acc}}}{\sqrt{\beta(l_{\mathrm{ss,n}}) \cdot (2\,\alpha(l_{\mathrm{ss,n}}) - \beta(l_{\mathrm{ss,n}}))}}\right] + \right. \\ & \left. \arctan\left[\frac{\alpha(l_{\mathrm{ss,n}}) - \beta(l_{\mathrm{ss,n}})}{\sqrt{\beta(l_{\mathrm{ss,n}}) \cdot (2\,\alpha(l_{\mathrm{ss,n}}) - \beta(l_{\mathrm{ss,n}}))}} \, \frac{\beta(l_{\mathrm{ss,n}})\, \tau_{\mathrm{acc}}}{\sqrt{1 + \beta(l_{\mathrm{ss,n}})^2\, \tau_{\mathrm{acc}}^2}}\right] \right) \Bigg\}^2 , \end{aligned} \tag{9.16a}$$

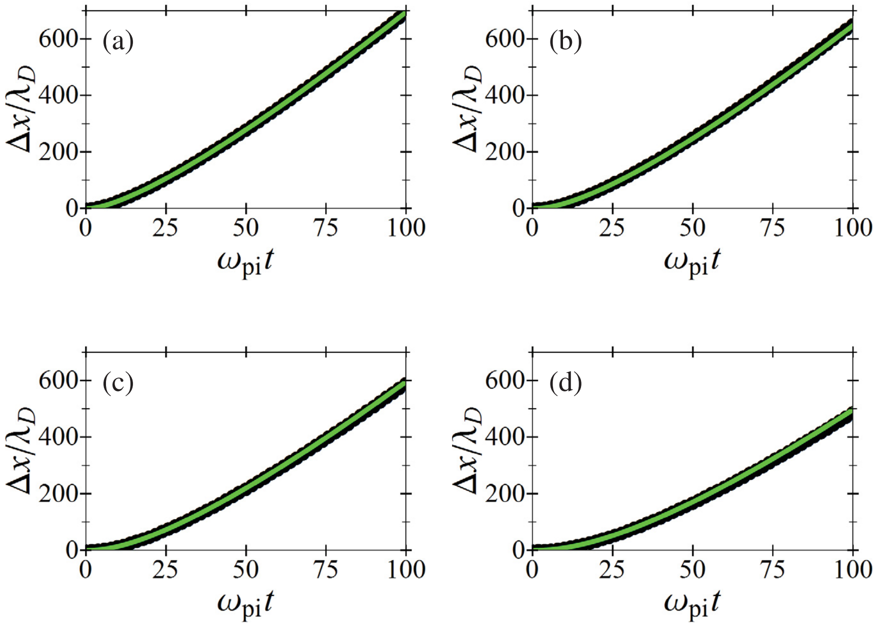

Figure 9.9.: The propagation distance $\Delta x = x(t) - x(0)$ of the ion front is shown. Here, the green curves correspond to the analytic result (9.8), with α and β specified by Eqs. (9.10), while the black dots represent the simulation results. (a)–(d) correspond to $l_{\mathrm{ss}}/\lambda_{\mathrm{D}} = \{1, 10, 25, 100\}$, respectively.

with

$$l_{\mathrm{ss,n}} = l_{\mathrm{ss}} \Big/ \sqrt{\frac{\varepsilon_0\, T_{\mathrm{e},0}(\lambda_{\mathrm{L}}, I_{\mathrm{L}})}{e^2\, n_{\mathrm{e},0}(r_{\mathrm{L}}, L, l_{\mathrm{ss}}, \lambda_{\mathrm{L}}, I_{\mathrm{L}}, \alpha_{\mathrm{in}}, \theta_{\mathrm{e}}, \eta)}} \tag{9.16b}$$

$$\tau_{\mathrm{acc}} = \sqrt{\frac{Z_{\mathrm{i}}\, e^2\, n_{\mathrm{e},0}(r_{\mathrm{L}}, L, l_{\mathrm{ss}}, \lambda_{\mathrm{L}}, I_{\mathrm{L}}, \alpha_{\mathrm{in}}, \theta_{\mathrm{e}}, \eta)}{m_{\mathrm{i}}\, \varepsilon_0}}\; \frac{t_{\mathrm{acc}}(\tau_{\mathrm{L}})}{\sqrt{2\exp(1)}} \tag{9.16c}$$

and t_{acc}, $T_{\mathrm{e},0}$, $n_{\mathrm{e},0}$, α, β being determined via Eqs. (8.1), (8.2), (9.15), (9.10), respectively. Note that Eq. (9.16) is equivalent to the result (8.4) of the Mora model.

(ii) Certainly, the size of the plasma extent l_{ss} has to be specified in some way. In this context, we remind that the plasma gradient on the rear side of the target is induced by the prepulse of the laser. Since the prepulse irradiates the front of the target, it is evident that its effective impact on the density gradient on the target rear side is influenced by the initial target thickness. Thus, in contrast to the fit parameters η and θ_{e} which are assumed to be constant numbers — for constant laser parameters — l_{ss} is a function of the initial target thickness L. Therefore, one has to make an ansatz for the dependence $l_{\mathrm{ss}}(L)$. As far as we know, there are no detailed studies concerning this relation so far. Therefore, in this section we use empirical expressions to close this gap. In principal, the relation $l_{\mathrm{ss}}(L)$ has to fulfill three conditions: (1) For $L \to 0$ the value of l_{ss} must tend towards a finite value. This condition is physically evident. (2) In the opposite limit, $L \to \infty$, we demand $l_{\mathrm{ss}} = 0$, since the influence of a realistic prepulse on the rear side of very thick targets is negligible. (3) The function $l_{\mathrm{ss}}(L)$ should decrease monotonically with increasing target thickness. This assumptions might be not correct for all cases since the actual laser-matter interaction is very complex. However, from a simplifying point of view this assumption seems quite reasonable and it is in accordance with the experimental results discussed below.

From a mathematical point of view, numerous relations $l_{\mathrm{ss}}(L)$ are conceivable. To test the principal potential of our extended model, in a first attempt we use the ansatz

$$l_{\mathrm{ss}}(L) = \xi \exp(-\sigma L) \; . \tag{9.17}$$

Here, ξ and σ are used as fit parameters. Hence, in comparison to the expression of the Mora model, (8.4) on has two additional fit parameters which empirically determine the relation between l_{ss} and L. Here, we point out that Eq. (9.17) is a purely empirical ansatz which fulfills the above conditions and has no further physical motivation. Inserting this ansatz into the expression for the final maximum ion energy (9.16) the experimental data of Ref. 60 is fitted quite well, as shown in Fig. 9.10 (see solid red and green curves labeled by ”1”).

Another ansatz for $l_{\mathrm{ss}}(L)$ is motivated by studies on the influence of the ASE prepulse[91, 181, 182] (see chapter 8 too). As discussed in these studies, the ablation pressure associated with the ASE prepulse launches a shock wave into the target which propagates at a constant velocity v_{s} parallel to the target normal direction through the unperturbed target. As soon as it reaches the target rear surface it causes a deformation of the initially plane surface with a deformation velocity v_{d}. The deformation process starts at the time t_1 when the shock-wave reaches the target rear surface and it proceeds till the time t_2 when the hot electrons associated with the main pulse arrive at the actual target rear side and induce the TNSA process(2). By setting $t = 0$ for the arrival of the main pulse at the target front side (as in Fig. 8.2), one has $t_1 = -t_{\mathrm{ASE}} + L/v_{\mathrm{s}}$, with t_{ASE} being the ASE prepulse duration, since it takes the time L/v_{s} for the shock wave to propagate through the so far unperturbed target. Moreover, it takes the time $t_2 = (L + l_{\mathrm{ss}})/c$ for the relativistic electron bunch induced by the main pulse at $t = 0$ to propagate though the target which has an increased thickness of $L + l_{\mathrm{ss}}$. Summarizing, the period of time over which the target rear side is expanding due to the ASE prepulse impact is given by

$$t_{\mathrm{d}} = t_2 - t_1 = \frac{l_{\mathrm{ss}} + L}{c} + t_{\mathrm{ASE}} - \frac{L}{v_{\mathrm{s}}} \; . \tag{9.18}$$

Since l_{ss} is approximately of the same order of magnitude as L and one has $v_{\mathrm{s}} \ll c$, one can neglect the first compared to the third term in Eq. (9.18). Thus, one has $t_{\mathrm{d}} \approx t_{\mathrm{ASE}} - L/v_{\mathrm{s}}$. As a result, the final extent of the density gradient at the target rear side, l_{ss}, reads as

$$l_{\mathrm{ss}} = v_{\mathrm{d}} t_{\mathrm{d}} = v_{\mathrm{d}} t_{\mathrm{ASE}} - \frac{v_{\mathrm{d}}}{v_{\mathrm{s}}} L \; . \tag{9.19}$$

By introducing the definitions

$$\xi = v_{\mathrm{d}} t_{\mathrm{ASE}} \tag{9.20a}$$

$$\sigma = v_{\mathrm{d}} / v_{\mathrm{s}} \tag{9.20b}$$

---

(2) Of course, the deformation of the target continues also for times $t > t_2$. However, since the deformation velocity v_{d} is typical of the order 10^3 m/s while the ion velocities associated with the TNSA plasma expansion process are approximately given by the ion acoustic velocity c_{s} which is of the order 10^7 m/s, assuming protons and MeV electrons, one can neglect the deformation process induced by the shock wave for times $t > t_2$.

(3) Remark: The experimental data of Fig. 1 in Ref 60 corresponding to an prepulse duration of 0.5ns is not included, since Eq. (9.9) cannot be fitted precisely to the data. There are too few data points for values smaller than the optimal thickness.

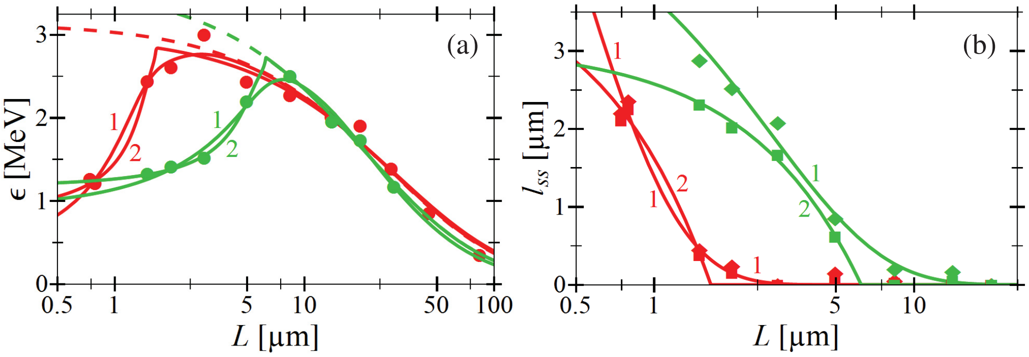

Figure 9.10.: (a) shows the same experimental data (colored dots) as Fig. 8.1. Hence, the red and green curves correspond to prepulse durations[(3)] of $t_{\text{ASE}} = 0.7\,\text{ns}$ and $t_{\text{ASE}} = 2.5\,\text{ns}$, respectively. The analytic result of Mora's model for the maximum ion energy, Eq. (8.4), is shown by dashed curves (identical to Fig. 8.1), the result of the extended model, Eq. (9.16), is depicted by solid curves. Here, curves labeled by "1" correspond to the exponential ansatz (9.17) for the relation $l_{\text{ss}}(L)$, whereas the curves labeled by "2" depict the linear ansatz (9.21). (b) shows the fit result for $l_{\text{ss}}(L)$ for both data sets and both approaches. Furthermore, the dots mark the values of l_{ss} which would exactly lead to the observed ion energies in Eq. (9.16). Here, diamonds and squares depict the exponential and the linear ansatz, respectively. Note that the values of l_{ss} are slightly different in the exponential and the linear ansatz since η and θ_{e} are slightly different in both approaches, too. The following fit parameters are used. (1) $t_{\text{ASE}} = 0.7\,\text{ns}$. Exp. ansatz: $\eta = 12.2\%$, $\theta_{\text{e}} = 4.4°$, $\xi = 12.94\,\mu\text{m}$, $\sigma = 2.24\,\mu\text{m}^{-1}$. Lin. ansatz: $\eta = 11.5\%$, $\theta_{\text{e}} = 4.1°$, $\xi = 4.10\,\mu\text{m}$, $\sigma = 2.48$. (2) $t_{\text{ASE}} = 2.5\,\text{ns}$. Exp. ansatz: $\eta = 22.2\%$, $\theta_{\text{e}} = 8.8°$, $\xi = 5.24\,\mu\text{m}$, $\sigma = 0.35\,\mu\text{m}^{-1}$. Lin. ansatz: $\eta = 15.7\%$, $\theta_{\text{e}} = 6.3°$, $\xi = 3.07\,\mu\text{m}$, $\sigma = 0.49$.

in Eq. (9.19), this motivates the linear ansatz

$$l_{\text{ss}}(L) = \begin{cases} \xi - \sigma L & : \quad \text{for } L < L_{\text{und}} = \xi/\sigma \\ 0 & : \quad \text{else}\,. \end{cases} \tag{9.21}$$

As in the exponential ansatz (9.17), ξ and σ are used as fit constants. Evidently, the expression (9.21) depicts a linear dependency between l_{ss} and L up to a maximal target thickness $L_{\text{und}} = \xi/\sigma = v_{\text{s}} t_{\text{ASE}}$. For targets with an initial thickness greater than L_{und}, Eq. (9.21) assumes that there is no laser prepulse influence on the target rear side at all ($l_{\text{ss}} = 0$) and the TNSA process starts from an ideal, undisturbed target rear surface.

As shown in Fig. 9.10 (solid red and green curves labeled by "2"), by applying the linear ansatz (9.21) in the expression for the final maximum ion energy of the extended model, Eq. (9.16), the experimental findings of Ref. 60 are quite well reproduced, too. In comparison to the results using the exponential ansatz (9.17), the curves for the linear ansatz have a noticeable salient point. Here, one has $L = L_{\text{und}}$. Hence, for values larger than L_{und} the curves correspond to the result of the Mora model, Eq. (8.4). Beside that, the results in the exponential and the linear ansatz look quite similar. This is not surprising since both relations predict similar values of the scale length for similar values of the target thickness (see Fig. 9.10b). This also illustrates that as long as the ansatz $l_{\text{ss}}(L)$ fulfills the conditions (1)–(3) discussed above, the results will be qualitatively the same. Thus, the particular ansatz is not crucial. However, since the linear ansatz (9.21) is based on a physical motivation we have used it to reproduce the further experimental findings of Ref. 60 (see Fig. 9.11).

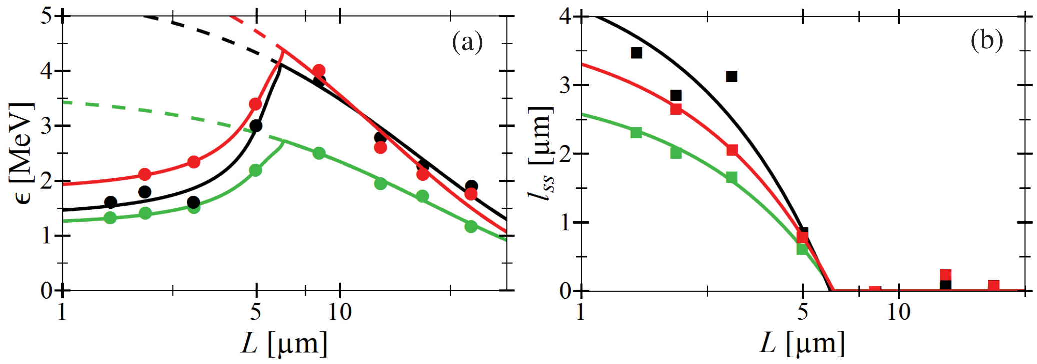

Figure 9.11.: The experimental data (colored dots) shown in (a) corresponds to Fig. 2 in Ref. 60. Here, the prepulse duration is constant (2.5ns) while the laser intensities are $I_{\mathrm{L}} = 1 \cdot 10^{19}\,\mathrm{W/cm^2}$ (green), $I_{\mathrm{L}} = 1.3 \cdot 10^{19}\,\mathrm{W/cm^2}$ (black) and $I_{\mathrm{L}} = 1.5 \cdot 10^{19}\,\mathrm{W/cm^2}$ (red). The corresponding ASE prepulse intensities are approximately $5 \cdot 10^{11}\,\mathrm{W/cm^2}$ (green), $6.5 \cdot 10^{11}\,\mathrm{W/cm^2}$ (black) and $7.5 \cdot 10^{11}\,\mathrm{W/cm^2}$ (red). The further laser parameters used are identical to Fig. 8.1. The result (9.16) of the extended model is shown (solid lines) using the linear ansatz (9.21) for $l_{\mathrm{ss}}(L)$. (b) shows the results for $l_{\mathrm{ss}}(L)$ for the three intensities. Here, the squares mark the values of l_{ss} which would exactly lead to the observed ion energies using Eq. (9.16). The following fit parameters are used. $I_{\mathrm{L}} = 1 \cdot 10^{19}\,\mathrm{W/cm^2}$: $\eta = 15.7\%$, $\theta_{\mathrm{e}} = 6.3°$, $\xi = 3.07\,\mu\mathrm{m}$, $\sigma = 0.49$. $I_{\mathrm{L}} = 1.3 \cdot 10^{19}\,\mathrm{W/cm^2}$: $\eta = 22.7\%$, $\theta_{\mathrm{e}} = 7.7°$, $\xi = 4.906\,\mu\mathrm{m}$, $\sigma = 0.805$. $I_{\mathrm{L}} = 1.5 \cdot 10^{19}\,\mathrm{W/cm^2}$: $\eta = 25.0\%$, $\theta_{\mathrm{e}} = 10.8°$, $\xi = 3.940\,\mu\mathrm{m}$, $\sigma = 0.632$.

In the last part of this section, we want to mention two essential problems which occurred during the application of the above model. (i) From the physical point of view, one would expect the scale length of the plasma on the target rear side to increase with the prepulse duration as well as with the prepulse intensity (assuming a constant initial target thickness). This physical picture is consistent with the fits in Fig. 9.10b. Here, a longer prepulse duration results in a larger values of l_{ss} (see red curves depicting the case $t_{\mathrm{ASE}} = 0.7\,\mathrm{ns}$ in comparison to the green ones corresponding to $t_{\mathrm{ASE}} = 2.5\,\mathrm{ns}$). However, by considering 9.11b one can recognize that the fit curve corresponding to the highest prepulse intensity (red), $I_{\mathrm{ASE}} \approx 7.5 \cdot 10^{11}\,\mathrm{W/cm^2}$, lies in between the curves depicting the cases $I_{\mathrm{ASE}} \approx 5 \cdot 10^{11}\,\mathrm{W/cm^2}$ (green) and $I_{\mathrm{ASE}} \approx 6.5 \cdot 10^{11}\,\mathrm{W/cm^2}$ (black). Hence, here the highest value of I_{ASE} does not correspond to the largest values of l_{ss}. To exclude the possibility that this is the result of a qualitatively bad fit — since for the mid-level prepulse intensity of $I_{\mathrm{ASE}} = 6.5 \cdot 10^{11}\,\mathrm{W/cm^2}$ (black curve) the measured data points show an unexpected local minimum around $L \approx 3\,\mu\mathrm{m}$ —- we have removed that data point in a second attempt. However, the discrepancy still remains.

(ii) Assuming the linear relation (9.21) for $l_{\mathrm{ss}}(L)$, one can retrospectively calculate the shock-wave velocity v_{s} and the deformation velocity v_{d} from the fit constants ξ and σ via the expressions (9.20). For the data shown in Fig. 9.10 one finds $v_{\mathrm{s}} = 5.9\,\mathrm{km/s}$ and $v_{\mathrm{d}} = 2.4\,\mathrm{km/s}$ for the case of a prepulse duration of 0.7 ns and $v_{\mathrm{s}} = 4.4\,\mu\mathrm{m/ns}$ and $v_{\mathrm{d}} = 9.0\,\mu\mathrm{m/ns}$ for $t_{\mathrm{ASE}} = 2.5\,\mathrm{ns}$. These values can be compared to theoretical results calculated by Lundh et al. in Ref. 182. In this study the velocities are given by

$$v_\mathrm{s} = \frac{c_0}{2} \cdot \left(\sqrt{1 + \frac{4\,\alpha_\mathrm{M}}{\rho_0\, c_0^2} P_\mathrm{abl}} + 1 \right) \tag{9.22a}$$

$$v_\mathrm{d} = \frac{c_0}{\alpha_\mathrm{M}} \cdot \left(\sqrt{1 + \frac{4\,\alpha_\mathrm{M}}{\rho_0\, c_0^2} P_\mathrm{abl}} - 1 \right) , \tag{9.22b}$$

with the ablation pressure P_abl related to the prepulse intensity I_ASE by

$$P_\mathrm{abl}\,[\mathrm{Pa}] = \zeta_\mathrm{M} \cdot \left(I_\mathrm{ASE}\,\left[\mathrm{W/m^2}\right]\right)^{2/3} . \tag{9.22c}$$

Here, c_0 and ρ_0 denote the sound velocity and the mass density of the unperturbed target material, respectively. In addition, α_M and ζ_M are material constants. For α_M one finds numbers $\approx 1 \ldots 1.7$ and ζ_M is close to 1, see Ref. 182. From the above expressions, one gets the values $v_\mathrm{s} = 7.3\,\mu\mathrm{m/ns}$ and $v_\mathrm{d} = 3.0\,\mu\mathrm{m/ns}$ for $I_\mathrm{ASE} = 5 \cdot 10^{11}\,\mathrm{W/cm^2}$ and aluminum ($\rho_0 = 2.7\,\mathrm{g/cm^3}$, $c_0 = 5.24\,\mu\mathrm{m/ns}$ and $\alpha_\mathrm{M} = 1.4$). By considering Eqs. (9.22) one can notice a first problem. Obviously, the theoretical values only depend on material constants and the prepulse intensity — but they are not influenced by t_ASE. However, v_s and v_d calculated from the fit parameters are different for both data sets plotted in Fig. 9.10, although they only differ in t_ASE but not in I_ASE. Furthermore, the theoretical values agree approximately with the values calculated from the fit parameters for $t_\mathrm{ASE} = 0.7\,\mathrm{ns}$ while there is large discrepancy in the case $t_\mathrm{ASE} = 2.5\,\mathrm{ns}$.

Since the large discrepancy occurs for the longest prepulse duration, hence, the largest prepulse impact, this might by a hint that the targets with $L \ll L_\mathrm{und}$ are strongly distorted or are even already completely destroyed by the prepulse. In this case, the initial ion distribution assumed in our extended model, Eq. (9.4) resp. Eq. (9.5) might be an oversimplified description of the real situation. In addition, the heating of the target by the laser prepulse[128, 161] has not yet been considered. Normally, the heat wave propagates with a velocity which is larger than that of the shock wave. As a result, the temperature of the target material is changed in front of the shock wave, which effects the velocity of the shock wave, v_s, and the deformation velocity v_d as well, since the density ρ_0 and sound velocity c_0 in the target material are functions of the temperature. Thereby, we expect this effect to be more pronounced in case of the long prepulse durations. Another possible explanation might be given by multi-dimensional effects. For large values of the scale length — when l_ss becomes comparable to the transverse extent of the electron spot on the target rear side — the one-dimensional approximation of the acceleration process becomes invalid (see also the discussion on multi-dimensional effects in Sec. 7.3). With respect to these issues, we think that it is necessary to investigate the prepulse influence on the ion-acceleration process in more detail — experimentally as well as numerically.

VI. Conclusion and outlook

The primary part of this thesis was concerning models for the TNSA process. These models are based on the pioneering work of Gurevich.[1] There are two degrees of freedom in this one-dimensional description of the plasma expansion at the rear surface of a laser-irradiated target: (i) the initial hot electron energy distribution and (ii) the initial spatial ion distribution. In the original work as well as in the majority of the following publications usually a Maxwellian hot electron distribution as well as a step-like target were assumed. In our studies we have investigated the impact of those assumptions on the ion acceleration process. While different aspects of models assuming Maxwellian electrons were considered in part III, the problems (i) and (ii) have been discussed in parts IV and V, respectively.

Concerning the influence of the initial hot electron energy distribution, in chapter 6 we could show that the use of the density relation in the stationary hydrodynamic approach, Eq. (6.12), for the modeling of the one-dimensional, collisionless plasma expansion implies a specific electron phase space density (6.15). In addition, it was demonstrated that the hydrodynamic approach in general leads to inaccurate results with increasing time, since the initial electron phase space density given by Eq. (6.15) evolves with time and its initial shape is not preserved. However, the choice of the adiabatic index $\kappa = 3$ in Eq. (6.12), which implies a step-like form of the hot electron phase space density, allows to maintain this distribution function over time. As a result, the choice $\kappa = 3$ offers a simple analytic expression for the electron density, which is invariant in time. Therefore, it is equivalent to a time-dependent modeling of the electrons (as long as the preconditions of Ref. 64 are suitable with sufficient accuracy). Finally, our initially nonrelativistic analysis for the step-like hot electron energy distribution has been extended to the case of relativistic electron energies, which are characteristic for TNSA. An approximate expression for the relativistic electron density was derived, which depends on the number of the degrees of freedom of the electron gas as a function of the temperature.

Concerning the step-like electron energy distribution beyond this ansatz, it is interesting to investigate how the process of the ion acceleration changes, if one considers a step-like hot electron energy distribution instead of a Maxwellian hot electron phase space density. This was the subject of chapter 7. Here, we calculated a self-similar solution for the adiabatically expanding plasma assuming a step-like electron energy distribution. It includes the well known self-similar solution[1–3] for the expansion driven by isothermal Maxwellian electrons as a limiting case. Moreover, we were able to formulate empirical expressions for the electric field strength, the velocity and the position of the ion front. In analogy, we have extended the study of Mora[62] describing the adiabatic expansion of a plasma driven by Maxwellian hot electrons.

Comparing the results of the different models, we have found that the hydrodynamic approach leads to a remarkably different evolution of the ion acceleration process in comparison with the models using Maxwellian distributions, even though approximately the same initial parameters such as temperature, density and total thermal energy of the hot electrons were assumed. Thereby, it turned out that the different shape of the hot electron energy distribution in the hydrodynamical approach leads to a rapidly dropping electron temperature at the ion front in contrast to the Maxwellian models — resulting in much lower maximum ion energies.

Furthermore, we have compared our analytical estimates to experimental results considering the maximum kinetic energy and the spectrum of the accelerated protons. Here, we obtained a surprisingly good agreement between results for the maximum ion energy estimated with the hydrodynamic model (implying a step-like hot electron energy distribution) and the data from experiments with laser pulse durations shorter than 80 fs. The predictions of our model fit to the measured ion energies in absolute numbers as well as with respect to the intensity scaling. In contrast, the plasma expansion models which are based on a Maxwellian hot electron energy distribution do not reproduce the experimentally observed intensity scaling.

Moreover, beside some exceptional examples, in the majority of the analyzed ultrashort-pulse experiments the measured spectra are more likely described by the theoretical ion spectrum linked to the hydrodynamic approach rather than by the ion spectrum associated with Maxwellian electrons. Based on these insights we may suspect that non-Maxwellian hot electron energy distributions are often involved in ultrashort-pulse experiments.

Concerning the non-Maxwellian character of the hot electron spectrum (6.15), the use of a step-like electron energy distribution at first seems to be questionable for the modeling of the plasma expansion, since numerical simulations often predict Maxwellian electrons. However, in general the assumption of preserved Maxwellian electron distributions during collisionless adiabatic cooling may become obsolete. Since groups of electrons with different energies cool down at different rates, their distribution function will change to a non-Maxwellian form in the absence of electron-electron collisions[65] (see Sec. 5.1.2). In addition, we think that another reason for the presence of non-Maxwellian hot electron energy distributions in ultrashort-pulse experiments might be that the electron heating process is too short to allow for the formation of an equilibrium energy distribution of the electrons. Therefore, we believe that the different shape of the electron phase space density leads to the observed discrepancy. Hence, we reason that it is necessary to pay more attention to the particular shape of the hot electron energy distribution in future theoretical studies and in experiments. This includes the investigation of the Maxwellian character of the energy distribution itself, e.g., in dependence on the pulse length of the driving laser beam. It comprises also the knowledge of the scaling laws for the hot electron temperature in the case of an obtainable equilibrium distribution function.

Note that ion acceleration in an expanding rarefied plasma with non-Maxwellian electrons was previously analyzed in Ref. 55. A tophat or waterbag hot electron energy distribution was supposed, for example, in the scheme of ion acceleration from laser-heated nanoclusters.[108] In contrast, the Maxwellian character of the distribution function can be kept in the case of special initial ion density profiles, as it is demonstrated in Refs. 110, 225. The dependence of the modeling results on the assumed distribution function was shown for example in Ref. 69, where the use of either Maxwellian or super-Gaussian initial electron distributions leads to considerably different ion spectra.

The influence of the initial spatial ion distribution is illustrated in part V. Here, we extended the well-known Mora model (see Sec. 4.2) to the case of a target with a finite initial ion density gradient. This modification of the initial ion distribution is motivated by experiments studying the dependency of the final maximum ion energy on the initial foil thickness (see Refs. 10, 60, 79, 80, 124, 125, 222, e.g.). It was found that the final maximum ion energy increases with decreasing foil thickness in case of sufficiently thick targets. This is in agreement with the Mora model in combination with the estimates of Fuchs[10] for the electron parameters (see chapter 8). However, the experiments also show that the final maximum energy starts to decrease, if the foil thickness is further reduced below a certain optimal value. While the Mora model, Eq. (8.4), does not reproduce this experimental result, our plasma expansion model assuming a target with an initial density gradient, Eq. (9.16), is able to describe the experimental findings. Here, a relation between the scale length of the initial density gradient and the initial foil thickness was assumed to fit the experimental data, which follows from a simple estimate of the laser prepulse interaction with the target. This relation should be confirmed in future studies with help of hydro-simulations.

Although the above model is able to explain the local maximum in the proton energy in dependence on the initial target thickness we want to mention that there are also other effects which may contributed to this dependency. As discussed by numerous studies,[179–182, 207] the prepulse can also lead to a deflection of the ion beam from the (initial) target normal direction. Since the deflection of a particular ion depends on its energy as well as on its original position on the target rear side, the resulting ion spectrum in general depends on the angle under which it has been detected. Hence, the interpretation of experimental data has to be done carefully. Finally, we want to mention the effect of *hot-electron recirculation*.[183, 226] This is an effect which depends also on the initial target thickness and may be essential even at very high laser contrast ratios, where the prepulse impact will be small. It has been proposed that for a target with a thickness smaller than $c\,\tau_L/2$ the resulting hot electron density on the target rear side is enhanced because the hot electrons may return to the laser focal region and will be accelerated in forward direction by the laser field another time. More generally, a thin target, $L \ll c\,\tau_L/2$, may lead to repeated interactions of the same part of the hot electron bunch with the laser, which may result in a modified hot electron and ion spectrum.

In summary, the present thesis has shown that not only the qualitative parameters of an experiment — such as the laser intensity and pulse duration, the target thickness, the hot electron density and temperature — but also more specific parameters — such as the prepulse characteristics and the hot electron energy distribution — may influence the ion acceleration process remarkably. In the following we want to outline some of the problems which occur in context of the central question *”How should one choose the various experimental parameters (laser/target) in order to achieve the highest ion energies in the TNSA process?”* and we want to give a short prospective.

From a physical point of view, the search for optimal experimental conditions is very challenging. For example: (i) Since an undisturbed, steep target rear side is optimal for maximum ion energies, it also becomes inevitable to realize high-power laser systems with ultra-hight laser contrast,[72, 116, 227] see chapter 8. However, since most laser-contrast enhancement techniques, such as plasma mirrors, not only lead to a reduction of the laser prepulse intensity but also to a reduced maximum laser intensity, it is necessary to consider the question how far such techniques really ensure an increasing maximum ion energy for a particular experiment. (ii) In Sec. 7.3, we saw that relatively long pulse durations lead to higher maximum ion energies in comparison to ultrashort pulse durations. However, one should keep in mind that those experiments were compared assuming constant laser intensities. In contrast, for a given laser system normally the laser pulse energy $\varepsilon_L \propto I_L\,\tau_L$ is a constant quantity and, as a consequence, the decreasing maximum ion energy due to the reduced pulse duration might be overcompensated by the increasing laser intensity. (iii) Starting from the result for the maximum ion energy of the one-dimensional Mora model, Eq. (8.4), one would expect that decreasing the focal spot size of the laser leads to an increasing maximum ion energy — as a consequence of an increasing laser intensity. However, this is a purely one-dimensional consideration. As discussed in Sec. 7.3, in reality the ion acceleration process is almost completely terminated as soon as the plasma expansion on the target rear side becomes multi-dimensional. Since this happens when the longitudinal plasma extend is approximately equal to the transverse size of the electron spot on the target rear side — which is proportional to the laser focal size, see Eq. (7.21) — these are two counteracting processes.

The points discussed above illustrate exemplary the general complexity in the optimization of the experimental conditions. However, from a mathematical point of view, the question for optimal experimental conditions could (in principal) answered rather easily. Starting with an expression f which maps from the parameter space $(I_\mathrm{L}, \varepsilon_\mathrm{L}, P_\mathrm{L}, r_\mathrm{L}, \tau_\mathrm{L}, \lambda_\mathrm{L}, L, t_\mathrm{ASE}, I_\mathrm{ASE}, \alpha_\mathrm{in}, \mathrm{etc.})$ onto the maximum ion energy ε_max, one has to find the global maximum of f under certain constraints. These constraints include basic physical relations, such as $I_\mathrm{L} = \cos(\alpha_\mathrm{in})\, \varepsilon_\mathrm{L} / \tau_\mathrm{L}\, \pi\, r_\mathrm{L}^2$, $I_\mathrm{L} = P_\mathrm{L}/\pi r_\mathrm{L}^2$, etc. as well as particular experimental conditions. The latter specify the possible range of the parameters in the particular experiment as well as further relations between the parameters, as for example(4) $I_\mathrm{ASE}/I_\mathrm{L} \approx \mathrm{const}$. Then, in order to find the highest ion energies one could use the methods of the *nonlinear optimization*.[228–230]

However, from a practical point of view there is an elementary problem: so far there is no single relation which maps from the whole parameter space onto the maximum ion energy. Up to now, in the interpretation of experiments one most often uses the result of Mora, Eq. (4.13), together with the estimates of Fuchs et al., Eqs. (8.1)–(8.3), providing the relation (8.4). In chapter 8, we saw that Eq. (8.4) is only suitable in the case of a negligible laser prepulse influence, thus for t_ASE, $I_\mathrm{ASE} \to 0$ or for $L \to \infty$. In contrast, by using the expression (9.16), which is based on the result (9.9) of our extended model and, again, the estimates of Fuchs et al., Eqs. (8.1)–(8.3), one is able to include prepulse effects. In other words, the domain on which the relation for the maximum ion energy is sufficiently accurate has been extended to the case t_ASE, $I_\mathrm{ASE} > 0$.

However, in our opinion there are a number of weak points which should be addressed in future studies. (i) The estimate of Fuchs et al. which specifies the effective acceleration time, Eq. (8.1), was found with help of a series of simulations. It works quite well for the parameters considered in these simulations. But it is an empirical fit and the data on which it is based are rare in comparison to the (infinitely) large number of possible variations of experimental conditions. Therefore, we think that is necessary to search for an alternative relation which determines the effective acceleration time in a more physical way. A possible ansatz might be the concept that the effective acceleration distance of the ions is approximately equal to the transverse size of the hot electron spot on the target rear surface (see Sec. 7.3). In order to study this problem in more detail we are planning to perform a series of multi-dimensional PIC simulations. (ii) Another source of uncertainty is the model of Fuchs et al. for the electron transport inside the target and the effective half-opening angle of the electron beam, θ_e. Since the estimate (8.3) for the hot electron density at the target rear side is based on that model, which might be oversimplifying, further investigations are necessary to remove this uncertainty. (iii) Our extended model contains an empirical relation for the initial scale length of the plasma on the target rear side, l_ss, as a function of the initial target thickness L which has been fitted to the experimental data. Hence, the unknown relation $l_\mathrm{ss}(L)$ has been determined retrospectively. In order to remedy this weak point a series of hydro-simulations will be performed in the future. Based on it, we hope to determine the actual form of $l_\mathrm{ss}(L)$ in dependence of the experimental conditions (t_ASE, I_ASE, L, target material, etc.).

---

(4) The relation $I_\mathrm{ASE}/I_\mathrm{L} \approx \mathrm{const}$ expresses the fact that for a particular experiment the prepulse intensity is normally related to the laser peak intensity via an (almost) constant contrast ratio.

If one would succeed, the domain on which the relation for the maximum ion energy is working quite well would be remarkable extended. However, we want to emphasize that afterwards it would be still not possible to optimize the experimental conditions for the whole range of possible laser and target parameters. This is due to the reason that the result (9.9) of our extended model is derived assuming Maxwellian hot electrons. However, as we saw in Sec. 7.3 ultrashort pulse experiments show evidence for the presence of non-Maxwellian hot electrons. Hence, in dependence on the laser pulse duration one would need to choose between two different expansion models. From that it is clear that a continuous scan in the parameter ”laser pulse duration” is not yet possible. With respect to this problem (iv), we think that it is necessary to investigate the properties of the generated hot electron energy distribution as a function of the laser and target parameters in more detail. Based on these results, one might be able to connect the two expansion models discussed in Secs. 4.2 and 7.1, respectively.

Afterwards one might even be able to include these results into our extended model. By solving this problem (v), our model, which assumes Maxwellian hot electrons, would also include the case of a non-Maxwellian hot electron energy distribution. Therewith, our extended model could not only be used in the interpretation of prepulse effects in experiments with relatively long pulse durations (as shown in Sec. 9.3) but also in experiments with prepulse effects in the ultrashort pulse regime (i.e. pulse durations shorter than $\approx$ 80fs). In our opinion, this would be an important step towards a single relation covering most of the experimental conditions present in numerous TNSA experiments today and, hence, would likely to be helpful for a global parameter optimization.

Bibliography

[1] Gurevich, A. V., Pariiskaya, L. V., and Pitaevskii, L. P. *Sov. Phys. JETP* **22**, 449 February (1966).

[2] Widner, M., Alexeff, I., and Jones, W. D. *Phys. Fluids* **14**, 795 (1971).

[3] Crow, J. E., Auer, P. L., and Allen, J. E. *J. Plasma Phys.* **14**, 65–76 August (1975).

[4] Wickens, L. M., Allen, J. E., and Rumsby, P. T. *Phys. Rev. Lett.* **41**(4), 243–246 (1978).

[5] Denavit, J. *Phys. Fluids* **22**, 1384 (1979).

[6] Snavely, R. A., Key, M. H., Hatchett, S. P., Cowan, T. E., Roth, M., Phillips, T. W., Stoyer, M. A., Henry, E. A., Sangster, T. C., Singh, M. S., Wilks, S. C., MacKinnon, A., Offenberger, A., Pennington, D. M., Yasuike, K., Langdon, A. B., Lasinski, B. F., Johnson, J., Perry, M. D., and Campbell, E. M. *Phys. Rev. Lett.* **85**, 2945–2948 Oct (2000).

[7] Hatchett, S. P., Brown, C. G., Cowan, T. E., Henry, E. A., Johnson, J. S., Key, M. H., Koch, J. A., Langdon, A. B., Lasinski, B. F., Lee, R. W., Mackinnon, A. J., Pennington, D. M., Perry, M. D., Phillips, T. W., Roth, M., Sangster, T. C., Singh, M. S., Snavely, R. A., Stoyer, M. A., Wilks, S. C., and Yasuike, K. *Phys. Plasmas* **7**(5), 2076–2082 (2000).

[8] Clark, E. L., Krushelnick, K., Davies, J. R., Zepf, M., Tatarakis, M., Beg, F. N., Machacek, A., Norreys, P. A., Santala, M. I. K., Watts, I., and Dangor, A. E. *Phys. Rev. Lett.* **84**, 670–673 Jan (2000).

[9] Wilks, S. C., Langdon, A. B., Cowan, T. E., Roth, M., Singh, M., Hatchett, S., Key, M. H., Pennington, D., MacKinnon, A., and Snavely, R. A. *Phys. Plasmas* **8**, 542 (2001).

[10] Fuchs, J., Antici, P., D'Humières, E., Lefebvre, E., Borghesi, M., Brambrink, E., Cecchetti, C. A., Kaluza, M., Malka, V., Manclossi, M., Meyroneinc, S., Mora, P., Schreiber, J., Toncian, T., Pépin, H., and Audebert, P. *Nature Phys.* **2**, 48–54 January (2006).

[11] Fuchs, J., Cowan, T. E., Audebert, P., Ruhl, H., Gremillet, L., Kemp, A., Allen, M., Blazevic, A., Gauthier, J.-C., Geissel, M., Hegelich, M., Karsch, S., Parks, P., Roth, M., Sentoku, Y., Stephens, R., and Campbell, E. M. *Phys. Rev. Lett.* **91**, 255002 Dec (2003).

[12] Cowan, T. E., Fuchs, J., Ruhl, H., Kemp, A., Audebert, P., Roth, M., Stephens, R., Barton, I., Blazevic, A., Brambrink, E., Cobble, J., Fernández, J., Gauthier, J.-C., Geissel, M., Hegelich, M., Kaae, J., Karsch, S., Le Sage, G. P., Letzring, S., Manclossi, M., Meyroneinc, S., Newkirk, A., Pépin, H., and Renard-LeGalloudec, N. *Phys. Rev. Lett.* **92**, 204801 May (2004).

[13] Borghesi, M., Mackinnon, A. J., Campbell, D. H., Hicks, D. G., Kar, S., Patel, P. K., Price, D., Romagnani, L., Schiavi, A., and Willi, O. *Phys. Rev. Lett.* **92**(5), 055003 (2004).

[14] Passoni, M., Tikhonchuk, V. T., Lontano, M., and Bychenkov, V. Y. *Phys. Rev. E* **69**, 026411 Feb (2004).

[15] Bulanov, S. V., Esirkepov, T. Z., Khoroshkov, V. S., Kuznetsov, A. V., and Pegoraro, F. *Phys. Lett. A* **299**(2-3), 240–247 (2002).

[16] Fourkal, E., Shahine, B., Ding, M., Li, J. S., Tajima, T., and Ma, C. M. *Med. Phys.* **29**, 2788 (2002).

[17] Ledingham, K. W. D., McKenna, P., and Singhal, R. P. *Science* **300**(5622), 1107–1111 (2003).

[18] Ledingham, K. W. D., McKenna, P., McCanny, T., Shimizu, S., Yang, J. M., Robson, L., Zweit, J., Gillies, J. M., Bailey, J., Chimon, G. N., Clarke, R. J., Neely, D., Norreys, P. A., Collier, J. L., Singhal, R. P., Wei, M. S., Mangles, S. P. D., Nilson, P., Krushelnick, K., and Zepf, M. *J. Phys. D: Appl. Phys.* **37**, 2341–2345 August (2004).

[19] Malka, V., Fritzler, S., Lefebvre, E., d'Humières, E., Ferrand, R., Grillon, G., Albaret, C., Meyroneinc, S., Chambaret, J.-P., Antonetti, A., and Hulin, D. *Med. Phys.* **31**(6), 1587–1592 (2004).

[20] Ma, C. M., Veltchev, I., Fourkal, E., Li, J. S., Luo, W., Fan, J., Lin, T., and Pollack, A. *Laser Phys.* **16**(4), 639–646 (2006).

[21] Ma, C. M., Fourkal, E., Veltchev, I., Li, J. S., Fan, J., Lin, T., and Tafo, A. In *World Congress on Medical Physics and Biomedical Engineering, September 7-12, 2009, Munich, Germany*, 66–69. Springer, (2010).

[22] Borghesi, M., Schiavi, A., Campbell, D. H., Haines, M. G., Willi, O., MacKinnon, A. J., Gizzi, L. A., Galimberti, M., Clarke, R. J., and Ruhl, H. *Plasma Phys. Controlled Fusion* **43**, A267 (2001).

[23] Borghesi, M., Campbell, D. H., Schiavi, A., Haines, M. G., Willi, O., MacKinnon, A. J., Patel, P., Gizzi, L. A., Galimberti, M., Clarke, R. J., Pegoraro, F., Ruhl, H., and Bulanov, S. *Phys. Plasmas* **9**, 2214 (2002).

[24] Cobble, J. A., Johnson, R. P., Cowan, T. E., Renard-Le Galloudec, N., and Allen, M. *J. Appl. Phys.* **92**, 1775 (2002).

[25] Romagnani, L., Borghesi, M., Cecchetti, C. A., Kar, S., Antici, P., Audebert, P., Bandhoupadjay, S., Ceccherini, F., Cowan, T., Fuchs, J., Galimberti, M., Gizzi, L. A., Grismayer, T., Heathcote, R., Jung, R., Liseykina, T. V., Macchi, A., Mora, P., Neely, D., Notley, M., Osterholtz, J., Pipahl, C. A., Pretzler, G., Schiavi, A., Schurtz, G., Toncian, T., Wilson, P. A., and Willi, O. *Laser Part. Beams* **26**(02), 241–248 (2008).

[26] Cecchetti, C. A., Borghesi, M., Fuchs, J., Schurtz, G., Kar, S., Macchi, A., Romagnani, L., Wilson, P. A., Antici, P., Jung, R., Osterholtz, J., Pipahl, C. A., Willi, O., Schiavi, A., Notley, M., and Neely, D. *Phys. Plasmas* **16**, 043102 (2009).

[27] Willingale, L., Nilson, P. M., Kaluza, M. C., Dangor, A. E., Evans, R. G., Fernandes, P., Haines, M. G., Kamperidis, C., Kingham, R. J., Ridgers, C. P., Sherlock, M., Thomas, A. G. R., Wei, M. S., Najmudin, Z., Krushelnick, K., Bandyopadhyay, S., Notley, M., Minardi, S., Tatarakis, M., and Rozmus, W. *Phys. Plasmas* **17**(4), 043104 (2010).

[28] Patel, P. K., Mackinnon, A. J., Key, M. H., Cowan, T. E., Foord, M. E., Allen, M., Price, D. F., Ruhl, H., Springer, P. T., and Stephens, R. *Phys. Rev. Lett.* **91**(12), 125004 (2003).

[29] Woolsey, N. C., Gregory, C. D., Kodama, R., Koenig, M., Loupias, B., Myers, S. A., Oya, A., and Sakawa, Y. In *Journal of Physics: Conference Series*, volume 112, 042009. IOP Publishing, (2008).

[30] Bulanov, S. V., Esirkepov, T. Z., Habs, D., Pegoraro, F., and Tajima, T. *Eur. Phys. J. D* **55**(2), 483–507 (2009).

[31] Norreys, P. A., Beg, F. N., Sentoku, Y., Silva, L. O., Smith, R. A., and Trines, R. *Phys. Plasmas* **16**, 041002 (2009).

[32] Park, H.-S., Ryutov, D. D., Ross, J. S., Kugland, N. L., Glenzer, S. H., Plechaty, C., Pollaine, S. M., Remington, B. A., Spitkovsky, A., Gargate, L., Gregori, G., Bell, A., Murphy, C., Sakawa, Y., Kuramitsu, Y., Morita, T., Takabe, H., Froula, D. H., Fiksel, G., Miniati, F., Koenig, M., Ravasio, A., Pelka, A., Liang, E., Woolsey, N., Kuranz, C. C., Drake, R. P., and Grosskopf, M. J. *High Energy Density Phys.* **8**(1), 38 – 45 (2012).

[33] Esirkepov, T. Z. and Bulanov, S. V. *Arxiv Preprint arXiv:1202.4552* (2012).

[34] Kimura, S. and Bonasera, A. *Nucl. Instrum. Methods Phys. Res. A* **637**, 164–170 (2011).

[35] Krushelnick, K., Clark, E. L., Allott, R., Beg, F. N., Danson, C. N., Machacek, A., Malka, V., Najmudin, Z., Neely, D., Norreys, P. A., Salvati, M. R., Santala, M. I. K., Tatarakis, M., Watts, I., Zepf, M., and Dangor, A. E. *IEEE Trans. Plasma Sci.* **28**(4), 1110–1155 (2000).

[36] Kodama, R., Norreys, P. A., Mima, K., Dangor, A. E., Evans, R. G., Fujita, H., Kitagawa, Y., Krushelnick, K., Miyakoshi, T., Miyanaga, N., Norimatsu, T., Rose, S. J., Shozaki, T., Shigemori, K., Sunahara, A., Tampo, M., Tanaka, K. A., Toyama, Y., Yamanaka, T., and Zepf, M. *Nature* **412**, 798–802 August (2001).

[37] Roth, M., Cowan, T. E., Key, M. H., Hatchett, S. P., Brown, C., Fountain, W., Johnson, J., Pennington, D. M., Snavely, R. A., Wilks, S. C., Yasuike, K., Ruhl, H., Pegoraro, F., Bulanov, S. V., Campbell, E. M., Perry, M. D., and Powell, H. *Phys. Rev. Lett.* **86**, 436–439 Jan (2001).

[38] Temporal, M., Honrubia, J. J., and Atzeni, S. *Phys. Plasmas* **9**, 3098 (2002).

[39] Hora, H., Badziak, J., Read, M. N., Li, Y.-T., Liang, T.-J., Cang, Y., Liu, H., Sheng, Z.-M., Zhang, J., Osman, F., Miley, G. H., Zhang, W., He, X., Peng, H., Glowacz, S., Jablonski, S., Wolowski, J., Skladanowski, Z., Jungwirth, K., Rohlena, K., and Ullschmied, J. *Phys. Plasmas* **14**(7), 072701 (2007).

[40] Naumova, N., Schlegel, T., Tikhonchuk, V. T., Labaune, C., Sokolov, I. V., and Mourou, G. *Phys. Rev. Lett.* **102**, 025002 Jan (2009).

[41] Fernandez, J. C., Albright, B. J., Bowers, K. J., Gautier, D. C., Hegelich, B. M., Huang, C.-K., Jung, D., Letzring, S., Palaniyappan, S., Shah, R., Yin, L., Wu, H.-C., and Honrubia, J. J. In *APS Meeting Abstracts*, 7003, November (2011).

[42] Tikhonchuk, V., Schlegel, T., Regan, C., Temporal, M., Feugeas, J.-L., Nicolaï, P., and Ribeyre, X. *Nucl. Fusion* **50**(4), 045003 (2010).

[43] Regan, C., Schlegel, T., Tikhonchuk, V. T., Honrubia, J. J., Feugeas, J.-L., and Nicolaï, P. *Plasma Phys. Controlled Fusion* **53**(4), 045014 (2011).

[44] Modena, A., Najmudin, Z., Dangor, A. E., Clayton, C. E., Marsh, K. A., Joshi, C., Malka, V., Darrow, C. B., Danson, C., Neely, D., and Walsh, F. N. *Nature* **377**, 606–608 October (1995).

[45] Malka, V., Fritzler, S., Lefebvre, E., Aleonard, M.-M., Burgy, F., Chambaret, J.-P., Chemin, J.-F., Krushelnick, K., Malka, G., Mangles, S. P. D., Najmudin, Z., Pittman, M., Rousseau, J.-P., Scheurer, J.-N., Walton, B., and Dangor, A. E. *Science* **298**, 1596–1600 November (2002).

[46] Bell, A. R., Davies, J. R., Guerin, S., and Ruhl, H. *Plasma Phys. Controlled Fusion* **39**(5), 653–660 (1997).

[47] Gremillet, L., Bonnaud, G., and Amiranoff, F. *Phys. Plasmas* **9**, 941 (2002).

[48] Tatarakis, M., Beg, F. N., Clark, E. L., Dangor, A. E., Edwards, R. D., Evans, R. G., Goldsack, T. J., Ledingham, K. W. D., Norreys, P. A., Sinclair, M. A., Wei, M.-S., Zepf, M., and Krushelnick, K. *Phys. Rev. Lett.* **90**, 175001 Apr (2003).

[49] Bell, A. R. and Kingham, R. J. *Phys. Rev. Lett.* **91**, 035003 Jul (2003).

[50] Jäckel, O., Polz, J., Pfotenhauer, S. M., Schlenvoigt, H. P., Schwoerer, H., and Kaluza, M. C. *New J. Phys.* **12**, 103027 (2010).

[51] Allen, J. E. and Andrews, J. G. *J. Plasma Phys.* **4**(01), 187–194 (1970).

[52] Widner, M., Alexeff, I., and Jones, W. D. *Phys. Lett. A* **32**(3), 177–178 (1970).

[53] Wickens, L. M. and Allen, J. E. *J. Plasma Phys.* **22**, 167–185 (1979).

[54] Bezzerides, B., Forslund, D. W., and Lindman, E. L. *Phys. Fluids* **21**, 2179 (1978).

[55] Gurevich, A. V., Anderson, D., and Wilhelmsson, H. *Phys. Rev. Lett.* **42**(12), 769–772 (1979).

[56] Mora, P. and Pellat, R. *Phys. Fluids* **22**, 2300–2304 December (1979).

[57] Fritzler, S., Malka, V., Grillon, G., Rousseau, J. P., Burgy, F., Lefebvre, E., d'Humieres, E., McKenna, P., and Ledingham, K. W. D. *Appl. Phys. Lett.* **83**, 3039 (2003).

[58] Kaluza, M. C. *Characterisation of Laser-Accelerated Proton Beams*. PhD thesis, Max-Planck-Institut für Quantenoptik Garching, (2004).

[59] Mora, P. *Phys. Rev. Lett.* **90**(18), 185002 May (2003).

[60] Kaluza, M., Schreiber, J., Santala, M. I. K., Tsakiris, G. D., Eidmann, K., Meyer-ter-Vehn, J., and Witte, K. J. *Phys. Rev. Lett.* **93**(4), 045003 (2004).

[61] Betti, S., Ceccherini, F., Cornolti, F., and Pegoraro, F. *Plasma Phys. Controlled Fusion* **47**, 521–529 (2005).

[62] Mora, P. *Phys. Rev. E* **72**, 056401 (2005).

[63] Thaury, C., Mora, P., Adam, J. C., and Héron, A. *Phys. Plasmas* **16**(9), 093104 September (2009).

[64] Grismayer, T., Mora, P., Adam, J. C., and Héron, A. *Phys. Rev. E* **77**, 066407 (2008).

[65] Mora, P. and Grismayer, T. *Phys. Rev. Lett.* **102**(14), 145001 April (2009).

[66] Baitin, A. V. and Kuzanyan, K. M. *J. Plasma Phys.* **59**(1), 83–90 (1998).

[67] Dorozhkina, D. S. and Semenov, V. E. *Phys. Rev. Lett.* **81**(13), 2691–2694 September (1998).

[68] Kovalev, V. F., Bychenkov, V. Y., and Tikhonchuk, V. T. *JETP Lett.* **74**(1), 10–14 July (2001).

[69] Kovalev, V. F., Bychenkov, V. Y., and Tikhonchuk, V. T. *J. Exp. Theor. Phys.* **95**(2), 226–241 (2002).

[70] Tikhonchuk, V. T., Andreev, A. A., Bochkarev, S. G., and Bychenkov, V. Y. *Plasma Phys. Controlled Fusion* **47**, B869–B877 (2005).

[71] Robinson, A. P. L., Bell, A. R., and Kingham, R. J. *Phys. Rev. Lett.* **96**(3), 035005 January (2006).

[72] Antici, P., Fuchs, J., D'Humières, E., Lefebvre, E., Borghesi, M., Brambrink, E., Cecchetti, C. A., Gaillard, S., Romagnani, L., Sentoku, Y., Toncian, T., Willi, O., Audebert, P., and Pépin, H. *Phys. Plasmas* **14**(3), 030701–030701 (2007).

[73] Robinson, A. P. L. and Gibbon, P. *Phys. Rev. E* **75**(1), 015401–+ January (2007).

[74] Henig, A., Steinke, S., Schnürer, M., Sokollik, T., Hörlein, R., Kiefer, D., Jung, D., Schreiber, J., Hegelich, B. M., Yan, X. Q., Meyer-ter Vehn, J., Tajima, T., Nickles, P. V., Sandner, W., and Habs, D. *Phys. Rev. Lett.* **103**, 245003 Dec (2009).

[75] Kar, S., Kakolee, K. F., Qiao, B., Macchi, A., Cerchez, M., Doria, D., Geissler, M., McKenna, P., Neely, D., Osterholz, J., Prasad, R., Quinn, K., Ramakrishna, B., Sarri, G., Willi, O., Yuan, X. Y., Zepf, M., and Borghesi, M. *Phys. Rev. Lett.* **109**, 185006 Nov (2012).

[76] Aurand, B., Kuschel, S., Jäckel, O., Rödel, C., Zhao, H. Y., Herzer, S., Paz, A. E., Bierbach, J., Polz, J., Elkin, B., Paulus, G. G., Karmakar, A., Gibbon, P., Kuehl, T., and Kaluza, M. C. *New J. Phys.* **15**(3), 033031 March (2013).

[77] Diaw, A. and Mora, P. *Phys. Rev. E* **84**, 036402 Sep (2011).

[78] Diaw, A. and Mora, P. *Phys. Rev. E* **86**, 026403 Aug (2012).

[79] Andreev, A. A., Lévy, A., Ceccotti, T., Thaury, C., Platonov, K. Y., Loch, R. A., and Martin, P. *Phys. Rev. Lett.* **101**(15), 155002 (2008).

[80] Andreev, A. A., Steinke, S., Sokollik, T., Schnürer, M., Ter-Avetisyan, S., Platonov, K. Y., and Nickles, P. V. *Phys. Plasmas* **16**, 013103 (2009).

[81] Kiefer, T. and Schlegel, T. *Phys. Plasmas* **19**(10), 102101 October (2012).

[82] Kiefer, T., Schlegel, T., and Kaluza, M. C. *Phys. Rev. E* **87**, 043110 Apr (2013).

[83] Pearlman, J. S. and Morse, R. L. *Phys. Rev. Lett.* **40**, 1652–1655 Jun (1978).

[84] Kishimoto, Y., Mima, K., Watanabe, T., and Nishikawa, K. *Phys. Fluids* **26**(8), 2308–2315 (1983).

[85] Lontano, M. and Passoni, M. *Phys. Plasmas* **13**, 042102 (2006).

[86] Passoni, M. and Lontano, M. *Phys. Rev. Lett.* **101**(11), 115001 (2008).

[87] Passoni, M., Bertagna, L., and Zani, A. *New J. Phys.* **12**, 045012 (2010).

[88] Bennaceur-Doumaz, D. and Djebli, M. *Phys. Plasmas* **17**, 074501 (2010).

[89] Arefiev, A. V. and Breizman, B. N. *Phys. Plasmas* **16**, 055707 (2009).

[90] Schreiber, J., Bell, F., Grüner, F., Schramm, U., Geissler, M., Schnürer, M., Ter-Avetisyan, S., Hegelich, B. M., Cobble, J., Brambrink, E., Fuchs, J., Audebert, P., and Habs, D. *Phys. Rev. Lett.* **97**, 045005 Jul (2006).

[91] Zeil, K., Kraft, S. D., Bock, S., Bussmann, M., Cowan, T. E., Kluge, T., Metzkes, J., Richter, T., Sauerbrey, R., and Schramm, U. *New J. Phys.* **12**(4), 045015 (2010).

[92] Bulanov, S. V. and Khoroshkov, V. S. *Plasma Phys. Rep.* **28**(5), 453–456 (2002).

[93] Hegelich, B. M., Albright, B. J., Cobble, J., Flippo, K., Letzring, S., Paffett, M., Ruhl, H., Schreiber, J., Schulze, R. K., and Fernandez, J. C. *Nature* **439**(7075), 441 (2006).

[94] Schwoerer, H., Pfotenhauer, S., Jäckel, O., Amthor, K.-U., Liesfeld, B., Ziegler, W., Sauerbrey, R., Ledingham, K. W. D., and Esirkepov, T. *Nature* **439**, 445–448 January (2006).

[95] Albright, B. J., Yin, L., Hegelich, B. M., Bowers, K. J., Kwan, T. J. T., and Fernández, J. C. *Phys. Rev. Lett.* **97**, 115002 Sep (2006).

[96] Brantov, A. V., Tikhonchuk, V. T., Bychenkov, V. Y., and Bochkarev, S. G. *Phys. Plasmas* **16**(4), 043107 April (2009).

[97] Esirkepov, T. Z., Bulanov, S. V., Nishihara, K., Tajima, T., Pegoraro, F., Khoroshkov, V. S., Mima, K., Daido, H., Kato, Y., Kitagawa, Y., Nagai, K., and Sakabe, S. *Phys. Rev. Lett.* **89**, 175003 Oct (2002).

[98] Bychenkov, V. Y., Novikov, N. V., Batani, D., Tikhonchuk, V. T., and Bochkarev, S. G. *Phys. Plasmas* **11**(6), 3242–3250 (2004).

[99] Bochkarev, S. G., Bychenkov, V. Y., and Tikhonchuk, V. T. *Plasma Phys. Rep.* **32**(3), 205–221 (2006).

[100] Brantov, A. V. and Bychenkov, V. Y. *Plasma Phys. Rep.* **36**(3), 256–262 (2010).

[101] Ter-Avetisyan, S., Schnürer, M., Nickles, P. V., Kalashnikov, M., Risse, E., Sokollik, T., Sandner, W., Andreev, A. A., and Tikhonchuk, V. T. *Phys. Rev. Lett.* **96**, 145006 Apr (2006).

[102] Brantov, A. V., Tikhonchuk, V. T., Klimo, O., Romanov, D. V., Ter-Avetisyan, S., Schnürer, M., Sokollik, T., and Nickles, P. V. *Phys. Plasmas* **13**(12), 122705 December (2006).

[103] Brantov, A. V. and Bychenkov, V. Y. In *Proceedings of SPIE*, volume 7993, 79931D, (2010).

[104] Pfotenhauer, S. M., Jäckel, O., Sachtleben, A., Polz, J., Ziegler, W., Schlenvoigt, H.-P., Amthor, K.-U., Kaluza, M. C., Ledingham, K. W. D., Sauerbrey, R., Gibbon, P., Robinson, A. P. L., and Schwoerer, H. *New J. Phys.* **10**(3), 033034 March (2008).

[105] Robinson, A. P. L., Gibbon, P., Pfotenhauer, S. M., Jäckel, O., and Polz, J. *Plasma Phys. Controlled Fusion* **51**(2), 024001 February (2009).

[106] Psikal, J., Limpouch, J., Kawata, S., and Andreev, A. A. *Czech. J. Phys.* **56**, 515–521 (2006).

[107] Psikal, J., Tikhonchuk, V. T., Limpouch, J., Andreev, A. A., and Brantov, A. V. *Phys. Plasmas* **15**, 053102 (2008).

[108] Breizman, B. N. and Arefiev, A. V. *Phys. Plasmas* **14**, 073105 (2007).

[109] Murakami, M., Kang, Y. G., Nishihara, K., Fujioka, S., and Nishimura, H. *Phys. Plasmas* **12**, 062706 (2005).

[110] Murakami, M. and Basko, M. M. *Phys. Plasmas* **13**, 012105 (2006).

[111] Robinson, A. P. L., Neely, D., McKenna, P., and Evans, R. G. *Plasma Phys. Controlled Fusion* **49**, 373 (2007).

[112] Bychenkov, V. Y. and Dudnikova, G. I. *Plasma Phys. Rep.* **33**(8), 655–658 (2007).

[113] Denavit, J. *Phys. Rev. Lett.* **69**, 3052–3055 Nov (1992).

[114] Esirkepov, T. Z., Borghesi, M., Bulanov, S. V., Mourou, G., and Tajima, T. *Phys. Rev. Lett.* **92**(17), 175003 (2004).

[115] Yin, L., Albright, B. J., Hegelich, B. M., Bowers, K. J., Flippo, K. A., Kwan, T. J. T., and Fernández, J. C. *Phys. Plasmas* **14**, 056706 (2007).

[116] Klimo, O., Psikal, J., Limpouch, J., and Tikhonchuk, V. T. *Phys. Rev. Spec. Top. Accel Beams* **11**, 031301 Mar (2008).

[117] Steinke, S., Henig, A., Schnürer, M., Sokollik, T., Nickles, P. V., Jung, D., Kiefer, D., Hörlein, R., Schreiber, J., Tajima, T., Yan, X. Q., Hegelich, M., Meyer-ter Vehn, J., Sandner, W., and Habs, D. *Laser Part. Beams* **28**(01), 215–221 (2010).

[118] Steinke, S., Hilz, P., Schnürer, M., Priebe, G., Bränzel, J., Abicht, F., Kiefer, D., Kreuzer, C., Ostermayr, T., Schreiber, J., Andreev, A. A., Yu, T. P., Pukhov, A., and Sandner, W. *Phys. Rev. ST Accel. Beams* **16**, 011303 Jan (2013).

[119] Grismayer, T. and Mora, P. *Phys. Plasmas* **13**, 032103 (2006).

[120] Andreev, A. A., Sonobe, R., Kawata, S., Miyazaki, S., Sakai, K., Miyauchi, K., Kikuchi, T., Platonov, K. Y., and Nemoto, K. *Plasma Phys. Controlled Fusion* **48**, 1605 (2006).

[121] Ceccotti, T., Lévy, A., Popescu, H., Réau, F., D'Oliveira, P., Monot, P., Geindre, J. P., Lefebvre, E., and Martin, P. *Phys. Rev. Lett.* **99**, 185002 Oct (2007).

[122] Fuchs, J., Cecchetti, C. A., Borghesi, M., Grismayer, T., d'Humières, E., Antici, P., Atzeni, S., Mora, P., Pipahl, A., Romagnani, L., Schiavi, A., Sentoku, Y., Toncian, T., Audebert, P., and Willi, O. *Phys. Rev. Lett.* **99**, 015002 Jul (2007).

[123] Batani, D., Jafer, R., Veltcheva, M., Dezulian, R., Lundh, O., Lindau, F., Persson, A., Osvay, K., Wahlström, C.-G., Carroll, D. C., McKenna, P., Flacco, A., and Malka, V. *New J. Phys.* **12**(4), 045018 April (2010).

[124] Spencer, I., Ledingham, K. W. D., McKenna, P., McCanny, T., Singhal, R. P., Foster, P. S., Neely, D., Langley, A. J., Divall, E. J., Hooker, C. J., Clarke, R. J., Norreys, P. A., Clark, E. L., Krushelnick, K., and Davies, J. R. *Phys. Rev. E* **67**, 046402 Apr (2003).

[125] Flacco, A., Sylla, F., Veltcheva, M., Carrié, M., Nuter, R., Lefebvre, E., Batani, D., and Malka, V. *Phys. Rev. E* **81**(3), 036405 March (2010).

[126] Fuchs, J., Sentoku, Y., D'Humières, E., Cowan, T. E., Cobble, J., Audebert, P., Kemp, A., Nikroo, A., Antici, P., Brambrink, E., Blazevic, A., Campbell, E. M., Fernández, J. C., Gauthier, J.-C., Geissel, M., Hegelich, M., Karsch, S., Popescu, H., Renard-Legalloudec, N., Roth, M., Schreiber, J., Stephens, R., and Pépin, H. *Phys. Plasmas* **14**(5), 053105 May (2007).

[127] Robinson, A. *Kinetic Simulation of Fast Electron Transport and Proton Acceleration in Ultraintense Laser-Solid Interactions*. PhD thesis, Imperial College London,, (2005).

[128] Gibbon, P. *Short Pulse Laser Interactions with Matter: An Introduction*. Imperial College Press London, (2005).

[129] Perry, M. D., Szoke, A., Landen, O. L., and Campbell, E. M. *Phys. Rev. Lett.* **60**, 1270–1273 Mar (1988).

[130] Perry, M. D., Landen, O. L., Szöke, A., and Campbell, E. M. *Phys. Rev. A* **37**, 747–760 Feb (1988).

[131] Chin, S. L., Rolland, C., Corkum, P. B., and Kelly, P. *Phys. Rev. Lett.* **61**, 153–156 Jul (1988).

[132] Freeman, R. R., Bucksbaum, P. H., Milchberg, H., Darack, S., Schumacher, D., and Geusic, M. E. *Phys. Rev. Lett.* **59**, 1092–1095 Sep (1987).

[133] Freeman, R. R. and Bucksbaum, P. H. *J. Phys. B: At., Mol. Opt. Phys.* **24**, 325–347 January (1991).

[134] Eberly, J., Javanainen, J., and Rzżewski, K. *Phys. Rep.* **204**(5), 331 – 383 (1991).

[135] Mohideen, U., Sher, M. H., Tom, H. W. K., Aumiller, G. D., Wood, O. R., Freeman, R. R., Boker, J., and Bucksbaum, P. H. *Phys. Rev. Lett.* **71**, 509–512 Jul (1993).

[136] Ammosov, M. V., Delone, N. B., and Krainov, V. P. In *1986 Quebec Symposium*, 138–141, (1986).

[137] Augst, S., Strickland, D., Meyerhofer, D. D., Chin, S. L., and Eberly, J. H. *Phys. Rev. Lett.* **63**, 2212–2215 Nov (1989).

[138] Gibson, G., Luk, T. S., and Rhodes, C. K. *Phys. Rev. A* **41**, 5049–5052 May (1990).

[139] Ammosov, M. V., Golovinsky, P. A., Kiyan, I. Y., Krainov, V. P., and Ristic, V. M. *J. Opt. Soc. Am. B* **9**, 1225–1230 August (1992).

[140] Krainov, V., Xiong, W., and Chin, S. *Laser Phys.* **2**, 467–475 (1992).

[141] Augst, S., Meyerhofer, D. D., Strickland, D., and Chint, S. L. *J. Opt. Soc. Am. B* **8**(4), 858–867 Apr (1991).

[142] Burgdörfer, J., Lerner, P., and Meyer, F. W. *Phys. Rev. A* **44**, 5674–5685 Nov (1991).

[143] Krainov, V. P. *J. Opt. Soc. Am. B* **14**(2), 425–431 Feb (1997).

[144] Wilks, S. C. and Kruer, W. L. *IEEE J. Quantum Electron.* **33**(11), 1954–1968 (1997).

[145] Kruer, W. *The Physics Of Laser Plasma Interactions*. Westview Press, January (2003).

[146] Langdon, A. B. *Phys. Rev. Lett.* **44**, 575–579 Mar (1980).

[147] Lindl, J. *Inertial Confinement Fusion: The Quest for Ignition and Energy Gain Using Indrect Drive*. American Institute of Physics, May (1998).

[148] Ginzburg, V. L. *Propagation of Electromagnetic Waves In Plasmas*. Pergamon Press, (1964).

[149] Forslund, D. W., Kindel, J. M., and Lee, K. *Phys. Rev. Lett.* **39**, 284–288 Aug (1977).

[150] Mulser, P., Kanapathipillai, M., and Hoffmann, D. H. H. *Phys. Rev. Lett.* **95**, 103401 Sep (2005).

[151] Brunel, F. *Phys. Rev. Lett.* **59**, 52–55 Jul (1987).

[152] Bonnaud, G., Gibbon, P., Kindel, J., and Williams, E. *Laser Part. Beams* **9**, 339–354 5 (1991).

[153] Gibbon, P. and Bell, A. R. *Phys. Rev. Lett.* **68**, 1535–1538 Mar (1992).

[154] Kato, S., Bhattacharyya, B., Nishiguchi, A., and Mima, K. *Phys. Fluids B - Plasma* **5**(2), 564–570 (1993).

[155] Chen, L. M., Zhang, J., Dong, Q. L., Teng, H., Liang, T. J., Zhao, L. Z., and Wei, Z. Y. *Phys. Plasmas* **8**(6), 2925–2929 (2001).

[156] Mulser, P., Weng, S. M., and Liseykina, T. *Phys. Plasmas* **19**(4), 043301 (2012).

[157] Kruer, W. L. and Estabrook, K. *Phys. Fluids* **28**(1), 430–432 (1985).

[158] Gamaliy, E. G. and Dragila, R. *Phys. Rev. A* **42**, 929–935 Jul (1990).

[159] Wilks, S. C., Kruer, W. L., Tabak, M., and Langdon, A. B. *Phys. Rev. Lett.* **69**, 1383–1386 Aug (1992).

[160] Gamaliy, E. and Tikhonchuk, V. T. *JETP Lett.* **48**, 453–455 (1988).

[161] Rozmus, W. and Tikhonchuk, V. T. *Phys. Rev. A* **42**, 7401–7412 Dec (1990).

[162] Yang, T.-Y. B., Kruer, W. L., More, R. M., and Langdon, A. B. *Phys. Plasmas* **2**(8), 3146–3154 (1995).

[163] Catto, P. J. and More, R. M. *Phys. Fluids* **20**(4), 704–705 (1977).

[164] Yang, T.-Y. B., Kruer, W. L., Langdon, A. B., and Johnston, T. W. *Phys. Plasmas* **3**(7), 2702–2709 (1996).

[165] Rastunkov, V. and Krainov, V. *Laser Phys.* **15**(2), 262–267 (2005).

[166] Sentoku, Y., Bychenkov, V. Y., Flippo, K., Maksimchuk, A., Mima, K., Mourou, G., Sheng, Z. M., and Umstadter, D. *Appl. Phys. B: Lasers Opt.* **74**(3), 207–215 (2002).

[167] Korneev, P. A., Popruzhenko, S. V., Zaretsky, D. F., and Becker, W. *Laser Phys. Lett.* **2**(9), 452–458 (2005).

[168] Macchi, A., Cornolti, F., Pegoraro, F., Liseikina, T. V., Ruhl, H., and Vshivkov, V. A. *Phys. Rev. Lett.* **87**, 205004 Oct (2001).

[169] Macchi, A., Cornolti, F., and Pegoraro, F. *Phys. Plasmas* **9**(5), 1704–1711 (2002).

[170] Kahaly, S., Yadav, S. K., Wang, W. M., Sengupta, S., Sheng, Z. M., Das, A., Kaw, P. K., and Kumar, G. R. *Phys. Rev. Lett.* **101**, 145001 Sep (2008).

[171] Umstadter, D. *J. Phys. D: Appl. Phys.* **36**, 151 April (2003).

[172] Jungreuthmayer, C., Geissler, M., Zanghellini, J., and Brabec, T. *Phys. Rev. Lett.* **92**, 133401 Mar (2004).

[173] Cowan, T., Roth, M., Johnson, J., Brown, C., Christl, M., Fountain, W., Hatchett, S., Henry, E., Hunt, A., Key, M., MacKinnon, A., Parnell, T., Pennington, D., Perry, M., Phillips, T., Sangster, T., Singh, M., Snavely, R., Stoyer, M., Takahashi, Y., Wilks, S., and Yasuike, K. *Nucl. Instrum. Methods Phys. Res. A* **455**(1), 130 – 139 (2000). <ce:title>Proceedings of the Int. Symp. on New Visions in Laser-Beam</ce:title>.

[174] Allen, M., Sentoku, Y., Audebert, P., Blazevic, A., Cowan, T., Fuchs, J., Gauthier, J. C., Geissel, M., Hegelich, M., Karsch, S., Morse, E., Patel, P. K., and Roth, M. *Phys. Plasmas* **10**, 3283 (2003).

[175] Kar, S., Markey, K., Simpson, P. T., Bellei, C., Green, J. S., Nagel, S. R., Kneip, S., Carroll, D. C., Dromey, B., Willingale, L., Clark, E. L., McKenna, P., Najmudin, Z., Krushelnick, K., Norreys, P., Clarke, R. J., Neely, D., Borghesi, M., and Zepf, M. *Phys. Rev. Lett.* **100**, 105004 Mar (2008).

[176] Hegelich, M., Karsch, S., Pretzler, G., Habs, D., Witte, K., Guenther, W., Allen, M., Blazevic, A., Fuchs, J., Gauthier, J. C., Geissel, M., Audebert, P., Cowan, T., and Roth, M. *Phys. Rev. Lett.* **89**, 085002 Aug (2002).

[177] Allen, M., Patel, P. K., Mackinnon, A., Price, D., Wilks, S., and Morse, E. *Phys. Rev. Lett.* **93**(26), 265004 (2004).

[178] Krushelnick, K., Clark, E. L., Zepf, M., Davies, J. R., Beg, F. N., Machacek, A., Santala, M. I. K., Tatarakis, M., Watts, I., Norreys, P. A., and Dangor, A. E. *Phys. Plasmas* **7**(5), 2055–2061 (2000).

[179] Santala, M. I. K., Zepf, M., Watts, I., Beg, F. N., Clark, E., Tatarakis, M., Krushelnick, K., Dangor, A. E., McCanny, T., Spencer, I., Singhal, R. P., Ledingham, K. W. D., Wilks, S. C., Machacek, A. C., Wark, J. S., Allott, R., Clarke, R. J., and Norreys, P. A. *Phys. Rev. Lett.* **84**, 1459–1462 Feb (2000).

[180] Brandl, F., Pretzler, G., Habs, D., and Fill, E. *Europhys. Lett.* **61**, 632–638 March (2003).

[181] Lindau, F., Lundh, O., Persson, A., McKenna, P., Osvay, K., Batani, D., and Wahlström, C.-G. *Phys. Rev. Lett.* **95**, 175002 Oct (2005).

[182] Lundh, O., Lindau, F., Persson, A., Wahlström, C.-G., McKenna, P., and Batani, D. *Phys. Rev. E* **76**, 026404 Aug (2007).

[183] Mackinnon, A. J., Sentoku, Y., Patel, P. K., Price, D. W., Hatchett, S., Key, M. H., Andersen, C., Snavely, R., and Freeman, R. R. *Phys. Rev. Lett.* **88**(21), 215006 (2002).

[184] Pukhov, A. *Phys. Rev. Lett.* **86**, 3562–3565 Apr (2001).

[185] Tikhonchuk, V. T. *Phys. Plasmas* **9**, 1416 (2002).

[186] Robinson, A. P. L. and Sherlock, M. *Phys. Plasmas* **14**(8), 083105 August (2007).

[187] Yogo, A., Daido, H., Bulanov, S. V., Nemoto, K., Oishi, Y., Nayuki, T., Fujii, T., Ogura, K., Orimo, S., Sagisaka, A., Ma, J.-L., Esirkepov, T. Z., Mori, M., Nishiuchi, M., Pirozhkov, A. S., Nakamura, S., Noda, A., Nagatomo, H., Kimura, T., and Tajima, T. *Phys. Rev. E* **77**, 016401 Jan (2008).

[188] Top 500 Supercomputer Sites. Online (http://www.top500.org/lists/2012/11/), November (2012). List of the 500 fastest supercomputers in the world.

[189] Spatschek, K. H. *Theoretische Plasmaphysik*. Teubner, (1990).

[190] Kegel, W. *Plasmaphysik*. Springer Verlag, (1998).

[191] Bittencourt, J. *Fundamentals of Plasma Physics*. Springer, (2004).

[192] Cubero, D., Casado-Pascual, J., Dunkel, J., Talkner, P., and Hänggi, P. *Phys. Rev. Lett.* **99**(17), 170601 (2007).

[193] Chen, F. *Introduction to Plasma Physics and Controlled Fusion: Plasma Physics*, volume 1. Springer, (1984).

[194] Landau, L. D. and Lifschitz, E. M. *Lehrbuch der theoretischen Physik, 10 Bde., Bd.1, Mechanik*. Deutsch (Harri), 14. a. edition, December (1997).

[195] Mora, P. *Phys. Plasmas* **12**, 112102 (2005).

[196] Sack, C. and Schamel, H. *Phys. Rep.* **156**(6), 311–395 (1987).

[197] Andreev, A. A., Ceccotti, T., Levy, A., Platonov, K. Y., and Martin, P. *New J. Phys.* **12**(4), 045007 April (2010).

[198] Oishi, Y., Nayuki, T., Fujii, T., Takizawa, Y., Wang, X., Yamazaki, T., Nemoto, K., Kayoiji, T., Sekiya, T., Horioka, K., Okano, Y., Hironaka, Y., Nakamura, K. G., Kondo, K., and Andreev, A. A. *Phys. Plasmas* **12**, 073102 (2005).

[199] Robson, L., Simpson, P. T., Clarke, R. J., Ledingham, K. W. D., Lindau, F., Lundh, O., McCanny, T., Mora, P., Neely, D., Wahlström, C.-G., Zepf, M., and McKenna, P. *Nature Phys.* **3**, 58–62 January (2007).

[200] Clark, E. L., Krushelnick, K., Zepf, M., Beg, F. N., Tatarakis, M., Machacek, A., Santala, M. I. K., Watts, I., Norreys, P. A., and Dangor, A. E. *Phys. Rev. Lett.* **85**, 1654–1657 Aug (2000).

[201] Fuchs, J., Audebert, P., Borghesi, M., Pépin, H., and Willi, O. *C. R. Phys.* **10**(2-3), 176–187 (2009).

[202] Fujii, T., Oishi, Y., Nayuki, T., Takizawa, Y., Nemoto, K., Kayoiji, T., Horioka, K., Okano, Y., Hironaka, Y., Nakamura, K. G., and Kondo, K.-I. *Appl. Phys. Lett.* **83**(8), 1524–1526 (2003).

[203] McKenna, P., Ledingham, K. W. D., Yang, J. M., Robson, L., McCanny, T., Shimizu, S., Clarke, R. J., Neely, D., Spohr, K., Chapman, R., Singhal, R. P., Krushelnick, K., Wei, M. S., and Norreys, P. A. *Phys. Rev. E* **70**, 036405 Sep (2004).

[204] Nishiuchi, M., Fukumi, A., Daido, H., Li, Z., Sagisaka, A., Ogura, K., Orimo, S., Kado, M., Hayashi, Y., Mori, M., Bulanov, S. V., Esirkepov, T., Nemoto, K., Oishi, Y., Nayuki, T., Fujii, T., Noda, A., Iwashita, Y., Shirai, T., and Nakamura, S. *Phys. Lett. A* **357**(4), 339–344 (2006).

[205] Nishiuchi, M., Daido, H., Yogo, A., Orimo, S., Ogura, K., Ma, J., Sagisaka, A., Mori, M., Pirozhkov, A. S., Kiriyama, H., Bulanov, S. V., Esirkepov, T. Z., Choi, I. W., Kim, C. M., Jeong, T. M., Yu, T. J., Sung, J. H., Lee, S. K., Hafz, N., Pae, K. H., Noh, Y.-C., Ko, D.-K., Lee, J., Oishi, Y., Nemoto, K., Nagatomo, H., Nagai, K., and Azuma, H. *Phys. Plasmas* **15**(5), 053104–053104 (2008).

[206] Borghesi, M., Toncian, T., Fuchs, J., Cecchetti, C. A., Romagnani, L., Kar, S., Quinn, K., Ramakrishna, B., Wilson, P. A., Antici, P., Audebert, P., Brambrink, E., Pipahl, A., Jung, R., Amin, M., Willi, O., Clarke, R. J., Notley, M., Mora, P., Grismayer, T., D'Humières, E., and Sentoku, Y. *Eur. Phys. J. Spec. Top.* **175**, 105–110 August (2009).

[207] Zepf, M., Clark, E. L., Krushelnick, K., Beg, F. N., Escoda, C., Dangor, A. E., Santala, M. I. K., Tatarakis, M., Watts, I. F., Norreys, P. A., Clarke, R. J., Davies, J. R., Sinclair, M. A., Edwards, R. D., Goldsack, T. J., Spencer, I., and Ledingham, K. W. D. *Phys. Plasmas* **8**, 2323 (2001).

[208] Murakami, Y., Kitagawa, Y., Sentoku, Y., Mori, M., Kodama, R., Tanaka, K., Mima, K., and Yamanaka, T. *Phys. Plasmas* **8**, 4138 (2001).

[209] Maksimchuk, A., Flippo, K., Krause, H., Mourou, G. A., Nemoto, K., Shultz, D., Umstadter, D., Vane, R., Bychenkov, V. Y., Dudnikova, G. I., Kovalev, V. F., Mima, K., Novikov, V. N., Sentoku, Y., and Tolokonnikov, S. V. *Plasma Phys. Rep.* **30**(6), 473–495 (2004).

[210] Beg, F. N., Bell, A. R., Dangor, A. E., Danson, C. N., Fews, A. P., Glinsky, M. E., Hammel, B. A., Lee, P., Norreys, P. A., and Tatarakis, M. *Phys. Plasmas* **4**(2), 447–457 (1997).

[211] Tampo, M., Awano, S., Bolton, P. R., Kondo, K., Mima, K., Mori, Y., Nakamura, H., Nakatsutsumi, M., Stephens, R. B., Tanaka, K. A., Tanimoto, T., Yabuuchi, T., and Kodama, R. *Phys. Plasmas* **17**(7), 073110 (2010).

[212] Prasad, R., Ter-Avetisyan, S., Doria, D., Quinn, K. E., Romagnani, L., Foster, P. S., Brenner, C. M., Green, J. S., Gallegos, P., Streeter, M. J. V., Carroll, D. C., Tresca, O., Dover, N. P., Palmer, C. A. J., Schreiber, J., Neely, D., Najmudin, Z., McKenna, P., Zepf, M., and Borghesi, M. *Nucl. Instrum. Methods Phys. Res. A* **653**, 113–115 October (2011).

[213] Zhidkov, A. G., Sasaki, A., Fukumoto, I., Tajima, T., Auguste, T., D'Oliveira, P., Hulin, S., Monot, P., Faenov, A. Y., Pikuz, T. A., and Skobelev, I. Y. *Phys. Plasmas* **8**, 3718–3723 August (2001).

[214] Quinn, K., Wilson, P. A., Cecchetti, C. A., Ramakrishna, B., Romagnani, L., Sarri, G., Lancia, L., Fuchs, J., Pipahl, A., Toncian, T., Willi, O., Clarke, R. J., Neely, D., Notley, M., Gallegos, P., Carroll, D. C., Quinn, M. N., Yuan, X. H., McKenna, P., Liseykina, T. V., Macchi, A., and Borghesi, M. *Phys. Rev. Lett.* **102**, 194801 May (2009).

[215] Dudnikova, G. I., Bychenkov, V. Y., Maksimchuk, A., Mourou, G., Nees, J., Bochkarev, S. G., and Vshivkov, V. A. *Phys. Rev. E* **67**, 026416 Feb (2003).

[216] Jäckel, O. *Characterization of ion acceleration with relativistic laser-plasma*. PhD thesis, Physikalisch-Astronomische Fakultät Friedrich-Schiller-Universität Jena, (2009).

[217] Antici, P., Fuchs, J., Borghesi, M., Gremillet, L., Grismayer, T., Sentoku, Y., d'Humières, E., Cecchetti, C. A., Mančić, A., Pipahl, A. C., Toncian, T., Willi, O., Mora, P., and Audebert, P. *Phys. Rev. Lett.* **101**, 105004 Sep (2008).

[218] Antici, P., Albertazzi, B., Audebert, P., Buffechoux, S., Hannachi, F., d'Humières, E., Gobet, F., Grismayer, T., Mancic, A., Nakatsutsumi, M., Plaisir, C., Romagnani, L., Tarisien, M., Pépin, H., Sentoku, Y., and Fuchs, J. *New J. Phys.* **14**(6), 063023 June (2012).

[219] Yu, J., Jiang, Z., Kieffer, J. C., and Krol, A. *Phys. Plasmas* **6**, 1318–1322 April (1999).

[220] Stephens, R. B., Snavely, R. A., Aglitskiy, Y., Amiranoff, F., Andersen, C., Batani, D., Baton, S. D., Cowan, T., Freeman, R. R., Hall, T., Hatchett, S. P., Hill, J. M., Key, M. H., King, J. A., Koch, J. A., Koenig, M., MacKinnon, A. J., Lancaster, K. L., Martinolli, E., Norreys, P., Perelli-Cippo, E., Rabec Le Gloahec, M., Rousseaux, C., Santos, J. J., and Scianitti, F. *Phys. Rev. E* **69**, 066414 Jun (2004).

[221] Lancaster, K. L., Green, J. S., Hey, D. S., Akli, K. U., Davies, J. R., Clarke, R. J., Freeman, R. R., Habara, H., Key, M. H., Kodama, R., Krushelnick, K., Murphy, C. D., Nakatsutsumi, M., Simpson, P., Stephens, R., Stoeckl, C., Yabuuchi, T., Zepf, M., and Norreys, P. A. *Phys. Rev. Lett.* **98**, 125002 Mar (2007).

[222] Badziak, J., Woryna, E., Parys, P., Platonov, K. Y., Jabłoński, S., Ryć, L., Vankov, A. B., and Wołowski, J. *Phys. Rev. Lett.* **87**, 215001 Nov (2001).

[223] Hornung, M., Keppler, S., Bödefeld, R., Kessler, A., Liebetrau, H., Körner, J., Hellwing, M., Schorcht, F., Jäckel, O., Sävert, A., Polz, J., Arunachalam, A. K., Hein, J., and Kaluza, M. C. *Opt. Lett.* **38**(5), 718–720 Mar (2013).

[224] Mackinnon, A. J., Borghesi, M., Hatchett, S., Key, M. H., Patel, P. K., Campbell, H., Schiavi, A., Snavely, R., Wilks, S. C., and Willi, O. *Phys. Rev. Lett.* **86**, 1769–1772 Feb (2001).

[225] Kovalev, V. F. and Bychenkov, V. Y. *Phys. Rev. Lett.* **90**(18), 185004 (2003).

[226] Huang, Y., Lan, X., Duan, X., Tan, Z., Wang, N., Shi, Y., Tang, X., and He, Y. *Phys. Plasmas* **14**(10), 103106 (2007).

[227] Lévy, A., Ceccotti, T., Popescu, H., Réau, F., D'Oliveira, P., Monot, P., Martin, P., Geindre, J. P., and Lefebvre, E. *Eur. Phys. J. Spec. Top.* **175**(1), 111–116 (2009).

[228] Ruszczynski, A. *Nonlinear Optimization*. Princeton University Press, 1 (2006).

[229] Bonnans, J.-F., Gilbert, J. C., Lemarechal, C., and Sagastizábal, C. A. *Numerical Optimization: Theoretical and Practical Aspects (Universitext)*. Springer, 2nd edition, 9 (2006).

[230] Nocedal, J. and Wright, S. *Numerical Optimization (Springer Series in Operations Research and Financial Engineering)*. Springer, 2nd edition, 7 (2006).

[231] Dawson, J. M. *Rev. Mod. Phys.* **55**(2), 403–447 (1983).

[232] Pritchett, P. L. In *Space Plasma Simulation*, volume 615, 1, (2003).

[233] Birdsall, C. and Langdon, A. *Plasma Physics via Computer Simulation*. Taylor & Francis, 1 edition, October (2004).

[234] Griebel, M., Knapek, S., Zumbusch, G., and Caglar, A. *Numerische Simulation in der Moleküldynamik: Numerik, Algorithmen, Parallelisierung, Anwendungen*. Springer, September (2003).

[235] Jiang, B. *The Least-Squares Finite Element Method: Theory and Applications in Computational Fluid Dynamics and Electromagnetics*. Springer, softcover reprint of hardcover 1st ed. 1998 edition, December (2010).

[236] Braess, D. *Finite Elemente: Theorie, schnelle Löser und Anwendungen in der Elastizitätstheorie*. Springer, 4 edition, April (2010).

[237] Hackbusch, W. *Iterative Lösung großer schwachbesetzter Gleichungssysteme*. Teubner Verlag, January (1993).

[238] Saad, Y. *Iterative Methods for Sparse Linear Systems, Second Edition*. Society for Industrial and Applied Mathematics, 2 edition, April (2003).

[239] Hackbusch, W. *Integralgleichungen: Theorie und Numerik*, volume 68. BG Teubner, (1989).

List of Figures

1.1 Sketch illustration of the TNSA process. 6

3.1 Flowchart of the central model. 21

4.1 Self-similar solution assuming Maxwellian electrons. 26
4.2 Plot of Mora's results. 27

5.1 Simulation results for the expansion of a foil in the adiabatic Maxwellian model. 31
5.2 Algorithm of Grismayer et al. for the evolution of the electron phase space density. 32
5.3 Electron phase space density in the adiabatic and the kinetic Maxwellian model. . 33
5.4 Simulation results for the expansion of a foil in the kinetic Maxwellian model. . . 34
5.5 Influence of the cold electrons on the plasma expansion process at $t = 0$. 38
5.6 Influence of the cold electrons on the plasma expansion process for $t > 0$. 40
5.7 Sketch illustration of basic multi-ion targets and the test-particle model. 41
5.8 Maximum ion velocity and ion spectrum in the test-particle model. 43

6.1 Plot of the electron phase space density implied by the hydrodynamic ansatz. . . 47
6.2 Stationary kinetic and stationary hydrodynamic approach for $\kappa = 2$. 50
6.3 Stationary kinetic and stationary hydrodynamic approach for $\kappa = 3$. 51
6.4 Electron density relation in the relativistic hydrodynamic approach. 53

7.1 Self-similar solution assuming a step-like electron energy distribution. 56
7.2 Asymptotic electric field at the ion front in the hydrodynamic approach. 58
7.3 Analytic results for the expansion assuming a step-like electron energy distribution. 60
7.4 Maximum ion energy and energy spectrum in the hydrodynamic approach. 61
7.5 Plot of the hot electron energy distributions underlying the different models. . . . 62
7.6 Final maximum ion energy and total initial energy for the different models. . . . 63
7.7 Electric field, electron density and temperature evolution in the different models. 64
7.8 Spatial electron temperature distributions in the different models. 65
7.9 Maximum ion energy from various experiments performed in the last two decades. 68
7.10 Maximum ion energy of the hydrodynamic approach against experiments. 70
7.11 Comparison of the scaling of the different adiabatic models. 70
7.12 Experimental proton spectrum against the different models. 72
7.13 Experimental proton spectrum against the different models — exceptional cases. 73
7.14 Electron temperature scaling under the condition of equal maximum ion energies. 74

8.1 Experimental data for the maximum ion energy against the Mora model. 77
8.2 Temporal laser profile of the POLARIS system[223] 78

9.1 Electric field in the presence of an initial density gradient. 81

9.2 Evolution of the ion phase space for targets with different initial density gradients. 82
9.3 Impact of the wave breaking for different shapes of the initial density gradient. . 83
9.4 Evolution of the electric field for different shapes of the initial density gradient. . 84
9.5 Asymptotic electric field at the ion front for a target with a linear density gradient. 84
9.6 Plot of the best-fit values for α and β of the extended model. 87
9.7 Analytic expression for the electric field at the ion front against simulation results. 87
9.8 Analytic expression for the ion front velocity against simulation results. 88
9.9 Analytic expression for the displacement of the ion front against simulation results. 89
9.10 Comparison of the extended model to experimental results — Part I. 91
9.11 Comparison of the extended model to experimental results — Part II. 92

A.1 Plot of the central model and the different parts of the computer code. 126
A.2 Approximation of a smooth ion phase space density through PIC particles. 129
A.3 Solution of the Vlasov equation via the PIC ansatz. 130
A.4 Sketch of the field interpolation and the particle weighting in the PIC approach. . 132
A.5 Nonrelativistic Velocity Verlet Integration. 133
A.6 Flowchart of the relativistic particle stepper. 135
A.7 Plot of a linear finite element function on an uniform grid. 138

B.1 Plot of different quantities in the complex domain. 143

Nomenclature

A_e	Size of the electron spot at the target rear side, see p. 76
α_in	Angle of laser incidence on target, see p. 76
β	Inverse normalized electron temperature, $\beta = m_\mathrm{e} c^2 / T_\mathrm{e,0}$, see p. 18
c_0	Sound velocity of the (unperturbed) target material, see p. 93
c_s	Ion acoustic velocity, $c_\mathrm{s} = \sqrt{Z_\mathrm{i}, T_\mathrm{e,0}/m_\mathrm{i}}$, see p. 23
$c_\mathrm{s,h}$	Ion acoustic velocity associated with the hot electrons, $c_\mathrm{s,h} = \sqrt{Z_\mathrm{i} T_\mathrm{e,h,0}/m_\mathrm{i}}$, see p. 40
D_e	Diameter of the electron spot at the target rear side, see p. 66
δ	Dirac Delta distribution, see p. 11
D_L	Diameter of the laser spot on the target front side, see p. 66
E_0	Characteristic electric field strength associated with the hot electrons, $E_0 = \sqrt{n_\mathrm{e,0} T_\mathrm{e,0}/\varepsilon_0}$, see p. 23 and p. 36
E_f	Electric field strength at ion front, see p. 25
ε_f	Kinetic energy of the ions at the ion front, see p. 26
ε_L	Energy of the laser pulse in the focal spot, see p. 67
F	Incomplete elliptic integral of the first kind, see p. 30
K	Complete elliptic integral of the first kind, see p. 30
ε_max	Final maximum ion energy, see p. 60
$\varepsilon_\mathrm{max\,iso}$	Final maximum ion energy predicted by the isothermal Mora model assuming a finite acceleration time, see p. 67
ε_0	Vacuum permittivity, see p. 2
E_ss	Self-similar electric field, see p. 23
η	Conversion efficiency of laser energy into hot electron energy within the laser focus, see p. 67
ε_e	Thermal electron energy, see p. 28
Γ	Gamma function, see p. 47

γ	Relativistic gamma factor, see p. 11
Θ	Heaviside Theta function, see p. 47
I_L	Laser peak intensity, see p. 6
I_ASE	Intensity of the ASE laser prepulse, see p. 93
κ	Adiabatic index, see p. 3
K_n	Modified Bessel functions of second kind and n-th order, see p. 29
λ_D	Debye length, $\lambda_\mathrm{D} = \sqrt{\varepsilon_0 T_{\mathrm{e},0}/e^2 n_{\mathrm{e},0}}$, see p. 25
$\lambda_\mathrm{D,c}$	Cold electron Debye length, $\lambda_\mathrm{D,c} = \sqrt{\varepsilon_0 T_{\mathrm{e,c},0}/e^2 n_{\mathrm{e,c},0}}$, see p. 37
$\lambda_\mathrm{D,h}$	Hot electron Debye length, $\lambda_\mathrm{D,h} = \sqrt{\varepsilon_0 T_{\mathrm{e,h},0}/e^2 n_{\mathrm{e,h},0}}$, see p. 37
$\lambda_\mathrm{D,local}$	Local Debye length, $\lambda_\mathrm{D,local} = \sqrt{\varepsilon_0 T_{\mathrm{e},0}/(n_\mathrm{e}(x)\, e^2)}$, see p. 57
λ_L	Laser wavelength, see p. 67
λ_skin	Skin depth, see p. 36
l	Normalized (initial) target thickness, $l = L/\lambda_\mathrm{D}$, see p. 29
l_ss	Local scale length of the ion density distribution, $l_\mathrm{ss} = \lvert n_\mathrm{i}/(\partial n_\mathrm{i}/\partial x)\rvert$, see p. 57
$l_\mathrm{ss,n}$	Normalized scale length of the initial density gradient, $l_\mathrm{ss,n} = l_\mathrm{ss}/\lambda_\mathrm{D}$, see p. 85
m_e	Electron mass, see p. 44
m_i	Ion mass, see p. 2
μ_0	Vacuum permeability, see p. 10
N_e	Total number of (hot) electrons, see p. 67
n_e	Density of the hot electrons, see p. 2
$n_\mathrm{e,c}$	Density of the cold background electrons, see p. 35
$n_{\mathrm{e,c},0}$	Density of the cold background electrons in absence of an electric potential ($\phi \equiv 0$), see p. 35
$n_\mathrm{e,h}$	Density of the hot electrons, see p. 35. **Note**: One has $n_\mathrm{e,h} = n_\mathrm{e}$. The notation $n_\mathrm{e,h}$ is only used in Sec. 5.2.
$n_{\mathrm{e,h},0}$	Density of the hot electrons in absence of an electric potential ($\phi \equiv 0$), see p. 35. **Note**: One has $n_{\mathrm{e,h},0} = n_{\mathrm{e},0}$. The notation $n_{\mathrm{e,h},0}$ is only used in Sec. 5.2.
$n_{\mathrm{e},0}$	Initial spatial density of the hot electrons, see p. 2
N_i	(Total) Number of ions, see p. 24

n_i	Spatial ion density, see p. 1
$n_{\mathrm{i},0}$	Initial spatial ion density, see p. 1
$n_{\mathrm{i,ss}}$	Self-similar ion density, see p. 23 and p. 55
ω_pi	Ion plasma frequency, $\omega_\mathrm{pi} = \sqrt{Z_\mathrm{i}\, n_{\mathrm{e},0}\, e^2/\varepsilon_0\, m_\mathrm{i}}$, see p. 23
P_abl	Ablation pressure, see p. 93
P_e	Pressure of the electron fluid, see p. 44
$P_{\mathrm{e},0}$	Pressure of the electron fluid corresponding to the electron density $n_{\mathrm{e},0}$, see p. 45
ϕ	Electrostatic potential, see p. 2
ϕ_f	Electric potential at ion front, see p. 36
ϕ_ss	Self-similar electric potential, see p. 23 and p. 55
P_L	Power of the laser pulse, see p. 67
ρ	Charge density, see p. 10
ρ_0	Mass density of the (unperturbed) target material,, see p. 93
r_L	Laser spot radius at the target front side, see p. 67
t_acc	Effective acceleration time of the most energetic ions, hence, time at which the ion front velocity is almost saturated, see p. 67
τ	Normalized time, $\tau = \omega_\mathrm{pi}\, t/\sqrt{2\exp(1)}$, see p. 25
T_e	Temperature of the hot electrons (as a function of time), see p. 28
$T_\mathrm{e,c}$	Temperature of the cold background electrons, see p. 35
$T_{\mathrm{e,c},0}$	Initial temperature of the cold background electrons, see p. 35
$T_\mathrm{e,h}$	Temperature of the hot electrons electrons, see p. 35. **Note**: One has $T_\mathrm{e,h} = T_\mathrm{e}$. The notation $T_\mathrm{e,h}$ is only used in Sec. 5.2.
$T_{\mathrm{e,h},0}$	Initial temperature of the hot electrons, see p. 35. **Note**: One has $T_{\mathrm{e,h},0} = T_{\mathrm{e},0}$. The notation $T_{\mathrm{e,h},0}$ is only used in Sec. 5.2.
$T_{\mathrm{e},0}$	Initial hot electron temperature. **Note:** The temperature is measured in energy units, hence, $T_{\mathrm{e},0}$ is the short form of $k\,T_{\mathrm{e},0}$, see p. 2
θ_e	Half-opening angle of the electron beam inside the target, see p. 66
$\mathscr{T}_j$	Period of motion of an electron with total energy ε_j, see p. 31
τ_L	Laser pulse duration, see p. 67

t_{ASE}	Duration of the ASE prepulse, see p. 90
$t_{1\mathrm{D}\blacktriangleright 3\mathrm{D}}$	Time at which the plasma expansion process approximately becomes three-dimensional, hence, cannot accurately be described any longer using a one-dimensional model, see p. 66
v_{d}	Deformation velocity of the target rear side after the ASE prepulse induced shock wave has break-through, see p. 93
V_{e}	Approximative volume into which the generated hot electrons are spread, see p. 76
v_{e}	Velocity of the electron fluid, see p. 44
$\mathbf{B}$	Three-dimensional magnetic field vector, see p. 10
$\mathbf{E}$	Three-dimensional electric field vector, see p. 10
$\mathbf{F}_{\mathrm{L}}$	Lorentz force, see p. 11
$\mathbf{J}$	Three-dimensional current density, see p. 10
$\mathbf{p}$	Three-dimensional particle momentum, see p. 11
$\mathbf{r}$	Three-dimensional particle position vector, see p. 11
v_{f}	Ion front velocity, see p. 25
v_{i}	Ion fluid velocity (function of space and time) in the x-direction, see p. 2
$v_{\mathrm{i,ss}}$	Self-similar ion velocity, see p. 23 and p. 55
v_{max}	Final maximum ion velocity, see p. 59
v_{s}	Velocity of the shock wave associated with the ASE prepulse inside the target, see p. 93
x_{f}	Position of the ion front, see p. 25
$\mathbb{Z}$	Internal degrees of freedom of the electron gas, see p. 29
Z_{i}	Ion charge state, see p. 2
a_0	Normalized amplitude of the vector potential (also: relativistic amplitude), see p. 75
c	Speed of light, see p. 10
E	Electric field in the x direction, see p. 14
e	Elementary charge, see p. 2
f_α	Phase space density (one-particle distribution function) of species α, see p. 13
k	Boltzmann constant, see p. 2
L	(Initial) Target thickness, see p. 29

$n_{\alpha,0}$	Initial particle density of species α, see p. 16
n_α	Particle density of species α, see p. 16
p	Particle momentum in the x-direction, see p. 14
P_α	Partial pressure of species α, see p. 16
t	Time, see p. 1
t_ϕ	Characteristic time of variation of the potential ϕ, $t_\phi = \phi \cdot \frac{\partial t}{\partial \phi}$, see p. 33
$T_{\alpha,0}$	Initial temperature (in energy units) of species α, see p. 16
T_α	Temperature (in energy units) of the species α, see p. 16
v_α	Mean particle velocity (fluid velocity) of species α, see p. 16
x	Spatial coordinate of the one-dimensional model, corresponds to the direction normal to the target front and rear surface, see p. 1

Appendix

A. The simulation code

In this chapter, we want to give a brief overview on the computer code which has been written in context of this thesis. By using the code we are able to perform simple simulations of plasma phenomena. More precisely, one is able to evaluate the central model of this thesis, which is described in chapter 3, numerically. Hence, one can consider physical situations in this framework without further simplifications and assumptions. An impossibility using pure analytic calculus. An schematic overview of the code is plotted in Fig. 3.1. In principal, the code can be divided in several tasks:

1. Calculation of the spatial ion density from a give phase space density
2. Determination of the electron density as a function of the potential
3. Solving the nonlinear Poisson equation (3.7)
4. Determination of the ion distribution at the next time step
5. Specifying the electron phase space density at the next time step

As common practice, the code works on a finite grid (see Sec. A.4). Since different standard computational techniques⁽¹⁾ cannot applied straightforward to nonuniform grids, the code uses uniform grids only. The restriction to uniform grids has the disadvantage that it leads to a large number of grid nodes — and hence, to large computational efforts — in a situation one needs a high (local) spatial grid resolution as well as has a large simulation area.

In the code, the ion distributions are modeled by the kinetic ansatz (see Sec. 2.1, Eq. (2.11b)), since this approach is more general than the hydrodynamic description. Especially, one is able to perform simulations which include multi-ion species or complex shaped targets (see Sec. 5.3 and chapter 9, resp.). Here, in general, the plasma expansion involves overtaking in the ions and a hydrodynamic approach would fail. In the code, the kinetic treatment of the ions is realized by a standard *Particle-in-Cell* (PIC) approach (see Sec. A.1). In the PIC method, the evaluation of the ion density on the grid (task 1) is realized via a *weighting of particles*, see Sec. A.1.2. Task 4, the evaluation of the ion distribution at the next time step involves an interpolation of the electric field strength from the grid nodes to the positions of the particles (see Sec. A.1.2) and the calculation of the motion of the (virtual) particles, which is central part of the PIC method. In our code, the evaluation of the motion of the particles is realized by the *Störmer-Verlet method* (see Sec. A.2).

A simple generalization of this non-relativistic method to the case of relativistic velocities is given in Sec. A.3. By applying this method the trajectories of the highly relativistic electrons in the electron kinetic model (Sec. 5.1.2) are obtained. Beside the kinetic approach, also the standard isothermal model (Sec. 5.1), the adiabatic model (Sec. 5.1.1) and the stationary hydrodynamic description of the electrons (chapter 6) are included in the code. Together, these methods

---

(1) In more detail, a meaningful weighting of the PIC particles (see Sec. A.1.2) to a nonuniform grid is a hard task.

represent task 5 in the schema — the modeling of the temporal evolution of the electron phase space density. Task 2, the calculation of the spatial electron density n_e starting from a given electron phase space density f_e is done by a straightforward numerical integration of Eq. (2.22).

The numerical solution of nonlinear Poisson equation (task 3) is described in Sec. A.4. Here, one first determines a nonlinear system of equations for the electric potential at the grid points via the *Finite Element Method*. Then, an iterative scheme — the so called *Newton Method* — is used to solve that system of equations.

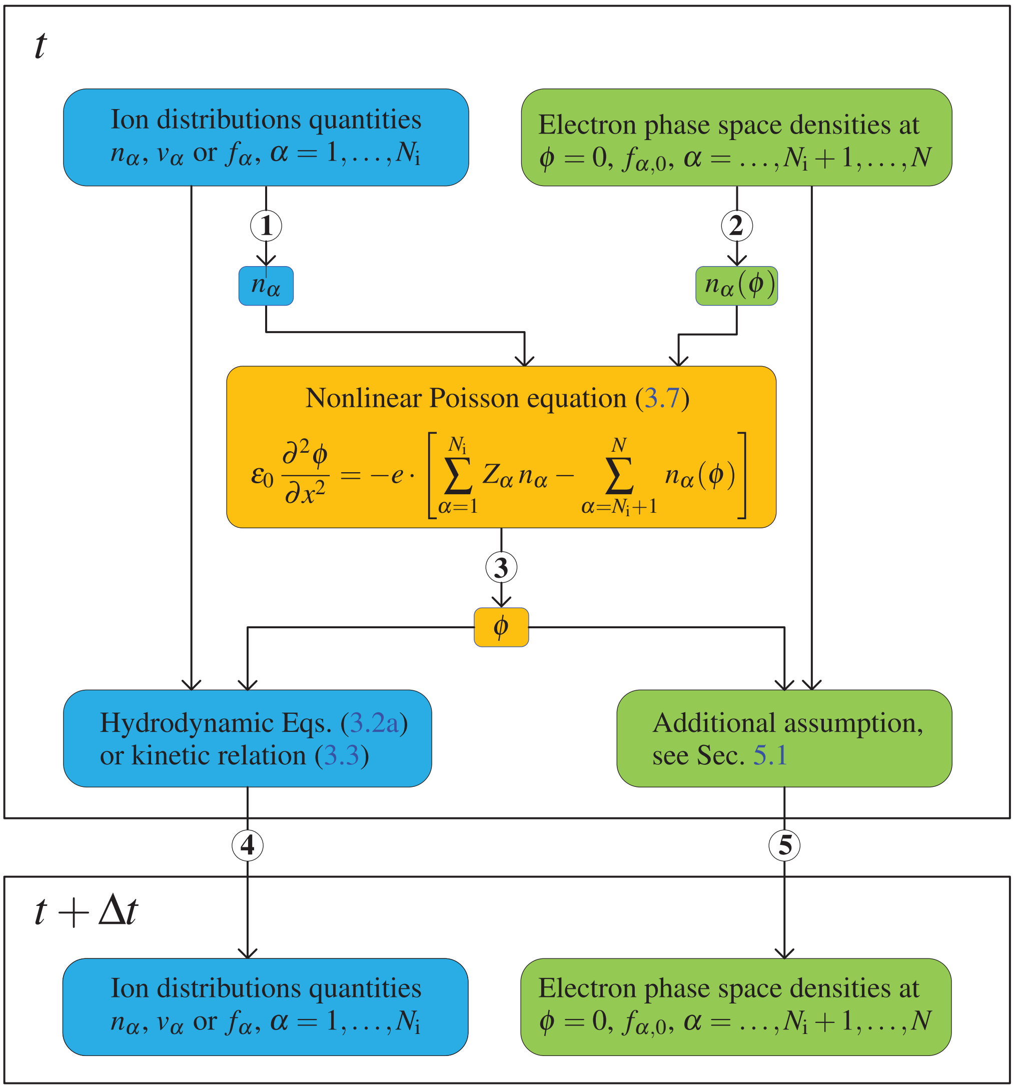
t
Ion distributions quantities n_α, v_α or f_α, $\alpha = 1,\dots,N_i$
Electron phase space densities at $\phi = 0$, $f_{\alpha,0}$, $\alpha = \dots,N_i+1,\dots,N$
1
2
n_α
$n_\alpha(\phi)$
Nonlinear Poisson equation (3.7)
$\varepsilon_0 \frac{\partial^2\phi}{\partial x^2} = -e \cdot \left[\sum_{\alpha=1}^{N_i} Z_\alpha n_\alpha - \sum_{\alpha=N_i+1}^{N} n_\alpha(\phi)\right]$
3
ϕ
Hydrodynamic Eqs. (3.2a) or kinetic relation (3.3)
Additional assumption, see Sec. 5.1
4
5
$t+\Delta t$
Ion distributions quantities n_α, v_α or f_α, $\alpha = 1,\dots,N_i$
Electron phase space densities at $\phi = 0$, $f_{\alpha,0}$, $\alpha = \dots,N_i+1,\dots,N$

Figure A.1.: Plot of the central model of chapter 3 and the different parts (1-5) of the code.

A.1. The Particle-in-Cell (PIC) approach

Here, the *Particle-in-Cell* (PIC) approach is briefly explained. First, in Sec. A.1.1 the concept of virtual particles is introduced. It constitutes the main idea behind the PIC ansatz and offers a simple possibility to calculate the temporal evolution of the ion phase space density. Second, since our computer code operates on a spatial grid, one has to extrapolate the spatial particle densities to the grid nodes as well as to interpolate the electric field strength from the grid nodes to the particle positions. This task will be the topic of Sec. A.1.2.

A.1.1. The concept

Here, we address the numerical solution of the Vlasov equation (3.3)),

$$\frac{\partial f_\alpha}{\partial t} + \frac{p}{m_\alpha}\frac{\partial f_\alpha}{\partial x} - Z_\alpha e \frac{\partial \phi}{\partial x}\frac{\partial f_\alpha}{\partial p} = 0\,. \tag{A.1}$$

Hence, we formulate a computational strategy which allows to (approximately) calculate the temporal evolution of a initial ion phase density f_α. For this purpose, we use a PIC approach.[128,231–233] The idea behind this is the following. Roughly speaking, one starts by approximating a given phase space density through a sum of N *virtual particles*(2). Then, in order to calculate the evolution of the ion distribution, one does not solve the Vlasov equation (A.1) directly (by using *finite difference schemes*, etc.). Instead, one assumes that the pseudo particles behave like real, point-like particles. Thus, the virtual particles will be propagated along the trajectories of point-like particles. As a consequence, the phase space density at an arbitrary instant of time is simply given by the sum over the pseudo particles at this instant of time.

Another point of view on the concept beyond the PIC approach is the following. Strictly speaking, in reality the ion distribution function f_α is a sum of N_α point-like particles (cf. Eq. (2.9)). Here, N_α refers to the real, total number of ions of the species α in the plasma. Now, in order to calculate an exact solution of the Vlasov equation (A.1), one "simply" has to solve the equations of motion for all N_α ions. However, due to the fact that N_α is too large for most plasmas of interest (see chapter 2), one replaces a number of $n = N_\alpha/N$ real, adjacent ions by a single virtual particle. Then, instead of solving the equations of motion for the n individual particles, one only propagates the single virtual particle as a representative for the n real particles. This approximation is quite good as long as the size of the virtual particle in the phase space, $\Delta x \Delta p$, is small enough. Due to the fact that initially adjacent ions stay adjacent as long as the micro-scale field fluctuations are negligible (hence, the electric field is smooth and almost constant over the size of the virtual particle) and the time of propagation is not too large.

In the following, we want to explain the PIC concept a little more in detail. For this purpose, one first has to find an approximation $f^{\mathrm{K}}_{\alpha,0}$ of pseudo particles to the initial ion phase space density(3) $f_\alpha(t=0)$. More precisely, $f^{\mathrm{K}}_{\alpha,0}$ is assumed to have the form

$$f_{\alpha,0}(x,p) \approx f^{\mathrm{K}}_{\alpha,0}(x,p) := \sum_{\mu=0}^{N-1} \mathrm{K}_\mu(x,p)\,. \tag{A.2}$$

---

(2) Alternatively, the virtual particles will also be denoted as *pseudo particles* or *macro particles*.

(3) Beyond this paragraph we will not distinguish between f^{K}_α and f_α. Instead we will use the term f_α, independently of which function is meant.

Here, K_μ denotes the *particle shape function* of the μ-th pseudo particle. Commonly, the shape functions have a simple mathematical structure (polynomials, etc.). In addition, the pseudo particles should have a small extent in the phase space. Hence, the diameters $\mathrm{diam}(\omega_\mu)$ of their supports

$$\omega_\mu = \mathrm{supp}(\mathrm{K}_\mu) = \overline{\left\{(x,p) : \mathrm{K}_\mu(x,p) \neq 0\right\}} \tag{A.3}$$

should be as small as possible(4). The center of ω_μ — which we identify with the initial position of the μ-th virtual particle in the phase space — will be denoted by $(x_{\mu,0}, p_{\mu,0})$. In principal, the shape functions can individually be chosen for each pseudo particle μ. However, for practical reasons one usually uses a definition which is independent of μ,

$$\mathrm{K}_\mu(x,p) = \alpha_\mu \, \mathrm{S}(x - x_{\mu,0}, p - p_{\mu,0}) \, . \tag{A.4}$$

Here, S denotes the general particle shape function and α_μ is a real number. Therewith, the approximation (A.2) is rewritten as

$$f^{\mathrm{K}}_{\alpha,0}(x,p) = \sum_{\mu=0}^{N-1} \alpha_\mu \, \mathrm{S}(x - x_{\mu,0}, p - p_{\mu,0}) \, . \tag{A.5}$$

A simple possibility for a particle shape function S is given by a (two-dimensional) step-like distribution(5)

$$\mathrm{S}(x,p) = \frac{1}{\Delta x \Delta p} \Theta(\Delta x - 2\,|x|) \cdot \Theta(\Delta p - 2\,|p|) \, , \tag{A.6}$$

with Θ referring to the Heaviside-Theta function and Δx and Δp denoting the width of pseudo-particle in the x- and p-direction, respectively (see Fig. A.2).

After the initial distribution $f^{\mathrm{K}}_{\alpha,0}$ is specified, the solution of the Vlasov equation (A.1) is obtained by calculating the trajectories $(x_\mu(t), p_\mu(t))$ of the virtual particles. As mentioned above, for this purpose, one considers the virtual particles as real, point-like particles with a specific charge q_α/m_α in the electrical field $E(x,t)$. Thus, one has to evaluate the $2N$ equations of motion(6)

$$\frac{\partial x_\mu(t)}{\partial t} = \frac{1}{m_\alpha} p_\mu(t) \tag{A.7a}$$

$$\frac{\partial p_\mu(t)}{\partial t} = q_\alpha E(x_\mu(t),t) \, , \tag{A.7b}$$

with the initial conditions

$$x_\mu(0) = x_{\mu,0} \tag{A.7c}$$

$$p_\mu(0) = p_{\mu,0} \, . \tag{A.7d}$$

---

(4) The smaller one chooses the support of the K_μ the better the numerical solution of the Vlasov equation (A.1) will be. However, we cannot make the support ω_μ to small. Since the supports of the different functions K_μ should overlap. Otherwise the approximation of $f_{\alpha,0}(x,p)$ by $f^{\mathrm{K}}_{\alpha,0}(x,p)$ would be to rough. As a consequence, in general, there is only one possibility to ensure both issues, a good approximation and small supports: By making the number of pseudo particles N large enough.

(5) Here, the particle shape function S is normalized in the way that $\int_{\mathbb{R}^2} \mathrm{S}(x,p)\, \mathrm{d}x\, \mathrm{d}p = 1$.

(6) Note that Eqs. (A.7) constitute nonrelativistic expressions, in coincidence with the nonrelativistic version of the Vlasov equation, Eq. (A.1).

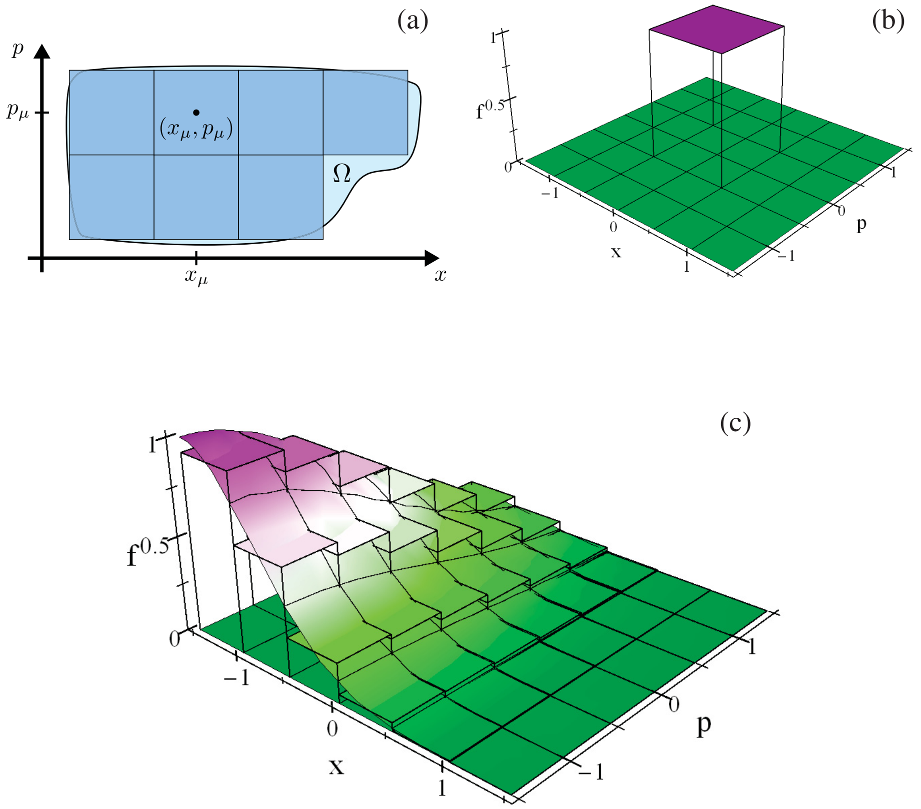

Figure A.2.: Approximation of a smooth ion phase space density by a sum of step-like kernel functions. For this purpose one defines an uniform overlay on a domain Ω in the phase space through a set of rectangular shaped areas ω_μ (see (a)). On each domain ω_μ, one specifies a step-like Kernel function (see (b)) in such a way that the initial, smooth phase space density is quite well approximated by the sum over all Kernel functions (see (c)).

Then, according to the PIC approach, the ion distribution at an arbitrary instant of time t is given by

$$f_\alpha(t,x,p) \approx f_\alpha^{\mathrm{K}}(t,x,p)\ , \tag{A.8}$$

with

$$f_\alpha^{\mathrm{K}}(t,x,p) = \sum_{\mu=0}^{N-1} \mathrm{K}_\mu(x-(x_\mu(t)-x_{\mu,0}), p-(p_\mu(t)-p_{\mu,0}))\ . \tag{A.9}$$

By using a general shape function S Eq. (A.9) becomes

$$f_\alpha^{\mathrm{K}}(t,x,p) = \sum_{\mu=0}^{N-1} \alpha_\mu\ \mathrm{S}(x-x_\mu(t), p-p_\mu(t))\ . \tag{A.10}$$

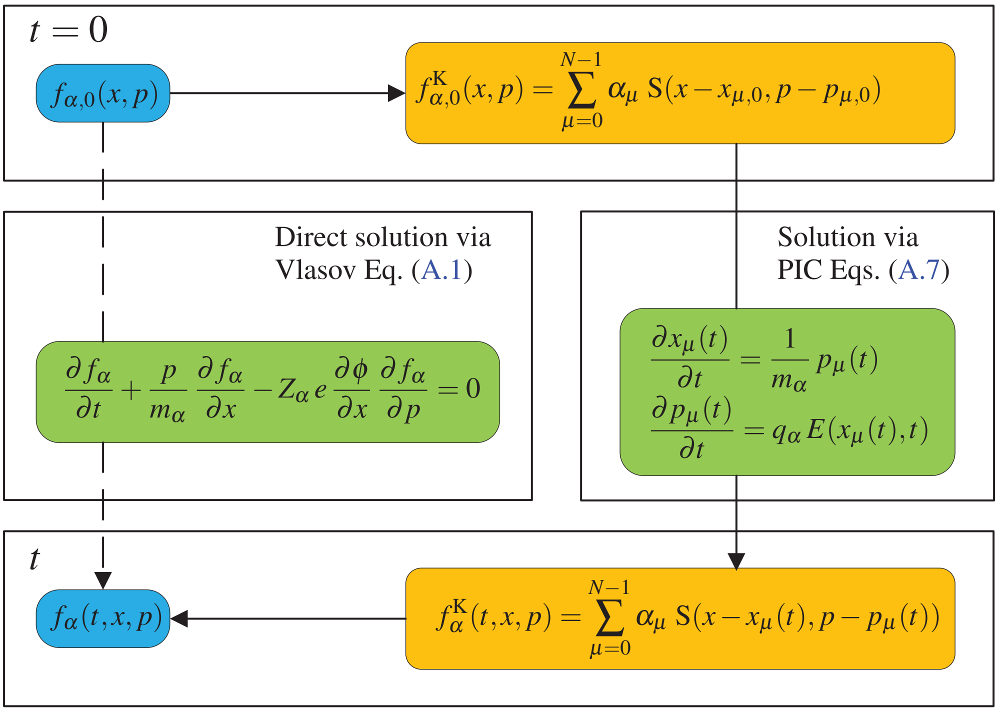
$t=0$
$f_{\alpha,0}(x,p)$
$f^{\mathrm{K}}_{\alpha,0}(x,p)=\sum_{\mu=0}^{N-1}\alpha_\mu\,\mathrm{S}(x-x_{\mu,0},p-p_{\mu,0})$
Direct solution via
Vlasov Eq. (A.1)
$\frac{\partial f_\alpha}{\partial t}+\frac{p}{m_\alpha}\frac{\partial f_\alpha}{\partial x}-Z_\alpha e\frac{\partial\phi}{\partial x}\frac{\partial f_\alpha}{\partial p}=0$
Solution via
PIC Eqs. (A.7)
$\frac{\partial x_\mu(t)}{\partial t}=\frac{1}{m_\alpha}p_\mu(t)$
$\frac{\partial p_\mu(t)}{\partial t}=q_\alpha E(x_\mu(t),t)$
t
$f_\alpha(t,x,p)$
$f^{\mathrm{K}}_{\alpha}(t,x,p)=\sum_{\mu=0}^{N-1}\alpha_\mu\,\mathrm{S}(x-x_{\mu}(t),p-p_{\mu}(t))$

Figure A.3.: Schematic plot of the PIC approach. To solve the Vlasov equation (A.1), we do not choose a direct way (dashed arrow) by using finite difference schemes, etc. Instead we apply the PIC ansatz. Here, one approximates the initial phase space density by a sum of "pseudo particles" (cf. Eq. (A.2)) and then evolves the ensemble of pseudo particles by evaluating Eqs. (A.7) (solid arrows).

A schematically plot of the PIC approach is shown in Fig. A.3. The main computational effort of the PIC approach is the numerical calculation of the particle trajectories (A.7). In the code, we address this problem by the so-called *Störmer-Verlet* algorithm, which is an example for a nonrelativistic particle stepper(7) . This method will be the topic of Sec. A.2.

A.1.2. Weighting of particle and grid quantities

In the last section, Sec. A.1.1, we introduced the PIC concept. In this approach, the main task is the solution of the equations of motion (A.7) for the pseudo particles. To proceed, one has to know the force which acts on each pseudo particle μ. However, in general the electrical field is not given at the particle positions x_μ. Since the code operates on a discrete, spatial grid, the electric field will only be calculated at the grid points (see Sec. A.4). As a consequence, one has to interpolate the values of the electric field from the grid nodes to the particle positions. Even before, in oder to evaluate the electric field at the grid nodes by solving Eq. (3.7), one has to specify the charge density which is created by the pseudo particles at these grid nodes.

In this section, we briefly address these two problems, (i) the interpolation of the electric field strength from the grid nodes to the particle positions and (ii) the extrapolation of the particle density to the grid nodes. The process by which particle and grid quantities are connected through inter- and extrapolation is called *weighting*. From a numerical point of view, the details of these problems can be very complex. Especially in case of nonuniform grids. Therefore, we perform simulations only on uniform grids — although other parts of the code can deal with arbitrary grids, such as the implemented nonlinear Poisson solver (see Sec. A.4), for example. Here, we will only briefly describe the interpolation and extrapolation method which is used in our simulations. An introduction to more advanced methods is given in Ref.,[233] for example.

---

(7) In case of the ions a nonrelativistic method is sufficient because the velocities are small compared to the speed of light. However, the PIC ansatz works also for the relativistic Vlasov equation. Then, one has to use the relativistic equations of motion of the particles instead, see Sec. A.3.

In the code, we in general use a linear interpolation ansatz. Hence, if y_i and y_{i+1} denote the values of an arbitrary physical quantity y at the grid nodes i and $i+1$ with the positions x_i and x_{i+1}, respectively, then the value $y(x)$ of y at a point x in between the nodes i and $i+1$ is given by

$$y(x) = y_i + \frac{y_{i+1} - y_i}{\Delta x} \cdot (x - x_i) \ . \tag{A.11}$$

Here, $\Delta x = x_{i+1} - x_i$ refers to the spacing of the grid. This interpolation scheme (A.11) is used to evaluate the electric field which acts on a pseudo particle located in the grid interval $[x_i, x_{i+1}]$ (task (i)) and is illustrated in Fig. A.4a.

Concerning task (ii), we note that we use a linear weighting, too. Although this is technical not mandatory, it shows that it is desirable for numerical purposes to use the same scheme for both tasks.[233] The linear extrapolation works as follows. Since the grid has a spacing of Δx, the pseudo particles are assumed to have a spatial width Δx, too. Moreover, following Sec. A.1.1 we use step-like particles in the code (see Eq. (A.6)). Thus, the particle density n is assumed to be constant at the domain of the particle, $n(x) = n_\mu = \text{const}$ for x in $[x_\mu - \Delta x/2, x_\mu + \Delta x/2]$. Clearly, the pseudo particle μ represent a total number of $N_\mu = n_\mu \Delta x$ (real) particles.

Now, in the linear ansatz, the fraction $N_{\mu,i}$ of the total number of particles, N_μ, which lays closer to the grid node i than to the grid point $i+1$ will be related to the node i. In addition, the remaining amount $N_{\mu,i+1} = N_\mu - N_{\mu,i}$ will be related to the node $i+1$. This partition of the PIC particle is shown in Fig. A.4b. After a short calculus one finds

$$N_{\mu,i} = N_\mu \cdot \left(1 - \frac{x_\mu - x_i}{\Delta_x}\right) \tag{A.12a}$$

$$N_{\mu,i+1} = N_\mu \frac{x_\mu - x_i}{\Delta_x} \ . \tag{A.12b}$$

Under the assumption that the particle numbers $N_{\mu,i}$ and $N_{\mu,i+1}$ create the spatial densities $n_{\mu,i} = N_{\mu,i}/\Delta x$ and $n_{\mu,i+1} = N_{\mu,i+1}/\Delta x$ at the nodes i and $i+1$, respectively, one obtains

$$n_{\mu,i} = n_\mu \cdot \left(1 - \frac{x_\mu - x_i}{\Delta_x}\right) \tag{A.13a}$$

$$n_{\mu,i+1} = n_\mu \frac{x_\mu - x_i}{\Delta_x} \ , \tag{A.13b}$$

while there is no contribution to other nodes, hence, $n_{\mu,k} = 0$ for $k \neq i, i+1$. From the above relations one can directly see the mentioned linear dependency on x_μ. This procedure is repeated for all pseudo particles μ. Finally, the (total) spatial particle density at the grid nodes i implied by the particles is given through the sum

$$n_i = \sum_{\mu=0}^{N-1} n_{\mu,i} \ . \tag{A.14}$$

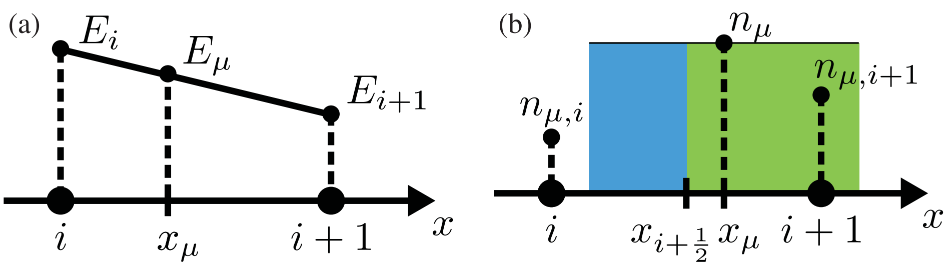

Figure A.4.: The interpolation of the electric field is shown in (a). Starting from the values E_i and E_{i+1} at the grid nodes i and $i+1$, respectively, the electric field E_μ at the position x_μ of the pseudo particle μ is obtained by a linear weighting, according to Eq. (A.11). In addition, the spatial densities $n_{\mu,i}$ and $n_{\mu,i+1}$ at the nodes i and $i+1$, respectively, which are associated with the pseudo particle μ, are obtained by a linear weighting, too, see (b). Here, the fraction of the μ-th pseudo particle which lays closer to the node i (blue shaped) is assigned to the node i, while the remaining part (green shaped) — for which the node $i+1$ is the nearest grid point — is assigned to the node $i+1$. As a consequence, a linear dependency of the assigned spatial densities $n_{\mu,i}$ and $n_{\mu,i+1}$ is obtained, see Eq. (A.13).

A.2. The Störmer Verlet algorithm

In this section, we want to discuss a numerical scheme for the calculation of the equations of motion of the particles, Eqs. (A.7). In the code, we address this problem with the velocity-form of the *Störmer Verlet* method.[234] Note that this algorithm is valid for nonrelativistic velocities, only. This is sufficient for our purpose, since in the code we are going to use this method only for the ions, which do not gain relativistic energies in the TNSA experiments performed so far. Later on, in Sec. A.3, we will generalize this method to relativistic velocities. Therewith, one will be able to calculate the trajectories of the laser-heated, relativistic electron, too.

We start with a particle of mass m in a given force field $F(x,t)$. Note that we assume explicitly that the force is not a function of the particle momentum(8). In order to specify the trajectory of the particle, one has to solve the set of equations

$$\frac{\partial x(t)}{\partial t} = \frac{1}{m} p(t) \tag{A.15a}$$

$$\frac{\partial p(t)}{\partial t} = F(x(t),t) \; . \tag{A.15b}$$

As usual, the set of equations is completed by the initial conditions

$$x(t_k) = x_k \tag{A.15c}$$

$$p(t_k) = p_k \; , \tag{A.15d}$$

---

(8) For particular cases, there exist variations of the Störmer Verlet method which can deal with a force which depends on the particle momentum, see Ref.[234]

with (x_k, p_k) being the phase space point of the particle at the initial point in time t_k. The Störmer Verlet method solves the Eqs. (A.15) in the following way. One starts by calculating the position x_{k+1} of the particle at the next instant of time $t_{k+1} = t_k + \Delta t$, with Δt being a small time step, via

$$x_{k+1} = x_k + \frac{p_k}{m}\,\Delta t + \frac{F_k}{2\,m}\,\Delta t^2\,. \tag{A.16a}$$

Here, $F_k = F(x_k, t_k)$ denotes the force which acts on the particle at t_k. For $k > 0$, F_k is already know from the previous iteration of the Störmer Verlet method. At the initial point of time, $t = t_0$, the force has to be evaluated in an auxiliary calculation. In the next step, the force at the position x_{k+1} and the time t_{k+1} is determined,

$$F_{k+1} = F(x_{k+1}, t_{k+1})\,. \tag{A.16b}$$

Finally, the momentum p_{k+1} at the time t_{k+1} is evaluated by

$$p_{k+1} = p_k + \frac{1}{2}\,(F_k + F_{k+1})\,\Delta t\,. \tag{A.16c}$$

A schematic flowchart of the Störmer Verlet method is shown in Fig. A.5.

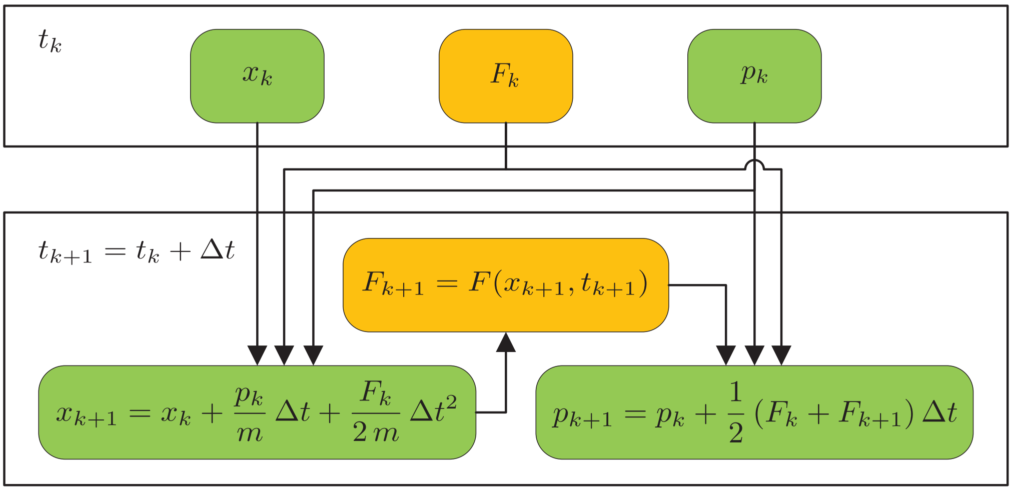
t_k
x_k
F_k
p_k
$t_{k+1} = t_k + \Delta t$
$F_{k+1} = F(x_{k+1}, t_{k+1})$
$x_{k+1} = x_k + \frac{p_k}{m}\Delta t + \frac{F_k}{2\,m}\Delta t^2$
$p_{k+1} = p_k + \frac{1}{2}(F_k + F_{k+1})\Delta t$

Figure A.5.: Schematic plot of the nonrelativistic Velocity Störmer Verlet Integration (A.16).

A.3. A relativistic particle-stepper

In this section, we want to extend the Störmer Verlet method (A.16) to the case of relativistic velocities. In the code, this extended form is used for the calculation of the trajectories of the electrons in the kinetic algorithm(9) of Sec. 5.1.2. We start the discussion on the relativistic particle stepper by considering the relativistic version of Eqs. (A.15)

---

(9) Of course, from a numerical point of view one could also use the nonrelativistic equations of motion, as it was done in the original publication.[64] However, with respect to the large electron temperatures $T_{e,0} \gtrsim m_e c^2$ this ansatz is physical questionable.

$$\frac{\partial x(t)}{\partial t} = \frac{1}{m\gamma(p)}\, p(t) \tag{A.17a}$$

$$\frac{\partial p(t)}{\partial t} = F(x(t),t)\ , \tag{A.17b}$$

with the initial conditions

$$x(t_k) = x_k \tag{A.17c}$$

$$p(t_k) = p_k\ . \tag{A.17d}$$

The set of equations describe the motion of a particle with mass m which experiences the force F. In the context of special relativity dynamics, it experiences an acceleration $a = F/m$ seen in its current inertial frame. Of course, the set of equations (A.17) cannot be solved for an arbitrary function F. Therefore as usual, in the numerical approach one divides the motion of the particle into small pieces and assumes the force F to be constant at each piece of motion. The analytic solution of Eqs. (A.17) for a constant force F_k is given by

$$x(t) = x_k + \frac{mc^2}{F_k}\cdot\left(\sqrt{1+\left(\frac{F_k\cdot\Delta t}{mc}+\frac{p_k}{mc}\right)^2} - \sqrt{1+\left(\frac{p_k}{mc}\right)^2}\right) \tag{A.18a}$$

$$p(t) = p_k + F_k\cdot\Delta t\ , \tag{A.18b}$$

with $\Delta t = t - t_k$.

Now, we bring this result together with the scheme of the Störmer Verlet method, Eqs. (A.16). Therewith, one obtains a simple, relativistic particle stepper. Similar to Eq. (A.16), one starts by calculating the position of the particle at $t = t_{k+1}$, x_{k+1}, via

$$x_{k+1} = x_k + \frac{mc^2}{F_k}\cdot\left(\sqrt{1+\left(\frac{F_k\cdot\Delta t}{mc}+\frac{p_k}{mc}\right)^2} - \sqrt{1+\left(\frac{p_k}{mc}\right)^2}\right)\ , \tag{A.19a}$$

where $F_k = F(x_k,t_k)$ is the force which acts on the particle at t_k. In the next step, the force at the position x_{k+1} and the instant t_{k+1} is evaluated,

$$F_{k+1} = F(x_{k+1},t_{k+1})\ . \tag{A.19b}$$

Finally, the momentum p_{k+1} at time t_{k+1} is obtained by

$$p_{k+1} = p_k + \frac{1}{2}\left(F_k + F_{k+1}\right)\Delta t\ . \tag{A.19c}$$

A schematic flowchart of the relativistic particle stepper is shown in Fig. A.6. At least, we want to point out two facts. (i) Although the relativistic particle stepper (A.19) is based on the (nonrelativistic) Störmer-Verlet method, it is not symplectic(10) at all — in contrast to the nonrelativistic version (A.16). (ii) In the limit $v_k = p_k/(m\gamma(p_k)) \ll c$, the algorithm (A.19) converges into the nonrelativistic Störmer Verlet method (A.16).

---

(10) A symplectic algorithm conserves the volume of a given (small) phase space element, see Ref. 234. Due to this property a symplectic method has several advantages, such as a long-time stability.

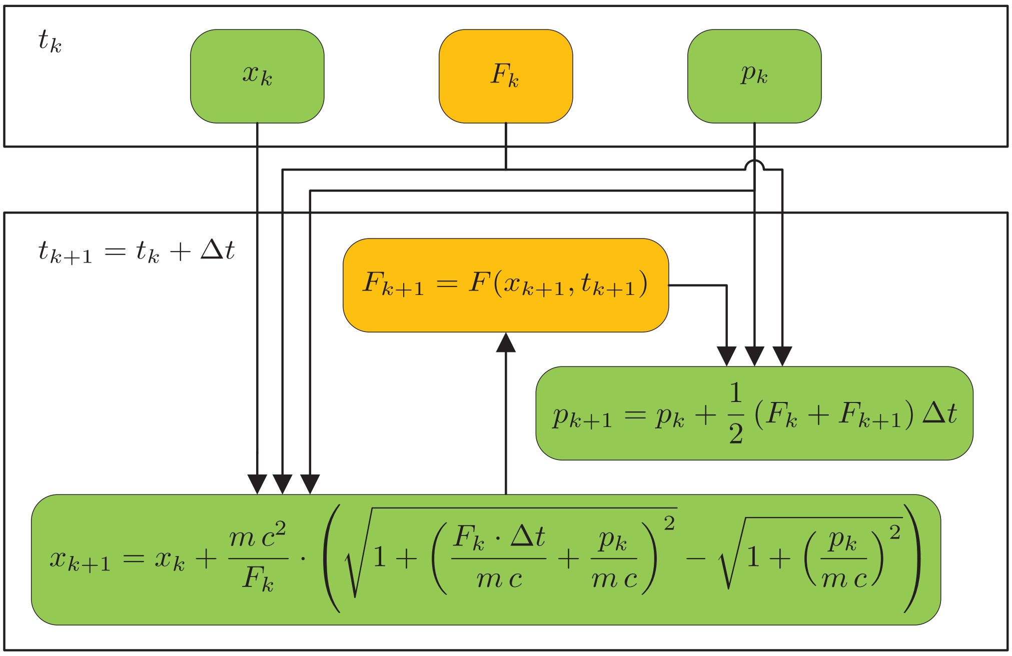
t_k
x_k
F_k
p_k
$t_{k+1} = t_k + \Delta t$
$F_{k+1} = F(x_{k+1}, t_{k+1})$
$p_{k+1} = p_k + \frac{1}{2}(F_k + F_{k+1})\,\Delta t$
$x_{k+1} = x_k + \frac{m\,c^2}{F_k} \cdot \left(\sqrt{1 + \left(\frac{F_k \cdot \Delta t}{m\,c} + \frac{p_k}{m\,c}\right)^2} - \sqrt{1 + \left(\frac{p_k}{m\,c}\right)^2}\right)$

Figure A.6.: Flowchart of the relativistic particle stepper (A.19) used in the code. The algorithm is based on the (nonrelativistic) Velocity Verlet Integration (A.16) (cf. Fig. A.5).

A.4. Solution of the nonlinear Poisson equation

In this section, we want to discuss shortly the numerical solution of the nonlinear Poisson equation (3.7),

$$\varepsilon_0 \frac{\partial^2 \phi}{\partial x^2} = -\rho(x, \phi) = -e \cdot \left[\sum_{\alpha=1}^{N_\mathrm{i}} Z_\alpha n_\alpha(x) - \sum_{\alpha=N_\mathrm{i}+1}^{N} n_\alpha(\phi) \right] . \tag{A.20}$$

Before we can address this problem, we have to take a closer look at the boundary conditions of Eq. (A.20). Due to the fact that there are no electrical fields at infinity, the boundary conditions[11] are given by

$$\phi'(-\infty) = 0 \tag{A.21a}$$
$$\phi'(+\infty) = 0 \,. \tag{A.21b}$$

However, since in a computer code one cannot handle an infinitely large domain, in general, the boundary conditions (A.21) have to replaced by relations for a finite computational domain $\Omega = [x_\mathrm{min}, x_\mathrm{max}]$, with x_min, x_max being real numbers. Here, we chose the computational boundaries x_min

---

[11] The form (A.21) is denoted as *Neumann boundary conditions*. In general, Neumann conditions do not specify the solution uniquely. In more detail, if ϕ is a solution then $\phi + C$ is a solution, too, with C being a constant. However, for Eq. (A.20) the solution is uniquely defined, since a shift $\phi \to \phi + C$ would violated the global charge neutrality which is implied by the boundary conditions (A.21).

and $x_{\max}$ that large that the spatial ion densities n_α are constant[12] outside of the computational domain. Hence, we assume $n'_\alpha(x) = 0$ for all x, with $x \leq x_{\min} \vee x \geq x_{\max}$ and all ion species α. Therewith, Eq. (A.20) can be integrated once and, under the consideration of the boundary conditions (A.21), we get the expressions

$$\frac{\varepsilon_0}{2}\,\phi'(x_{\min})^2 = e \cdot \left[\sum_{\alpha=1}^{N_\mathrm{i}} Z_\alpha\, n_\alpha(-\infty) \cdot (\phi(-\infty) - \phi(x_{\min})) - \sum_{\alpha=N_\mathrm{i}+1}^{N} (F_\alpha(\phi(-\infty)) - F_\alpha(\phi(x_{\min}))) \right] \tag{A.22a}$$

$$\frac{\varepsilon_0}{2}\,\phi'(x_{\max})^2 = e \cdot \left[\sum_{\alpha=1}^{N_\mathrm{i}} Z_\alpha\, n_\alpha(\infty) \cdot (\phi(\infty) - \phi(x_{\max})) - \sum_{\alpha=N_\mathrm{i}+1}^{N} (F_\alpha(\phi(\infty)) - F_\alpha(\phi(x_{\max}))) \right] . \tag{A.22b}$$

Here, $F_\alpha(\phi)$ denotes an antiderivative of the electron density $n_\alpha(\phi)$ with respect to ϕ. Moreover, the values $\phi(\pm\infty)$ of the potential at $\pm\infty$ have to determined from the relations

$$\varepsilon_0 \frac{\partial^2 \phi}{\partial x^2} \overset{!}{=} 0 = -e \cdot \left[\sum_{\alpha=1}^{N_\mathrm{i}} Z_\alpha\, n_\alpha(\pm\infty) - \sum_{\alpha=N_\mathrm{i}+1}^{N} n_\alpha(\phi(\pm\infty)) \right] . \tag{A.22c}$$

Since the boundary conditions (A.22) might be complicated, one often alternatively uses the simple but strictly speaking not accurate boundary conditions

$$\phi'(x_{\min}) = 0 \tag{A.23a}$$
$$\phi'(x_{\max}) = 0\,. \tag{A.23b}$$

In summary, one has to evaluate a solution of Eq. (A.20) on the finite domain Ω under the boundary conditions (A.22) or (A.23).

In order to solve the Poisson equation numerically different techniques are known. Maybe the most common and simple one is the so-called *Finite Difference Method* (FDM). In this approach, the domain Ω is discretized by a uniform grid with n nodes i (see Fig. A.7) and the central task is the calculation of the function values $\phi_i = \phi(x_i)$ at the positions of the grid nodes, $x_i = x_{\min} + i \cdot (x_{\max} - x_{\min})/(n-1)$. For this purpose, the differential operator $\partial^2/\partial x^2$ is replaced by the difference operator

$$\frac{\Delta^2 \phi}{\Delta x^2} = \frac{\phi_{i+1} - 2\,\phi_i + \phi_{i-1}}{\Delta x^2}\,, \tag{A.24}$$

---

[12] While in the case of a finite target one has $n_\alpha(x) \equiv 0$ for all x outside the target and all ion species α, in the case of a semi-finite plasma slab (see chapter 4) one does not have $n_\alpha(x) \equiv 0$ in general. Therefore, we use the less restrictive condition $n_\alpha(x) \equiv \text{const}$ for all x outside the computational domain and all ion species α.

with $\Delta x = (x_{\max} - x_{\min})/(n-1)$ being the interval length of the grid. Therewith, Eq. (A.20) becomes

$$\varepsilon_0 \frac{\phi_{i+1} - 2\,\phi_i + \phi_{i-1}}{\Delta x^2} = -\rho(x_i, \phi_i)\,, \tag{A.25}$$

for $i = 1, \ldots, n-1$. The $n-2$ relations together with the Neumann boundary conditions at $x = x_{\min}$ and $x_{\max}$ form a complete set of n nonlinear equations for the n unknown values ϕ_i. The FDM is a simple and commonly used numerical method. However, it has some drawbacks. It is hardly to generalize to nonuniform grids or to multidimensional problems on complex domains Ω. In addition, it leads to convergence problems in case of rapidly varying ion densities (e.g. in case of Dirac-delta distributions). Due to that reason, we will address the solution of the Poisson equation (A.20) by another approach which is much more flexible and powerful than the FDM.

For this purpose, we reformulate the above problem. At first, we multiply Eq. (A.20) with an arbitrary, integrable function u. Then, by integrating the obtained expression over the domain Ω, on which the Poisson equation has to be solved, we find

$$\varepsilon_0 \int\limits_\Omega u\,\frac{\partial^2\phi}{\partial x^2}\;\mathrm{d}x = -\int\limits_\Omega \rho\;\mathrm{d}x\,. \tag{A.26}$$

Next, we integrate the left-hand side of Eq. (A.26) by parts. Therewith, we get

$$-\varepsilon_0 \int\limits_\Omega \frac{\partial u}{\partial x}\frac{\partial \phi}{\partial x}\;\mathrm{d}x + \varepsilon_0\, u\,\frac{\partial\phi}{\partial x}\bigg|_{\partial\Omega} = -\int\limits_\Omega \rho\;\mathrm{d}x\,. \tag{A.27}$$

The last relation is often denoted as the *weak formulation*, while the original problem (A.20) is called *strong formulation*. The weak formulation has to be understood in the following sense: One has to find a function ϕ which fulfills the relation (A.27) for every function u. Clearly, every solution of the strong problem is a solution of the weak formulation, too. Strictly speaking, the reverse statement is not true. This is obvious since it is sufficient for ϕ to be once differentiable in order to be a possible solution of the weak formulation. In contrast, a solution of the strong formulation has to be twice differentiable. Hence, there exist solutions of Eq. (A.27) in cases when Eq. (A.20) does not have solutions at all. However, if the functions ϕ and u are sufficiently smooth, both formulations are equivalent.

Regarding the weak formulation from a mathematical point of view, one has to specify the functions space $\mathscr{H}$ in which the functions ϕ and u are contained. Normally, $\mathscr{H}$ is a *Sobolev space*[235,236] which contains a infinite number of elements. Of course, for numerical purposes one has to operate on a finite function space $\mathscr{H}^n$, with a dimension $n < \infty$ instead. As a consequence, the numerical solution is in general only an approximation to the exact solution, since $\mathscr{H}^n \subset \mathscr{H}$. To find the approximative solution ϕ we will use the *Galerkin method*. In this method, one starts by defining a basis $\{u_j\}_{j=1}^n$ of the function space $\mathscr{H}^n$. Therewith, the numerical solution ϕ may be written as a linear form in this basis, $\phi = \sum\limits_{j=1}^{n} c_j\,u_j$, with c_j being real coefficients. Moreover, since Eq. (A.27) is linear in u, it is sufficient for ϕ to fulfill the expression (A.27) for the n basis function u_j in order to ensure that Eq. (A.27) is true for all functions u in $\mathscr{H}^n$. Thus, in order to specify the numerical solution ϕ in $\mathscr{H}^n$ one considers the relations y_i,

$$y_i = -\varepsilon_0 \int\limits_\Omega \frac{\partial u_i}{\partial x}\frac{\partial \phi}{\partial x}\;\mathrm{d}x + \varepsilon_0\, u_i\,\frac{\partial\phi}{\partial x}\bigg|_{\partial\Omega} + \int\limits_\Omega \rho\;\mathrm{d}x = 0\,, \tag{A.28}$$

for $i = 1,\dots,n$. These relations form a set of n equations for the n unknown coefficients c_i. By using the notations $\mathbf{c} = (c_0, c_1, \dots, c_{n-1})$ and $\mathbf{y} = (y_0, y_1, \dots, y_{n-1})$, it can be written in a more compact form as $\mathbf{y}(\mathbf{c}) = 0$. Clearly, although the Galerkin method is founded on an entirely different approach in comparison to the FDM, in both cases the main computational effort is the solution of a system pf nonlinear equations.

The quality of the numerical approximation depends strongly on the choice of the set of basis functions u_i, respectively, the subset $\mathscr{H}^n$ which is spanned by the basis u_i. Hence, it is in principal a good strategy to adapt the basis to the given problem. However, since in praxis this can be a hard task without already knowing the exact solution of the problem (in which case a numerical solution would become obsolete), we choose a more general strategy to define a basis, the so-called *Finite Element Method* (FEM). As the FDM, it is based on a spatial grid. Although the FEM can easily implied on nonuniform grids, we again assume an uniform grid with n nodes which covers the domain $\Omega = [x_{\min}, x_{\max}]$. Hence, the interval length is given by $\Delta x = (x_{\max} - x_{\min})/(n-1)$ and the nodes are located at $x_i = x_{\min} + i \cdot (x_{\max} - x_{\min})/(n-1)$. A central aspect of the FEM is use basis functions with a small support. In more detail, one uses functions $u_i(x)$ with the properties

$$u_i(x_i) > 0 \tag{A.29a}$$

$$u_i(x) \equiv 0 \quad \forall x:\ x \le x_{i-1} \vee x \ge x_{i+1}\ . \tag{A.29b}$$

A basis function of that kind is called *Finite Element Function*(13). In addition, in our case, the finite element function must be steady but not necessary differentiable(14). Hence, the functions must be elements of $\mathbb{C}^0$. A simple function u_i which fulfills the above conditions is the triangular function (see Fig. A.7) given by

$$u_i(x) = \begin{cases} \frac{x - x_{i-1}}{\Delta x} & :\ x_{i-1} \le x \le x_i \\ \frac{x_{i+1} - x}{\Delta x} & :\ x_i \le x \le x_{i+1} \\ 0 & :\ \text{else}\ . \end{cases} \tag{A.30}$$

In order to solve the resulting nonlinear equation system (A.28) we use the *Newton method*. It is a standard, iterative technique which works in the following way. First, an initial coefficient vector $\mathbf{c}_0$ for the solution of the nonlinear equation system $\mathbf{y}(\mathbf{c}) = 0$ is guessed. Since $\mathbf{c}_0$ is normally not the exact solution of the system, there will by a residuum vector $\mathbf{d}_0 = \mathbf{y}(\mathbf{c_0})$, with $\|d_0\| > 0$.

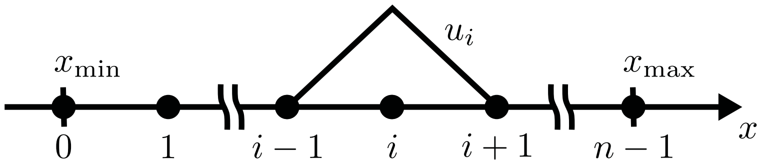

Figure A.7.: The plot shows an uniform grid with n nodes i, $i = 0,1,\dots,n-1$, on the domain $\Omega = [x_{\min}, x_{\max}]$. In addition, the triangular finite element function u_i, Eq. (A.30), is shown.

---

(13) Sometimes, one denotes such a basis function shortly as an "element". However, other authors refer by "element" to the intervals in the domain or they denote the function as well as the interval as a "Finite Element".

(14) There are other types of differential equations, where the corresponding weak formulation needs functions u_j which lay in the class $\mathbb{C}^n$, with $n > 0$.

In the next step, an iterated coefficient vector $\mathbf{c}_1$ is evaluated via $\mathbf{c}_1 = \mathbf{c}_0 + J^{-1}(\mathbf{c}_0) \cdot \mathbf{d}_0$. Here, J denotes the Jacobi matrix of the function system $\mathbf{y}$, which is defined by

$$J = \begin{pmatrix} \frac{\partial y_0}{\partial c_0} & \frac{\partial y_0}{\partial c_1} & \cdots & \frac{\partial y_{n-1}}{\partial c_{n-1}} \\ \frac{\partial y_1}{\partial c_0} & \frac{\partial y_1}{\partial c_1} & \cdots & \frac{\partial y_{n-1}}{\partial c_{n-1}} \\ \vdots & \vdots & \vdots & \vdots \\ \frac{\partial y_{n-1}}{\partial c_0} & \frac{\partial y_{n-1}}{\partial c_1} & \cdots & \frac{\partial y_{n-1}}{\partial c_{n-1}} \end{pmatrix} , \tag{A.31}$$

and $J^{-1}(\mathbf{c}_0)$ denotes the inverse of J at the point $\mathbf{c}_0$. In the Newton method, the iteration

$$\mathbf{c}_{k+1} = \mathbf{c}_k + J^{-1}(\mathbf{c}_k) \cdot \mathbf{d}_k \tag{A.32}$$

is repeated until the norm $\|\mathbf{d}_k\|$ of the residuum vector is smaller than a certain, small value ε(15). Due to the fact that the numerical calculation of a large inverse matrix is elaborate, we perform the Newton iteration (A.32) in a slightly different form. Instead of evaluating J^{-1}, in each iteration we solve the system of linear equations

$$J \cdot (\mathbf{c}_{k+1} - \mathbf{c}_k) = \mathbf{d}_k , \tag{A.33}$$

for the unknown coefficient vector $\mathbf{c}_{k+1}$. From a numerical point of view, the calculation of J and the solution of the system of linear equations $J \cdot (\mathbf{c}_{k+1} - \mathbf{c}_k) = \mathbf{d}_k$ are the costly parts of the Newton method. Especially, the solution of the linear equation system (A.33) via a standard algorithm, such as the *Gauss method*, would need $\mathcal{O}\left(n^3\right)$ operations. Which implies large numerical efforts in the case of grids with several thousand nodes. However, here, we profit form the FEM approach. Due to the small support of the elements (A.29), the system of nonlinear equations (A.28) has a special structure. Namely, the i-th equation does only depend on the coefficients c_{i-1}, c_i and c_{i+1}. As a consequence, the Jacobi matrix is a sparse matrix which has the structure

$$J = \begin{pmatrix} * & * & & & & & & & \\ * & * & * & & & & & & \\ & * & * & * & & & 0 & & \\ & & \ddots & \ddots & \ddots & & & & \\ & & & * & * & * & & & \\ & & & & \ddots & \ddots & \ddots & & \\ & & 0 & & & * & * & * & \\ & & & & & & * & * & * \\ & & & & & & & * & * \end{pmatrix} . \tag{A.34}$$

Here, the $*$ symbols refer to the only nonzero elements of the Jacobi matrix. Now, a system of linear equations for a sparse matrix can efficiently solved by applying iterative methods, such as *Krylov subspace methods*.[237,238] These methods only need $\mathcal{O}(n)$ operations per iteration and the usually converge to sufficient precision in a few iterations. In the code, we use a preconditioned form of the *biconjugate gradient stabilized* (BiCGSTAB) method (see Ref. 238), since this method converged most quickly in comparison to the other iterative methods which we tested.

---

(15) In the code, we usually use $\varepsilon = 10^{-8}$ for the absolute precision.

In summary, in order to solve the nonlinear Poisson equation (A.20) together with the boundary conditions (A.22) numerically, we use the Galerkin method (A.28), which is a finite-dimensional approximation of the weak formulation (A.27) of the original problem (A.22). The Galerkin approach (A.28) leads to a nonlinear equation system which can be solved with the Newton method. Since we set the basis functions u_i in Eq. (A.28) equal to the finite element functions (A.30), the corresponding Jacobi matrix (A.31) is a sparse matrix and the system of linear equations (A.33), which is the central task of the Newton method, can be solved efficiently using an iterative method (preconditioned BiCGSTAB method).

B. Maths

B.1. Inversion of the integral equation (6.13)

Since the solution of the integral equation (6.13),

$$n_\mathrm{e}(\phi) = \int_{\mathbb{R}} f_{\mathrm{e},0}\left(\sqrt{p^2 - 2\,m_\mathrm{e}\,e\,\phi(x)}\right) \mathrm{d}p\,, \tag{B.1}$$

will involve Fourier and inverse Fourier transforms, here, we first recall the classical definitions of the Fourier transform and of its inverse operation.

Definition 1 (Fourier transform) *The Fourier transform $\mathscr{F}_x[f](\omega)$ of a function f with respect to the variable x into a function g of the variable ω is given by*

$$g(\omega) = \mathscr{F}_x[f](\omega) = \frac{1}{\sqrt{2\pi}} \int_{-\infty}^{\infty} f(x)\exp(i\,x\,\omega)\,\mathrm{d}x\,. \tag{B.2}$$

Definition 2 (Inverse Fourier transform) *The inverse Fourier transform $\mathscr{F}_\omega^{-1}[g](x)$ of a function g with respect to the variable ω into a function f of the variable x is given by*

$$f(x) = \mathscr{F}_\omega^{-1}[g](x) = \frac{1}{\sqrt{2\pi}} \int_{-\infty}^{\infty} g(\omega)\exp(-\,i\,\omega\,x)\,\mathrm{d}\omega\,. \tag{B.3}$$

In order to solve the integral equation (B.1), we proceed as follows. First we note that when assuming a Maxwellian distribution $f_{\mathrm{e},0}$, the resulting electron density is given by an exponential function of the electrostatic potential,

$$f_{\mathrm{e},0}(p) = \frac{n_{\mathrm{e},0}}{\sqrt{2\,\pi\,m_\mathrm{e}\,T_{\mathrm{e},0}}}\exp\left(-\frac{p^2}{2\,m_\mathrm{e}\,T_{\mathrm{e},0}}\right) \quad \Longleftrightarrow \quad n_\mathrm{e}(\psi) = n_{\mathrm{e},0}\exp\left(\frac{\psi}{T_{\mathrm{e},0}}\right)\,, \tag{B.4}$$

see Sec. 2.3. Here, ψ is an abbreviation for the product $e\,\phi$, since this product often appears in the following derivation. Next, we introduce the parameter $i\,\beta = 1/T_{\mathrm{e},0}$ with the imaginary unit

i, set $n_{\mathrm{e},0} = 1/\sqrt{2\pi}$ and multiply the expressions (B.4) by an arbitrary function[(1)] $\chi(\beta)$. Hence, we get

$$f_{\mathrm{e},0}(p) = \frac{\sqrt{i\beta}\,\chi(\beta)}{2\pi\sqrt{m_\mathrm{e}}} \exp\left(-i\frac{p^2}{2m_\mathrm{e}}\beta\right) \quad \Longleftrightarrow \quad n_\mathrm{e}(\psi) = \frac{\chi(\beta)}{\sqrt{2\pi}} \exp\left(i\beta\,\psi\right) . \tag{B.5}$$

In the next step, we integrate the above expressions over β from $-\infty$ to ∞. With the assumption, that the previously chosen $\chi(\beta)$ allows to interchange the order of integration in β and p, one obtains

$$f_{\mathrm{e},0}(p) = \frac{1}{\sqrt{2\pi m_\mathrm{e}}} \mathscr{F}_\beta\left[\sqrt{i\beta}\,\chi(\beta)\right]\left(-\frac{p^2}{2m_\mathrm{e}}\right) \quad \Longleftrightarrow \quad n_\mathrm{e}(\psi) = \mathscr{F}_\beta\left[\chi(\beta)\right](\psi) . \tag{B.6}$$

The relations (B.6) contain the Fourier transforms of the functions $\sqrt{i\beta}\,\chi(\beta)$ and $\chi(\beta)$, respectively, relative to the variable β. Applying the definition of the inverse Fourier transform to the right-hand side of Eq. (B.6), one gains an explicit expression for the function χ,

$$\chi(\beta) = \mathscr{F}_\psi^{-1}\left[n_\mathrm{e}(\psi)\right](\beta) , \tag{B.7}$$

and can finally rewrite Eq. (B.6) in the form

$$f_{\mathrm{e},0}(p) = \frac{1}{\sqrt{2\pi m_\mathrm{e}}} \mathscr{F}_\beta\left[\sqrt{i\beta}\,\mathscr{F}_\psi^{-1}\left[n_\mathrm{e}(\psi)\right](\beta)\right]\left(-\frac{p^2}{2m_\mathrm{e}}\right) \quad \Longleftrightarrow \quad n_\mathrm{e}(\psi) . \tag{B.8}$$

The above result constitutes an inversion formula for the relation (B.1). Thus, for an arbitrary density relation $n_\mathrm{e}(\psi)$, the left-hand side of Eq. (B.8),

$$f_{\mathrm{e},0}(p) = \frac{1}{\sqrt{2\pi m_\mathrm{e}}} \mathscr{F}_\beta\left[\sqrt{i\beta}\,\mathscr{F}_\psi^{-1}\left[n_\mathrm{e}(\psi)\right](\beta)\right]\left(-\frac{p^2}{2m_\mathrm{e}}\right) , \tag{B.9}$$

gives the corresponding electron phase space density $f_{\mathrm{e},0}$. Note that although the inversion formula (B.9) was derived using the classical expressions (B.2) and (B.3) for the Fourier transform and its inverse, this approach remains still valid in the generalized sense of Fourier transforms on tempered distributions. This is important in the final step, where we are going to simplify the result.

Since the relation contains a product, one might suggest to use the convolution theorem. Unfortunately, the application of the convolution theorem the context with tempered distributions is a complex task. For this reason, we choose a different way. First, we introduce a special class of spatial electron densities, which are given by Lorentz functions

$$\widehat{n}_\mathrm{e}^\varepsilon(\psi-\zeta) = \frac{1}{\pi}\frac{\varepsilon}{\varepsilon^2+(\psi-\zeta)^2} , \tag{B.10}$$

with ε being a positive real number and ζ an arbitrary potential. Using Eq. (B.9) one finds the corresponding phase space densities

$$f_{\mathrm{e},0}^\varepsilon(p,\zeta) = \frac{1}{2\pi i\sqrt{8m_\mathrm{e}}} \cdot \left\{\left(\zeta+\frac{p^2}{2m_\mathrm{e}}-i\varepsilon\right)^{-3/2} - \left(\zeta+\frac{p^2}{2m_\mathrm{e}}+i\varepsilon\right)^{-3/2}\right\} . \tag{B.11}$$

---

(1) Note that the convergence of the integral in Eq. (B.1) is still ensured.

Thus, we have

$$\widehat{n}_{\mathrm{e}}^{\varepsilon}(\psi-\zeta) \quad \Longleftrightarrow \quad f_{\mathrm{e},0}^{\varepsilon}(p,\zeta)\,. \tag{B.12}$$

Now, due to the linearity of Eq. (B.1) in $f_{\mathrm{e},0}$, we directly obtain the relation

$$\int\limits_{-\infty}^{\infty} \widehat{n}_{\mathrm{e}}^{\varepsilon}(\psi-\zeta)\, n_{\mathrm{e}}(\zeta)\,\mathrm{d}\zeta \quad \Longleftrightarrow \quad \int\limits_{-\infty}^{\infty} f_{\mathrm{e},0}^{\varepsilon}(p,\zeta)\, n_{\mathrm{e}}(\zeta)\,\mathrm{d}\zeta \tag{B.13}$$

by multiplying Eq. (B.12) with an arbitrary spatial density $n_{\mathrm{e}}(\zeta)$ and integrating over ζ. Next we take the limit $\varepsilon \to 0$ of Eq. (B.13). The left-hand side of Eq. (B.13) is simply given by $n_{\mathrm{e}}(\psi)$, because Eq. (B.10) converges in the sense of distributions to the Dirac δ-distribution for $\varepsilon \to 0$. Therefore, we derive the following expression

$$n_{\mathrm{e}}(\psi) \quad \Longleftrightarrow \quad f_{\mathrm{e},0}(p)\,, \tag{B.14}$$

with

$$f_{\mathrm{e},0}(p) = \lim_{\varepsilon\to 0} \int\limits_{-\infty}^{\infty} f_{\mathrm{e},0}^{\varepsilon}(p,\zeta)\, n_{\mathrm{e}}(\zeta)\,\mathrm{d}\zeta\,. \tag{B.15}$$

At this point we emphasize that the result (B.15) is equivalent to Eq. (B.9). In the last step of the simplification one has to evaluate the above limit. This step has to be done carefully because of the complex roots in Eq. (B.15). Since the evaluation is extensive, it is outsourced to Sec. B.2 and we here give only the final result,

$$f_{\mathrm{e},0}(p) = \frac{m_{\mathrm{e}}}{\pi} \int\limits_{-\infty}^{-\frac{p^2}{2m_{\mathrm{e}}}} \frac{n_{\mathrm{e}}\left(-\frac{p^2}{2m_{\mathrm{e}}}\right) - n_{\mathrm{e}}(\zeta)}{|p^2 + 2m_{\mathrm{e}}\,\zeta|^{3/2}}\,\mathrm{d}\zeta\,. \tag{B.16}$$

The above result is a compact inversion formula for the density relation(2) (B.1).

B.2. Evaluation of the limit in Eq. (B.15)

This section deals with the evaluation of the limit in Eq. (B.15), which led to the central inversion formula of Sec. 6.1, Eq. (6.14) (resp. Eq (B.16)) Hence, we want to show that

$$f_{\mathrm{e},0}(p) = \lim_{\varepsilon\to 0} \int\limits_{-\infty}^{\infty} f_{\mathrm{e},0}^{\varepsilon}(p,\zeta)\, n_{\mathrm{e}}(\zeta)\,\mathrm{d}\zeta\,, \tag{B.17}$$

with

$$f_{\mathrm{e},0}^{\varepsilon}(p,\zeta) = \frac{1}{2\pi i\sqrt{8m_{\mathrm{e}}}} \cdot \left\{ \left(\zeta + \frac{p^2}{2m_{\mathrm{e}}} - i\varepsilon\right)^{-3/2} - \left(\zeta + \frac{p^2}{2m_{\mathrm{e}}} + i\varepsilon\right)^{-3/2} \right\}, \tag{B.18}$$

---

(2) Note again, that it is just a reformulation of the interim findings Eq. (B.9) and Eq. (B.15). Hence, all relations are equivalent.

equals Eq. (B.16),

$$f_{\mathrm{e},0}(p) = \frac{m_\mathrm{e}}{\pi} \int\limits_{-\infty}^{-\frac{p^2}{2m_\mathrm{e}}} \frac{n_\mathrm{e}\left(-\frac{p^2}{2m_\mathrm{e}}\right) - n_\mathrm{e}(\zeta)}{|p^2 + 2m_\mathrm{e}\,\zeta|^{3/2}}\,\mathrm{d}\zeta\,. \tag{B.19}$$

In order to evaluate Eq. (B.17) (resp. Eq. (B.15)), we start by considering the integral[239]

$$\Phi(z) = \int\limits_{\Gamma} \frac{f(\zeta)}{\zeta - z}\,\mathrm{d}\zeta\,, \tag{B.20}$$

which defines a function on the complex plane $\mathbb{C}$. Here, Γ is an interval on the real axis, $\Gamma = \{\zeta + 0\cdot i : \zeta_a \le \zeta \le \zeta_b\}$, and f is a holomorphic function on $\mathbb{C}$ which fulfills additionally the Hölder condition $\|f(x) - f(y)\| \le H \cdot \|x-y\|^{\alpha_H}$ for all x, y on Γ, with some constants $H > 0$ and $0 < \alpha_H \le 1$.

In the context of the evaluation of Eq. (B.17), the most important issue of Eq. (B.20) is that

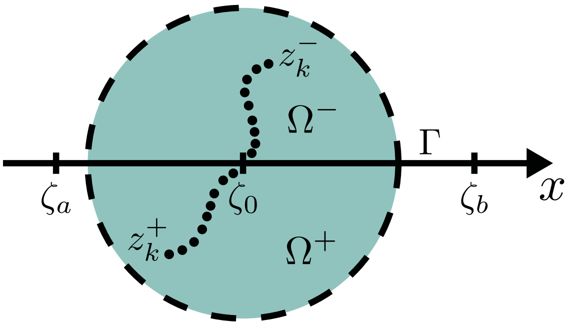

Figure B.1.: The function $\Phi(z)$, Eq. (B.20), resp., Eq. (B.27), is defined on the complex domain $\mathbb{C}$. Γ is an interval on the real axis, with $\Gamma = [\zeta_a, \zeta_b]$ and ζ_0 is a point in between ζ_a and ζ_b. Further, Ω^- and Ω^+ refer to the left- and the right-hand region of Γ around the point ζ_0. The sequences of points z_k^- and z_k^+ converges from the left- and the right-hand side against the point ζ_0, respectively.

Φ jumps at Γ. More precisely, let $\{z_k^+\}_{k=0}^\infty$ be a sequence of points in the right region Ω^+ of Γ, which tends towards a point ζ_0 on Γ for $k_1 \to \infty$. Equivalent, $\{z_k^-\}_{k=0}^\infty$ denotes a sequence of points tending towards ζ_0 from the left-hand region Ω^-. Then, one has

$$\Phi^+(\zeta_0) - \Phi^-(\zeta_0) = -2\pi i f(\zeta_0)\,, \tag{B.21}$$

with

$$\Phi^\pm(\zeta_0) := \lim_{k\to\infty} \Phi(z_k^\pm) \tag{B.22}$$

denoting the limits of Φ when approaching ζ_0 from the right- and left-hand side, respectively. According to Eq. (B.21), the one-sided limits of Φ are distinct — or in other words Φ jumps on Γ. In order to prove Eq. (B.21) one could simply apply the Cauchy integral formula. However, this would not work in the more general case which we will consider below. For this reason, we take another path. At first, we rewrite Eq. (B.20) in the following form

$$\Phi(z) = \underbrace{\int\limits_{\Gamma} \frac{f(\zeta)-f(z)}{\zeta - z}\,\mathrm{d}\zeta}_{T_1} + f(z)\cdot \underbrace{\int\limits_{\Gamma} \frac{1}{\zeta - z}\,\mathrm{d}\zeta}_{T_2} \; . \tag{B.23}$$

As discussed in Ref. 239, the integrand in T_1 is a holomorphic function for each $z \in \mathbb{C}\backslash\Gamma$. Furthermore, T_1 is improperly integrable on Γ. Therefore, the left and right limits T_1^- and T_1^+ are equal,

$$T_1^+(\zeta_0) - T_1^-(\zeta_0) = 0 \; . \tag{B.24}$$

The term T_2 can be integrated to

$$\begin{aligned} T_2(z) = \ln(\zeta - z)|_\Gamma = \ln\|\zeta - z\| + i\cdot \arg(\zeta - z)|_\Gamma = \\ \ln\|\zeta_b - z\| + i\cdot\arg(\zeta_b - z) - \ln\|\zeta_a - z\| - i\cdot\arg(\zeta_a - z) \; . \end{aligned} \tag{B.25}$$

Here, we want to recall a central issue of the argument function $\arg(z)$. While it is smooth on $\mathbb{C}\backslash\mathbb{R}_-$, it jumps along the negative real axis $\mathbb{R}_-$ from π to $-\pi$, if one crosses $\mathbb{R}_-$ with a positive orientation. More precisely, one has $\lim\limits_{\varepsilon\to 0} \arg(\zeta \pm i\cdot\varepsilon) = \pm\pi$ for all $\zeta < 0$. As a consequence, one finds

$$T_2^+(\zeta_0) = \ln\|\zeta_b - \zeta_0\| + i\cdot 0 - \ln\|\zeta_a - \zeta_0\| - i\cdot\pi \tag{B.26a}$$

and

$$T_2^-(\zeta_0) = \ln\|\zeta_b - \zeta_0\| + i\cdot 0 - \ln\|\zeta_a - \zeta_0\| + i\cdot\pi \; . \tag{B.26b}$$

Summarizing Eqs. (B.24) and (B.26), one obtains the jump relation (B.21).

Next, we want to generalize the results of Ref. 239 to the expression

$$\Phi(z) = \int\limits_{\Gamma} \frac{f(\zeta)}{(\zeta - z)^\kappa}\,\mathrm{d}\zeta \; , \tag{B.27}$$

with $\kappa > 0$. Equivalent to Eq. (B.23), we partition Eq. (B.27) into

$$\Phi(z) = \underbrace{\int\limits_{\Gamma} \frac{f(\zeta)-f(z)}{(\zeta - z)^\kappa}\,\mathrm{d}\zeta}_{T_1} + f(z)\cdot \underbrace{\int\limits_{\Gamma} \frac{1}{(\zeta - z)^\kappa}\,\mathrm{d}\zeta}_{T_2} \; . \tag{B.28}$$

The term T_2 can be handled similar to the procedure above. The integration yields

$$\begin{aligned} T_2(z) = \frac{1}{1-\kappa}\cdot(\zeta - z)^{1-\kappa}\Big|_\Gamma = \frac{1}{1-\kappa}\cdot\|\zeta - z\|^{1-\kappa}\cdot\exp\left(i\cdot(1-\kappa)\cdot\arg(\zeta - z)\right)\Big|_\Gamma = \\ \frac{1}{1-\kappa}\cdot\|\zeta_b - z\|^{1-\kappa}\cdot\exp\left(i\cdot(1-\kappa)\cdot\arg(\zeta_b - z)\right) - \\ \frac{1}{1-\kappa}\cdot\|\zeta_a - z\|^{1-\kappa}\cdot\exp\left(i\cdot(1-\kappa)\cdot\arg(\zeta_a - z)\right) \; . \end{aligned} \tag{B.29}$$

From which one gets

$$T_2^+(\zeta_0) = \frac{1}{1-\kappa} \cdot \|\zeta_b - \zeta_0\|^{1-\kappa} \cdot \exp\left(i \cdot (1-\kappa) \cdot 0\right) - \frac{1}{1-\kappa} \cdot \|\zeta_a - \zeta_0\|^{1-\kappa} \cdot \exp\left(i \cdot (1-\kappa) \cdot \pi\right) \tag{B.30}$$

and

$$T_2^-(\zeta_0) = \frac{1}{1-\kappa} \cdot \|\zeta_b - \zeta_0\|^{1-\kappa} \cdot \exp\left(i \cdot (1-\kappa) \cdot 0\right) - \frac{1}{1-\kappa} \cdot \|\zeta_a - \zeta_0\|^{1-\kappa} \cdot \exp\left(-i \cdot (1-\kappa) \cdot \pi\right) \ . \tag{B.31}$$

Thus, one has

$$T_2^+(\zeta_0) - T_2^-(\zeta_0) = -\frac{2i}{1-\kappa} \cdot \|\zeta_a - \zeta_0\|^{1-\kappa} \cdot \sin\left((1-\kappa) \cdot \pi\right) = -\frac{2i}{1-\kappa} \cdot \|\zeta_a - \zeta_0\|^{1-\kappa} \cdot \sin\left(\kappa\pi\right) \ . \tag{B.32}$$

The treatment of T_1 needs a precise study. For this purpose, we partition T_1 in form of

$$T_1(z) = \int\limits_{\zeta_a}^{\zeta_0} \frac{f(\zeta) - f(z)}{(\zeta - z)^\kappa} \, \mathrm{d}\zeta + \int\limits_{\zeta_0}^{\zeta_b} \frac{f(\zeta) - f(z)}{(\zeta - z)^\kappa} \, \mathrm{d}\zeta = \underbrace{\int\limits_{\zeta_a}^{\zeta_0} \frac{f(\zeta) - f(z)}{\|\zeta - z\|^\kappa} \cdot \exp\left(-i\kappa \cdot \arg(\zeta - z)\right) \, \mathrm{d}\zeta}_{T_{1,1}} + \underbrace{\int\limits_{\zeta_0}^{\zeta_b} \frac{f(\zeta) - f(z)}{\|\zeta - z\|^\kappa} \cdot \exp\left(-i\kappa \cdot \arg(\zeta - z)\right) \, \mathrm{d}\zeta}_{T_{1,2}} \ . \tag{B.33}$$

Assuming $\zeta > \zeta_0$, one has $\lim\limits_{k \to 0} \arg(\zeta - z_k^+) = 0$ as well as $\lim\limits_{k \to 0} \arg(\zeta - z_k^-) = 0$. Thus, one finds $T_{1,2}^+(\zeta_0) - T_{1,2}^-(\zeta_0) = 0$ under the condition that the improper integral

$$\int\limits_{\zeta_0}^{\zeta_b} \frac{f(\zeta) - f(\zeta_0)}{(\zeta - \zeta_0)^\kappa} \, \mathrm{d}\zeta \tag{B.34}$$

exists. This is guaranteed for $\alpha_H - \kappa > -1$. In contrast, for $\zeta < \zeta_0$ the relations $\lim\limits_{k \to 0} \arg(\zeta - z_k^+) = \pi$ and $\lim\limits_{k \to 0} \arg(\zeta - z_k^-) = -\pi$ are found. Therewith, one has

$$T_{1,1}^+(\zeta_0) - T_{1,1}^-(\zeta_0) = \exp(-i\kappa\pi) \int\limits_{\zeta_a}^{\zeta_0} \frac{f(\zeta) - f(\zeta_0)}{\|\zeta - \zeta_0\|^\kappa} \, \mathrm{d}\zeta - \exp(i\kappa\pi) \int\limits_{\zeta_a}^{\zeta_0} \frac{f(\zeta) - f(\zeta_0)}{\|\zeta - \zeta_0\|^\kappa} \, \mathrm{d}\zeta = -2i \cdot \sin(\kappa\pi) \cdot \int\limits_{\zeta_a}^{\zeta_0} \frac{f(\zeta) - f(\zeta_0)}{\|\zeta - \zeta_0\|^\kappa} \, \mathrm{d}\zeta \tag{B.35}$$

for the jump characteristic of the term $T_{1,1}$. Altogether, one finds the result

$$\Phi^+(\zeta_0) - \Phi^-(\zeta_0) = -2i \cdot \sin(\kappa\pi) \cdot \left[\frac{f(\zeta_0)}{1-\kappa} \cdot \|\zeta_a - \zeta_0\|^{1-\kappa} + \int\limits_{\zeta_a}^{\zeta_0} \frac{f(\zeta) - f(\zeta_0)}{\|\zeta - \zeta_0\|^{\kappa}} \, \mathrm{d}\zeta \right] , \tag{B.36}$$

which is valid[3] for $\kappa < 1 + \alpha_H$. The case $\kappa = 1$ is included by taking the corresponding limit in Eq. (B.36).

Now, by comparing the expression (B.17) with the general expression for $\Phi(z)$, Eq. (B.27), one can rewrite Eq. (B.17) as

$$f_{\mathrm{e},0}(p) = \Phi^+(\zeta_0) - \Phi^-(\zeta_0) , \tag{B.37}$$

by setting $\kappa = 3/2$, $\Gamma = \mathbb{R}$, $\zeta_0 = -p^2/(2m_\mathrm{e})$ and

$$f(\zeta) = -\frac{n_\mathrm{e}(\zeta)}{2\pi i \sqrt{8m_\mathrm{e}}} \tag{B.38}$$

in Eq. (B.27). Then, by using the expression (B.36), we finally confirm the result (B.19) (resp. Eq. (6.14)).

B.3. Proof of Eq. (7.18)

In this section, we want to confirm the statement (7.18),

$$E(t) = \sqrt{2/\varepsilon_0} \sqrt{n_\mathrm{e}(t)\, T_\mathrm{e}(t)} . \tag{B.39}$$

Here, we want to remind that the above expression assumes nonrelativistic electrons. As discussed in Sec. 7.2, in the relativistic case Eq. (B.39) (resp. Eq. (7.18)) in general fails.

To proof Eq. (B.39) we make the following consideration. The integration of the Poisson equation (7.1g),

$$\varepsilon_0 \frac{\partial^2 \phi}{\partial x^2} = e \cdot [n_\mathrm{e}(\phi) - Z_\mathrm{i}\, n_\mathrm{i}] . \tag{B.40}$$

at the boundaries of the ion distribution yields

$$\frac{\varepsilon_0}{2} \left(\frac{\partial \phi}{\partial x} \right)^2 = H(\phi) . \tag{B.41}$$

Here, H is an antiderivative of $e n_\mathrm{e}(\phi)$, thus, $\partial H(\phi)/\partial\phi = e n_\mathrm{e}(\phi)$. By comparing Eqs. (B.39) and (B.41) we find $H(\phi) = n_\mathrm{e}(\phi)\, T_\mathrm{e}(\phi)$. This implies that if Eq. (B.39) is a true statement then $n_\mathrm{e} T_\mathrm{e}$ has to be an antiderivative of n_e,

$$\frac{\partial}{\partial \phi} [n_\mathrm{e}(\phi)\, T_\mathrm{e}(\phi)] = e n_\mathrm{e}(\phi) . \tag{B.42}$$

---

[3] We want to note that the limit $\Phi^+(\zeta_0) - \Phi^-(\zeta_0)$ might exist in the case $\kappa \geq 1 + \alpha_H$. However, it cannot be calculated using Eq. (B.36), since the integral on the right-hand side is not improper integrable any more.

Next, we recall that the local temperature is connected to the local thermal energy ε_e via

$$\varepsilon_\mathrm{e} = \frac{\mathbb{Z}(T_\mathrm{e})}{2} n_\mathrm{e} T_\mathrm{e} \,, \tag{B.43}$$

with $\mathbb{Z}$ referring to the degrees of freedom, Eq. (7.1c),

$$\mathbb{Z}(\beta) = 2 \cdot \left(1 + \beta \cdot \left[\frac{\mathrm{K}_0(\beta)}{\mathrm{K}_1(\beta)} - 1\right]\right) \,. \tag{B.44}$$

Following Ref. 191, the thermal energy for an electron population with the phase space density f_e is given by

$$\varepsilon_\mathrm{e} = \int_{\mathbb{R}} f_\mathrm{e}\, \varepsilon_\mathrm{kin} \,\mathrm{d}p \,. \tag{B.45}$$

Since we only consider the nonrelativistic limit, one has $\mathbb{Z} = 1$ and $\varepsilon_\mathrm{kin}(p) = p^2/2m_\mathrm{e}$. Expressing T_e via the thermal energy (B.43) and f_e through the general result for a nonrelativistic stationary distribution (2.20b),

$$n_\mathrm{e}(x) = \int_{\mathbb{R}} f_{\mathrm{e},0}\left(\sqrt{p^2 - 2m_\mathrm{e}\, e\, \phi(x)}\right) \mathrm{d}p \,, \tag{B.46}$$

the proposition (B.42) becomes

$$\frac{\partial}{\partial \phi}\left[2 \int_{\mathbb{R}} f_{\mathrm{e},0}(r(\phi, p)) \frac{p^2}{2m_\mathrm{e}} \,\mathrm{d}p\right] = e n_\mathrm{e}(\phi) \,, \tag{B.47}$$

with $r = \sqrt{p^2 - 2m_\mathrm{e}\, e\, \phi(x)}$. Now, according to the relations

$$\frac{\partial r}{\partial p} = \frac{p}{r} \tag{B.48a}$$

$$\frac{\partial r}{\partial \phi} = -\frac{e m_\mathrm{e}}{r} \,, \tag{B.48b}$$

one can rewrite $\partial r/\partial \phi$ as

$$\frac{\partial r}{\partial \phi} = -\frac{e m_\mathrm{e}}{p} \frac{\partial r}{\partial p} \tag{B.49}$$

and Eq. (B.47) becomes

$$-\int_{\mathbb{R}} p \frac{\partial}{\partial p} f_{\mathrm{e},0}(r(\phi, p)) \,\mathrm{d}p = n_\mathrm{e}(\phi) \,. \tag{B.50}$$

Next, integration by parts results in

$$-\, p\, f_{\mathrm{e},0}(r(\phi, p))\big|_{-\infty}^{\infty} + \int_{\mathbb{R}} f_{\mathrm{e},0}(r(\phi, p)) \,\mathrm{d}p = n_\mathrm{e}(\phi) \,. \tag{B.51}$$

Since the first term on the left-hand side of Eq. (B.51) is zero(4) and the second term is exactly the definition of the spatial electron density in the nonrelativistic limit, Eq. (B.46), the relation (B.51) is true. This in turn confirms the proposition (B.42) and, consequently, the statement (B.39) (resp. Eq. (7.18)).

---

(4) To ensure the existence of the electron density (2.22b), the electron phase space density $f_{\mathrm{e},0}$ has to be absolutely integrable on $\mathbb{R}$ implying $\lim\limits_{p\to\pm\infty} p\, f_{\mathrm{e},0} = 0$ as a precondition.

Tabellarischer Lebenslauf

Persönliche Daten

Geburtsdatum und Geburtsort:	23.05.1982 in Saalfeld/Saale
Staatsangehörigkeit:	Deutsch

Schulische Ausbildung, Zivildienst und Studium

1988–1992	Grundschule *Hans Beimler*, Saalfeld
1992–2000	Gymnasium *Erasmus Reinhold Gymnasium*, Saalfeld Abschluss: Abitur
2000–2001	Zivildienst
2001–2006	Physikstudium an der *Friedrich-Schiller Universität Jena*, Jena Abschluss: Diplom

Beruflicher Werdegang und Promotion

November 2006 – Mai 2007	wissenschaftlicher Mitarbeiter an der Physikalisch-Astronomischen Fakultät der *Friedrich-Schiller Universität Jena*, Jena
ab Mai 2007	Doktorand an der Physikalisch-Astronomischen Fakultät der *Friedrich-Schiller Universität Jena*, Jena angestrebter Abschluss: Dr. rer. nat.

Jena, den 18.09.2013

Thomas Kiefer

Thomas Kiefer

Ehrenwörtliche Erklärung

Ich erkläre hiermit ehrenwörtlich, dass ich die vorliegende Arbeit selbstständig und ohne unzulässige Hilfe Dritter und ohne Benutzung anderer als der angegebenen Hilfsmittel und Literatur angefertigt habe.

Die aus anderen Quellen direkt oder indirekt übernommenen Daten und Konzepte sind unter Angabe der Quelle gekennzeichnet. Weitere Personen waren nicht an der inhaltlich-materiellen Erstellung der vorliegenden Arbeit beteiligt.

Insbesondere habe ich hierfür nicht die entgeltliche Hilfe von Vermittlungs- bzw. Beratungsdiensten (Promotionsberater oder andere Personen) in Anspruch genommen. Niemand hat von mir unmittelbar oder mittelbar geldwerte Leistungen für die Arbeiten erhalten, die im Zusammenhang mit dem Inhalt der vorgelegten Dissertation stehen.

Die Arbeit wurde bisher weder im In- noch im Ausland in gleicher oder ähnlicher Form einer anderen Prüfungsbehörde vorgelegt. Die geltende Promotionsordnung der Physikalisch-Astronomischen Fakultät ist mir bekannt.

Ich versichere ehrenwörtlich, dass ich nach bestem Wissen die reine Wahrheit gesagt und nichts verschwiegen habe.

Jena, den 18.09.2013

Thomas Kiefer

Thomas Kiefer

Danksagung

Ich möchte mich bei meinem Doktorvater Prof. Malte C. Kaluza für die Bereitstellung des Themas der Promotion, den stets freundlichen Umgang, für das entgegengebrachte Vertrauen und die große Handlungsfreiheit sowie die kompetente Betreuung während all der Jahre bedanken.

Meine größte Dankbarkeit gehört Dr. Theodor Schlegel, ohne den die vorliegende Arbeit undenkbar gewesen wäre. Ich bedanke mich herzlich für seinen unermüdlichen Einsatz, seine permanente Unterstützung sowie die unzähligen wertvollen Gespräche, die immer in freundlicher und motivierender Atmosphäre stattfanden.

Bei Prof. Reinhard Meinel möchte ich mich herzlich bedanken, dass er mir auch nach meiner Zeit als Diplomand immer hilfreich zur Seite stand. Wann immer ich bei physikalischen und mathematischen Problemen einen fachlichen Rat benötigte, haben mir seine Intuition und Fachkenntnis stets helfen können.

Des weiteren möchte ich mich bei Prof. Winfried Schäfer für eine Reihe von freundlichen und konstruktiven Gesprächen zu mathematischen Fragestellungen bedanken sowie die gründliche Prüfung einiger verwickelter mathematischer Rechnungen.

Bei der gesamten Arbeitsgruppe ”Relativistische Laserphysik” bedanke ich mich für jegliche Hilfe und ein immer freundliches, kollegiales Miteinander.

An dieser Stelle möchte ich außerdem meine tiefe Dankbarkeit gegenüber meinen Freunden und meiner Familie ausdrücken, ohne die all dies hier ohne Bedeutung für mich wäre. Namentlich möchte ich dabei insbesondere meine Großmutter Elisabeth Koch, meine Mutter Petra Kiefer und nicht zuletzt meine beiden Geschwister Susan und Stefan Kiefer hervorheben.